Toward Detection and Characterization of Exoplanetary Magnetic Fields via Low Frequency Radio Observation

by

Mary Knapp

B.S. in Aerospace Engineering, MIT (2011)

Submitted to the Department of Earth, Atmospheric, and Planetary Science
in partial fulfillment of the requirements for the degree of

Ph.D. in Planetary Science

at the

MASSACHUSETTS INSTITUTE OF TECHNOLOGY

February 2018

Author .....
Department of Earth, Atmospheric, and Planetary Science
October 27, 2017

Certified by .....
Sara Seager
Class of 1941 Professor, Department of Earth, Atmospheric, and Planetary Sciences and Department of Physics
Thesis Supervisor

Accepted by .....
Robert D. van der Hilst
Schlumberger Professor of Earth and Planetary Sciences
Head, Department of Earth, Atmospheric, and Planetary Sciences

Toward Detection and Characterization of Exoplanetary Magnetic Fields via Low Frequency Radio Observation

by

Mary Knapp

Submitted to the Department of Earth, Atmospheric, and Planetary Science
on October 27, 2017, in partial fulfillment of the
requirements for the degree of
Ph.D. in Planetary Science

Abstract

Low frequency radio emission from planets is produced by the interaction of energetic charged particles from the planet's ionosphere and/or the solar wind with the planet's magnetic field. The temporal and spectral characteristics and variability of planetary radio emission encode information about a planet's magnetic field strength and morphology, rotation, and interior. This thesis describes three distinct approaches to detecting radio emission from extrasolar planets (exoplanets).

The first is a novel approach using 'big data' and computer aided discovery tools to mine radio survey images for faint radio emission from the location of nearby stars. The flexible approach described in this thesis produced upper limits of ∼100x Jovian radio flux for a large sample of nearby stars and known exoplanet systems. The sensitivity is sufficient that large radio bursts from nearby stars or planets could have been detected if they took place during the survey observation(s). The framework developed here can be used for automated exoplanet radio emission searches in future radio survey data.

The second approach described herein is a blind survey of the nearest Northern hemisphere stars across a broad range of frequencies in order to detect as-yet unknown planets or set tight constraints on radio emission from the stars and possible substellar companions. The survey approach used here is novel because it makes no assumptions about which stars are most likely to host radio emitting planets and it covers frequencies from 30 MHz to 4 GHz. This survey produced a detection of multiple ∼50% circularly polarized flares from the M dwarf binary system Ross 614 as well as limits at the 10x Jovian flux level for the remaining stars observed. The limits attained from this survey are the first published at 1-4 GHz for these objects and the only available radio limits for a newly discovered cool (T9) brown dwarf. The limits from this survey place a preliminary constraint on the magnetic field of the brown dwarf at <350 G.

The third approach focuses on known exoplanet systems and targets key orbital phases where intense radio emission is predicted. In the case of eccentric hot Jupiter HD 80606 b, radio flux from the planet is expected to increase by a factor of up

to 3000 compared to the quiescent flux as the planet passes within 6 $R_\star$of its host at periastron due to high density stellar wind impinging on HD 80606 b's putative magnetosphere. Data obtained from LOFAR LBA is used to set the lowest limits to date on radio flux from HD 80606 b near planetary periastron. The same concept of orbital phase targeting is used to optimize an observing strategy for recently-discovered multiple planet host TRAPPIST-1. In the case of TRAPPIST-1, the quadrature phases of planets TRAPPIST-1 b and TRAPPIST-1 c are targeted to maximize the chance of observing Io-Jupiter like planetary modulation of stellar radio emission. The quadrature phase targeting approach is new to this field.

The thesis concludes with a discussion of the benefits of space-based observation for exoplanetary radio searches. Ground-based observations are limited by the plamsa frequency of the ionosphere, so planets with Earth-like magnetic fields cannot be observed. Telescopes on the ground also suffer from ionospheric phase errors that are difficult to fully calibrate. Space-based observation does not suffer from the effects of the ionosphere and can therefore support lower frequency observations than ground-based instruments. A novel instrument, the vector sensor, optimized for space-based radio interferometry is introduced. New algorithms for all-sky vector sensor imaging have been developed and tested in simulation and on sky data with encouraging results. Finally, the prospects for detecting Earth- or Jupiter-analogs in the solar neighborhood, either from the ground or from space, are assessed. Very large space-based arrays are required to detect either Jupiter or the Earth at 10 pc; at least 10^5–10^6 antennas are needed for sufficient sensitivity.

Thesis Supervisor: Sara Seager
Title: Class of 1941 Professor, Department of Earth, Atmospheric, and Planetary Sciences and Department of Physics

Acknowledgments

First and foremost, I thank my Ph.D. advisor, Sara Seager, for taking a chance on an engineer and turning me into a scientist. You have opened up new worlds to me and I will be forever grateful for your mentoring and friendship. Ad astra!

I thank my thesis committee, Ben Weiss, Tom Herring, Frank Lind, Daniel Winterhalter, and Dan Cziczo. Special thanks to Dan Czizo for coming onboard at the last minute.

Thank you to Frank Lind, Mike Hecht, Colin Lonsdale, Ryan Volz, Geoff Crew, Phil Erickson, and many others at Haystack for patiently teaching me radio astronomy. Here's to long nights of proposal writing and cold days trying to make the ATOM antenna work. Thank you to Frank Robey of MIT Lincoln Lab for teaching me the language of array processing and introducing me to the wonderful world of vector sensors.

I want to thank Daniel Winterhalter of JPL for spirited discussions about radio astronomy and many other topics, the use of your lovely office when I visited JPL, and your company on our trips into the Dutch wilderness to visit ASTRON. Thank you also to Joe Lazio and Walid Majid of JPL for radio astronomy insights.

I would not have made it through this process without the support and advice of members of the Seager research group, past and present. Thank you Julien, Vlada, Andras, Stephen, Clara, Janusz, and William. Thank you also to Catherine, for bringing me brownies exactly when I needed them most.

LOFAR data acquisition and reduction would not have been possible without the dedicated and hardworking science support team at ASTRON and others involved with LOFAR software development. Thank you to Manu Orrú, Marco Iacobelli, Tammo Jan Dijkema, Luciano Cerrigone, Aleksandar Shulevski, Andreas Horneffer, Roberto Pizzo, Francesco de Gasperin, Adam Stewart, David Rafferty, Raymond Oonk, and many others for answering my endless questions and emails with unfailing patience and unparalleled expertise.

Special thanks to Reinout van Weeren for meeting with me in person at CfA several times to delve into the complexities of LOFAR data. Your advice was invaluable in clearing up confusion about why my data reduction was not working. Thank you also to Tim Bastian for advice on VLA observations and for teaching me about stellar radio flares.

Finally, thank you to my sister Anna for buying me pickles and making me proud. You're up next for a Ph.D. - good luck, sis!

This material is based upon work supported by the National Science Foundation Graduate Research Fellowship.

This research was carried out (in part) at the Jet Propulsion Laboratory, California Institute of Technology, under a contract with the National Aeronautics and Space Administration and funded through the Director's Research and Development Fund Program.

Some parts of work had its inception at the "Planetary Magnetic Fields: Planetary

Interiors and Habitability" (2013) study funded by the W.M. Keck Institute for Space Studies.

The National Radio Astronomy Observatory is a facility of the National Science Foundation operated under cooperative agreement by Associated Universities, Inc.

I thank the staff of the GMRT that made these observations possible. GMRT is run by the National Centre for Radio Astrophysics of the Tata Institute of Fundamental Research.

This research has made use of the SIMBAD database, VizieR catalogue access tool, and Aladin sky atlas, CDS, Strasbourg, France.

This research has made use of the Exoplanet Orbit Database and the Exoplanet Data Explorer at exoplanets.org.

This thesis is dedicated to my parents, Ellen and Jason Knapp. You encouraged me to keep asking "why?" and inspired me to go out and find my own answers. Thank you for your love and support. This is for you.

Contents

List of Figures

List of Tables

Chapter 1

Introduction

This chapter provides an overview of planetary magnetic fields in the solar system (1.1), the sources and properties of radio emission from solar system planets and their connection to magnetic fields (1.2), gives an overview of searches for exoplanetary radio emission (1.3), and concludes with an extended discussion of the connection between planetary magnetic fields and habitability (1.4).

1.1 Planetary Magnetic Fields in the Solar System

Planetary magnetic fields are generated deep in the interiors of planets by the dynamo effect where a seed magnetic field is amplified and maintained by vigorous convection and rotation in an electrically conductive medium. The conductive fluid in which the dynamo is generated varies among solar system planets but the overall mechanism is thought to be similar. Planets with no intrinsic magnetic field may have an induced magnetic field if they have an ionosphere that interacts with the solar wind. See Figure 1-1. Venus and Mars both exhibit induced magnetic fields. Induced magnetic fields are generally weaker than dynamo fields and difficult to detect remotely; induced fields will not be discussed in this work. The exception is induced magnetic fields of planets or moons that interact with the field of their primary (e.g. Io/Europa and Jupiter). This type of interaction is discussed in Section 1.2.4. The following discussion focuses on intrinsic planetary magnetic fields that arise from interior dynamos.

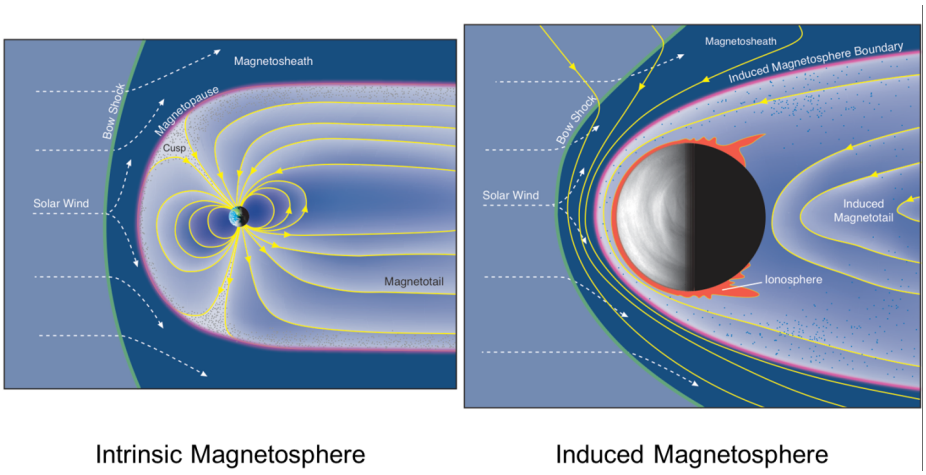

Figure 1-1: Intrinsic magnetosphere (Earth, left) and induced magnetosphere (Mars/Venus, right). Images courtesy of S. Bartlett via David Brain

The magnetic fields and magnetic histories of the four terrestrial planets are as varied as their surface environments. The Earth and Mercury have present-day global fields generated in their liquid iron outer cores. The Earth's Moon and Mars have only local, weak magnetic fields that originate in magnetized minerals in rocks in certain areas on their surfaces. This local magnetism is the remnant of a past global magnetic field. Mars and the Moon had dynamos in their early history, but lost them. Venus has no present-day global magnetic field and little or no remnant magnetization. The surface temperature of Venus (730 K [259]) is above the Curie point of most magnetic minerals, so any remnant magnetization of Venusian surface rocks has likely been destroyed [251]. If the Venusian magnetic record has indeed been wiped clean, there is no direct way to determine whether Venus had a global magnetic field in the past. The contrast between the Earth and Venus, two similarly sized terrestrial bodies, presents a key question for the study of terrestrial-sized exoplanets: which planets are expected to have magnetic fields? Size alone apparently cannot answer that question.

All four of the gas giant planets have present-day global magnetic fields. Jupiter and Saturn exhibit strong dipolar magnetic fields that look like a scaled-up version of the Earth's magnetic field. Jupiter's dipole is slightly inclined from its spin axis (10°), while Saturn's magnetic dipole axis is exactly aligned with its rotation axis

Table 1.1. Magnetic fields of the solar system planets

Planet	Mass ($M_\oplus$)	Radius ($R_\oplus$)	Rotation Period (days)	Obliquity (°)	Magnetic Moment[a]	Equatorial Surface Field (G)	Dipole Tilt[b] (°)	Dipolarity[c]
Mercury	0.0553	0.383	58.8	0.034	0.0007	0.003	<0.8	0.71
Earth	1	1	1	23.4	1	0.305	10.8	0.61
Jupiter	317.8	11.21	0.415	3.1	20,000	4.2	-9.6	0.61
Ganymede	0.025	0.413	7.154	0	0.0017	0.00719[d]	-4[d]	0.95[d]
Saturn	95.2	9.45	0.445	26.7	600	0.20	<0.5	0.85
Uranus	14.5	4.01	-0.729[e]	97.8	50	0.23	-59	0.42
Neptune	17.1	3.88	0.673	28.3	25	0.14	-47	0.31

[a]All values are referenced to Earth's magnetic dipole moment (7.94×10^{22} A·m^2).

[b]The sign indicates the orientation of the dipole relative to the rotation axis 'north' pole. Value is positive if dipole 'south' pole is closest to rotational 'north' pole (as is the case for the Earth), negative if dipole 'north' pole is closest to the rotational 'north' pole.

[c]Ratio of dipole to total magnetic field.

[d]From Kivelson et al. (2002) [156].

[e]Retrograde rotation.

Note. — All values from Planetary Fact Sheets [316] unless otherwise noted. Dipole tilt and dipolarity values from [256].

[276]. The Jovian and Saturnian dynamos are generated in a convecting, conductive metallic hydrogen layer [56, 277].

The ice giants, Uranus and Neptune, are the least studied of all of the solar system planets. They have received only one visit from a spacecraft: Voyager 2 as part of its 'Grand Tour'. Voyager 2 observations indicate that both planets have magnetic fields with strong non-dipolar spherical harmonic components compared to the gas giants. The dynamo-generating region in the ice giants is thought to be a thin, convecting superionoic water layer [275, 241] above a stably stratified core, which accounts for the more complicated magnetic field topology. Since higher order components of the magnetic field fall of faster with distance, the dipole component dominates when the field generating region is deep within a planet, like the Earth, but higher order components can be detected when the field generating region is closer to the surface. See Table 1.1 for a comparison of solar system planetary magnetic field properties.

The sample of solar system planetary magnetic fields is small and idiosyncratic. There are simply not enough planets of similar masses/radii which can be compared

and contrasted to draw conclusions about how magnetic field properties are correlated with planetary properties. The dichotomy between Earth's strong magnetic field and Venus's total lack of a magnetic field is a prime example. Do most Earth-sized planets have Earth-like magnetic fields, or is Venus a more typical case? The motivating goal of this work is to lay the framework for a sample of measured (exo)planetary magnetic fields in order to build a population amenable to statistical analysis.

1.2 Radio Emission from Solar System Planets

Detailed characterization of the solar system magnetic fields was accomplished primarily by in-situ magnetometer measurements by orbiter or flyby spacecraft (Pioneer, Voyager 1 & 2, Galileo, Cassini, etc.). In-situ magnetometer measurements of exoplanetary magnetic fields are not currently possible, so a remote sensing technique is necessary to make progress in this area. This section focuses on cyclotron emission as a remote probe for planetary magnetic fields. Synchrotron emission from relativistic particles in radiation belts and atmospheric lightning also generate planetary radio emission, but have small fluxes compared to cyclotron (non-relativistic) emission, so they are not discussed here. Mercury and Ganymede are not included in the following discussion of planetary radio emission since neither has a measured radio spectrum to date.

1.2.1 Radio Emission Mechanism

Coherent, non-thermal radio emission from charged particle-magnetic field interactions serve as a remote sensing probe of planetary magnetic fields. Electrons from either the solar wind or planet's ionosphere (or both) gyrate around planetary magnetic field lines and radiate at radio frequencies via the electron cyclotron maser instability (CMI) [303]. The peak emission frequency f_{ce} from CMI emission is equal to the electron cyclotron frequency (ω_{ce}) divided by 2π and is therefore directly related to the magnetic field strength (B) **at the emission region** (e and m_e are electron charge and mass, respectively). The cyclotron frequency can be easily de-

rived by balancing the centripetal force on a particle circling a magnetic field line and the Lorenz force.

$$f_{ce} = \frac{\omega_{ce}}{2\pi} = \frac{eB}{2\pi m_e} \tag{1.1}$$

Magnetic field strength increases as altitude decreases, so electrons at different altitudes emit at a range of frequencies. Measuring the frequency spectrum of planetary radio emission therefore directly yields the magnetic field strength at a range of heights. The maximum observable frequency ("peak frequency" or "cutoff frequency") gives the magnetic field at the lowest height above the planetary surface where the CMI mechanism can function. The CMI mechanism stops working at low altitudes where the ionosphere transitions into the neutral atmosphere.

CMI emission is beamed into a thin-walled, wide opening angle cone centered on a magnetic field line. As the emission cone sweeps past an observer due to planetary rotation, it creates the illusion of a periodic signal. The emission cone(s) move with the planet, so the periodicity of the CMI emission is the rotation period of the dynamo-generating region of the planet. Planetary CMI emission is often called auroral radio emission or auroral kilometric radiation (AKR) because it originates in the auroral zones above magnetic poles where field lines converge/diverge (assuming a dipolar magnetic field geometry).

Measuring a planet's magnetic field strength via radio emission from the surface of the Earth requires that the peak emission frequency must be above the Earth's ionospheric cut-off. The Earth's ionosphere is opaque to electromagnetic radiation below the ionospheric plasma frequency. The ionospheric plasma frequency is given by

$$f_p = \sqrt{\frac{n_e e^2}{m_e \epsilon_0}} \cdot \frac{1}{2\pi} \tag{1.2}$$

$$f_p \sim 9\sqrt{n_e}\ [kHz] \tag{1.3}$$

where f_p is the plasma frequency, n_e is the electron number density, and ϵ_0 is the permittivity of free space. When n_e is in units of cm^{-3}, f_p in kHz can be approximated

as shown in Equation 1.3. The Earth's ionospheric cutoff frequency ranges from ∼2–15 MHz depending on solar wind conditions, time of day, and latitude. As shown in Figure 1-2, only Jupiter out of the solar system planets has a magnetic field strong enough to produce radio emission above the Earth's ionospheric cut-off frequency. The magnetic fields of the rest of the gas giants were not measured until space-based observations were made by the Voyager 2 mission [331] using both radio and in-situ instruments.

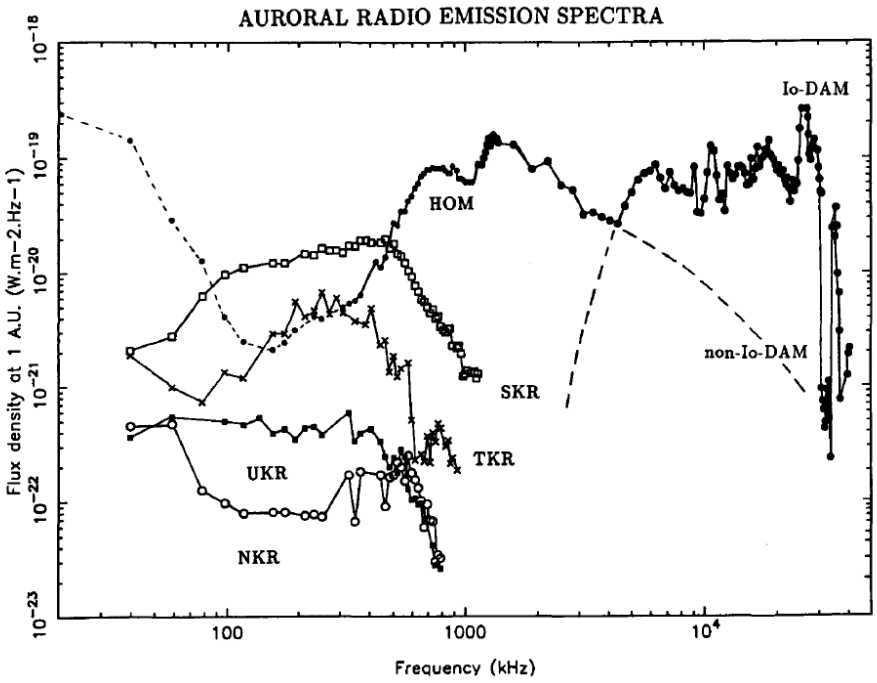

Figure 1-2: Radio spectra of five solar system planets as measured by Voyager 2. TKR, SKR, UKR, and NKR refer to terrestrial, Saturnian, Uranian, and Neptunian kilometric radiation, respectively. Two components of Jupiter's decametric (DAM) emission are shown: Io-induced and non-Io related. The flux densities for all planets have been normalized to 1 AU. Mercury and Ganymede are not included because neither has measured radio emission. Image reproduced from [331].

Radio emission from Jupiter was measured from the surface of the Earth in 1955 [41] at 22 MHz and used to calculate a Jovian magnetic field strength of 7 Gauss and a rotation period of just under 10 hours [267]. The measured magnetic field strength inferred from the ground-based observations agrees well with the value from in-situ measurements (14 G north pole, 11 G south pole, 4 G equator) performed

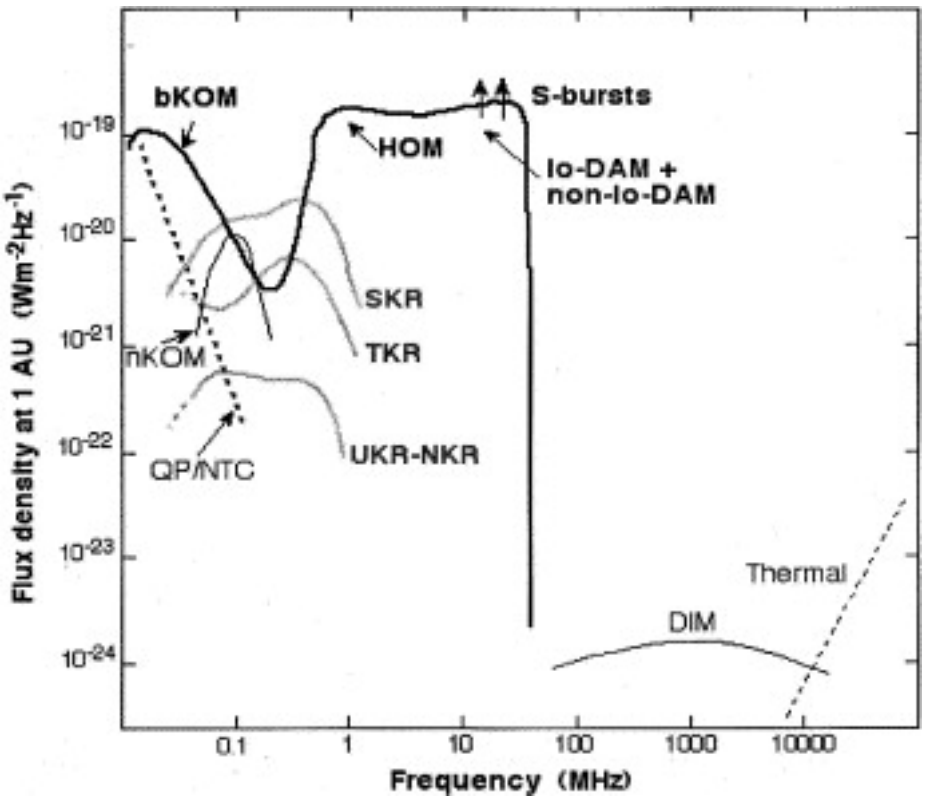

Figure 1-3: Radio spectra of Jovian radio emission. This plot expands the horizontal axis of Figure 1-2 to higher frequencies. The bold black curve shows Jovian cyclotron emission. The spectra of four other solar system planets (Earth, Saturn, Uranus, Neptune) are shown in gray for comparison. Jupiter's synchrotron emission (decimetric, DIM) and thermal emission are also shown. Both are 4-5 orders of magnitude less bright than Jovian cyclotron emission. Figure reproduced from [333]. DIM/thermal emission measured by ground-based telescopes (VLA), lower frequency measured by Voyager 2.

by Pioneer 10 and 11 [271, 270], Voyager 1 and 2 and Ulysses [56] as well as Galileo [155]. Jupiter's moon Io plays in modulating radio emission (see Section 1.2.4). The following discussion focuses on using radio emission to infer magnetic field properties, but it is important to note that the periodicity of radio emission allows for precise measurement of planetary (or exoplanetary) rotation rate as well.

1.2.2 Characteristics of Planetary Radio Emission

Planetary radio emission is highly variable in time and frequency and circularly polarized. The electron population that fuels CMI emission varies due to solar illumination,

solar wind input (1.2.3), reconnection in the magnetic field, and the presence or absence of other plasma sources (1.2.4). Periodic temporal variation is imprinted on the radio signal by the rotation of the magnetic field with the planet and the beaming cone sweeping over the observer, much like a pulsar. The dynamic magnetic field and changing particle population also causes spectral variation as emitting regions turn on or off. These effects combine to generate complex structure in time-frequency space.

The coherent cyclotron emission mechanism produces nearly 100% polarized emission [285, 331]. Right-hand circular polarization (RHCP) corresponds to a 'north' magnetic pole, left-hand circular polarization (LHCP) to a 'south' pole. Coherent processes like the electron CMI are highly efficient at converting electron energy into electromagnetic flux. Planetary CMI emission is therefore orders of magnitude brighter than thermal emission or even synchrotron emission (Figure 1-3). Jovian non-thermal radio emission often outshines the sun [336]. The favorable contrast ratio between planetary emission and solar/stellar radio emission is a key advantage in the quest to detect exoplanetary magnetospheric radio emission.

1.2.3 Effect of Solar Wind

The solar wind influences planetary radio emission in three ways: 1) delivery of energetic charged particles into planetary magnetospheres, 2) compression of magnetospheres via kinetic and magnetic pressure, and 3) reconnection between solar and planetary magnetic fields. Electrons delivered by the solar wind and accelerated toward planetary magnetic poles by magnetic reconnection power CMI emission, especially at Earth. The influence of solar wind pressure on planetary radio emission is quantified by the 'Radiometic Bode's Law', an empirical relationship between input solar wind power and output planetary radio flux [70]. The scaling relationship was first developed using data for the Earth, Jupiter, and Saturn from Voyager 2 and was then used to make predictions for the radio power Voyager 2 would measure when it flew by Uranus and Neptune [72, 68, 197]. The Radiometric Bode's Law takes the

form of a power law:

$$P_{rad} = \epsilon P_{sw}^{x} \tag{1.4}$$

where P_{rad} is the observed planetary radio power, P_{sw} is the input solar wind power, ϵ is an empirically determined efficiency factor ($\sim 10^{-5} - 10^{-6}$), and x is the power law index [91, 167]. In simple terms, the Radiometric Bode's Law states that a planet collects power from the solar wind across the solar-facing surface area of its magnetosphere and some fraction of that power is converted into radio flux. Planets that are close to the Sun experience a higher density solar wind and therefore emit more radio power than a planet with a similarly sized magnetosphere at a larger distance from the Sun. Higher density solar wind compresses magnetospheres, so, for example, Jupiter's emitted power would scale with Solar distance as $({}^{d}/_{d_{Jup}}{}^{-1.6})$.

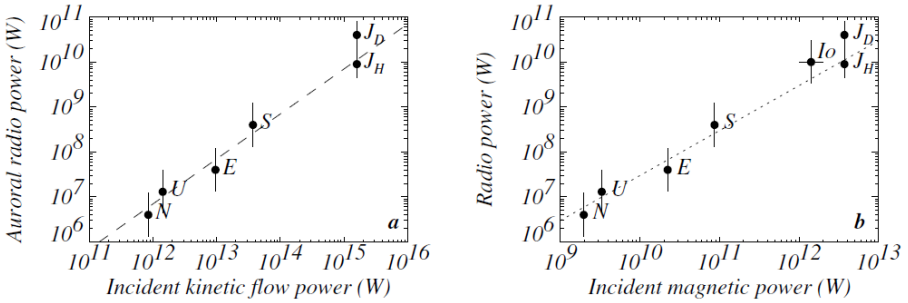

Figure 1-4: Radiometric Bode's Law for solar system planets. J_D and J_H are the non-Io related decametric and hectometric Jovian emissions, while the point labeled 'Io' represents Io-driven Jovian emission. Figure reproduced from [337]

The Radiometric Bode's Law uses an average or 'steady state' value for the solar wind. The solar wind is highly temporally and spatially variable, however, especially during coronal mass ejection (CME) events. Solar wind temporal/spatial fluctuations are correlated with planetary radio power variations [103, 71, 69]. Solar wind variability drives non-periodic or quasi-periodic temporal variability in planetary radio emission. CMEs are particularly strong density and velocity enhancements in the solar wind. CME shock passages have been correlated with particularly strong planetary radio emission [236, 123, 235]. Solar wind and CME enhancement of planetary radio emission is an important consideration for exoplanet radio emission searches (see Chapter 5).

1.2.4 Effect of Moons

The previous sections have described radio emission that arises due only to the interaction of a planetary magnetic field and internally generated plasma and/or solar wind plasma. This section describes the influence of moons on planetary radio emission. Jupiter and its Galilean satellites provide the solar system's best example of this phenomenon. The influence of Io on Jupiter's radio emission was first described in [23] and expanded by [80]. Io's extreme volcanism, caused by resonance-induced tidal heating, expels large volumes of material into the Jovian magnetosphere. That material is quickly ionized and forms the Io plasma torus. Some of this material forms an electrical current, called the Io flux tube, that connects Io's ionosphere with Jupiter along a magnetic field line. The Io flux tube is responsible for a strong UV auroral 'footprint' near Jupiter's poles. It also contributes to strong auroral radio emission. Europa, which has an induced magnetic field due to its subsurface salty ocean, and Ganymede, which has an intrinsic dynamo, both interact with Jupiter's magnetic field and produce periodic enhanced radio emission as well.

Zarka (2007) [334] generalizes satellite interactions with a strongly magnetized parent into two categories. The first category consists of unmagnetized or weakly magnetized satellites (Io, Europa, Callisto). These bodies present an obstacle to Jovian magnetic field lines as they move through Jupiter's magnetosphere, causing magnetic field lines to pile up in a 'wake' behind the satellite. Zarka calls this mode of interaction a 'unipolar inductor'. The second category consists of intrinsically magnetized bodies with stronger magnetic fields (Ganymede). In this case, there is magnetic reconnection between the satellite's magnetic field lines and Jovian field lines. This is classified as a 'dipolar' interaction. Zarka generalizes this approach to planets and stars as well as satellites and planets. Interaction of either a 'unipolar' or 'dipolar' type drives radio emission on the primary (see [334] for formalism and scaling relations). Jupiter's Galilean moon system serves as model for potential indirect detection of exoplanetary magnetic fields via modulation and/or enhancement of stellar radio emission.

1.3 Detecting Exoplanetary Magnetospheres

The success of measuring Jupiter's rotation and magnetic field strength using ground-based radio measurements suggests that the same technique could be used to probe exoplanet properties as well. Measuring the magnetic field of an exoplanet would provide insight into the planetary interior where the field is generated, inform atmospheric evolution models, and perhaps assist in determining habitability (see Section 1.4). Additionally, obtaining a statistical sample of planetary magnetic field properties would allow us to investigate the underlying physics of magnetic field generation and time evolution for the full spectrum of planet sizes and compositions.

The ever-growing statistical sample of exoplanets has yielded new insights into planet properties as a function of a wide range of variables. For example, the sample of exoplanets with precisely measured masses and radii suggests that there is a breakpoint between planets with thin atmospheres (like the Earth) and planets with thicker envelopes (more like Neptune) at $\sim 1.5 R_{\oplus}$[309]. This discovery was only possible through the accumulation of exoplanet measurements; the Solar System sample does not contain any planets between $1 R_{\oplus}$and $\sim 4 R_{\oplus}$. The study of planetary magnetic fields as a function of planetary properties (e.g. mass, surface temperature, age, composition) is in its infancy because only the small Solar System sample is available.

Figure 1-5 summarizes Solar System planet magnetic fields as a function of mass. B-field vs. mass is one of many possible representations of planetary magnetic field properties as a function of planetary properties. The key observable quantity, the cyclotron frequency that corresponds to magnetic field strength, is shown on the right vertical axis. The region occupied by higher mass objects, brown dwarfs and the lowest mass M-dwarfs, is shown in the upper right. One key question that can be addressed by adding exoplanetary magnetic field measurements to this plot is whether magnetic field strength is strongly correlated to planet mass from Jupiter-mass bodies up to brown dwarfs or whether some other planetary property dominates instead. Another key question, which will likely require space-based observations (see Chapter 7), is whether planets with masses between those of Earth and Neptune (super-Earths

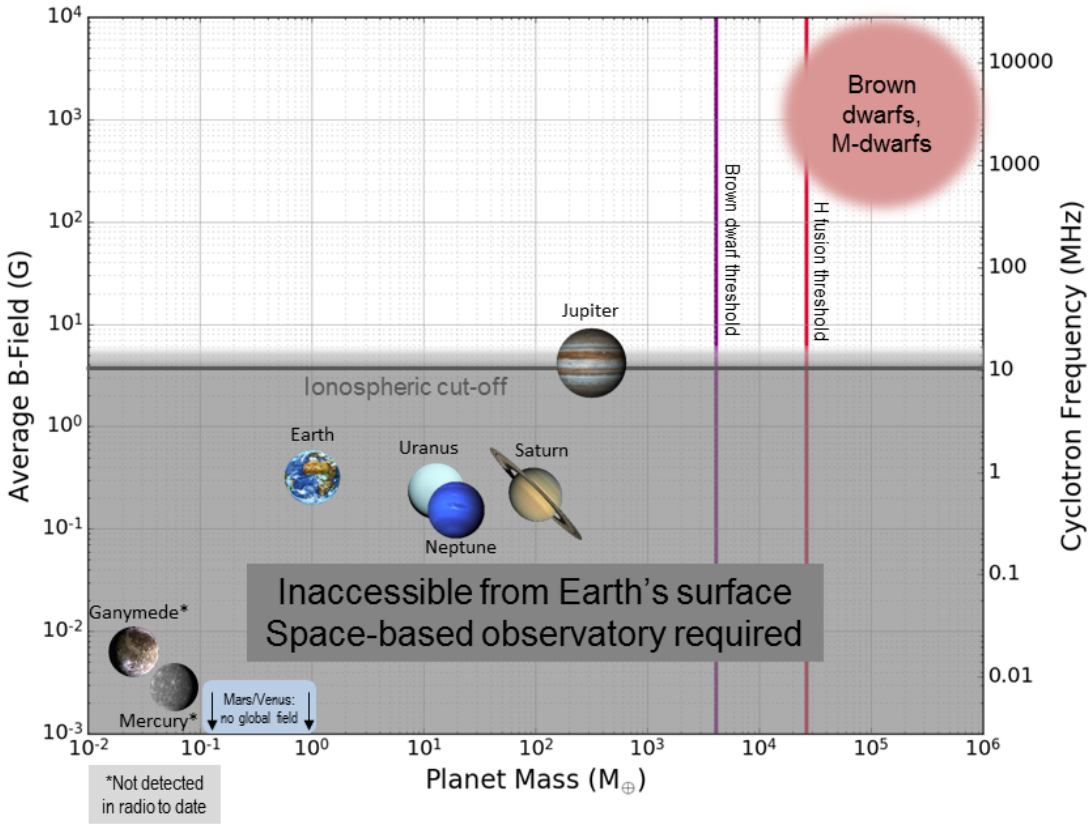

Figure 1-5: Schematic plot of Solar System planets' surface magnetic field strengths (left y-axis) and corresponding cyclotron frequency (right y-axis) as a function of planet mass. Brown dwarfs and M-dwarfs have magnetic field strengths and emission frequencies in the upper right region of the plot. The lower half of the plot (gray) is inaccessible for ground-based instruments due to the Earth's ionosphere. Values for equatorial magnetic field strength of Solar System planets can be found in Table 1.1, references therein. The mass boundary for brown dwarfs ($\sim$13 M_J) is indicated by the purple vertical line; the mass threshold for hydrogen fusion ($\sim$0.08 $M_\odot$) is indicated by the red vertical line.

and mini-Neptunes) have Earth-like strong, dipolar fields, or Neptune-like multipolar fields. These questions can only be answered by measuring exoplanetary magnetic fields and adding them to plots like Figure 1-5; this thesis is intended to lay the groundwork for obtaining more data on (exo)planetary magnetic fields in order to address the above questions.

1.3.1 Inferring Planetary Properties from Radio Timeseries and Spectra

The history of solar system planet radio observations informs the physical properties that could be inferred via radio detection of exoplanets. The magnetic field strength of the planet can be inferred from the high frequency cutoff of the radio spectrum (Eq. 1.1). The observation bandwidth must be wide enough, or fortuitously located, in order to capture the spectral cutoff. A timeseries of radio flux will yield the planetary rotation period and may also reveal the orbital period of satellites (as with Jupiter-Io), the planetary orbital period and/or the stellar rotation period. This technique has been used to determine the rotation period of brown dwarfs [127]. Attributing each period present in the timeseries would be aided by knowledge of some system periods, e.g. the stellar rotation period from photometry or the planetary orbit from radial velocity or transit measurements. In the case of tidally locked close-in planets, the planet's orbit and rotation period are the same, further reducing ambiguity. A time baseline several times the longest period in the system is needed to make a reliable periodogram, so again prior knowledge of some system parameters is beneficial. Aperiodic variability may be attributed to stellar wind forcing. CME passages are expected to generate brief, bright bursts. Higher frequency observations of stellar radio emission, correlated with a delayed planetary burst, would be strong evidence for a CME passage and would yield CME speeds. Less dramatic stellar radio fluctuations that correlate with planetary radio fluctuations could be used to measure the stellar wind speed by measuring the delay between the stellar event and the planetary response.

Polarization provides further information about the orientation of the planetary magnetic field and also can be used to distinguish between stellar and planetary emission. Stellar quiescent emission is unpolarized and stellar bursts may be unpolarized, partially polarized, or (occasionally) strongly circularly polarized, while planetary radio emission from CMI is expected to be fully circularly polarized all the time. Hess & Zarka (2011) [135] use detailed modeling to demonstrate how left-hand vs. right-hand circular polarization, as a function of time and frequency and in combination with intensity, can be used to infer obliquity, dipole tilt, and orbital inclination. These planetary properties are difficult to determine from other observational techniques like transit or radial velocity. As with all observational work, more data yields more planetary properties with smaller error bars.

Ideal radio observations for exoplanets should be continuous to avoid introducing artifacts in the periodogram, wide band or multi-band to capture the high frequency cutoff and perhaps stellar radio emission, finely sampled in time and frequency to capture fine structure in the time-frequency dynamic spectrum, and polarimetric. For the purpose of making a positive detection of exoplanetary radio emission, long, if discontinuous time baselines and wide spectral coverage should be prioritized in order to detect periodicity (or catch bright bursts that rise above the noise floor) and maximize the likelihood of covering the high frequency spectral cutoff.

1.3.2 Past Radio Exoplanet Searches

Low frequency radio emission was put forth as an exoplanet detection technique even before the first exoplanet was confirmed. Inspired by Jupiter's radio brightness, Yantis et al. searched nearby stars for radio companions using the Clark Lake telescope in 1977 [329]. Winglee et al. conducted a similar survey with the VLA in 1986 [319]. Winglee et al. observed 6 nearby stars for 3.5 hours each with VLA 330 MHz and 1.4 GHz, achieving noise levels of 30 mJy[1] and 300 μJy, respectively. Neither survey yielded any positive detections, though one of the stars in the Winglee et al. survey, Lalande 21185, is now known to have at least one planet [44]. Three

[1] 1 Jy = 10^{-26} $\mathrm{W/m^2 \cdot Hz}$

months before the announcement of the first exoplanet [324], Bernard Burke, the discoverer of Jupiter's radio emission, used his closing remarks at *Planetary Radio Emission III* to promote low frequency radio observation as both a planet detection and characterization technique [40].

After the discovery of the first exoplanet around a sun-like star, 51 Peg, in 1995 [192] and subsequent hot Jupiters, Farrell et al. (1999) [91] published estimated flux values for nine exoplanets based on Radiometric Bode's Law and a scaling law for planetary magnetic moments. This scaling law and variants are sometimes referred to as 'magnetic Bode's law' or Blackett's law [24]. Based on an empirical correlation between planetary angular momentum and magnetic moment for solar system planets, 'magnetic Bode's law' suggests that a planet's magnetic moment may be estimated using planetary density, rotation rate, and core radius. The validity of this scaling relation has been challenged [45, 50], but nevertheless it is often used in attempts to predict exoplanetary radio flux. Bastian et al. (2000) observed seven of the planets on with estimated fluxes from Farrell et al. (1999) and two additional objects using the VLA [17]. Upgrades to the VLA allowed Bastian et al. to achieve better limits, 50 mJy, 1-10 mJy, and 20-70 μJy at 74 MHz, 330 MHz, and 1.4 GHz, respectively, but again no detections were made. A VLBI campaign to perform astrometry for exoplanet detection in the radio (5 and 8 GHz) also yielded no detection [176].

Lazio et al. (2004) [167] and Griessmeier et al. (2007) [120] significantly expanded the list of exoplanets with radio flux predictions. These predictions launched many targeted observing campaigns which focused on the exoplanets with the highest predicted fluxes, usually hot Jupiters. Observations of HD 209458 b and HD 189773 b with the GMRT [171, 172], τ Boo b with the GMRT [128] and WSRT [279], and HD 80606 b with the VLA [170] all yielded non-detections. The only hint of exoplanetary radio emission was reported for an occultation observation of HAT-P-11 b [173] where the radio flux appeared to decrease as the planet passed behind the star, though the detection is marginal and has not, as of this writing, been replicated. Searches of archival radio survey data have been carried out for 74 MHz VLSS [168], GMRT 150 MHz TGSS [265], and MWA GLEAM [208], none yielding detections. The survey

searches are described in more detail and expanded upon in Chapter 3. Radio surveys of known planets are in progress [5] or complete [186], again with no detections to date. See Table 1.3.2 and Figure 8-4a for all available limits from literature to date.

1.3.3 Explaining the Lack of Detections to Date

Radio observations seem well suited to exoplanet detection/characterization for two reasons: at low frequencies, the non-thermal emission from planetary CMI are highly circularly polarized and therefore should stand out against background unpolarized sources (including the host star), and planetary radio flux can be as bright as stellar emission, providing a favorable contrast ratio. Some estimated exoplanet radio fluxes are well within the capabilities of existing instruments (>1 Jy) Why, then, have there not yet been any unambiguous detections of cyclotron maser emission from known exoplanets?

Possible reasons for non-detection of exoplanetary radio emission to date include:

- Some, if not all, of the scaling laws used to predict exoplanet radio fluxes are likely wrong. Inferring too much from the small sample of solar system planets is risky, though the solar system is the only starting point available. Predicting magnetic field strengths, which determine the high frequency spectral cutoff and therefore the required observing frequency window, is especially difficult.

- There are no space-based low frequency radio telescopes, so presently only exoplanets with magnetic fields equal to or stronger than Jupiter's can be detected at all (Chapter 7).

- if exoplanetary radio emission is bursty and beamed like that of the solar system planets, observations to date may have simply missed it. If the Earth is not within the emission cone, no radio emission will be observed.

- Large radio telescopes are oversubscribed and constrained by the horizon, so very long, continuous observations are not possible for most objects. The Owens Valley Long Wavelength Array (OVRO LWA) [126] is an important exception.

Table 1.2. Exoplanet radio observations to date.

Planet	Distance (pc)	Mass (M_J)	Freq. (MHz)	Flux (mJy)	Telescope	Ref	Notes
Gl 411 b	2.5	0.01	1465	<0.069	VLA	[17]	
			333	<12.0	VLA	[17]	
Gl 229 b	5.75	0.10	1465	<0.081	VLA	[17]	Recent RV candidate [287]
			333	<10.8	VLA	[17]	
Gl 229 B	5.75	∼40[a]	1465	<0.081	VLA	[17]	Brown dwarf via direct imaging [213]
			333	<10.8	VLA	[17]	
HD 98230 b	8.8	∼37[a]	74	<120.0	VLA	[17]	
55 Cnc b	12.53	0.80	1465	<2.04	VLA	[17]	
			333	<12.9	VLA	[17]	
55 Cnc c	12.53	0.16	1465	<2.04	VLA	[17]	
			333	<12.9	VLA	[17]	
55 Cnc d	12.53	3.54	1465	<2.04	VLA	[17]	
			333	<12.9	VLA	[17]	
55 Cnc e	12.53	0.03	1465	<2.04	VLA	[17]	
			333	<12.9	VLA	[17]	
			49.5	<230.0	LOFAR	[289]	
55 Cnc f	12.53	0.17	1465	<2.04	VLA	[17]	
			333	<12.9	VLA	[17]	
υ And b	13.47	0.67	1465	<0.063	VLA	[17]	
			333	<6.0	VLA	[17]	
			150	<9.0	GMRT	[321]	
υ And c	13.47	1.92	1465	<0.063	VLA	[17]	
			333	<6.0	VLA	[17]	
			150	<9.0	GMRT	[321]	
υ And d	13.47	4.12	1465	<0.063	VLA	[17]	
			333	<6.0	VLA	[17]	
			150	<9.0	GMRT	[321]	
47 UMa b	14.08	2.55	1465	<0.093	VLA	[17]	
			333	<33.0	VLA	[17]	
			74	<228.0	VLA	[17]	
47 UMa c	14.08	0.55	1465	<0.093	VLA	[17]	
			333	<33.0	VLA	[17]	
			74	<228.0	VLA	[17]	
51 Peg b	15.36	0.46	1465	<0.099	VLA	[17]	
			333	<5.4	VLA	[17]	
τ Boo A b	15.62	5.95	1700	<0.13	WSRT	[279]	
			150	<1.0	GMRT	[128]	
			74	<120.0	VLA	[90]	
70 Vir b	18.11	7.46	1465	<0.24	VLA	[17]	
			333	<41.4	VLA	[17]	
			150	<21.0	GMRT	[321]	
HD 189733 b	19.3	1.14	614	<0.16	GMRT	[171]	
			244	<2.0	GMRT	[171]	
			153	<2.1	GMRT	[172]	
HD 179949 b	27.55	0.90	150	<21.0	GMRT	[321]	
HD 162020 b	29.4	15.21	150	<21.0	GMRT	[321]	
HAT-P-11 b	37.5	0.08	150	3.87 ±1.29	GMRT	[173]	Detection (unconfirmed)
HD 114762 b	40.57	11.64	1465	<0.078	VLA	[17]	
			333	<13.2	VLA	[17]	
HD 209458 b	49.6	0.69	150	<3.6	GMRT	[172]	
HD 80606 b	58.4	3.89	1465	<0.048	VLA	[170]	
			330	<1.7	VLA	[170]	

[a] [17]

Note. — All limits are 3σ. Masses and distances from exoplanets.org [129] unless otherwise noted.

There are two key observational challenges: the lack of extremely high sensitivity low frequency telescopes and the need for advanced data reduction techniques to mitigate man-made radio frequency interference (RFI) and ionospheric distortion in such observations. Exoplanetary radio emission is very faint — even Jupiter's radio flux 10 pc would be undetectable with current telescopes ($\sim$1 μJy at 20 MHz). Highly capable existing telescopes, such as the LWA [82, 126], MWA [179], LOFAR [65], and planned telescopes, such as SKA-Low [73], offer improved sensitivity through large collecting areas. Massive collecting area is of no use, however, if sensitivity is limited by RFI or calibration deficiencies. This is currently the case for LOFAR's low frequency LBA (Ch. 2). Better calibration, especially for the effects of the ionosphere, is critical to fully exploiting the capabilities of ground-based instruments.

1.4 Planetary Magnetic Fields and Habitability

The search for life beyond Earth, or at least habitable environments, is a major motivation for exoplanet research. A discussion of the relationship between (exo)planetary magnetic fields and habitability is therefore needed to place exoplanetary radio detection efforts in a broader context. The purpose of this section is to address two questions. First, is a magnetic field necessary for Earth-sized planets to retain an atmosphere? Second, is a magnetic field necessary to protect surface or ocean life from ionizing radiation?

1.4.1 Magnetic Fields and Atmospheres

This section focuses on whether and how planetary magnetic fields influence atmosphere loss. Only Earth-sized, rocky worlds with relatively thin atmospheres (as a fraction of planetary radius) are considered here. There are three such planets that can be closely studied in this solar system: Venus, Earth, and Mars[2]. Unfortunately, Earth, Mars, and Venus are each special cases in their own way and it is therefore

[2]Mercury is excluded since it has no atmosphere, though it does have a weak dynamo magnetic field (Table 1.1).

difficult to compare the influence of magnetic fields on the evolution of their atmospheres. Nevertheless, they are the only well-studied sample of terrestrial planets available presently.

Stellar Wind and CME-driven Atmosphere Loss

The relationship between planetary magnetic fields and atmosphere loss depends strongly on the behavior of the host star. During the early lives of sun-like stars, activity and EUV flux is significantly increased compared to the present-day Sun. During the first 1 Gy of the Sun's life, the EUV flux was likely 100 to 1000 times greater than present [162]. This relative increase in highly energetic photons from the sun would have driven increased photoionization of the terrestrial planet atmospheres. Loss by hydrodynamic escape (atmospheric heating) is governed primarily by the gravity of the planet rather than the magnetic field, so the increased EUV flux during the early solar system is most useful to the question of magnetic fields and atmosphere loss as a proxy for increased solar wind density. The mixing ratios in the primordial (and perhaps secondary) atmospheres of the terrestrial planets would have an influence on the ability of the thermosphere to cool, so understanding the compositions of early atmospheres is key to estimating mass loss via thermal processes.

Solar wind density appears to be positively correlated with EUV flux for younger solar-type stars [162], so the terrestrial planets would have experienced a stronger solar wind in the early Solar System. Higher solar wind flux should increase non-thermal atmosphere loss processes (sputtering, ion pick-up, etc., see [263]). The increased incidence of CMEs and flares from the young sun also contributes to a harsher solar particle environment in the early solar system compared to present. Observationally, variations in solar activity (and corresponding EUV and particle fluxes) can serve as a proxy for early solar system conditions. CMEs are also useful as examples of greatly increased solar wind density and speed. Results from Mars indicate a correlation between solar activity and loss rates for heavy ions (O, O+) [185]. Similar correlations have been observed at Venus with the same instrument

[100].

CME-driven atmosphere loss has potentially dire consequences for exoplanets in the habitable zones of M dwarfs. M dwarfs are significantly more active than solar-type stars [312] and the conventional habitable zones (where liquid water could exist) of these low-mass, dim stars are much closer to the star than for solar-type stars [151]. There is some debate in the literature about whether the increased rate of flaring, which is likely accompanied by an increased rate of CMEs, would be detrimental to the atmosphere of a hypothetical habitable zone planet. According to [258], the UV excess from one of the strongest flares measured on an M dwarf would not cause significant damage to a planets ozone layer and would not significantly increase the UV flux at the surface for a long duration. Others, however, argue that increased XUV fluxes would inflate the atmosphere of a habitable zone planet and lead to loss of large volumes of atmosphere via ion pick up [153]. The dense plasma of a CME, however, could have more significant effects on a habitable zone planets atmosphere [153]. As is observed on Mars and Venus, CMEs could temporarily increase the rate of atmosphere loss due to sputtering and ion pick-up for planets without global magnetic fields and compress the magnetospheres of planets with dynamos so severely that a large portion of the atmosphere would be exposed to the CME plasma, resulting in a brief increase in atmosphere loss.

In general, planets with lower gravity and correspondingly low escape velocities for atmospheric neutral molecules and ions are most vulnerable to stellar wind erosion during the violent early phases of stellar evolution. If these small planets are not surrounded by an intrinsic magnetosphere, the solar wind can interact freely with their upper atmospheres in a manner not possible for planets with Earth-like dynamo magnetic fields. In this way, it seems that strong intrinsic magnetospheres are somewhat protective for smaller planets. Unfortunately, small planets cool quickly and therefore have more difficulty maintaining a strong dynamo field for geologically long times (see Ch. 6), so the fate of their atmospheres depends on both the timescale of their dynamo as well as the intensity of stellar activity and its rate of decline with time.

The "Hairdryer" and the "Funnel"

The previous discussion is based conceptually on the picture of the solar wind as a "hairdryer" blowing away the atmospheres of planets not protected by magnetic fields via non-thermal loss processes. Planets with large magnetospheres are 'shielded' from the solar wind "hairdryer" and therefore have reduced atmosphere loss.

For planets with a magnetosphere, the Sun-facing area of the magnetosphere can also be thought of as a "funnel" instead of a shield. The magnetosphere presents a larger 'cross section' to the solar wind than the atmospheric body radius of the planet and therefore collects more energetic particles. The magnetosphere acts like a funnel, directing the energetic solar wind particles along planetary magnetic field lines and into the magnetic poles of a planet, preferentially heating small sections of ionosphere/atmosphere. For a planet without a large magnetosphere, the energy flux of the solar wind is uniformly distributed over the surface of the atmosphere, but the same flux (or more, considering that the 'collecting area' of a large magnetosphere is greater than the diameter of the planet) is deposited in a smaller area, leading to significantly increased heating.

Concentrated heating at the poles could increase the loss rate for heavier species (O+) that would otherwise be gravitationally bound to the planet [34]. Such outflows have been observed for the Earth and have increased in direct proportion to increased solar wind energy flux [278].

The "hairdryer" and "funnel" conceptual pictures apply only to planets in the super-Alfvénic regime of the solar/stellar wind (where the solar wind velocity exceeds the Alfvén speed). A magnetosphere in a super-Alfvénic flow will form a bowshock, as seen in Figure 1-1, left. Close-in planets orbiting stars with strong magnetic fields (like many M dwarfs) are likely to be in a sub-Alfvénic regime at all times, or oscillate between regimes as they orbit [54]. Without a bow shock, the concept of a magnetospheric 'shield' falls apart. In the sub-Alfvénic regime, planetary magnetic field lines can freely reconnect with stellar field lines, providing an easy path for ion escape. Ganymede is a Solar System example of a magnetized body embeded in the

sub-Alfvénic region of a parent body's magnetic field [155]. Several of the planets in the TRAPPIST-1 system as well as Proxima Centauri b fall into this category [105, 104].

Conclusion: Atmosphere Loss

Several key factors determine the extent to which a magnetic field provides shielding to a planetary atmosphere: stellar age, stellar magnetic field, planetary orbit, and planetary mass. Overall, young, small planets need magnetic fields to shield their atmospheres more than larger planets in older systems. The study of magnetosphere moderated atmosphere loss is replete with models, but data-poor. Detection (or non-detection) of magnetic fields in Earth-sized planets coupled with detailed atmospheric characterization is necessary to augment the limited Solar System sample of terrestrial planets.

1.4.2 Magnetic Fields and Life

The previous subsection described the influence of planetary magnetic fields on atmosphere loss. When considering land-based life, the presence of an atmosphere is critical since it shields the surface of a planet from ionizing radiation. Life in oceans is somewhat different, although the maintenance of an atmosphere is probably necessary for the survival of oceans. Life as we understand it needs a planet with atmosphere and oceans, so the effect of the magnetosphere on life in bulk terms is indirect. The magnetosphere certainly influences the atmosphere and oceans in complex ways and therefore influences life on planetary timescales, although the geosphere is likely an equally important factor in the maintenance of atmospheres and oceans.

Living things on Earth are vulnerable to ionizing radiation because it damages cells and, critically, DNA. High flux of ionizing radiation to the surface of a planet might also disrupt the origin of life by destroying critical biomolecules faster than they can be created (assuming a sufacial origin for life rather than a deep see origin). The following section addresses what effect a planetary magnetic field has on the

penetration of ionizing radiation to the planetary surface and oceans.

Types of Ionizing Radiation

Ionizing radiation comes in two forms: electromagnetic radiation more energetic than visible light (photons) and energetic particles. Electromagnetic ionizing radiation is not affected by magnetic fields; it is absorption and scattering in the atmosphere that control how much ionizing electromagnetic radiation reaches a planet's surface. The presence or absence of a planetary magnetic field therefore only affects the flux of ionizing electromagnetic radiation indirectly by influencing the evolution of the planetary atmosphere (Section 1.4.1).

Energetic particles may be either charged or neutral. Neutral particles, like neutrons, are not influenced by magnetic fields[3]. Energetic charged particles, electrons or ions, are therefore the only form of ionizing radiation that is directly influenced by magnetic fields.

Sources of Energetic Charged Particles

There are three sources of energetic charged particles that are relevant for terrestrial planets: galactic cosmic rays, solar energetic particles, and radiation belts [60]. Galactic cosmic rays (GCR) are extremely energetic atomic nuclei that have been accelerated by astrophysical processes (supernovae, pulsars, black hole jets, etc.) outside of the Solar System [93]. Solar energetic particles (SEP) are electrons, protons, and some heavier ions accelerated by solar flares. Radiation belts, or Van Allen belts [292], are regions within a planetary magnetic field where energetic particles are trapped. Radiation belts are an important source of energetic particle flux for moons orbiting inside the magnetosphere of their host planet (e.g. Europa, Ganymede).

[3]Except in the case where the energetic neutral is generated by a charge exchange process in the ionosphere/magnetosphere.

Layers of Shielding: Astrosphere to Ocean

The solar/stellar magnetosphere (heliosphere/astrosphere) is the first line of defense against GCR. Even a relatively weak stellar magnetic field can bend the trajectories of lower energy GCR around the astrosphere and away from any planets orbiting the star. The rigidity, or momentum to charge ratio, of a GCR (or any other energetic charged particle) determines how much deflection is caused by a magnetic field [60, 290]. Astrospheres can be compressed by passage through dense interstellar clouds; in an extreme case, planets normally protected by an astrosphere could be left outside of the compressed astrosphere and directly exposed to GCRs [60, 269]. The influx of GCRs onto a planetary atmosphere like the Earth's (assuming a weak or non-existant planetary magnetic field) could have profound effects on atmospheric chemistry, particularly ozone [60, 229]. M dwarfs, which generally have stronger magnetic fields than solar-type stars, are less vulnerable to 'astrospheric collapse.'

A planetary magnetosphere is the next line of defense against GCRs that penetrate the astrosphere as well as internally generated SEPs. Similar to the astrosphere, a planet's magnetosphere will have a magnetic latitude-dependent rigidity cut-off [290], preventing some energetic charged particles from reaching the atmosphere. *Planets without a magnetic field will therefore experience a larger flux of energetic particles at the top of their atmospheres.* The strength of the magnetic field determines the level of shielding [60, 119].

A planet with a compressed magnetosphere due to high stellar wind ram pressure will also lose some protection as there is less space for the magnetic field to deflect the energetic particles' trajectory away from the planet, though this appears to be a secondary affect compared to the influence of intrinsic planetary magnetic field strength [118]. A weak or non-existent planetary magnetic field leaves the atmosphere vulnerable to ozone destruction due to high energetic particle flux.

The neutral atmosphere itself provides the last layer of shielding before energetic charged particles can reach the surface. Most incident energetic particles hit an atmospheric molecule and cause a cascade of secondary particles [93], which themselves

may be ionizing. The thickness of the atmosphere determines how much ionizing radiation (either primary from incident particles or secondary from particle showers) reaches the surface; on the Earth, there is a measurable difference in the radiation dose received at altitude (on a mountaintop or airplane) versus at sea level. For sea life, ocean water provides additional shielding. The oceans beneath icy worlds, like Europa or Enceladus, are therefore well shielded from GCRs, SEPs, and the radiation belts of their host planets.

All relevant 'shields' described above vary with time, often periodically. The extent of the astrosphere varies as a star traverses the variable density interstellar medium and also as the stellar magnetic field varies periodically (e.g. solar cycles) and with stellar age. Planetary magnetospheres may turn on or off or reverse with time. Stellar SEP flux varies with magnetic cycles (timescale of years) and on shorter timescales with magnetic activity like flares. In order for life to gain a foothold and develop in complexity, it must be robust to the inevitable variability in the ionizing radiation flux at the surface of a planet. Ocean-based life is particularly insulated from ionizing radiation.

The energy spectrum of incident charged particles, which is modified by the astrosphere, stellar activity, and the planetary magnetic field (if it exists), and the atmospheric thickness are the key parameters that determine the flux of ionizing charged particles at a planet's surface.

1.4.3 Conclusion

The relationship between planetary magnetospheres and life is complex and poorly understood even for the Earth and terrestrial planets. Available data and theoretical modeling indicate that planetary magnetic fields do play a role in determining whether life can develop and thrive on a planet. There is no simple binary answer, however, to the question of whether magnetic fields are *required* for habitability. The full context of a planetary system, including the stellar age, magnetic field, and activity level as well as the planetary mass, orbit, atmosphere, and geophysics must be considered holistically alongside the presence or absence of a planetary magnetic field to deter-

mine whether the planet in question has conditions favorable for the development of life. Teasing out the conditions under which a planetary magnetic field is essential for habitability will require more data. Coupling magnetic field measurements of terrestrial planets with atmospheric mass and composition from spectroscopy will be a key step towards understanding the interplay between magnetic fields and atmospheric evolution. Radio measurements of exoplanetary magnetic fields are therefore a key component in the quest to understand how to build a habitable planet.

Chapter 2

Methods

This chapter provides an overview of the process that converts incoming electromagnetic radiation at radio wavelengths into interferometric visibilities and then images. I describe the particular challenges of exoplanetary radio observations (Section 2.2) and attempts to address these challenges (Section 2.2.2), including my work on orbital phase targeting. The specifics of standard data reduction for two interferometers used in the following chapters, VLA and LOFAR, are described in detail (Sections 2.3, 2.4). The particular challenge of the ionosphere for large, low-frequency interferometers is described in Section 2.5. Future prospects for ground-based observation are explored in Section 2.7.

2.1 Standard Radio Astronomy Data Reduction

Detecting exoplanetary radio emission, either from the ground or from space, requires detailed understanding of the radio data processing pipeline. The purpose of this Chapter is to describe the critical steps in the data acquisition and analysis chain and highlight the special processing needs of exoplanet observations. Understanding and quantifying noise sources, instrumental effects, source contamination, etc. is critical to obtaining useful results. Recent advances in exoplanet science have been the result of massive efforts to improve data reduction, interferometric imaging, and image deconvolution. The Kepler [143] and HARPS [250] data processing pipelines

are prime examples.

The first step in low frequency radio astronomy is to use an antenna to convert EM waves into measurable voltages. In optical, IR, and high-frequency radio astronomy (mm/submm), parabolic reflectors are the antennas of choice to collect and focus energy onto a detector. At lower frequencies, however, the λ/D relationship between collecting area size (dish/reflector size) and angular resolution implies requirements for very large dishes to obtain even relatively modest resolution. It is often more cost-effective to use simpler antennas with relatively large main beams. For antennas that are electrically small (physically smaller than $\sim 1/4\lambda$), the effective collecting area $A_{eff} = \lambda^2/\Omega$, where Ω is the solid angle of the primary beam. Simple antennas, such as dipoles, can be arrayed to form interferometers for improved angular resolution. Regardless of the antenna chosen, in a modern system the analog voltages generated by incoming EM radiation are amplified and filtered before being digitized by an analog-to-digital converter (ADC). The number of bits required for the ADC depends on the frequency, purpose of the observation, and RFI environment. For some interferometric applications, a single bit is sufficient; for others, particularly observations with strong terrestrial interference, more bits are needed for higher dynamic range.

Digitized antenna voltages are either stored or sent directly to a correlator. For large interferometric arrays with high bandwidths, like the VLA or GMRT, the data volume from the antennas has generally been too great for intermediate storage and must be sent directly to the correlator to be processed in real time. Smaller arrays are able to store the raw voltage data for later processing while larger arrays must correlate in real time to produce manageable output data rates. Having access to the raw voltage data (along with necessary metadata) rather than correlator-generated visibilities allows for a wide variety of post-processing options. Raw data can be fully cross-correlated for full-beam imaging, or antenna-specific phase delays can be added to image a small patch of the main beam. Single-antenna data analysis can also be performed if the raw voltages are available. This is valuable for understanding the RFI environment or identifying instrumental artifacts (e.g. broken antennas, amplifiers, cables, etc.).

Whether correlation happens during an observation or later from stored data, the output of correlation is a set of complex visibilities. Typically, correlators transform voltage data into the Fourier domain using an FFT and then perform the cross-correlations in a set of narrow frequency channels. The resulting visibilities correspond to the correlation of two antennas (a baseline) at a specific time and in a narrow frequency channel. The number of visibilities is the number of baselines (n_{bl}) multiplied by the number of frequency channels and number of integrations ($\frac{t_{obs}}{t_{int}}$) in the observation.

$$\text{Visibility Data Size} = n_{bl} \cdot n_{chan} \cdot \frac{t_{obs}}{t_{int}}, \text{ where } n_{bl} = \frac{n_{ant}(n_{ant}-1)}{2} \tag{2.1}$$

This is a significantly smaller data set than the input voltage data, which is

$$\text{Raw Data Size} = n_{ant} \cdot n_{pol} \cdot \text{bits}_{\text{ADC}} \cdot 2B \cdot \frac{t_{obs}}{t_{int}} \tag{2.2}$$

where n_{pol} is the number of polarizations, bits_{ADC} is the precision of the ADC, and the minimum Nyquist sampling rate of 2x the observation bandwidth is used. Most correlators for radio astronomy applications are 'FX' correlators, meaning that the correlator first converts the voltage data into the frequency domain using an FFT, then performs the cross-correlation in a set of narrow frequency bands (channels).

After visibilities are generated by the correlator, the calibration process begins. Before beginning calibration, bad data, due to RFI, antenna shadowing, bad receivers, correlation errors, etc., must be removed. This step is referred to as flagging and may be done manually by visual inspection or automatically via statistical methods. RFI is particularly problematic a low frequencies, so great care must be taken in excising RFI from low frequency data sets. Once flagging is complete, calibration begins. Typically, one or more flux calibrators (bright astronomical sources with known spectra and absolute flux values) and phase calibrators (to account for instrumental and ionospheric gain/phase drifts) are observed before and/or after the target object is observed. This is somewhat analogous to the use of flats, darks, biases, standard

stars, and reference stars to calibrate optical astronomy images. The theory and practice of 'standard' interferometric data reduction can be found in, for example, [284, 282] and will not be reiterated here. Note that flagging can calibration are often iterated as needed to obtain clean calibration solutions.

When flagging and calibration are complete, the visibilities are ready to be converted into an image. This is accomplished through an inversion, most often spatial Fourier transform, of the visibilities (from the UV plane to the sky plane) and the deconvolution and iterative subtraction of the interferometer beam. The direct spatial transform of the visibility data produces a "dirty map" which is a convolution of the sky intensity map and the interferometer beam. The most commonly used algorithm to deconvolve the beam from the sky intensity pattern is called CLEAN [136]. CLEAN is implemented in most radio astronomy software, including the standard package `CASA`. In brief, the CLEAN algorithm assumes that the sky image is composed of point sources. It selects the brightest point on the map and places the interferometer beam at that point. It then subtracts the beam pattern from the dirty map. It repeats this process iteratively until a threshold is reached. The locations of the 'point sources' identified by clean are then used to reconstruct an image which represents the true sky intensity distribution. The flagging-calibration-CLEANing sequence is often repeated until the desired image quality, often quantified by the RMS image noise, is achieved. The final image, or intensity map, may then be analyzed further to answer relevant scientific questions about the target (e.g. properties of the source region, spatial distribution of material, etc.).

My work, described in the following sections, has focused on the latter stages of the interferometry data processing pipeline. The data obtained from LOFAR was pre-calibrated and flagged, although some additional flagging was required. The majority of effort was in imaging the data and analyzing the resulting images.

2.2 Unique Considerations for Exoplanet Searches

2.2.1 Challenges

The search for exoplanetary radio emission presents unique challenges when compared to 'traditional' extragalactic radio astronomy. 'Traditional' targets of radio observations are large radio galaxies outside of our own galaxy or slowly evolving sources like supernova remnants within the galaxy. Most such sources, or sources that are prototypes of an object class, can be observed with single dish telescopes, providing absolute flux measurements via Dicke switching [76]. More importantly, most 'typical' radio astronomy targets do not exhibit rapid variability in time or frequency, so long integrations, Earth rotation synthesis (where the u, v plane is filled in over time as Earth rotates the array), or stacking of observations over months or years maybe employed. In many cases, models already exist for known sources that need only be refined and updated with new data. In short, galactic/extragalactic radio astronomers usually know where their sources are, roughly how bright they are, and their morphology[1]. Exoplanet radio observers enjoy none of those advantages.

In the case of exoplanetary radio emission, there is no prior knowledge of the brightness or spectrum of exoplanetary radio emission. Indeed, the goal is to discover these properties if the source can be detected at all. Since the expected flux at any given time is not known, it is difficult to determine whether a non-detection means that the target has no magnetic field or rather if the noise level of the observation is just too high to make a detection. Similarly with frequency, it is always possible that the source is emitting, but at frequencies outside of the observing window. See Section 1.3.3.

Since no exoplanetary radio emission has been detected to date, the current 'best guesses' for the characteristics of exoplanetary radio emission come from observations of solar system planets, especially Jupiter and Saturn, observations of radio stars and brown dwarfs, and solar radio emission. Predictions from this observational foundation are described in the previous chapter. In short, exoplanetary radio emission is

[1]The exception to this generalization is the production of sky surveys.

expected to be:

- Temporally variable on multiple timescales (magnetospheric Alfvén timescale, planet rotation period, planet orbit period, stellar rotation period, stellar magnetic cycle period)
- Variable in flux by orders of magnitude with time
- Spectrally variable
- Highly polarized
- Low frequency, <100 MHz (though large uncertainties and difficult to predict peak frequency)
- Strongly beamed in many cases

Exoplanet radio observations should therefore be optimized for sensitivity (since simple scaling estimates from Jupiter to stellar distances suggest weak signals), time coverage, bandwidth, and polarization. Given the constraints on oversubscribed observatories and physical constraints on, for example, bandwidth, it is difficult to optimize all of the above in the same observation. In the chapters that follow, observations have been designed to emphasize wide frequency coverage using multiple observatories, sensitivity to time/frequency variability, and sensitivity.

2.2.2 Approaches

Previous radio searches for exoplanetary emission fall into four broad categories: surveys, interferometric observations, especially of hot Jupiters, beamformed observations, and interferometric observations targeting specific orbital phases. Past surveys are described in Section 1.3.2, an archival survey is described in Chapter 3, and an ongoing multi-wavelength survey is described in Chapter 4. In the category of targeted interferometric observations of known exoplanets, hot Jupiters like HD 209458 b, HD 189733 b, υ Andromeda, and τ Bootis have been popular targets because their size implies they may have Jupiter-like magnetic fields and their proximity to their

host stars provides high density stellar wind and the potential for star-planet interaction (see [128, 169, 268, 108, 252]). Some of these observations have attempted to planetary occultation to search for a dip in radio flux from the direction of the system while the planet is behind the star [173]. There have been 14 regular and Director's Discretionary Time (DDT) proposals to LOFAR alone (including four described in this work) requesting exoplanet radio observations, though little has been published to date, likely because of the difficult and time-intensive nature of LOFAR data reduction. Observations targeting hot Jupiters usually aim for long integration times to maximize sensitivity.

Beamformed observations, where an interferometric array is phased up so that it acts like a single large telescope, have been used for targeted exoplanet radio emission observations as well. Beamformed observations are often used for pulsar studies, so the extension to exoplanetary radio emission, which can be thought of as pulsar-like in terms of beaming, is a logical step. Beamformed observations also have the advantage of high time and frequency resolution which produces a potentially information-rich dynamic spectrum of the target location instead of an interferometric image. Beamformed observations can suffer from RFI contamination, so multiple beams on a calibrator, an empty part of the sky, and the target are used. For examples of beamformed exoplanet observations, see [322] (GMRT) and [288] (LOFAR for 55 Cnc e).

The approach described and implemented in this work is orbital phase targeting. This approach emphasizes observations at key orbital phases of known planets when radio emission is predicted to be strongest. Lazio et al. [168] pioneered this approach for HD 80606 b (see Chapter 5), focusing observations on the time before and after planetary periastron when high density stellar wind is predicted to amplify planetary radio emission to the point where it could be detectable. Similar orbital phase targeting was used to design an observation campaign for two other eccentric Jovian planets (Section 5.6.2). The TRAPPIST-1 observations used a different form of orbital phase targeting; they focused on the quadrature points of the orbit where star-planet interaction of the Io-Jupiter type was most likely to be visible at Earth. A

key advantage of orbital phase targeting is that it maximizes the chances of detection (assuming emission models are correct) given constraints on observing time. For hot Jupiters in circular orbits, it is less clear when emission is expected to be strongest since the stellar wind density doesn't change with orbital phase as it does for eccentric planets. Quadrature phases may provide good times to look for emission from hot Jupiters as well if star-planet interaction is expected. Of course, observing before, during, and after planetary occultation is another form of orbital phase targeting. The importance of selecting nearby targets due to the low radio flux levels expected from exoplanets is also emphasized in this work.

No exoplanetary radio emission has been detected with high confidence to date, so there is not yet any evidence to support one observation strategy over another. Ultimately, each observation strategy may be optimal for a subclass of planets — time will tell.

2.3 VLA Data Reduction

2.3.1 VLA Telescope

Karl G. Jansky Very Large Array (VLA) is located in the New Mexican high desert near Socorro. It is composed of 27 25-m dishes arranged in a 'Y' configuration to maximize snapshot (u, v) coverage. The antennas are on specialized railroad tracks so that the array can be configured for compact, intermediate or long baselines. The VLA rotates through four standard configurations, A, B, C, and D. The D configuration is the most compact, while the A configuration is the most extended. The VLA operates 10 frequency bands ranging from 74 MHz to 50 GHz. See Table 4.1 for the bands relevant to this work.

2.3.2 Calibration

The VLA, like most radio interferometers, observes well-characterized, bright sources to calibrate flux and phase. VLA observations are usually interleaved; a calibrator is

observed periodically throughout the target observation to update gains and phases. The VLA observes a bright flux calibrator and then (usually) a different phase calibrator close to the target field. In the case of the data described in Chapter 4, the flux calibrator and phase calibrator where observed before the target observation. The target observations were not long enough to require multiple flux/phase calibrator observations.

The VLA has a standard calibration pipeline that works well for most observations above 1 GHz. The pipeline is based on CASA [194] and performs all steps necessary to go from raw data to 'image ready' visibilities. The pipeline does flagging, flux/bandpass calibration, gain/phase calibration, applies solutions and weights to the target data, and produces inspection plots [295]. Of the 36 observations (L/S-band) described in Chapter 4, only one observation failed pipeline calibration and had to be discarded.

2.3.3 Imaging and Analysis

Target field imaging was performed in `CASA` using the CLEAN algorithm. Imaging and analysis were scripted in `python` for consistency and convenience. All images were 1024 x 1024 pixels. CLEAN was run in multi-frequency synthesis (MFS) mode with Briggs weighting [36] (robust=0.5). Both Stokes I (total intensity) and Stokes V (circular polarization) were imaged. The pixel size for each image was set so that there would be approximately four pixels across the synthesized beam. Since the size of the synthesized beam changes with frequency, images at different frequencies were different angular sizes even though they had the same number of pixels. No CLEAN mask was used.

Each observation was imaged in its entirety (full bandwidth and time) for maximum sensitivity and then was imaged in smaller time/frequency chunks to assess time/frequency variability. The imaging script had four imaging modes: Full time and bandwidth, imaging per spectral window with full time (used to make spectra), imaging per timestep using the full bandwidth (to make lightcurves), and imaging a set of time and bandwidth cells (used to construct a rough dynamic spectrum). The

timesteps were 30 seconds and 1 minute. Self-calibration was not employed since the noise levels in the full time/bandwidth images were reasonably close to the theoretical VLA noise calculations[2].

After imaging, the resulting images were run through an analysis procedure to extract fluxes for the target and reference sources and to assess the image noise floor. Statistics for each image were extracted from the residual using `CASA imstat()`. Next, `CASA imfit()` was used to fit known sources and extract flux measurements. A list of known radio sources in the field of view (FOV) of each image was generated from NVSS via VizieR [220] and `python astroquery`. The position of each target was calculated for each target at the time of observation based on the measured proper motion available in SIMBAD [310]. Since all the targets are nearby, they have high proper motion and in some cases moved more than a full synthesized beamwidth from their J2000 position by the date of the observation. Both `CASA imfit()` and `PyBDSF`[3] [198] were used to fit for sources in a subregion (100 x 100 pixels) centered on the target position at the time of observation. Two different tools were used for target source fitting since visual inspection revealed that `CASA imfit()` was missing real sources, especially in Stokes V. Finally, noise statistics were collected via `imstat()` for a subregion of the residual at the center of the image to establish the noise floor at the location of the target (used for setting upper limits). The 100 x 100 target subwindows were exported as PNG files for easy visual inspection.

2.3.4 Successes and Challenges

The time/frequency imaging of the VLA data was effective in producing both light curves and spectra when emission was present (as in the case of Ross 614, Section 4.4.2). See Figure 4-5. Imaging in Stokes V as well as I enabled polarization fraction measurement for the Ross 614 emission. Automated source identification and flux measurement using the results of both `imfit()` and `PyBDSF` was effective based on

[2]See https://obs.vla.nrao.edu/ect/.

[3]Available at https://github.com/lofar-astron/PyBDSF, documentation available at http://www.astron.nl/citt/pybdsf.

visual inspection spot checks. Scripting the entire imaging and analysis procedure allowed for quick iteration while maintaining consistency across all observations.

Further analysis of the nature of the Ross 614 emission would have benefited from a dynamic spectrum (time vs. frequency) with high resolution. The shape of features in dynamic spectra of solar and planetary radio bursts are diagnostic of the process involved and the type of emission. Though the time/frequency cell imaging was intended to produce a very coarse dynamic spectrum from the interferometric data, the resolution was not high enough to see any identifiable features. Attempts to increase the resolution by decreasing the cell size failed because there was not enough signal available in the smaller cells to produce reliable detections.

Solar radio flares are often observed using either a single dish or an interferometer operating in beamforming mode; both will produce a dynamic spectrum with high time/frequency resolution. See [299] for a study specifically targeting stellar flares with the VLA. As mentioned in Section 2.2.2, the dynamic spectrum approach has been suggested for exoplanet radio observations as well. Ideally, both beamformed and interferometric data for the same target would provide maximum information on stellar radio bursts like those observed for Ross 614.

2.4 LOFAR Data Reduction

LOFAR (Low Frequency ARray) is a newer telescope than VLA and it faces considerable challenges in ionospheric calibration (Section 2.5). The data reduction strategy for LOFAR is more involved and still evolving when compared the the VLA pipeline described above.

2.4.1 LOFAR Telescope

The LOFAR (**LO**w **F**requency **AR**ray) telescope is located in the Netherlands, with its core near Exloo. LOFAR is two telescopes in one: the Low Band Antenna/Array (LBA), which operates from 10-90 MHz, and the High Band Antenna/Array (HBA), which operates from 120-240 MHz. The gap between the LBA and HBA is the FM

Figure 2-1: LOFAR core stations. LBA stations are circled in red.

radio band, where astronomical observations are impossible in or near populated areas. The telescope is hierarchical; a set of 96 (LBA) or 24/48/96 (HBA, core, remote, international) dipole antennas (Figure 2-2) are beamformed (digital for LBA, analog for HBA) and electronically steered so that they act as a single station analogous to a single VLA dish. The signals from all stations participating in an observation are then cross-correlated at a central location. There are 18 stations of each type (LBA/HBA) in the telescope core, providing a large number of short baselinse (Figure 2-1), 18 remote stations of each type spread throughout the Netherlands, and 12 international stations located in Germany (6), France (1), Sweden (1), England (1), and Poland (3). A new international station currently is under construction in Ireland and another is planned for Latvia. Only the core and remote stations in the Netherlands were used for observations in this work.

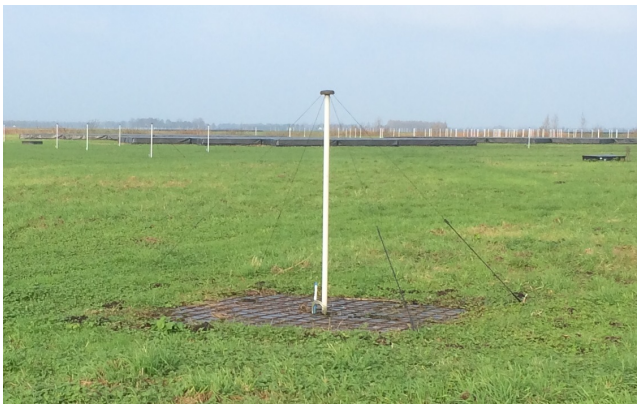

(a) LOFAR LBA dipole antenna

(b) HBA tile (background) and dipole (foreground)

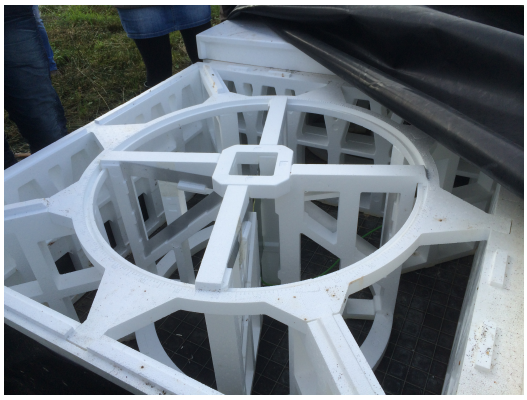

(c) Inside of an HBA tile

Figure 2-2: LOFAR LBA (top) and HBA (bottom) dipole antennas. The LBA dipoles are tensioned between ground stakes and a central pole that has the amplifier at the top. The central pole and dipoles sit on top of a metal ground screen. The HBA dipoles are encased in rectangular styrofoam 'tiles' (c) and covered with weatherproof tarps for protection from the element (b, background).

The LOFAR LBA is the most sensitive telescope in the world below 100 MHz due to its large collecting area. High sensitivity at low frequency makes LOFAR LBA ideal for exoplanet observations because it covers a range of frequency that corresponds to modest magnetic fields (Eq. 1.1) and has the best sensitivity available. The LBA is therefore the focus of the following discussion since it was the antenna set used for the observations described in Chapter 5. Both HBA and LBA were employed for TRAPPIST-1 observations (Chapter 6), but HBA data analysis is still in early phases and will not be discussed in this work. See [296] for an overview of the current state

of the art for HBA calibration and imaging.

The LBA uses only half of the antennas (48 out of 96) in a station for each observation due to hardware constraints. Fully utilizing all 96 antennas in each station would increase the sensitivity of the LBA by a factor of 2, which would aid in ionospheric calibration (see Section 2.5); upgrading the hardware to enable the use of all 96 antennas is under consideration for the 'LOFAR 2.0' upgrade. For all of the observations described in this work, the outer set of LBA antennas were used in each station in order to have the narrowest station primary beam possible to minimize contamination from bright sources in the primary beam sidelobes.

2.4.2 Calibration

LOFAR LBA takes advantage of digital beamforming to place one beam on a calibrator source and another on the target field simultaneously. This allows for the calibrator's flux to be monitored throughout the target observation. Such simultaneous, continuous calibrator monitoring is not possible for dish arrays that have to physically move to point to a source. There are a small number of calibrators bright enough to be used by the LBA: 3C196, CygA, 3C380, and 3C295. The brightest available calibrator that will be at high elevation throughout the target observation is usually chosen. Because there are so few suitable calibrators, the calibrator for any given observation may be far from the target field. For this reason, LBA calibrators are only used for flux (bandpass) calibration and to correct clock drift between stations (20–100 ns[4]). Clock drift is the result of the core stations and remote stations using clocks that are not perfectly synchronized. Phase calibration on the target field relies on a global sky model of the field rather than the calibrator phases.

Before proceeding to calibration, LOFAR data is pre-processed by the observatory[5]. Pre-processing involves several rounds of flagging to excise RFI, edge channels, autocorrelations, and other bad data, demixing of bright radio sources, and usually

[4] http://www.ira.inaf.it/meetings/MKSP2013/MKSP_pdf/Drabent.pdf

[5] In the case of the HD 80606 b data from Cycle 0 (see Ch. 5), the raw data was available in the LOFAR archive and was re-pre-processed in order to fix problems with flagging and overenthusiastic averaging in the original observatory pre-processing.

averaging (see [131]). The demixing process simulates the effect of bright radio sources (the 'A-Team', so called because all the sources have 'A' in their names, e.g. CygA, CasA, TauA) and then subtracts the simulated visibilities due to those sources from both the calibrator and target visibilities (see [294]). Without demixing, visibilities (especially for faint targets) are dominated by flux from the A-Team (mostly CasA, CygA) even when the A-Team sources are far from the phase center of the observation. The final averaging step in time and/or frequency reduces the size of each data file, allowing for more efficient storage, faster transfers, and manageable runtimes for the subsequent reduction steps. Most LOFAR LBA data in this work was averaged from a raw 64 channels per subband and 1 second integration time to 8 channels per subband and either a 1 second or 5 second integration time. Short time integration and high frequency resolution are necessary in order to calibrate for rapid ionospheric fluctuations that are strongly frequency-dependent.

The calibration strategy and pipeline for LOFAR LBA are under active development. The current strategy, and the one used in this work, has been developed by F. de Gasperin and adapted to the LOFAR generic pipeline framework[6] by A. Drabent. The **Pi**peline for **L**OFAR **L**BA (PiLL)[7] has three steps: calibrator calibration, skymodel-based target field calibration, and target field self-calibration.

The calibrator portion of the pipeline uses a detailed model of the calibrator to solve for time- and frequency-dependent amplitude gains and determine the shape of the instrument bandpass as a function of time. At LBA frequencies, the ionosphere induces small, rapid fluctuations in the observed calibrator flux. In order to transfer amplitude solutions to the target field that do not depend on the ionosphere in the direction of the calibrator, the amplitude solutions are averaged before being transferred. See Figure 2-3. PiLL then calculates the phase changes in the calibrator field due to clock delay, Faraday rotation, cross-delay between antenna polarizations[8], and ionospheric TEC (total electron content) as a function of frequency and time.

[6] See http://www.astron.nl/citt/genericpipeline/.

[7] Available at https://github.com/lofar-astron/PiLL.

[8] Cross delay is the phase delay between the 'XX' and 'YY' antenna polarizations. The physical source of this delay is unclear and is currently under investigation.

Though only the clock delay is transferred to the target field, all phase effects must be calculated and then disentangled to isolate the clock delay. The TEC solutions also give an indication of the ionospheric conditions during the observation. If the calibrator solutions show that ionosphere is particularly turbulent, an observation can be discarded before time is invested in attempting to calibrate the target field. Flagging of the data itself as well as the gain solutions happens at each step of the calibrator pipeline.

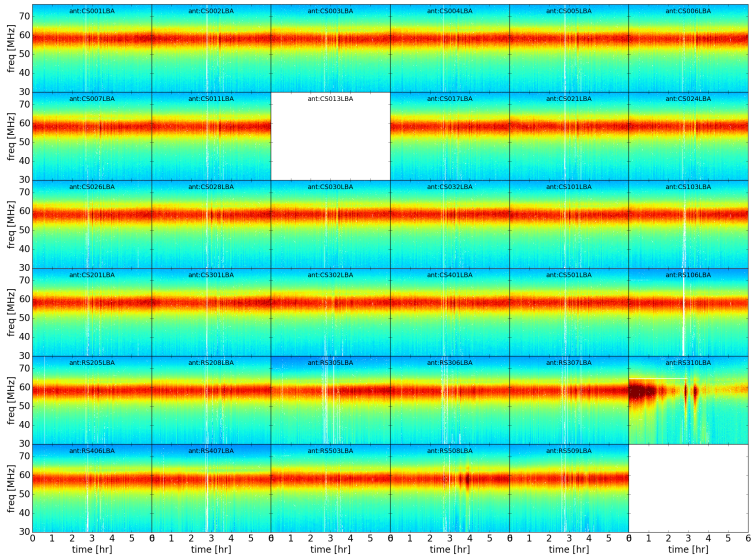

(a) Time-dependent amplitude solutions

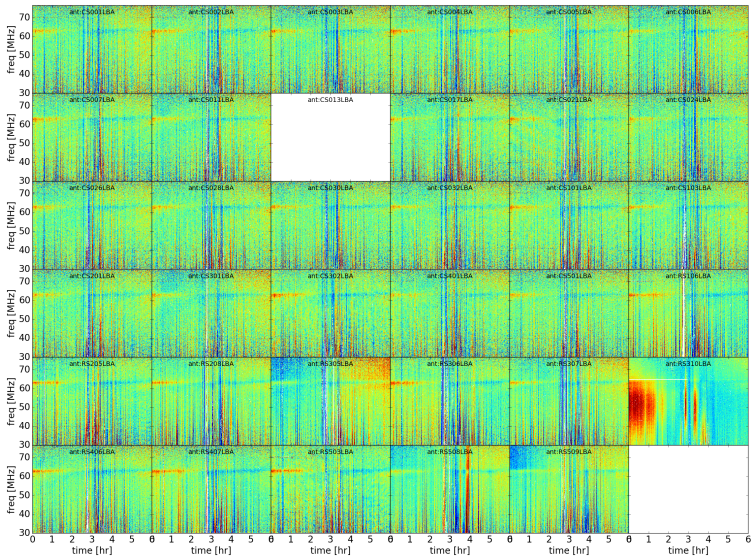

(b) Time-dependent amplitude residuals

Figure 2-3: PiLL calibrator amplitude solutions (top) and residuals (bottom). Red is higher relative amplitude, blue is lower. The LOFAR LBA bandpass peak at ∼60 MHz is clearly visible. Each box represents one LOFAR LBA station; they are arranged with the stations closest to the core at top left, most distant at bottom right. The residuals are the result of subtracting an average bandpass solution that is transferred to the target from the time-dependent bandpass solutions. The calibrator is 3C196 and the data are from HD 80606 Cycle 0 observations after re-pre-processing the raw data. One station shows anomalous bandpass behavior (RS310) and was flagged for the next pipeline steps so as not to introduce large amplitude errors. White spaces represent flagged data. These plots are a standard output of the PiLL pipeline.

Amplitude and clock delay solutions are transferred to the calibrator field for the next step: skymodel-based target field calibration. Calibrator Faraday rotation and TEC phase solutions are not transferred since they depend on the ionosphere in the direction of the calibrator, not the ionosphere in the direction of the target. A skymodel of all known sources in the target field is generated from the TGSS survey [140]. That model is used in a manner similar to the calibrator model to estimate what the complex visibilities 'should' be and then, using the difference between the predicted and measured visibilities, calculate Faraday rotation and TEC. Since there are unlikely to be many bright sources in the target field, multiple subbands (10, in this work) are concatenated together to increase the bandwidth and therefore the signal to noise for phase calibration.

Self-calibration of the target field is the newest addition to the PiLL pipeline[9]. The target field is imaged using WSClean[10] [223], a model is extracted, and phase solutions are adjusted based on the model components found in the image. Several rounds of this direction-independent process can yield 25-50% improvement in image RMS noise. The largest remaining phase errors are the result of differential ionospheric effects across the array, described in the following sections. The next step for PiLL is to incorporate direction-dependent calibration of the target field, perhaps in a manner similar to the FACTOR facet calibration pipeline [296] used by LOFAR HBA. Direction-dependent (DD) calibration is both essential for full exploitation of the LBA's capabilities and extremely difficult (perhaps impossible) given the low density of bright sources at LBA frequencies suitable for DD calibration.

2.5 The Challenge of the Ionosphere

The ionosphere, as alluded to in the previous sections, is the biggest challenge that low frequency ground-based observatories like LOFAR must overcome. The ionosphere, the ionized portion of the Earth's upper atmosphere, is a plasma and there-

[9]PiLL was not available when most of the work described in Ch. 5 was performed, so the imaging strategy was different.

[10]Available at https://sourceforge.net/p/wsclean/wiki/Home/.

fore a dispersive medium — the index of refraction is frequency-dependent. When the frequency of incoming radiation is lower than the peak plasma frequency of the ionosphere, refraction is total and the incoming radiation cannot propagate to the Earth's surface (see Eq. 1.2). At frequencies above the peak ionospheric plasma frequency, incoming radiation is refracted, scattered, and absorbed by the ionosphere. For the purposes of interferometry, ionospheric refraction imposes a frequency- and time-dependent phase delay on incoming radiation that varies in space as well depending on ionospheric density (TEC). See [240] for an overview of relevant ionospheric physics; see [22] for a review common radio astronomy techniques used to mitigate ionospheric effects; see [190] for a discussion of the limitations of current techniques, specifically the thin sheet ionosphere approximation.

The 'Lonsdale regimes' are a useful tool for understanding how ionospheric inhomogeneity will affect observations for different telescopes. Figure 2-4 shows the four Lonsdale regimes, with A as the antenna/station separation on the ground, V as the field of view or primary beam size at the ionosphere, and S is the scale size of ionospheric variations. The VLA falls into Regime 1 or 2, depending on the configuration. Compact low frequency arrays like the LWA [82], Owens Valley LWA [126], and MWA [179] fall into Regime 3. LOFAR LBA is solidly in Regime 4, where each station sees variations in the ionosphere across its primary beam and different stations are looking through different ionospheres toward the same target. There are well-established calibration techniques for Regimes 1–3. For Regimes 1 or 2, self-calibration works well. Regime 3 requires more sophisticated tools, like field-based calibration [58] or SPAM (Source Peeling and Atmospheric Modeling) [139]. Calibration in Regime 4 is an open problem.

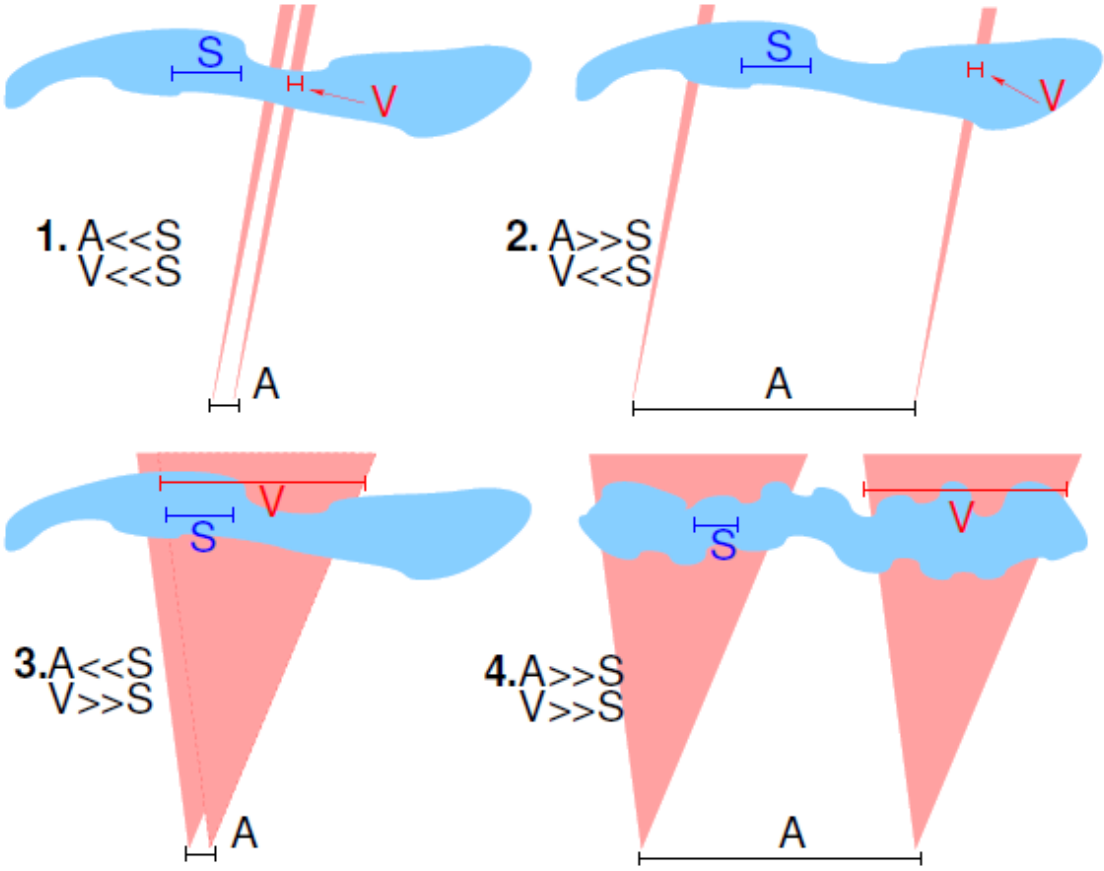

Figure 2-4: Lonsdale regimes 1-4. A is the antenna separation, V is the antenna (or station) field of view at the ionosphere, and S is the scale size of ionospheric variability. Figure reproduced from [180], Figure 1.

LOFAR LBA users are confronting the Regime 4 problem using a direction-dependent approach similar to the HBA FACTOR scheme. The field of view is split up into 'facets', each containing one or more bright sources. Self-calibration is then performed on each facet to extract a phase correction applicable to that facet. Once all directions have been calibrated, the TEC phase corrections from each facet are smoothed into a phase screen that covers the full field of view. The full field can then be imaged after the phase screen correction is applied. This approach has been successful for LOFAR HBA, but encounters a major problem at lower frequencies: the number of available direction calibrator sources. Each calibrator source must have a large enough signal-to-noise ratio (SNR) on short timescales (seconds to minutes) that self-calibration can succeed. For the current LBA, must be about 10 Jy to be

useful directional calibrators[11]. There are a limited number of 10 Jy calibrators in any given field - usually not more than 2–3. This is not enough directional calibrators to facet a wide field of view (commonly 10°) while ensuring that the ionospheric solution over a single facet is constant. In summary, LBA has fewer available directional calibrators than HBA while requiring more facets to achieve good direction-dependent calibration results.

The shortage of appropriate directional calibrators can be improved by increasing the sensitivity of the LBA stations so that fainter sources have sufficient SNR to serve as directional calibrators. Using all 96 LBA antennas in each station would be a major step in this direction. Building additional stations would also help. Section 2.7 discusses additional methods for improving ionospheric calibration for ground-based arrays. An alternative solution is to leave the surface of the Earth and observe from above the ionosphere (Chapters 7, 8).

2.6 Other Low Frequency Challenges

2.6.1 RFI

There are many man-made signals at low frequencies: radio stations, arcing power lines, analog and digital TV broadcasts, etc. At higher frequencies, RFI is usually restricted to line or sight or perhaps single reflections but at low frequencies the ionosphere can allow radio noise to propagate from much farther away. In theory, local RFI at one station will not correlate and so should drop out of the interferometric visibilities, but in practice very strong RFI can clip amplifiers and render some frequencies useless. Standard practice in radio data reduction is to simply 'flag' and remove RFI-contaminated channels, but this reduces the overall bandwidth and/or integration time of the observation, reducing sensitivity. There are well-developed tools for smart RFI flagging, such as AOFlagger [222], which preserve as much data as possible while efficiently excising RFI. For maximum sensitivity, however, it is nec-

[11] F. de Gasperin, private communication.

essary to build radio arrays in very radio-quiet places (like the MWA in Australia) or employ more sophisticated techniques to null RFI before it gets into interferometric visibilities.

2.6.2 Primary Beam

Digital beamforming has many advantages, like being able to do simultaneous target and calibrator observations, but it also makes LOFAR's primary beam time variable due to changes in the sidelobes as the station beamformer tracks the target source. If the primary beam is not accurately modeled, attempting to correct images for the beam shape will result in residual phase and amplitude errors. The LOFAR LBA beam model is far from perfect and indeed beam-induced errors are seen in LBA data, especially at low elevation. Proper beam modeling is also necessary for polarimetry observations, which are essential to exoplanet observations.

2.6.3 Widefield Imaging

The LOFAR primary beam (and resulting image FOV) is very wide ($\sim 10^\circ$), breaking the usual assumption that the image plane can be approximated as flat. The standard technique for dealing with widefield imaging, w-projection [57], quickly becomes very computationally intensive for such large fields. GPU support for already-efficient imagers like WSClean is a major step toward widefield imaging in reasonable computational time. There are other algorithms in the literature, however, that discard the planar assumption for the image plane [260, 47]. Investigating the utility of these algorithms is a topic of future work, particularly for the case of space-based interferometry (Chapter 7).

2.6.4 Big Data

Large scale low frequency interferometers that use digital beamforming and correlators have only become feasible as computational costs have come down in recent years. Telescopes like LOFAR, MWA, and LWA produce voluminous data, which

presents challenges for real-time correlation, storage, transmission, and processing. The future Square Kilometer Array (SKA) will produce an order of magnitude more data than existing telescopes. LOFAR raw datasets can be several terabytes (TB)[12]. Even averaged datasets are 100s of gigabytes (GB). Running these data through ever more complex calibration pipelines is infeasible on desktop machines and still time-intensive on multi-core servers. As a point of reference, running the PiLL calibrator portion only on a 2-hour LBA observation using a compute node with 40 CPUs takes ∼24 hours. Imaging, as discussed in the previous section, is equally computationally intensive. Improvements in parallelization for the software tools underlying pipelines like PiLL are essential for processing radio data sets in a reasonable amount of time (days instead of weeks/months).

2.7 Future Work

The primary topic of future work for LOFAR LBA data is improving ionospheric calibration. The ionosphere currently limits the sensitivity of LBA images to several times the theoretical thermal noise. While FACTOR has been successful in achieving near-thermal noise for HBA, the challenges described in Section 2.5 put thermal noise limited imaging with the current LBA out of reach. A key area of future work will be bringing auxiliary ionosphere data into the calibration process to improve the model of the ionosphere used to calculate phase delays as a function of time and space. Existing networks of dual-band GPS receivers and ionosondes could be exploited to provide additional ionospheric constraints beyond what is available in the LOFAR data itself. Ultimately, direct ionospheric measurements in three dimensions may be needed to allow LOFAR LBA and similar future telescopes to reach their theoretical sensitivity limits.

Polarization calibration is another critical area of future work for LBA data. Exoplanetary radio emission (and stellar flare emission) is expected to be strongly circularly polarized. LBA imaging and analysis to date has focused on Stokes I to

[12]LOFAR Cycle 0 HD 80606 b raw data is >6 TB per 6 hour observation before averaging.

refine reduction techniques and reduce imaging runtimes, but Stokes V calibration and imaging must be tackled. A first step towards reliable Stokes V results from LOFAR is to identify good candidate sources to serve as polarized calibration sources. Unpolarized sources will also be used to assess the degree of polarization leakage due to poor antenna and beam models.

LOFAR calibration and imaging are active areas of current research and development, while VLA calibration is essentially a solved problem above 1 GHz. The ionosphere is the biggest challenge, and a major update to LOFAR may be required before the LBA can reach its potential. In the interim, novel data fusion techniques using external ionospheric data will be pursued in an attempt to reach near-thermal noise levels in LBA images.

Chapter 3

Radio Sky Survey Archive Search for Exoplanetary Radio Emission [1]

3.1 Motivation

Nearly all large general-purpose radio observatories produce sky surveys as a service to the astronomy community. Often, one observatory will produce several surveys at different frequencies. The final data product from such surveys is typically a source catalog along with processed FITS images from which the catalog sources were extracted. These surveys contain a tremendous amount of information that may be relevant to a wide range of scientific questions, but some effort is required to extract that information. The catalogs that result from radio surveys are valuable, but they do not contain all of the information that is available in the images from which sources are extracted.

The work described in this chapter was motivated by a desire to develop a standard framework for scouring survey images for faint, uncataloged sources using modern software tools and a 'big data' approach. This framework was used to search for faint emisssion at the location of known nearby stars and exoplanets in this case, but could easily be adapted to other applications. It is also trivial to expand the

[1] The work in this chapter comes from the final class project of Astroinformatics (Spring 2015). Updates have been added based on newly available radio surveys.

framework presented here to other surveys if the image data can be obtained, allowing for fast searches of new catalogs as soon as they are made public. I demonstrated this capability with the TGSS ADR1 (see Section 3.3.3), which was released in late 2016. The tools described below were applied to this new data release in a matter of hours.

This chapter describes the search of two large low frequency surveys, the Very Large Array's (VLA's) 74 MHz VLA Low-frequency Sky Survey redux (VLSSr) [166] (Section 3.3.2 and Giant Metrewave Radio Telescope's (GMRT's) 150 MHz TIFR[2] GMRT Sky Survey [266] (TGSS, see Section 3.3.3), for signals from exoplanets and/or nearby stars. The simplest way to do this would be to check the coordinates of known stars (either nearby stars or known exoplanet hosts) against the source catalogs produced by the surveys. Typical catalog generation approaches only list sources that are many standard deviations (5-7σ) above the background, however, potentially leaving out real sources that are of lower significance. To fully exploit the data it is necessary to look at the survey images directly and attempt for low-sigma sources that the catalog generation process missed. In VLSSr, the average RMS noise in an image is $\sim$100 mJy, but the 5-σ catalog cutoff means that the faintest sources in the catalog are 500 mJy. A 3-σ source, which is very likely to be real, would not appear in the catalog. Even a 2-σ source at the location of a known exoplanet would be worthy of follow-up in other catalogs or additional observations. As discussed in Chapter 2, radio emission from exoplanets is likely to be faint and near the detection limits of existing telescopes; faint, low significance sources in survey data at the positions of known exoplanet systems or nearby stars could be planetary in origin and should be identified for follow-up.

3.2 Target List Generation

This work describes a targeted rather than blind search for exoplanetary radio emission in survey data. A targeted search is simpler to implement than a blind search

[2]Tata Institute of Fundamental Research

because only the locations of known stars are examined. A blind search for weak radio emission would entail a full reanalysis of all survey images. Images were therefore searched for faint sources only near the location of known stars. Two target lists were generated for this search. The first list included all known exoplanets with a measured system distance less than 100 pc. The 100 pc distance limit is arbitrarily chosen, but reflects the consensus that very distant exoplanet systems are unlikely to exhibit sufficiently bright radio emission to be detectable in current surveys. The 100 pc list was generated by searching the Open Exoplanet Catalog [242], an online database that collects exoplanet data, via `astroquery` for all exoplanet systems with a system distance value less than 100 pc. Entries with no distance entry were discarded. The results of this query were converted to a `VOTable` for compatibility with the source search module. The 100 pc sample contains 417 systems.

The second target list contains all stellar and sub-stellar (brown dwarf) objects within 8 pc. This list was taken from Kirkpatrick et al. (2012) [154]. This list was chosen because it incorporates recent discoveries from WISE and other searches for low-mass stars. There are 243 objects in 182 systems in the 8 pc sample. The list from Kirkpatrick et al. was downloaded from the journal website in a machine readable form and then parsed into a `VOTable` in `Python`. Though the table was technically machine readable, the format included blank lines and footnotes that made parsing very time consuming.

The goal of searching a list of very nearby objects is twofold: first, detecting stellar or brown dwarf radio emission at low frequencies is scientifically interesting in its own right; second, it is possible that some of these objects may have planets that have not yet been discovered. The most heavily used exoplanet discovery techniques, radial velocity and transit, are most sensitive to planetary systems that are 'edge on' from the Earth's line of sight. Searching nearby systems in radio offers the possibility of detecting new planets that are in a less favorable orientation via their radio emission.

Limiting the list to 8 pc improves the chances of detecting emission since source flux falls off as $1/r^2$. For example, a planet with Jupiters radio luminosity in orbit around Alpha Centauri would have a flux of $\sim$150 mJy. Such a planet would be just

below the detection limit of the VLSSr survey.

An intriguing question emerged from studying the objects in the 8 pc survey: Is there a list of all the stars that have been searched for exoplanets and have NOT had detections? Many of the nearby stars have been searched for planets multiple times with various techniques, but there is no simple way to collect information on null planet detections. Particularly in cases where multiple techniques have been applied, there should be a set of upper limits in mass, semi-major axis, inclination, etc. that result from null detections. Having access to such a catalog of non-detections would be useful for future searches as well as statistical characterization of stellar systems without planets. The concept of an exoplanet null result database is discussed further in Section 3.6.1.

3.3 Surveys and Search Methods

This section describes the two surveys that were searched for faint radio emission from nearby stars and known exoplanet hosts and the techniques used to conduct this search.

3.3.1 Prior Work

The original VLSS survey (prior to a recent re-reduction) was searched for radio emission from nearby stars, but nothing was detected [168]. This search attempted to build up signal and lower the noise floor by stacking multiple image 'postage stamps' centered on nearby stars together. The goal of this project is to perform a similar search on the new VLSSr survey results and expand the technique to additional catalogs. The previous partial TGSS data release (prior to TGSS ADR1, described below) images were searched for exoplanetary emission by Sirothia et al. (2014) [265]. Results from this study (prior to the ADR1) are compared to that work in Section 3.4.4, Table 3.4.4. The newly released full survey (TGSS ADR1) has been searched for exoplanetary radio emission and nearby radio stars for the first time in

this work. Very recently, the GLEAM[3] survey [307, 138] by the Murchison Widefield Array (MWA) [179] at ∼80–231 MHz was searched for emission from a small set of nearby exoplanets [208] and young exoplanetary systems [186]. Expanding this work to search the GLEAM images for emission from nearby stars is a topic of future work.

3.3.2 VLSSr: The Very Large Array (VLA) Low-frequency Sky Survey (redux)

The VLSS survey was observed between 2001 and 2007 (∼900 hrs) and covers almost all of the northern sky above -30 declination [53]. The survey used the VLAs 74 MHz system [150]. The VLSS data was re-reduced to produce the VLSSr (VLSS redux) [166, 165] which was released in 2014. The re-reduction of the survey data with improved ionospheric correction increased the number of catalog sources by 36%, reduced the mean RMS by 25% (120 mJy → 90 mJy), and slightly improved the beam size (80 arcsec → 75 arcsec). Figure 3-1 shows VLSSrs sky coverage. VLSSr FITS images are available as 17°x17° FITS images. These images are combinations of several pointings made at different times but reduced together. All of the VLSSr images (358) were downloaded from http://www.cv.nrao.edu/vlss/MAPS/ via `wget` and stored in a local folder for quick access.

3.3.3 TGSS: TIFR GMRT Sky Survey

TGSS is a 150 MHz survey conducted by the Giant Metrewave Radio Telescope (GMRT) that covers the sky north of -55° declination [266]. Until recently, only a small number are fully reduced and publicly available. Intema et al. [140] reduced the full survey using the SPAM [139] algorithm (TGSS ADR1). The initial reduction had angular resolution of about 20 arcseconds and RMS noise less than 10 mJy. The new, full reduction achieves ∼5 mJy beam^{-1} RMS noise and 25″x25″ arcsec resolution. Figure 3-2 shows the sky coverage and RMS noise of images for the complete TGSS ADR1. The full TGSS ADR1 is available as a source catalog as well as a set of

[3]GaLactic and Extragalactic All-sky MWA survey

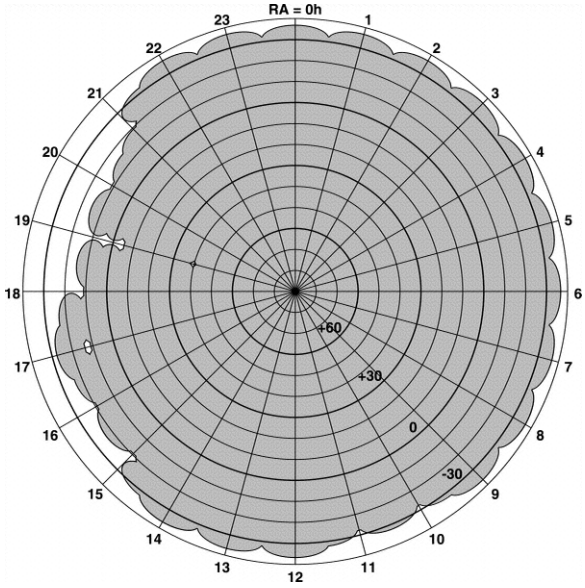

Figure 3-1: VLSS sky coverage. Concentric circles are declination, with the NCP at the center. Straight rays are right ascension. Figure reproduced from [53].

5336 5°x5° FITS images. All of the FITS images were downloaded to a local folder from http://tgssadr.strw.leidenuniv.nl/mosaics/ so that they could be searched for uncataloged faint sources.

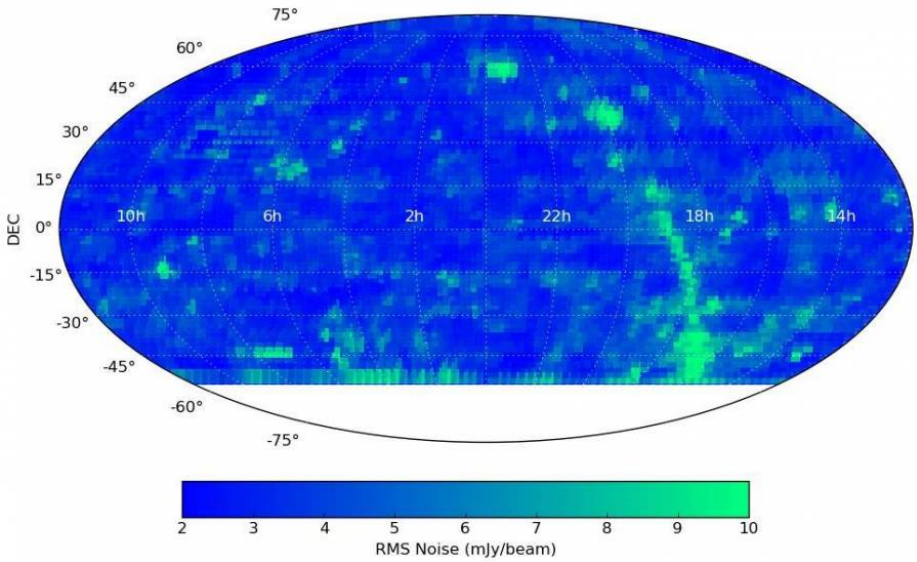

Figure 3-2: TGSS ADR1 RMS map. The map shows the full sky coverage of the survey in equatorial coordinates. Color indicates the RMS level of the survey images at each point. Figure reproduced from [140]. The stripe of higher RMS values is the galactic plane. Bright "A-team" (CygA, CasA, etc.) sources also have higher RMS values in the regions around them.

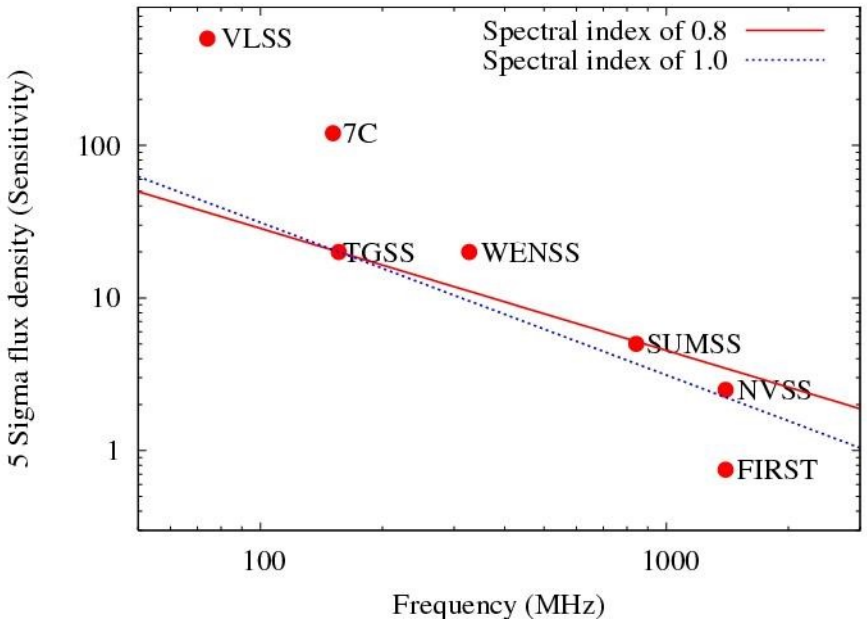

Figure 3-3: Comparison of radio surveys. Note that the VLSSr has improved sensitivity over the VLSS (shown here) by ∼25%. The red solid line is a typical spectral index for extragalactic sources (-0.8). The black dotted curve is a slightly steeper spectral index (-1). The vertical axis units are mJy. Figure source: http://tgss.ncra.tifr.res.in/150MHz/obsstrategy.html. This figure demonstrates that TGSS is more sensitive than previous 150 MHz surveys (7C).

3.3.4 Source Detection in FITS Images

The source detection pipeline is shown in flow chart form in Figure 3-4. The source detection pipeline loops through all of the coordinates in the target lists (8 pc sample and exoplanets within 100 pc). The first step of the pipeline uses a function called `chooseFits()` to pick out the appropriate FITS file from the selected survey (VLSSr or TGSS ADR1) by matching the objects RA/Dec coordinates to the FITS image file name. In the case of TGSS ADR1, each catalog entry lists the relevant image for easy retrieval. If no FITS file can be found that matches the object coordinates closely enough, the failure is recorded in a dictionary and the next coordinate set is entered into `chooseFits()`. If a FITS file is found successfully, the pipeline moves on to source detection.

Source detection in the FITS images is performed using a python package called `PyBDSF` (**B**lob **D**etection and **S**ource **F**inder) [238, 198]. `PyBDSF` was developed for

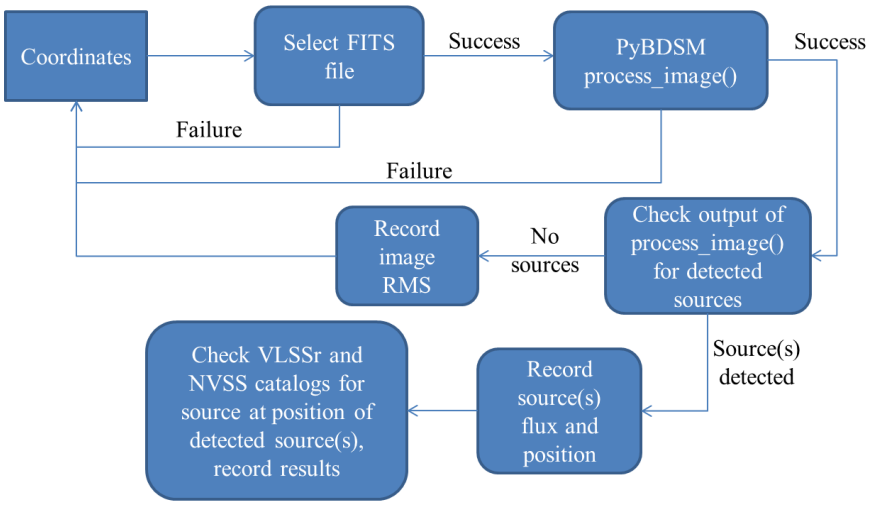

Figure 3-4: Source detection flow chart. With the exception of the PyBDSM block, all blocks contain code written by me for this experiment.

the LOFAR telescope [65]. Its primary purpose is the automatic generation of source catalogs from large surveys, so it is optimized for extracting sources from radio FITS images. `PyBDSF` has its own terminal interface, but it can also function like a normal `python` package (once it is installed from source) and be imported in a script or in an `ipython` session. The main function used for source detection was `process_image()`. `Process_image()` takes a FITS file as input along with a long list of optional parameters. In this case, the only additional parameters passed to `process_image()` were `thresh`, `thresh_pix`, and `trim_box`. Setting `thresh` to 'hard' and `thresh_pix` to 2.5 sets a detection threshold of 2.5 times the RMS noise value (2.5σ) reported in the FITS image header. The `trim_box` option selects a sub-window of the FITS image for source detection. The box size was set to 55 pixels and the box was centered on the coordinates of the object of interest. The appropriate pixel range was determined by converting the RA/Dec input coordinates to image pixel coordinates via the `astropy.wcs` package. The box size was chosen based on experiments with a range of sizes. Larger sizes typically led to detection of multiple sources far from the central coordinates while smaller box sizes made it difficult for the algorithm to accurately estimate the image RMS within the box.

`PyBDSF` detects sources by first finding 'islands' of pixels that are greater than

the threshold. `PyBDSF` then attempts to fit 2D Gaussians of various shapes to the island to recreate the brightness pattern in the image. If requested, the results of `process_image()` can be displayed in a standard format by `show_fit()` (see Figure 3-5). The first image (top left) shows the original sub-window from the FITS file. The second image (top center) shows the island (light blue crosses) and any Gaussians fit to that island (pink). The fifth image (bottom center) shows the model source made from the sum of the pink Gaussians. The fourth image (bottom left) shows the difference of the original image and the model image. If more than one island is detected, `PyBDSF` creates a `Source` object for each island. Before running the source detection pipeline on the actual target lists, it was tested against a list of bright known VLSSr sources (50-100 Jy). The results, both source locations and flux levels, were satisfactory for this test list.

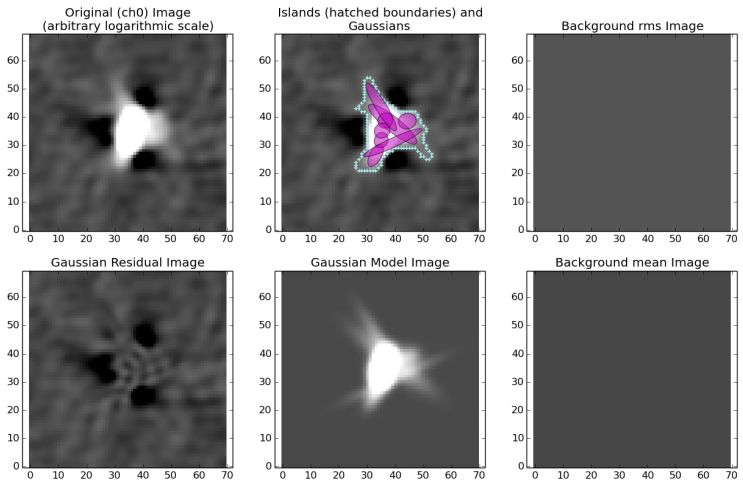

Figure 3-5: `PyBDSF` `show_fit()` example output for a bright test source. A description of each image is shown above the subimages. The top left image is the input image. Top center shows the island boundary (cyan hatch) and 2D Gaussians fit to the island (magenta). Top right shows the background RMS of the image which may vary spatially. Bottom left shows the original image with the Gaussians subtracted. Bottom middle shows the source model generated from the sum of the Gaussian fits. Bottom right shows the mean RMS across the image.

The output of `process_image()` is an `Image` object. The contents of this object are not described in [238], but examination of the `PyBDSF` source code (specifically

`image.py`, `gaul2srl.py`, and `island.py`) yield a definition of the `Image` class and `Source` class. If the output of `process_image()` contained no `Source` objects, the non-detection was noted in the results dictionary along with the image RMS for the purpose of setting luminosity upper limits. If at least one `Source` object was found, it was recorded and examined in more detail. The flux level of the source and the angular separation between the target coordinates and the detected source coordinates were recorded in the results dictionary. The detected source coordinates were searched in both the VLSSr and NVSS [55] catalogs via `astroquerys Vizier` package. `Vizier` is a database of astronomical catalogs [220]. A search radius of 2 arcminutes was used for VLSSr while a radius of 1 arcminute was used for NVSS. Matches from either catalog were added to the results dictionary.

Occasional errors with PyBDSF occurred when the FITS images were not complete or were corrupted in some way. These errors were recorded in the results dictionary. Most errors of this type were for targets with declinations below 0°, where Northern hemisphere telescopes are forced to make observations at low elevation. Once all coordinates in the target lists were run through the source detection pipeline, the positive results were narrowed further. Only detected sources within two beamwidths ($\sim$2.5 arcminutes for VLSSr) of the target coordinates are of interest, since sources farther away are unlikely to be associated with the target object. A list of detections within 2.5 arcminutes of the target object was compiled from the results dictionary and then the results of `process_image()` were displayed via `show_fit()`.

Targets with valid FITS images but no `PyBDSF` source detections were further processed to set an upper limit on planet/star radio luminosity based on the subwindow RMS reported by `PyBDSF`. The noise properties of these images were also investigated to determine whether the image noise was sufficiently Gaussian. Finally, all of the subimages from either VLSSr or TGSS were stacked as described in Lazio (2009) [168].

3.4 Results

A handful of targets of out of the initial list of several hundred yielded interesting signals. These specific cases are discussed below in detail. Detections were deemed worthy of additional follow-up when they were within two beamwidths of the target coordinates and they did not appear in the VLSSr catalog. Follow-up included literature searches and Vizier [220] catalog searches for the object. If the object appeared in other radio catalogs, a spectrum and spectral index were calculated in order to determine whether it was a background extragalactic source. Extragalactic sources are expected to have characteristic sychrotron spectral indices around -0.7. Planets and stars had flatter spectra and are expected to have a cutoff at higher frequency, so they are less likely to appear in higher frequency catalogs like NVSS/FIRST [55, 19].

3.4.1 Nearby Stars

There were three detections in VLSSr and one in TGSS for targets in the 8 pc list (see Table 3.4.1, Figures 3-6, 3-7, 3-8, 3-9). The most promising is GJ 382, an M2V star with known photometric variability and an X-ray association. The detection is quite close to the catalog coordinates of the star, and there is no NVSS counterpart. The variability and X-ray association point to the star itself as the radio source, but a planet cannot be ruled out. Further observation, preferably in circular polarization over many days, is needed to further constrain the source of radio emission at this location. The other detections are fairly far from the target coordinates, and two of them have NVSS associations. In the case of brown dwarfs and M dwarfs, higher frequency emission may come from the star itself. Further observations are required to definitively determine the origin of the detected radio emission; follow-up on the most promising targets is the subject of future work.

Table 3.1. Sources detected from the nearby objects (8 pc) list

Target	Survey	Separation from target (arcmin)	Flux density (mJy)	NVSS counterpart?	Notes
BD-03 2870 (GJ 382)	VLSSr	0.06	584.6 ±152.4	No	M2V, known variable with X-ray assn.
2MASSI J0937347+293142	VLSSr	2.17	316.6 ±72.0	Yes	Brown dwarf (T6)
G 157-77 (GJ 1286)	VLSSr	2.43	424.4 ±118.0	No	M5.5V
LP 656-38	TGSS	1.25	16.8 ±4.3	Yes	M4V, rotational variable

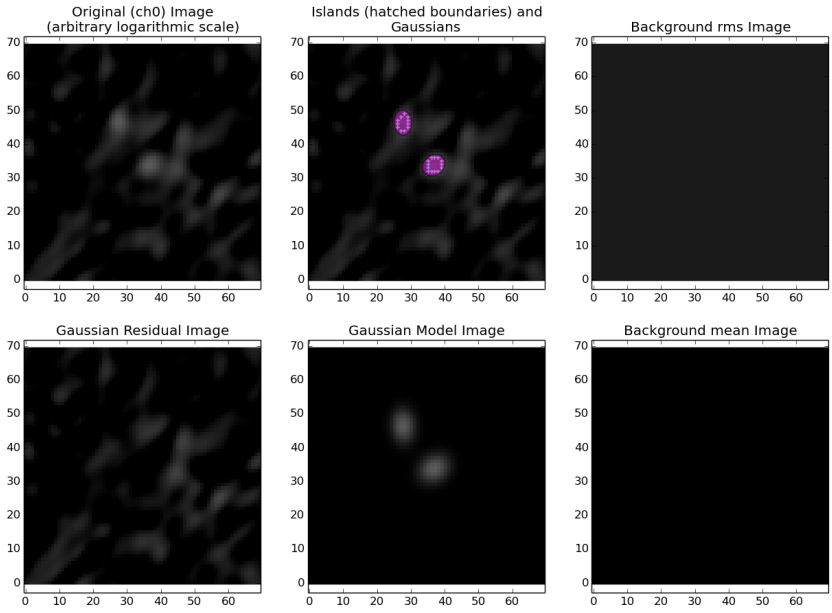

Figure 3-6: VLSSr detection near GJ 382. See Figure 3-5 for a description of each box.

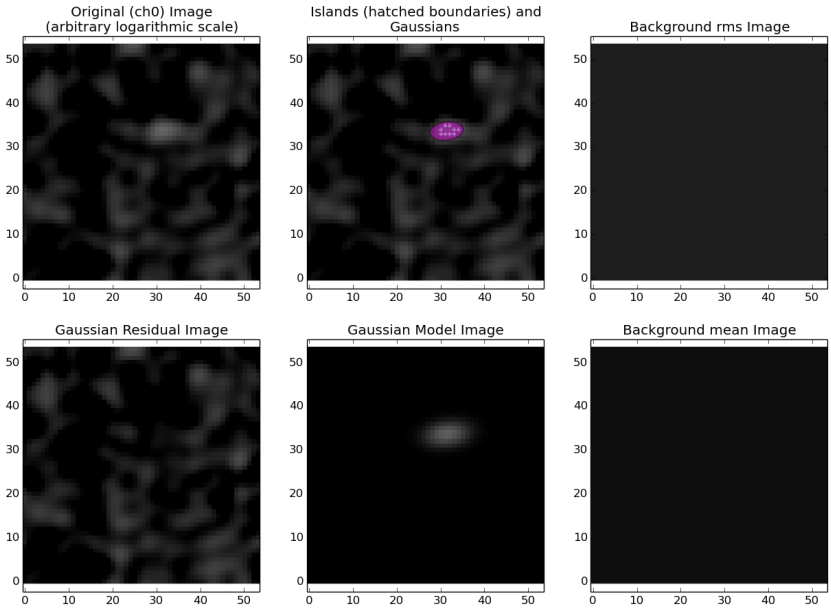

Figure 3-7: VLSSr detection near 2MASS J0937347+293142. See Figure 3-5 for a description of each box.

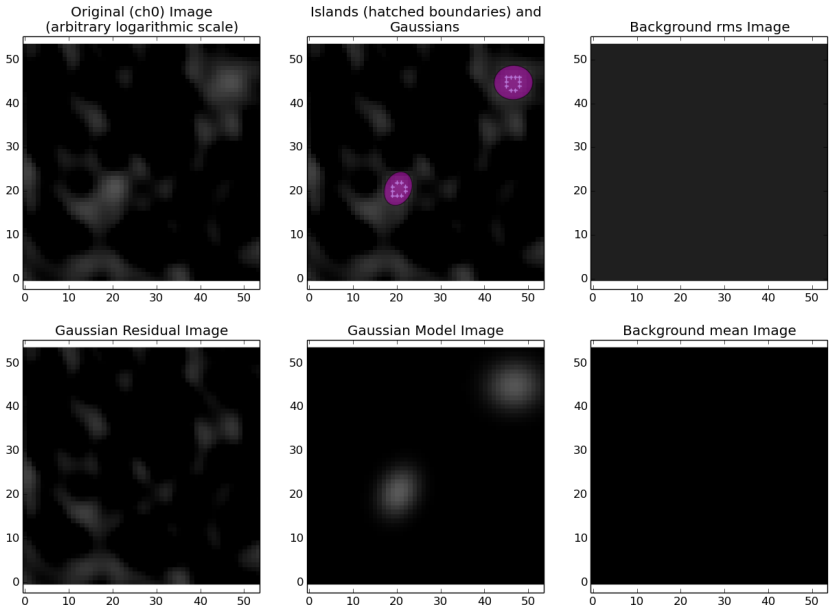

Figure 3-8: VLSSr detection near GJ 1286. See Figure 3-5 for a description of each box.

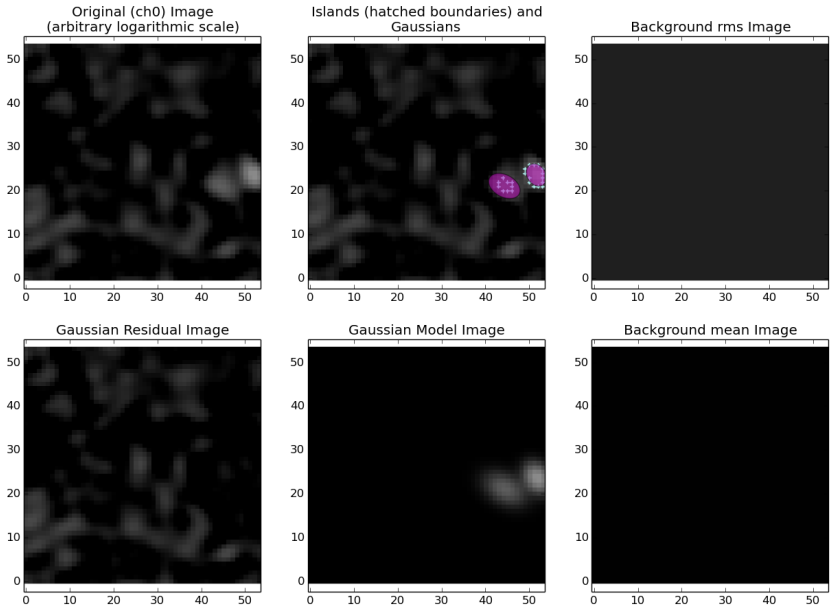

Figure 3-9: TGSS detection near LP 656-38. See Figure 3-5 for a description of each box.

3.4.2 Upper Limits for Nearby Stars Non-detections

Planet/star flux and luminosity upper limits were calculated for all non-detections in both lists. Figure 3-10 show these results. The right vertical axis in Figure 3-10b shows luminosity relative to Jupiter's radio luminosity at ∼30 MHz. All of the upper limits are at least two orders of magnitude above the Jovian value. Deeper observations are required to push the upper limits down to a more physically meaningful value (see next chapter).

3.4.3 Known Exoplanet Systems

This section presents the results for archival search for radio emission at the location of the nearest exoplanets.

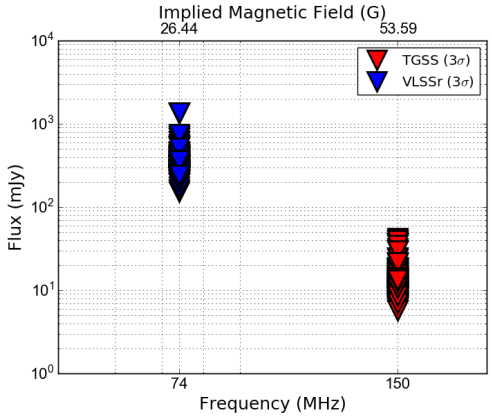

(a) Flux upper limits for stars within 8 pc

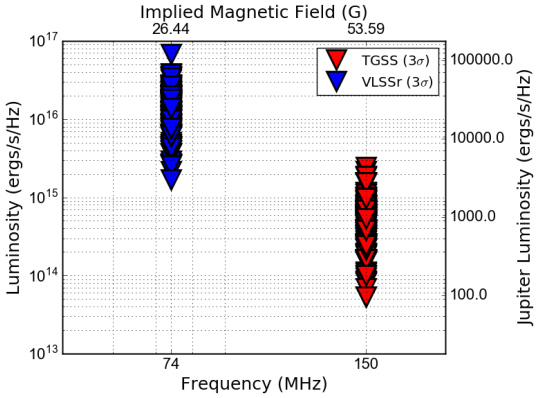

(b) Luminosity upper limits for stars within 8 pc

Figure 3-10: Upper limits on radio flux (left) and luminosity (right) for for nearby stars within 8 pc. Blue downward triangles represent 3σ limits at 74 MHz derived from VLSSr. Red downward triangles represent 3σ limits at 150 MHz derived from TGSS ADR1.

61 Vir

The strongest and most promising detection from the 100 pc exoplanet sample was 61 Vir. 61 Vir(ginis) is a nearby (8.5 pc) three-planet system detected via radial velocity [300]. None of the planets transit the host star. The host star is a relatively old (6.1 Gyr) G7V star. The output of `PyBDSF` for the coordinates of 61 Vir in VLSSr and TGSS are shown in Figure 3-11 and Figure 3-12 respectively. The VLSSr detection is close to the noise floor, but the TGSS detection is unambiguous. There is an NVSS source that corresponds to the coordinates of the detected source. Sirothia et al. (2014) [265] also reports the detection of emission very close to the known position of 61 Vir. The detected VLSSr source (which does not appear in the VLSSr catalog) is 5 arcseconds from the coordinates of 61 Vir and has a flux density of 493 mJy ($\pm$ 130 mJy).

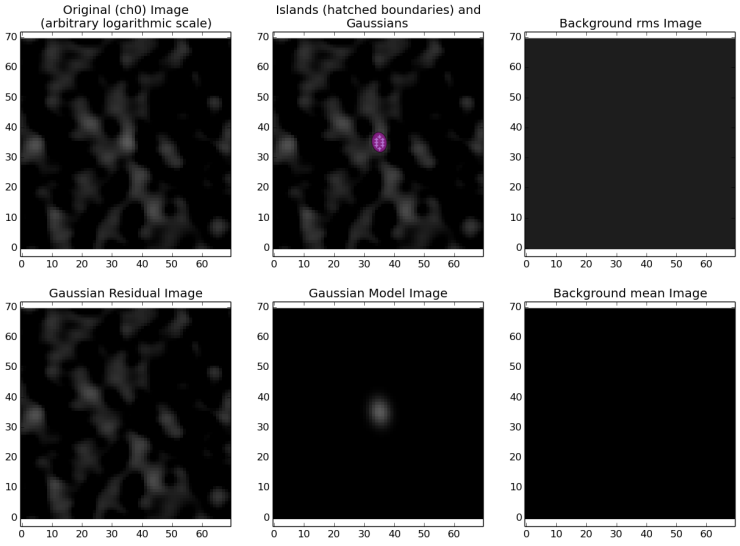

Figure 3-11: `PyBDSF` results for 61 Vir (VLSSr, 74 MHz). See Figure 3-5 for a description of each box.

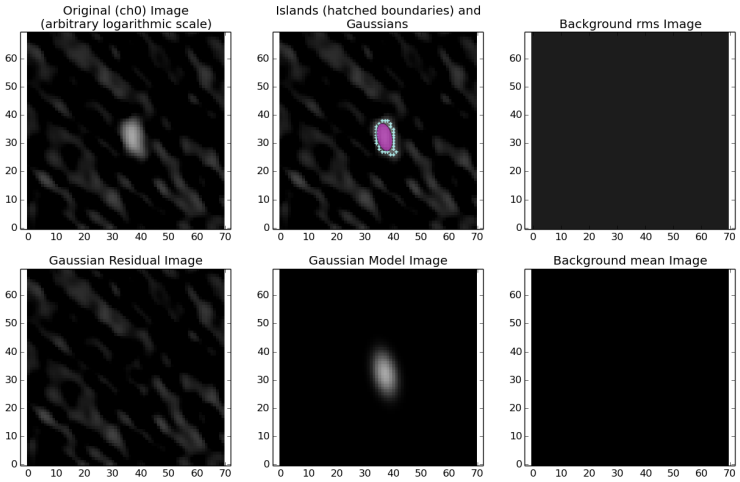

Figure 3-12: `PyBDSF` results for 61 Vir (TGSS, 150 MHz). See Figure 3-5 for a description of each box.

The 61 Vir detection was particularly interesting because it is listed as the 5^{th} most likely planetary system to show internally generated exoplanetary radio emission due to high ionizing X-ray flux from the host star [216]. While it is difficult to accurately estimate exoplanetary flux levels, the proximity of 61 Vir, the relatively large masses,

and the small semi-major axes of its planets make it a good candidate to exhibit bright radio emission. A literature search for 61 Vir in SIMBAD [310] revealed that the 61 Vir system had been imaged by Herschel as part of the DEBRIS survey [328]. A debris disk was detected with an inner radius of 30 AU, outer radius of 100 AU, and system inclination of 77°. Herschel images in 6 bands are shown in Figure 3-13.

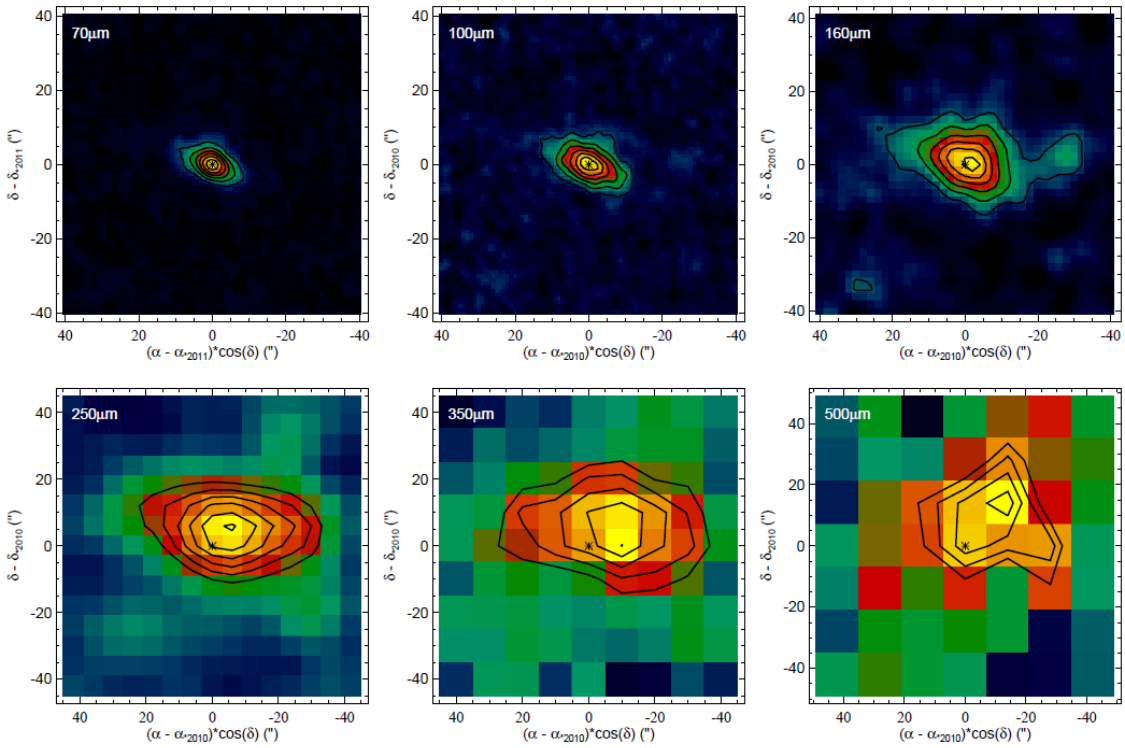

Figure 3-13: Herschel observations of 61 Vir in 6 bands [328]. The wavelength is indicated in the upper left corner of each image. The black asterisk indicates the coordinates of the star.

Wyatt et al. (2012) [328] note that 61 Vir is a high proper motion star that moves over an arcsecond per year. They searched the the VLA archive and discovered a 5 GHz observation of a field containing the current coordinates of 61 Vir. There is a double-lobed source in the field within a few arcseconds of 61 Virs current coordinates, but the 5 GHz observation was made in 1987 when 61 Vir was nearly 40 arcseconds away from the location of the double-lobed source which is approximately 4 times the pointing error of that measurement (see Figure 3-14). The authors conclude that the radio source detected at 5 GHz and 1.4 GHz (NVSS) is a background galaxy that is

currently in a chance alignment with 61 Vir.

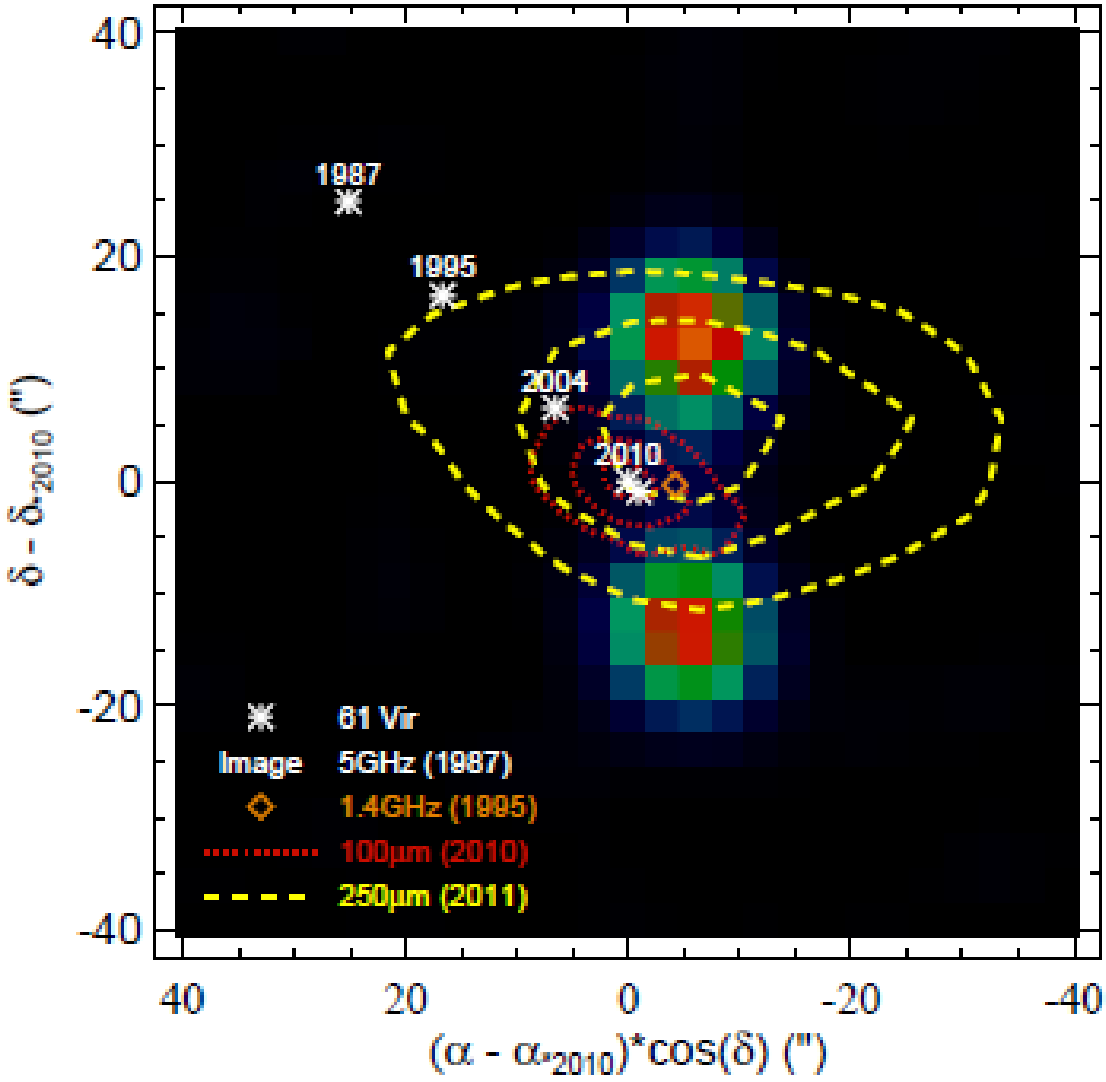

Figure 3-14: 5 GHz VLA source with 61 Vir positions superimposed. The location of the 1.4 GHz NVSS source is indicated with a small orange diamond. Figure reproduced from [328]. 61 Vir is clearly moving towards the static background source detected in radio (1.4 and 5 GHz).

In order to confirm that the radio source is most likely a background galaxy, a power law fit to all available data was performed (Figure 3-15). In addition to the flux densities calculated in this work, flux densities were extracted from NVSS (1.4 GHz), WISH [74] (325 MHz), Sirothia et al. (2014) (150 MHz), and Wyatt et al. (2012)

(5 MHz). The resulting spectral index of -0.85 [-1.102, -0.5886] is consistent with a non-thermal source. As shown in Figure 1-2, planetary spectra are generally fairly flat and show a sharp cut-off at the local electron cyclotron frequency (40 MHz for Jupiter). Based on the spectrum of this source as well as the sources lack of motion relative to the motion of 61 Vir, the most probable conclusion is that the radio source near 61 Vir is a background galaxy. Future radio observations should add evidence to this hypothesis if the source location continues to stay fixed as 61 Vir moves to the southeast.

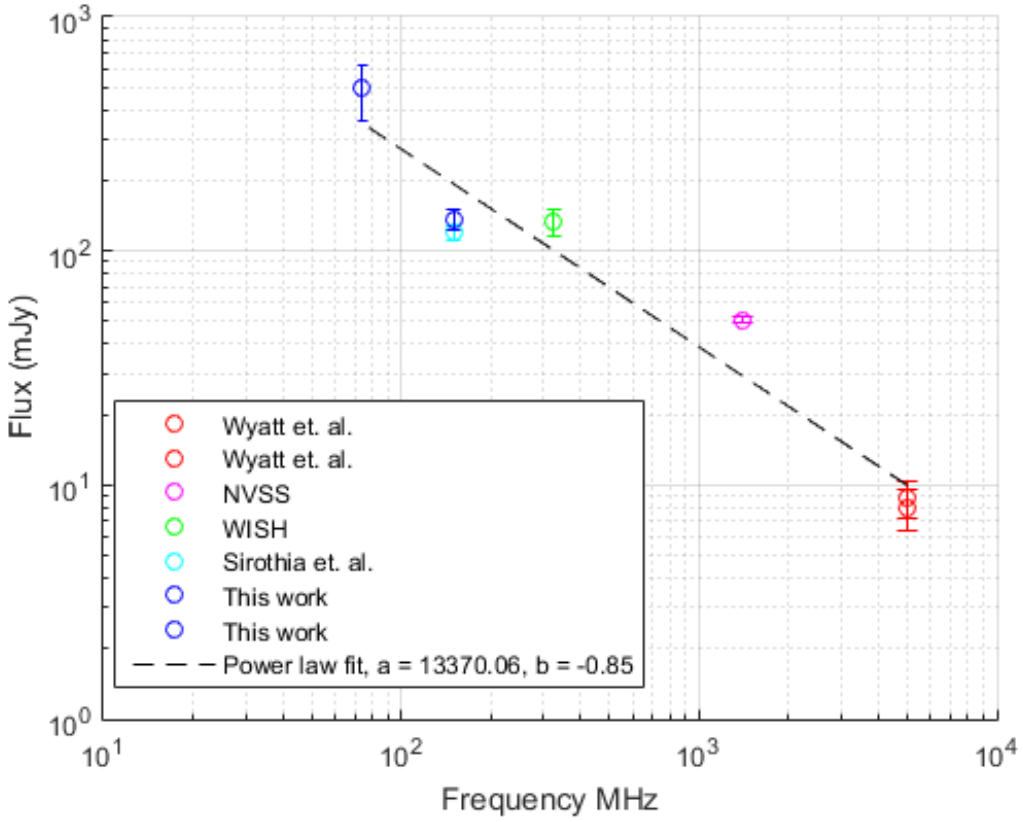

Figure 3-15: All available radio measurements of source near the position of 61 Vir. A power-law fit yielded a spectral index of -0.85, consistent with non-thermal emission from a galaxy.

3.4.4 HD 43197

The new TGSS ADR revealed another case like 61 Vir: HD 43197. Sirothia et al. [265] noted that this exoplanet host had an NVSS catalog source near its position.

The source also appears in the TGSS ADR and GLEAM catalogs, but not in VLSSr. Figures 3-17a, 3-17b, and 3-18 show the 2MASS image of the the star, the GLEAM image, and the VLSSr field centered on the location of the star. Fitting a spectrum based on the fluxes from those three catalogs reveals a steep spectral index of -1.59 [-2.071, -1.109] (see Figure 3-16). Fitting to the GLEAM fluxes only yields a similar spectral index (-1.468 [-1.914, -1.022]). Though GLEAM and VLSSr overlap in frequency, the source near the location of HD 43197 only appears in GLEAM. The flux measured by GLEAM should yield a 2-σ or higher detection in VLSSr based on the RMS noise calculated by `PyBDSF` for this field. The likeliest explanation for the non-detection in VLSSr is that data reduction at low declination (-29°, near the southern limit of VLSSr) was sub-standard. It is also possible that the GLEAM source is not real; perhaps a sidelobe or random noise bump.

HD 43197, a quiet metal-rich sun-like ($M_\star$=0.96$M_\odot$, G8V) star at 56 pc, hosts a sub-Jovian mass (M=0.6M_J) planet in an eccentric orbit (e=0.83) [211]. HD 43197 b's high eccentricity and close passage to its host star would make it a good candidate for high radio flux at periastron (see Chapter 5). The very steep spectrum of the sources available from surveys (Figure 3-16), however, is not consistent with planetary or stellar radio emission. Follow-up for this source is the subject of future work, although unfortunately it is too far south to be observed with LOFAR.

Additional Detections Near Known Exoplanets

There were 4 additional detections in VLSSr and 1 in TGSS (see Table 3.4.4 and Figures 3-19, 3-20, 3-21, 3-22, 3-23). Two of the four of the VLSSr detections have NVSS counterparts. It is possible, but perhaps unlikely, that planets have B-field strengths high enough to push the electron cyclotron frequency past 1.4 GHz, so finding an NVSS counterpart for a detected source is considered an indication that the source is probably not a planet. It should be noted, though, that some brown dwarfs have very high frequency radio emission [127]. If the emission is from the star, it may well appear in NVSS. The only way to know for certain whether the source is a planet/star or a background galaxy is to look at circular polarization, since stellar

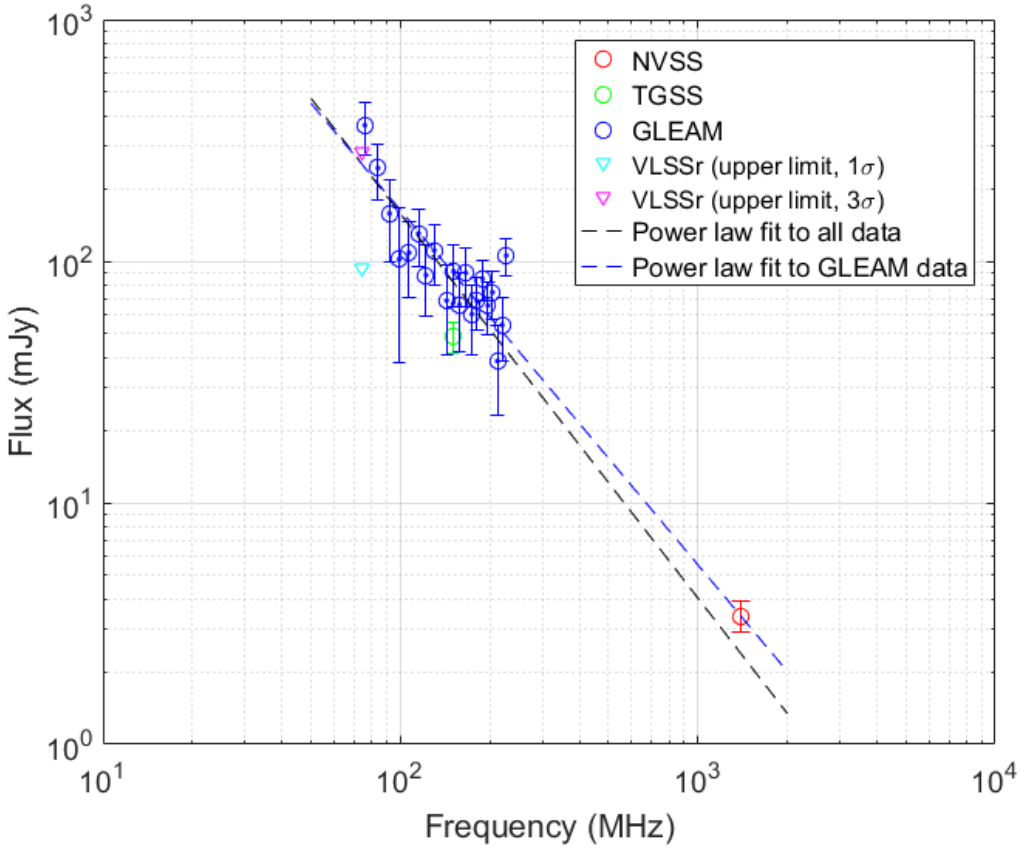

Figure 3-16: Spectrum for radio source(s) near HD 43197. A power-law fit to all available data yielded a spectral index of -1.59 (black dashed line), suggesting an extragalactic origin for this source. A fit to the GLEAM data only yielded a similar spectral index (-1.468, dashed blue line).

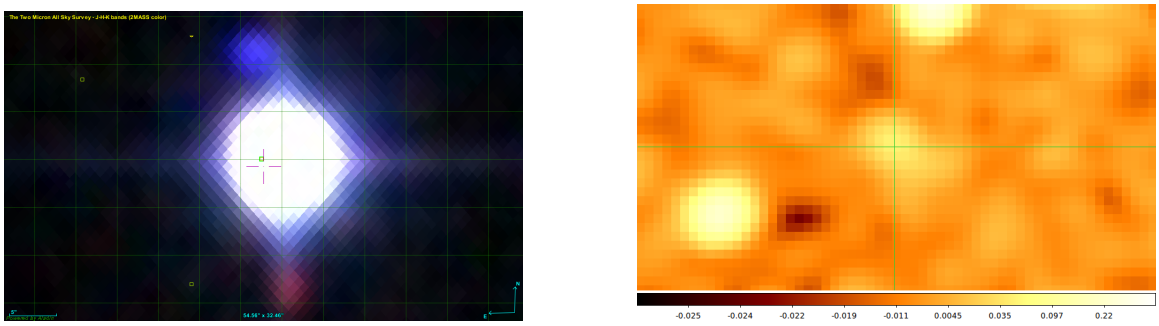

(a) 2MASS (b) GLEAM

Figure 3-17: 2MASS (left) and GLEAM (right) images of HD 43197. The green crosshair in (a) shows the position of the 2MASS star.

Table 3.2. Detections from the nearby exoplanet target list

Target	Survey	Separation from target (arcmin)	Flux density (mJy)	NVSS counterpart?
HD 220689	VLSSr	1.55	451.7 ±79.0	Yes
HD 24040	VLSSr	1.9	345.8 ±100.8	No
4 UMa	VLSSr	1	624.2 ±116.1	Yes
2M 0746+20	VLSSr	433.4	16.8 ±110.4	No
HD 86226	TGSS	0.19	22.35 ±5.8	No

and planetary emission is typically highly circularly polarized (see further discussion in Section 1.2.2).

The results from TGSS can be compared to Sirothia et al. (2014). Table 3.4.4 lists all of the radio associations found in Sirothia et al. (2014) and results from this work, both the TGSS DR5 partial release and the new TGSS ADR1, for the same objects. 61 Vir and HD 86226 are detected in both studies. Several objects are either too far away or have no listed distance and therefore were not included in the 100 pc exoplanet list. Two objects (WASP-77 and HD 164509) are close enough to be included, but were not detected. Possible reasons are listed in the table.

Non-Detection Upper Limits

As in Section 3.4.2, non-detection upper limits were calculated for all exoplanet host systems in the 100 pc sample. The results are shown in Figures 3-24 and 3-24. The sensitivity of the surveys again limits the derived luminosity limits to 2-5 orders of

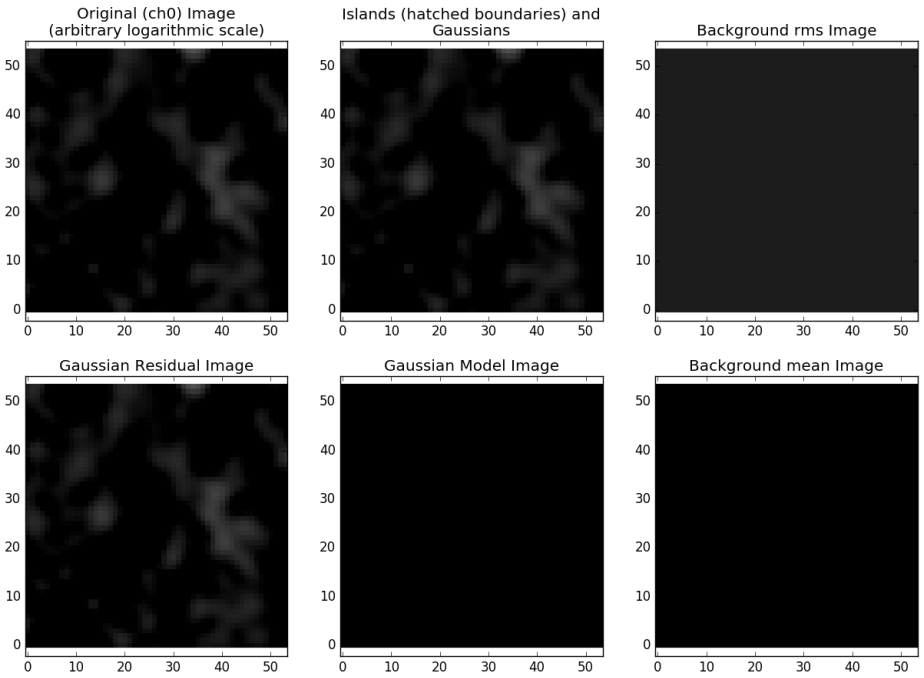

Figure 3-18: VLSSr field centered on HD 43197. The GLEAM source is not apparent and was not fit by `PyBDSF`. See Figure 3-5 for a description of each box.

magnitude above Jovian luminosity.

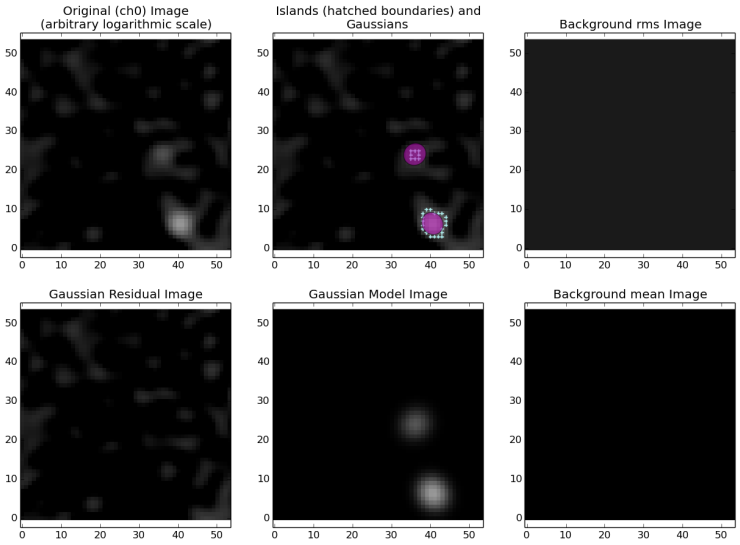

Figure 3-19: VLSSr detection near position of 2M 0746+20. The separation between the detected source is 2.58 arcminute from the position of the target and does not have a NVSS counterpart. See Figure 3-5 for a description of each box.

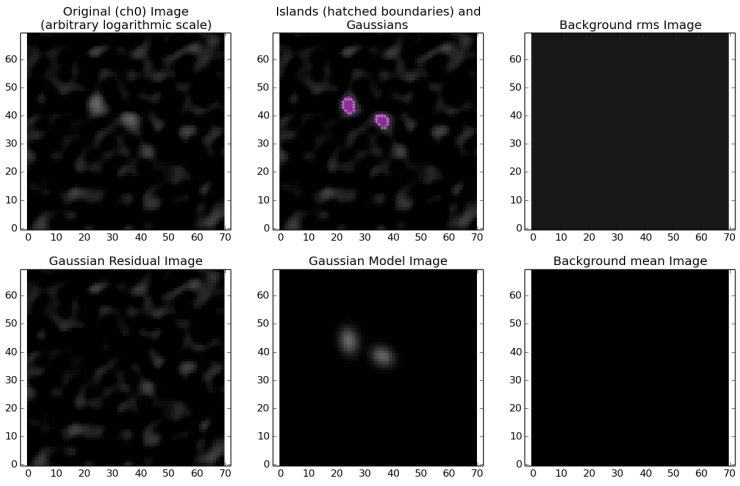

Figure 3-20: VLSSr detection of a source near the position of 4 UMa. The source is 1 arcminute from the position of the target and does have a NVSS counterpart. See Figure 3-5 for a description of each box.

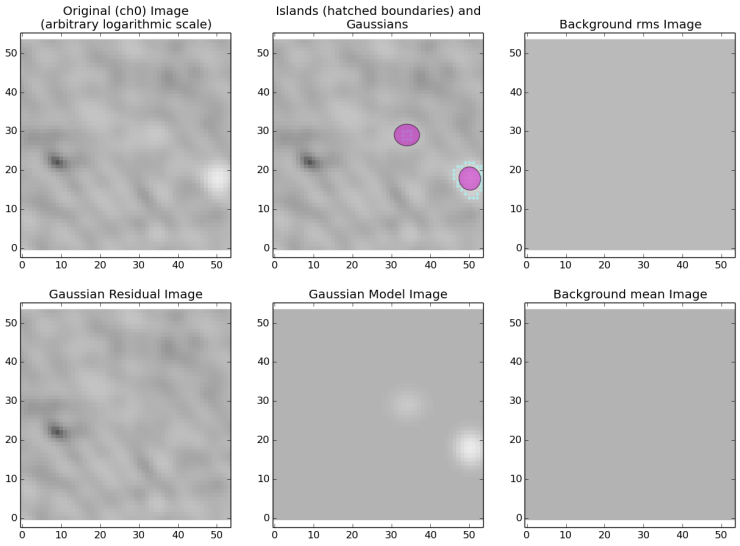

Figure 3-21: VLSSr source detected near the position of HD 24040. The detected source is 1.9 arcminutes from the target and it does not have a NVSS counterpart. Note that the image appears to be noisier than usual. In this case, the source may be a sidelobe. See Figure 3-5 for a description of each box.

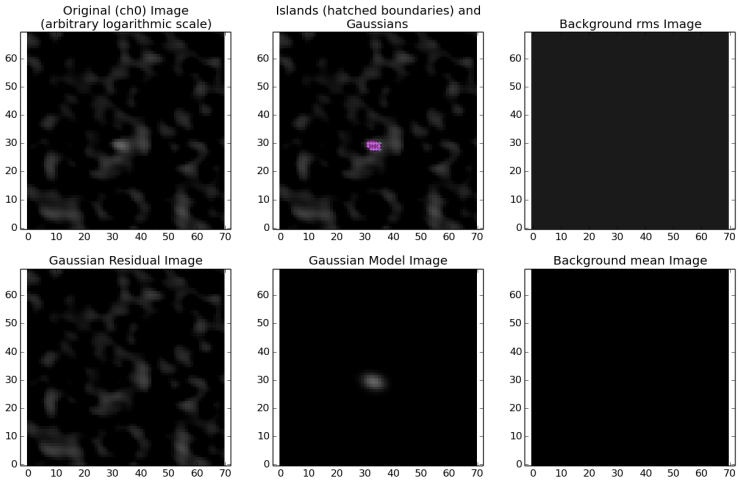

Figure 3-22: VLSSr source detected near the location of HD 220689. The detected source is 1.55 arcminutes from the target position. This source does have an NVSS counterpart. See Figure 3-5 for a description of each box.

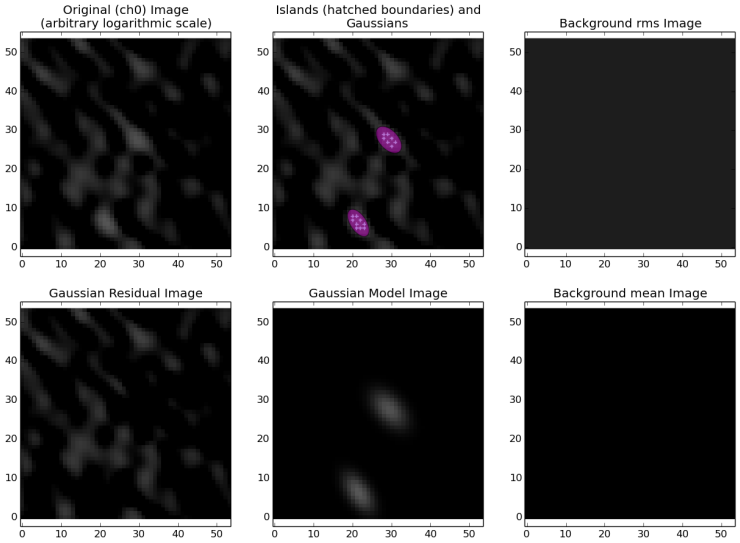

Figure 3-23: TGSS source detected near HD 86226. The detected source is 0.19 arcminutes (11 arcsec) away from the target. This source does not have a NVSS counterpart. This result should also be interpreted with caution because a second source was detected in the same image and their alignment suggests sidelobes. See Figure 3-5 for a description of each box.

Table 3.3. Comparison of results from Sirothia et al. (2004) and this work

Target	Detected in TGSS DR5	Detected in TGSS ADR1	Notes
PSR B1620-26	No	No	Distance (3800 pc) was outside 100 pc limit for planet list
61 Vir	Yes	Yes	See Section 3.4.3
HD 86226	Yes	Yes	Interesting target for follow-up
1RXS J160929.1-210524	No	No	Distance (145 pc) was outside of 100 pc list; YSO with distant brown dwarf companion
HD 164509	No	Yes	
HD 43197	No	Yes	See Section 3.4.4
WASP-77	No	No	At edge of TGSS image; may have caused error in `PyBDSF`

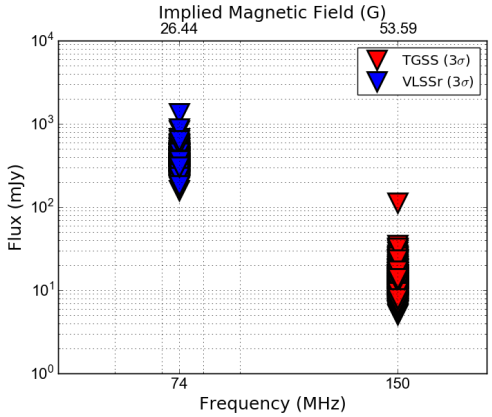

(a) Flux upper limits for nearby exoplanets

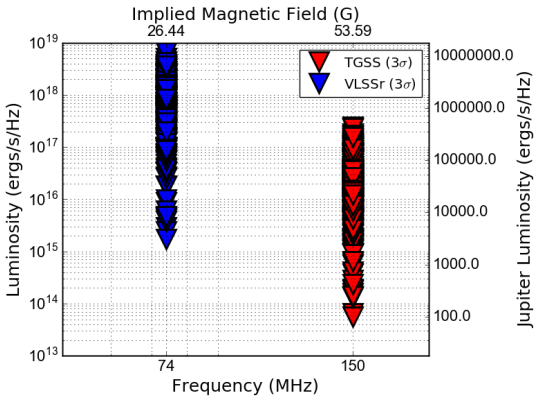

(b) Luminosity upper limits for nearby exoplanets

Figure 3-24: Upper limits on radio flux (left) and luminosity (right) for exoplanet hosts within 100 pc. Blue downward triangles represent 3σ limits at 74 MHz derived from VLSSr. Red downward triangles represent 3σ limits at 150 MHz derived from TGSS ADR1.

3.5 Follow-up

3.5.1 Additional Literature Review

All of the detections (besides 61 Vir) require further follow-up to determine the most likely source of the emission. Follow-up can be automated to some degree (searching specific catalogs, for example), but in general it requires a manual literature search on each object. SIMBAD [310] can produce a list of every paper that refers to a particular object, speeding up literature review considerably. The characteristics of the host star (variability, X-ray association, previous radio detections, spectral type, age, etc.) gleaned from literature and catalogs can be used to better understand whether the star is a likely source of radio emission. VizieR [220] can be used to search all radio catalogs at the same time in order to generate a spectrum for the source. Observatory archives (such as the VLA archive) should also be searched for any additional observations of the target field. Archival data could require re-reduction. The VLITE system [234] is another source of data for follow-up observations at low frequency.

While all of these sources will help build a more complete picture of each candi-

date source, there are fundamental degeneracies between background galaxies, stars, and planets that cannot be resolved without additional observations. In some cases, additional observations can be obtained by re-reducing existing archival data. For example, the VLSSr data could be re-imaged in circular polarization (Stokes V) instead of total intensity (I). Each VLSSr field was observed multiple times, so each observation could be imaged separately to look for time variability in targets of interest. Such reanalysis will take substantial time, but it does not require new observing proposals. An alternative method for checking whether a source is a background galaxy or a foreground star/planet is looking at the position of the source over time if archival observations exist. A background galaxy will have essentially zero proper motion, while nearby objects will move measurably over decades. The VLA archive is a rich source for such archival data; exploiting that resource is the subject of future work.

3.5.2 Other Catalog Searches

There are several other catalogs that should be searched for exoplanetary emission. Both the VLSSr and TGSS do not have any coverage of the far southern sky, but many known exoplanets are found in the southern sky because they were discovered by observatories in Chile (e. g. HARPS [27]). The MWA [179], located in Australia, is a prime instrument for seeking radio emission from exoplanets in the southern sky. MWA has recently completed a large-area survey called GLEAM [202, 138] which could be searched in the same way as VLSSr and TGSS ADR1. A clear next step is to obtain the FITS images from GLEAM and search them using the same lists of targets. The older WENSS [35] and WISH [74] surveys at 325 MHz are another good option if the FITS images can be obtained.

LOFAR is in the process of generating two surveys using the HBA (120–240 MHz) and one using the LBA (30–75 MHz). MSSS, the first HBA survey, [253, 132] has been observed and preliminary data released. The LOFAR Two-metre Sky Survey (LoTTS) [262] is a deeper survey in the HBA, with initial image noise <0.5 mJy beam^{-1} and $25''$ resolution. Observations are ongoing; the full survey will cover the

entire Northern sky. Observations for the LOFAR LBA Sky Survey (LoLss) are in progress[4]. Noise levels of 1–5 mJy are expected for LoLss, a significant improvement over VLSSr at even lower frequency. LoTss and LoLss will be a rich source for detection of radio emission from nearby stars and exoplanets when complete.

3.5.3 New Observations

Archival data has fundamental limits when applied to new questions that was not anticipated when the observations were conceived. For example, polarization is important for exoplanetary/stellar radio observations since CMI emission is strongly circularly polarized, but very few surveys provide polarization data (likely because it is difficult to calibrate, particularly at low frequencies). Several of the targets with detections in this work are good candidates for follow-up observations. In particular, GJ 382, 2MASS J0937347+293142, and HD 86226 are worthy of additional observations if further literature review is not helpful in identifying the source of radio emission for each object. LOFAR, GMRT, or the VLA are potential instruments for follow-up observations. Key goals for any additional observations should be to 1) image in circular polarization, 2) obtain measurements at as many frequencies as possible to construct a spectrum, and 3) observe over timescales appropriate to the fundamental periodicities of the system (stellar rotation/variability, planet orbital period). Previously unknown detections in VLSSr and/or TGSS will provide additional weight to observing proposals for these objects.

3.6 Future Work

3.6.1 Exoplanet Non-Detection Database

Constraining the detection space for exoplanets in systems that have been searched with more than one detection method may be of use for future searches. For example, it would have been useful in this work to know which nearby stars have well-

[4]Led by F. de Gasperin, no publication to date. See http://www.astron.nl/lowfrequencyobserving2017/Documents/Tuesday/LFO2017_deGasperin.pdf.

established upper limits on planet mass, semi-major axis, system inclination, etc. to better understand the likelihood of strong planetary radio emission in each system. Such a database would be useful for future exoplanet searches at any wavelength. It would also be useful for characterizing the type of stars that do not have planets.

There is no immediately obvious way to compile such a database. One approach would be to consider one object at a time and scan the literature for that object. Keywords could be used to identify papers that are related to exoplanets in order to narrow the list. It might be possible to automatically scan these papers to extract upper/lower limits on planetary parameters, but it might also be easier for a human to scan the papers and extract relevant information. Alternatively, a literature search for large exoplanet searches could be compiled, and then all of the SIMBAD objects listed in each paper could be checked against known exoplanets. This method would yield a list of non-detections, but not upper/lower limits.

Whatever method is used, the resulting list of non-detections and upper/lower limits could be used to construct an 'anti-OEC'. When upper/lower limits are available, visualizations could be produced to show where planets are not. Taken as a whole, such a database might provide interesting statistics on planet non-occurrence or perhaps highlight systems that are good targets for additional observations.

3.6.2 Background Galaxies

The 61 Vir results (Section 3.4.3) highlight the importance of background extragalactic sources. It is well understood that background sources can be distinguished from planets/stars by polarization, but perhaps the contamination rate of background sources in intensity alone could be estimated. Future observatories like the Square Kilometer Array (SKA) will be many times more sensitive than current arrays, so there will be a higher density of background sources. Estimating the contamination rate based on the known distribution and properties of extragalactic sources may be helpful for future radio exoplanet searches.

3.7 Future Prospects for Survey Searches

The radio surveys used in this analysis do not have the required sensitivity to detect exoplanets with Jupiter's radio flux, or even 10x Jupiter's radio flux. Examining existing data does, however, rule out superluminous exoplanets in existing datasets. See Section 8.2 for further discussion on the limitations of these upper limits.

This work serves as a proof of concept for 'big data' survey searches for exoplanets in the radio. Large-scale radio surveys are not designed with exoplanets in mind, but they can be exploited for exoplanet searches nonetheless. The Kepler survey was not explicitly designed to enable asteroseismology [207], stellar activity studies [15], or superflares [304, 261, 239], but Kepler data has been used in all of those fields and many more. Kepler demonstrated that a leap forward in capability (photometric precision in this case) advances many fields beyond the one for which the instrument was designed.

Upcoming advances in low frequency radio capability should similarly advance many areas of study, including the search for radio emission from exoplanets. The SKA Low-Frequency Aperture Array (LFAA), currently in the design phase, will provide a leap forward in sensitivity. LFAA will consist of 131,000 log-periodic crossed dipoles with baselines up to 100 km and will operate at frequencies between 50–350 MHz [63]. The first light date for SKA-LFAA is uncertain, but is at least 10 years away. LOFAR is considering a major upgrade (LOFAR 2.0) in a similar timeframe. If LOFAR takes steps to improve the sensitivity of the LBA, perhaps by building additional stations and/or making use of the full 96 antennas at each existing station, its sensitivity may improve beyond what is predicted by the increase in antenna number. This is because higher sensitivity would enable better ionospheric calibration. Ionospheric calibration currently enforces a noise floor due to uncorrected (and uncorrectable) phase errors induced by the rapid variation of the ionosphere in time and space [180].

Both SKA-LFAA and LOFAR 2.0 are likely to perform full sky surveys. These surveys will be more sensitive than any of the available surveys at the time of this

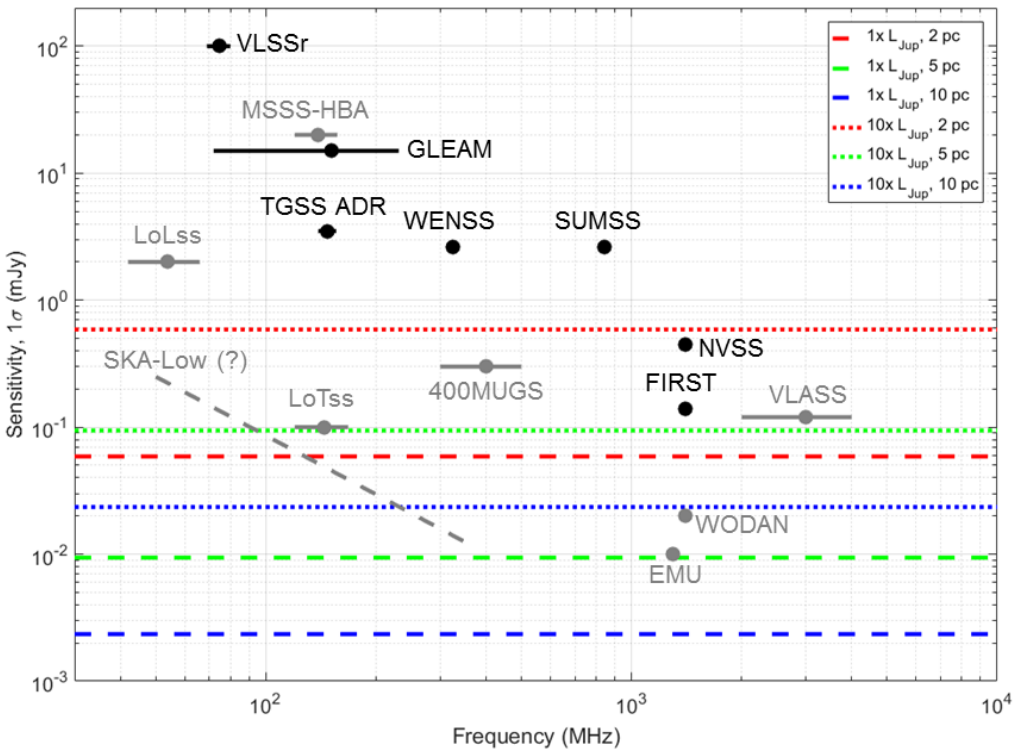

Figure 3-25: Comparison of existing and proposed future radio sky surveys. Existing surveys are marked by black points, surveys that are in progress or planned are gray. The horizontal line for each survey shows its frequency coverage. Jupiter's 20 MHz flux, scaled to 2, 5, and 10 pc is shown for comparison. It is important to note that higher frequency surveys reach lower flux limits, but a planet (or star) must have a very strong magnetic field to emit at high frequencies (see Eq. 1.1). Survey references: VLSSr [165], TGSS ADR1 [140], GLEAM [138], WENSS [35], SUMSS [191], NVSS [55], FIRST [19], VLASS [206], WODAN [248], EMU [217], LoTss [262], LoLss/400MUGS[5], SKA-Low[6].

writing. The techniques described above can be applied to those surveys as well, with an increased chance of success.

[6]No published description to date, see http://www.ncra.tifr.res.in/ncra/news-events/deGasperin_LoLSS400MUGS.pdf.

[6]Estimate only, see http://skatelescope.org/multimedia/image/ska-infographic-ska1-low/.

Chapter 4

VLA Nearest Stars Survey

Radio detection of exoplanets complements existing detection techniques (transit, radial velocity, direct imaging, etc.) since it is less dependent on orbital geometry than other methods and is optimal for a different population of stars. Active stars with frequent flares and/or coronal mass ejections (CMEs) are favorable for radio searches since the increased stellar wind energy impinging on a planetary magnetosphere increases output radio power [167, 334, 170] (see Section 1.2.3). Active and/or fast rotating stars are not favored for (and are often excluded from) transit and radial velocity surveys since activity-related jitter can cause false-positive planet detections [237, 26]. With these considerations in mind, we designed a survey of nearby stars across a wide range of radio frequencies in order to search the nearest stars for as-yet unknown planets.

The Nearest Stars radio survey focuses on the very closest stars because they offer the best opportunity to detect Jupiter-like radio emission from substellar companions. Scaling Jovian radio flux to 10 pc yields ~ 1 μJy, too faint a signal to be detected by current ground-based radio telescopes, but observations of stars within 5 pc can constrain exoplanet luminosity to within a factor of 10 of Jovian luminosity (see Figure 4-1). The Nearest Stars survey therefore selects only stars within 5 pc so that non-detection upper limits for these systems will provide physically meaningful constraints on non-thermal emission processes.

A second key design feature of the Nearest Stars survey is that it blindly chooses

nearby stars that meet observability criteria rather than attempting to select stars that are 'more likely' to host planets or exhibit strong radio emission. The goal of this unbiased selection method is to produce an unbiased result given the difficulty of predicting planetary magnetic field strengths and radio fluxes (Section 1.3.3).

4.1 Survey Motivation

Detection of exoplanets through low frequency magnetospheric radio emission [92] is a promising, though yet unproven, technique. Planets with strong magnetic fields (Earth, Jupiter, Saturn, Uranus, Neptune) show strong coherent radio emission through the cyclotron maser instability [331]. The emission frequency f_{ce} corresponds to the local electron cyclotron frequency ω_{ce} which depends directly on the local magnetic field strength:

$$f_{ce} = \frac{\omega_{ce}}{2\pi} = \frac{eB}{2\pi m_e} \; [Hz] \tag{4.1}$$

where B is the local magnetic field strength and e and m_e are the charge and mass of an electron, respectively (SI units).

Equation 4.1 points to the key observable for radio exoplanet searches: the high frequency spectral cutoff (see Figure 1-3 for Jupiter's dramatic high frequency cutoff). The high frequency cutoff corresponds to the lowest altitude where cyclotron emission can be generated and escape without being absorbed, low in the ionosphere. The magnetic field B that corresponds to the high frequency cutoff (via Eq. 4.1) can be used to estimate the 'surface' magnetic field of a planet ($R_{emission} \sim R_{planet}$). If the planet's radius is known, the 'surface' field strength can be converted into a magnetic moment. Assuming that the magnetic field is primarily dipolar, the magnetic field B inferred from the radio high frequency spectral cutoff can be roughly assumed to be coming from near the magnetic pole of the planet, as is the case with auroral radio emission in the solar system. The magnetic field strength of an undistorted dipole at the magnetic equator B_{eq} is therefore $\frac{1}{2}B$. The relationship between surface

Table 4.1. Telescope Bands

Telescope	Band Name	Frequency
LOFAR	LBA	30–75 MHz
VLA	P-band	230–470 MHz
VLA	L-band	1–2 GHz
VLA	S-band	2-4 GHz
VLA	LS-band	1.5–3.5 GHz
VLA	C-band	4–8 GHz

Note. — Telescope Bands used in the Nearest Stars survey. LOFAR LBA and VLA P-band data are not discussed in this Chapter; reduction of those data is the subject of future work.

equatorial magnetic field strength and magnetic moment is

$$\mathcal{M}_{planet} = \frac{\mu_0}{4\pi} \frac{1}{B_{eq} R_{planet}} \ [Am^2] \tag{4.2}$$

where μ_0 is the permeability of free space and $\mathcal{M}_{planet}$ is the planetary dipole moment. Magnetic moment is a more useful parameter for comparing planets of different sizes. The difference between the surface magnetic fields (B_{eq}) of the Earth and Jupiter is misleadingly small ($\sim$13), but Jupiter's magnetic moment is 20,000 times greater than the Earth's (see Table 1.1). If no sharp cutoff is detected within the observing bandwidth (but there is a significant detection), then only lower limits on magnetic field strength and magnetic moment can be calculated.

Observations for the Nearest Stars survey are carried out using the VLA (P-band, L-band, S-band, C-band) and LOFAR (LBA). See Table 4.1 for frequency ranges, Chapter 2 for data reduction details. Together, these facilities provide coverage from 30 MHz to 4 GHz. A wide range of frequencies are observed to maximize the chance of catching substellar companion radio emission. This Chapter describes only VLA L-band, S-band, and LS-band observations. No C-band observations were granted and the P-band and LOFAR LBA data are the subject of future work. Though solar system planets emit primarily below 40 MHz, brown dwarfs and low-mass stars have shown very high frequency cyclotron emission [127]. The only constraints used when choosing targets for the Nearest Stars survey, besides distance, were observational.

The ten closest targets out of the available 16 were selected for the Nearest Stars survey. The survey targets are listed in Table 4.2.

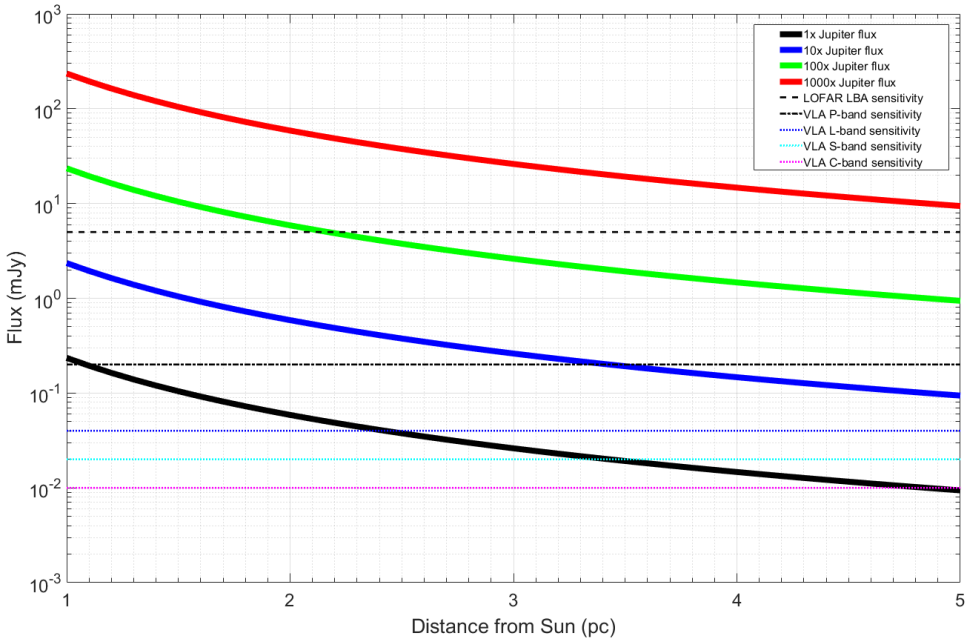

Figure 4-1: Jovian radio flux scaled from 1–5 pc. The solid black curve shows Jupiter's radio flux at $\sim$ 20 MHz ($\sim 10^8$ Jy) scaled over the range of distances covered by the Nearest Stars survey. Additional curves show Jupiter's flux scaled by 10x, 100x, and 1000x. The horizontal dashed, dash-dotted, and dotted lines show the predicted noise limits for all bands included in the survey.

Similar surveys have been carried out in the past, but have been unsuccessful [319, 17, 265, 168] (see Section 1.3.2). These searches may have been unsuccessful due to limited sensitivity, targets that were too distant, or simply unfortunate timing. Radio emission from the Sun and Solar System planets is known to be highly time-variable, so it is possible that past surveys simply missed stellar and/or planetary radio bursts. This survey is not immune to these challenges, but it has been designed to maximize the chance of catching bursty, unpredictable stellar or substellar radio emission, though it is constrained by the limited time granted by the time allocation committees (TACs). See Section 8.3.1 for further discussion of observation strategy.

4.2 Target Selection

The target list is composed of the top 10 nearest stars or star systems that are observable from both the VLA and LOFAR. See Table 4.2. The targets were chosen from the 8 pc volume-limited sample compiled by [154]. This sample was the most up-to-date at the time of observing proposal submission and includes recently discovered brown dwarfs and other nearby low mass objects. Only stars within 5 pc were considered from the 8 pc list. Targets at low declination that would appear below 30° elevation at LOFAR, the northernmost of the two observatories, were eliminated from the target list. Practically, this eliminated all targets with DEC < -5°. In addition to the elevation constraint, targets that were less than 20° away from 'A-team[1]' sources, the brightest radio sources in the sky such as CasA, CygA, TauA, etc., were discarded. Bright sources in the synthesized beam sidelobes contribute too much noise to achieve a noise floor in the final image that is close to the theoretical thermal noise. Object properties (spectral type, multiplicity, age, etc.) were not used in target list selection.

Sixteen systems met all three selection criteria (distance <5 pc, elevation at LOFAR >30°, distance to A-team sources >20°). Of these 16 systems, the nearest 10 were chosen for the initial VLA proposal in order to keep the observing time request reasonable. The target list contains nine M dwarfs, one T9 brown dwarf, two white dwarfs, and one F sub-giant in 7 single and 3 binary systems. The abundance of M dwarfs is both expected and beneficial to this survey. M dwarfs are generally more magnetically active than earlier type stars, likely due to their fully convective interiors [218]. For radio exoplanet detection, high magnetic activity is beneficial. As demonstrated by [71], CME passages are correlated with increased auroral radio emission. A similar effect has been predicted, though not yet observed, for exoplanets [120]. Additionally, the Kepler survey [29] has shown that M dwarfs host more planets on average, although they are often small [205]. At the time the VLA and LOFAR observation proposals were written, none of the targets had known exoplanets. Recently,

[1]The 'A-team' refers to the 'A' in the names of all of the brightest radio sources. Since these sources cause problems for most observations by leaking into the sidelobes of the synthesized beam (and primary beam), the name is an astronomer's joke.

Table 4.2. Target list for the Nearest Stars survey.

Discovery Name	Gliese Name	Distance (pc)	Spectral Type	RA (J2000)	Dec (J2000)
Wolf 359	Gl 406	2.39	M6 V	10:56:28.865	+07:00:52.77
Lalande 21185	Gl 411	2.55	M2 V	11:03:20.19400	+35:58:11.5682
Procyon A	Gl 280 A	3.51	F5 IV-V	07:39:18.118	+05:13:29.97
Procyon B	Gl 280 B	3.51	DA	07:39:17.88	+05:13:26.8
Sigma 2398 A	Gl 725 A	3.57	M3 V	18:42:46.67934	+59:37:49.4724
Sigma 2398 B	Gl 725 B	3.57	M3.5 V	18:42:46.96652	+59:37:36.3471
G 51-15	GJ 1111	3.63	M6.5 V	08:29:49.345	+26:46:33.74
Luyten's Star	Gl 273	3.80	M3.5 V	07:27:24.49975	+05:13:32.8332
Teegarden's Star	...	3.86	M6 V	02:53:00.849	+16:52:53.28
UGPS J072227.51-054031.2	...	4.07	T9	07:22:27.87	-05:40:31.1
Ross 614 A	Gl 234 A	4.13	M4-4.5 V	06:29:23.401	-02:48:50.32
Ross 614 B	Gl 234 B	4.13	M4.5-6.5 V	06:29:23.52	-02:48:51.1
van Maanen's Star	Gl 35	4.30	DZ8	00:49:09.90175	+05:23:19.0117

a mini-Neptune was discovered in a 10-day orbit around Gl 411 [44] and two planets were discovered in orbit around Luyten's Star [8].

Gl 411 and Luyten's Star both have recently discovered planets that had not yet been reported at the time the target list was compiled. Other objects on the target list have been searched for planets using various detection methods, but there have been no other confirmed detections. Both the transit method and the radial velocity method are insensitive the orbital inclinations far from 90° away from the line of sight to Earth. Since stellar spin vectors (and by extension planetary orbit vectors) are assumed to be randomly distributed, some targets in our sample are likely to have undetected planets due to the orientation of the system. Though population statistics from Kepler [98] can make no guarantees for planet occurrence for specific stars, the high frequency of planets around main sequence stars in the Kepler sample makes the search for new planets in a small sample plausible.

A brief description of each star on the Nearest Stars Survey list follows.

Wolf 359 Wolf 359[2] (GJ 406, CN Leo) is the nearest of the available targets at 2.39 pc [144]. It is an active M6.0 C dwarf with no known companions [109]. AAVSO lists Wolf 359 as a UV Ceti type variable flare star due to frequent flares [306]. Giant flares have been observed [99]. Radio sources near the position of Wolf 359 have also

[2]No indication of Borg activity in the data collected to date.

been observed at L-band and C-band [221], though the authors concluded that they were background extragalactic sources. Wolf 359 has a mean magnetic field of B $\simeq$ 2.2 kG measured via FeH absorption lines, though high magnetic flux variability was observed [244]. If the 2.2 kG measurement is accurate, cyclotron emission should be detectable at VLA frequencies, particularly S-band or C-band[3]. A combined RV and astrometric survey ruled out planets larger than 0.5 M_{Jup} with periods less than 3 days, 1.0 M_{Jup} for P $<$ 30 days, and 2.0 M_{Jup} for P $<$ 100 days using RV [61]. Large planets (3-7 M_{Jup}) were ruled out for periods greater than 2 years.

Procyon Procyon is a binary system composed of F5 subgiant (Procyon A) and a white dwarf (Procyon B). The two components orbit one another with a semi-major axis of 15 AU [48] and an orbit plane that is inclined by 31 o the line of sight. Planetary orbits around Procyon A but not B are stable as well as wider circumbinary orbits [88]. It has been suggested that the Procyon system may have failed to generate planets due to the orbits and evolution of the primaries [88]. There is some evidence that planetesimals may have accreted onto Procyon B [85].

Quiescent radio emission as well as a flare have been detected from Procyon A in X-band [79]. Procyon was observed in C-band in 1981 [32] and 1987 [28], but no emission was detected. Limits from these two VLA observations are $\sim$0.5 mJy and 0.09 mJy, respectively.

Gl 411 (Lalande 21185) Gl 411 (HD 95735, Lalande 21185) is an M2 dwarf that is classified as a variable flare star of the BY Draconis type [306]. The *Extreme Ultraviolet Explorer* Deep Survey showed EUV flare activity for this star [9]. Prior to the publication of [44], there was an unconfirmed astrometric detection of a Jovian-mass planet orbiting Gl 411 [106], but that planet has been ruled out by subsequent radial velocity measurements. Gl 411 was observed by Bastian et al. (2000) [17] with the VLA as part of a campaign to search nearby exoplanet systems for radio emission. No detections were made for Gl 411 or any other systems observed; limits were set

[3]To date, Wolf 359 has only been observed in VLA P-band and LOFAR LBA; neither have been fully reduced yet.

at 23 and 20 μJy at 1.4 GHz for Stokes I and V, respectively, and 4 and 1.23 mJy at 333 MHz for I and V, respectively.

GJ 725 (Σ2398) GJ 725 (also known as Σ2398) is a visual binary system composed of two M dwarf components. GJ 725 A is an M3 dwarf and GJ 725 B is an M3.5 dwarf. The semi-major axis of the binary is 56 AU (e=0.7, i=52.5) [293]. Both components have been searched unsuccessfully for planetary RV signatures [84, 11]. Endl et. al. (2006) [84] measured linear trends in each component of the binary, but since the linear trends are opposite sign, they are assumed to be due to the motion of the binary. No planets were detected (95% completeness for m sin $i > 3.5$ M_{Jup}, $a \leq 0.7$ AU. Bailey et al. (2012) [11] included GJ 725 A and B in their Keck RV survey as 'field stars', stars with no known planets, slow rotation, and relatively low activity. The RV dispersion of these field stars was used to demonstrate the survey observing precision of 50 m s^{-1}.

GJ 725 A and B are metal-poor ([Fe/H] = -0.49, -0.36 respectively) [33]. Metal-poor stars are less likely to have close-in giant planets [94], so the lack of giant planet detection for GJ 725 A/B is unsurprising. The relationship between metallicity and the formation of smaller (sub-Neptune) planets is less clear [38], however. Luisa et. al. (2014) [142] determined that there are stable orbits around both members of the binary. The radiative habitable zones for A and B are 0.18 - 0.31 AU and 0.14 - 0.24 AU respectively. The system is not considered to be a good candidate for transit searches since it was assigned a low transit probability score in [134]. If the spin axes of the binary members are roughly perpendicular to the plane of the binary, transits would indeed be unlikely (assuming that the planet orbits are also roughly perpendicular to the stellar spin axes).

GJ 725 was observed with the VLA in twice in 1986 at 4835 MHz, yielding limits of <180 μJy [318] and <200 μJy [97]. It was observed again as part of the Radio Interferometric Planet Search [31], but was undetected (<141 μJy).

GJ 1111 GJ 1111 (DX Cnc, LHS 292, G 51-15) is a late M dwarf (M6.5 [4], $M_\star$=0.10, T_{eff}=2700K) and is classified as a flare star [255]. GJ 1111 was on the target list for VLA observation as part of an astrometric search for exoplanets, but was not observed [31]. Morin et al. [203] used the Zeeman doppler imaging (ZDI) technique to measure GJ 1111's magnetic field. They found it to be strongly time variable and non-axisymmetric with an average field strength ranging from 80–110 Gauss and maximum field strength from 180–220 Gauss. They also measure a rotation period of 0.46 days and a high inclination, which they fix at 60°. Vidotto et al. [298] used the magnetic field measurements from Morin et al. to estimate the effect of the star's strong magnetic field on the magnetosphere of an Earth-like planet. An Earth-sized planet with an Earth-sized magnetic moment would have a much smaller magnetosphere due to stellar wind compression than the Earth does if it was located in the habitable zone.

GJ 1111 is a member of the Castor Moving Group [199], giving this star a relatively young age ($\sim$ 200 My) that agrees well with its fast rotation. There are no radio detections of GJ 1111 in the literature, though it is listed with a probable X-ray association [96]. GJ 1111 was observed with the VLA at 6 GHz by Williams et al. [317], but was not detected (upper limit 23 μJy). Flares have been reported in optical photometric observations [232] (U-band, 5-30% flux enhancement) and spectroscopic data [196]. GJ 1111 is often used as a spectroscopic standard. Guenther & Wuchter (2003) [122] suggest that GJ 1111 is a spectroscopic binary, but no companion has been detected or confirmed to date [317].

Luyten's Star Luyten's Star (GJ 273, HIP 36208, LHS 33, BD+05 1668) is an M3.5V dwarf ($0.29 M_\odot$[66], $0.293\pm0.027 R_\odot$, $T_{eff} = 3382\pm49$ K [33]). Luyten's Star is part of the HARPS M-dwarf sample [27]. Recently, two planets were announced by Astudillo-Defru et al. [8], a super-Earth ($2.89\pm0.26\ M_\oplus$) with a period of 18.650 ± 0.006 (GJ 273b) and an Earth-sized planet ($1.18\pm0.16\ M_\oplus$) with a period of 4.7234 ± 0.0004 days (GJ 273b). GJ 273b receives 1.06 times the Earth's insolation, placing it in the habitable zone.

The HARPS data are consistent with the estimated the rotation period of the star of ∼100 days [7, 281]. The HARPS H-α data show periodicity at ∼2000 days, perhaps indicating a magnetic cycle. This cycle period is in rough agreement with Suárez Mascareño et al. [280], who found a period of 6.6±1.3 years via photometry.

Luyten's Star was part of the Bower et al. [31] radio astrometric exoplanet search, but the star was not detected by the VLA at 5 GHz (<156 μJy) and therefore was not part of the VLBI astrometric campaign. No other radio detections or recorded flares are found in the literature, indicating that this star is inactive and likely old. Like GJ 1111, Luyten's Star is often used as a spectral standard.

Teegarden's Star Teegarden's Star (GAT 1370, SO J025300.5+165258) is a late M dwarf (M7.0V [4]). Its name comes from the lead author of the 2003 paper in which this object was 'discovered' to be nearby (3.6±0.4 pc) with very high proper motion (5".05±0".03 yr^{-1}) [283]. It is suspected of being young and was tentatively associated with the Argus Association (30-50 My, 15-48 pc) [101], though parallax measurements rule out this association [102]. Teegarden's Star has a measured rotational velocity (v sin i) of 10±4 km/s [13]. If this star is indeed young, the relatively low radial velocity could indicate its inclination is nearly 0° (pole-on). There are no documented radio detections of Teegarden's Star. There is a radio source in NVSS located 1.5 arcmin from Teegarden's Star [55], but this is likely a different object given the large separation.

Teegarden's Star was observed as part of the Red Optical Planet Search [14]. Teegarden's Star exhibited RV variations that could be consistent with a ∼0.2$M_J$planet in a 2.06 day orbit (a = 0.014 au), but the authors emphasize that there was not enough data to claim a planet detection. Additional observations rule out "planets more massive than m_p sin i = 0.5 $M_J$at 0.03 au" [13]. The authors note that the chromospheric activity of Teegarden's Star inhibits higher precision RV measurements. Teegarden's Star is a target of the MEarth survey [141] and has 1112 data points as of 2015 [77].

UGPS J072227.51-054031.2 UGPS J072227.51-054031.2 (UGPS 072205 for short) is a T9 C brown dwarf. It was discovered in 2010 [182] as part of the United Kingdom Infrared Telescope Deep Sky Survey (UKIDSS) Galactic Plane Survey (UGPS) [181]. At the time it was discovered, UGPS 072205 was the closest known isolated brown dwarf[4]. It is the coolest of the known T9 dwarfs (T_{eff} = 480–560 K). In the discovery paper, UGPS 072205's age is estimated to be between 0.2–2 Gyr and mass 5–15M_J. These values were refined with additional spectroscopy in [175] to T_{eff} = 505±10 K, M = 3–11M_J, and age 60 Myr to 1 Gyr. The revised mass brings UGPS 072205 into the planetary regime. It's measured rotational velocity (v sin i) is 40±10 km/s [25]. No companion was detected with adaptive optics imaging in H and K bands [30]. As with Teegarden's Star, there is a source in NVSS 1.9 arcsec from the position of UGPS 072205, but again it is likely a background source.

Ross 614 See Section 4.4.2

van Maanen's Star Van Maanen's Star (van Maanan 2, HIP 3829, Gl 35, Wolf 28, LHS 7, WD 0046+05) is a helium-rich white dwarf with a metal-contaminated atmosphere (DZ7.5 [311], M=0.69$M_\odot$, T=6200K [89]). It is the closest white dwarf to the Sun that is not part of a binary (Sirius B, Procyon B). The progenitor of van Maanan's Star was a M=2.6$M_\odot$and lived for 900 Myr. The total age of the white dwarf remnant is estimated at 4.1 Gyr [42].

An unseen companion has been suggested for van Maanan's Star based on *Hipparcos* astrometry with a period of 1.57±0.14 years and mass of 0.06±0.02$M_\odot$[188]. Farihi & Becklin (2004) searched for the companion with Keck AO and IRTF. Those observation ruled out the massive companion predicted in [86]. *Spitzer* observations further constrain the mass and temperature of possible companions [87] and found no evidence of a dust/debris disk [89].

Large Jovian-mass companions are ruled out for van Maanan's Star, but sub-Jovian planets may still exist now, or may have existed in the past. The metal-

[4]There are several sub-stellar objects closer to the Sun than UGPS 072205 discovered since Kirkpatrick et al. (2012) [154]. See [189, 184]

rich atmosphere of this DZ white dwarf may be the remains of planets that were accreted onto the star [85]. This process has been observed in action through transit photometry of another metal-rich white dwarf [297]. If there are present-day sub-Jovian planets orbiting van Maanan's star, and if van Maanan's star has a magnetic field, radio emission could be generated from interactions between the white dwarf's magnetic field and an orbiting planet [315]. There is no radio detection of this object in the literature to date, however.

4.3 Data

The data that comprises the Nearest Stars survey (to date) was obtained through two LOFAR proposals in Cycle 4 and Cycle 5, a VLA proposal (described below), and commensal observations with the VLITE P-band system [234]. Twenty-two LOFAR LBA hours were granted in Cycle 4[5]. The time was split between two targets (Gl 411, Gl 725). Each target was observed once for three hours and four times for two hours over a period of three months. Ten hours were granted in Cycle 5[6]. All Cycle 5 time was devoted to Wolf 359. The available time was divided into five 2-hour observations spread over four months. VLITE P-band data is available for all VLA observations upon request. The VLA proposal and observations are described below. This work describes the VLA L-band and S-band data only; data reduction for LOFAR data and VLA P-band data (both proposed and VLITE) is ongoing.

4.4 VLA Observations

Five of the ten nearby targets were observed with the VLA as part of observing proposal VLA-16A-379. The observations were carried out during 'filler time' or C-priority. Proposals granted this type of observation are fit in around other obser-

[5]Proposal LC4_018, D. Winterhalter (PI), J. Lazio, W. Majid, M. Knapp, P. Zarka, J-M. Griessmeier, T. Bastian, A. Beasley.

[6]Proposal LC5_009, D. Winterhalter (PI), J. Lazio, W. Majid, M. Knapp, P. Zarka, J-M. Griessmeier, T. Bastian, A. Beasley.

Table 4.3. Observations of Nearest Stars Survey targets to date.

Name	Gl/GJ number	Distance (pc)	Spectral type	Obs. L-band	Obs. LS-band	Obs. P-band	Obs. with LOFAR
Wolf 359	Gl 406	2.386	M6 V	–	–	5	Yes
Lalande 21185	Gl 411	2.547	M2 V	–	–	–	Yes
Procyon A	Gl 280 A	3.514	F5 IV-V	6	5	–	No
Procyon B	Gl 280 B	...	DA				No
Sigma 2398 A	Gl 725 A	3.569	M3 V	5	0	5	Yes
Sigma 2398 B	Gl 725 B	...	M3.5 V				Yes
G 51-15	GJ 1111	3.626	M6.5 V	5	0	–	No
Luyten's Star	Gl 273	3.803	M3.5 V	–	–	–	No
Teegarden's Star	...	3.857	M6 V	–	–	5	No
UGPS J072227.51-054031.2	...	4.065	T9	5	0	–	No
Ross 614 A	Gl 234 A	4.127	M4-4.5 V	5	5	–	No
Ross 614 B	Gl 234 B	...	M4.5-6.5 V				No
van Maanen's Star	Gl 35	4.301	DZ8	–	–	5	No

vations by the automated scheduler. Details of the VLA observations can be found in Table 4.4.

4.4.1 Methods: Data Reduction

The data were flux and phase calibrated using the standard VLA pipeline [295] in CASA [194]. The calibrated data were imaged using CLEAN [136] in Stokes I and V. Beam squint [59] was not an issue for these observations since the target source was at or very near the beam center. Additional self-calibration was unnecessary since the image noise floors were close to the predictions from the VLA exposure calculator, indicating that pipeline calibration was sufficient.

After the standard calibration pipeline, each five minute observation was first imaged using the full bandwidth and integration time for maximum sensitivity, then imaged in each spectral window separately in order to generate a coarse spectrum. Individual observations were also imaged in sub-integrations of 30 and 60 seconds to search for rapid time variability. After imaging, the central region of each image (100 pixels square) was searched for sources using CASA's `imfit` routine. The same region was also fit using `PyBDSM` [198], a source-fitting package developed for LOFAR. Fluxes and positions from `PyBDSM` were generally more accurate and less prone to sidelobe fitting than `imfit()`, so `PyBDSM` results were preferred.

The source position for detected flux was compared with the expected position of Ross 614 at the time of observation. Since Ross 614 is a high proper motion object, its current position is more than one synthesized beamwidth away from its J2000 position. The detected source is therefore shifted slightly from the center of the image since the J2000 position was used as the phase center for each observation.

4.4.2 Ross 614 Stellar Flare Detection

Ross 614 AB (Gl 234, V577 Mon, HIP 30920) is an M-dwarf binary system 4.1 parsecs from the Sun. Both binary components are mid- to late-M dwarfs, though there is some disagreement about the masses, particularly for Ross 614 B. SIMBAD [310] lists spectral types of M4V and M5.5V E for A and B respectively, while [264] lists M4.5V and M7V. The binary has a period of 16.6 years, is moderately eccentric (0.381), and inclined by 53.93° to the line of sight [107]. Mascareño et al. (2016) found a photometric rotation period for Ross 614 A of 8.1 ± 0.1 days and a longer variability cycle of 5.9 ± 0.5 years that may be a magnetic cycle [280]. Since the binary is unresolved in the photometry, these periodicities are assigned to Ross 614 A because it is the brighter component. The measured *vsini* from HARPS is 4.73 km/s [137]. This value does not agree with the values attained by Shulyak et al. [264] who found *vsini* of 6.15 m/s and 12.95 m/s for A and B, respectively.

Ross 614 AB is listed as a flare star of the UV Ceti type [306] and is associated with a ROSAT X-ray source [125]. Optical flares at a rate of ∼1 per hour were reported by Zalinian et al. (2002) [330]. There are previous radio detections of Ross 614 AB at L-band (420 μJy) and C-band (550 μJy) [313]. The system was not detected at C-band (<180 μJy) [318] two weeks prior to the observations in [313]. The binary was not detected by McLean et al. (2012) at X-band (< 81 μJy) [193]. There is an NVSS (1.4 GHz) 2.6 mJy source 0.1 arcmin from the position of Ross 614 AB [55]. High activity is unsurprising given the age of the system, though its activity is apparently intermittent since it is not detected in all observations. The magnetic field strength of the two components is also uncertain, but 2.5–2.75 kG has been estimated for A by [264] via infrared spectroscopy.

Ross 614 AB has been associated with either the Pleiades Moving Group (20-150 My) [199] or the Tucana-Horologium (30 My) [212]. In either case, the system is young, less than 150 My. The WISE survey detected no infrared excess in the system [10]. There are no known planets in the Ross 614 AB system, but [81] and [142] determined that there are stable orbits around each of the components and that the range of stable orbits spans the habitable zone of each star. Ross 614 AB was part of the Gemini Deep Planet Survey [163], but no large, long period companions were detected.

Ross 614 VLA Observations

Ross 614 AB, an M-dwarf binary, was observed 10 times during VLA's 2016A semester as part of proposal 16A-379. The timing of the observations was at the discretion of the observatory since the proposal was given 'C' priority. Each target field observation lasted approximately six minutes and was preceded by flux and phase calibrator scans of J0521+1638 and J0607-0834 respectively. The observation dates and band setups are shown in Table 4.4. Six observations were clustered in late February/early March 2016 and the remaining four observations occurred in April 2016.

Results

Strong radio emission was detected in each of the first six VLA observations of Ross 614 AB as well as the eighth. Example images are shown in Figure 4-2. No emission was detected in the other three observations. Figure 4-3 shows the detected flux in Stokes I (red) and V (blue) from full integration time and bandwidth images generated from each observation. The image RMS noise floor is indicated for each observation in the bottom panel. All six detections were moderately left-hand circularly polarized ($\sim$50%) as indicated in the middle panel of Figure 4-3.

The measured fluxes for the first six observations with detections vary from 1-7 mJy (Stokes I), while the last is $\sim$ 350 μJy. The image noise floors are below 30 μJy for LS-band and 45-90 μJy for L-band, yielding a signal-to-noise ratio greater than 10 on the first six detections. The last detection (4/27/16) is weaker, but still

Table 4.4. VLA observation log for Ross 614, VLA semester 2016A

Target	Start Time	Stop Time	Duration	Band(s)	VLA Config.	Calibrators (flux, phase)	Detection?
Ross 614	2/16/2016 1:24:09	2/16/2016 1:44:33	00:20:24	L, S	C	J0521+1638, J0607-0834	Yes
Ross 614	2/27/2016 00:05:25	2/27/2016 00:25:49	00:20:24	L, S	C	J0521+1638, J0607-0834	Yes
Ross 614	2/27/2016 02:55:04	2/27/2016 03:15:26	00:20:22	L, S	C	J0521+1638, J0607-0834	Yes
Ross 614	2/27/2016 23:50:56	2/28/2016 00:11:19	00:20:23	L, S	C	J0521+1638, J0607-0834	Yes
Ross 614	2/28/2016 23:56:50	2/29/2016 00:17:15	00:26:25	L, S	C	J0521+1638, J0607-0834	Yes
Ross 614	3/03/2016 23:31:55	3/03/2016 23:53:17	00:21:22	L	C	J0521+1638, J0607-0834	Yes
Ross 614	4/09/2016 23:09:59	4/09/2016 23:31:26	00:21:27	L	C	J0521+1638, J0607-0834	No
Ross 614	4/27/2016 01:18:36	4/27/2016 01:40:03	00:21:27	L	C → CnB	J0521+1638, J0607-0834	Yes
Ross 614	4/30/2016 20:18:39	4/30/2016 20:40:06	00:21:27	L	CnB	J0521+1638, J0607-0834	No
Ross 614	4/30/2016 20:40:08	4/30/2016 21:01:04	00:20:56	L	CnB	J0521+1638, J0607-0834	No

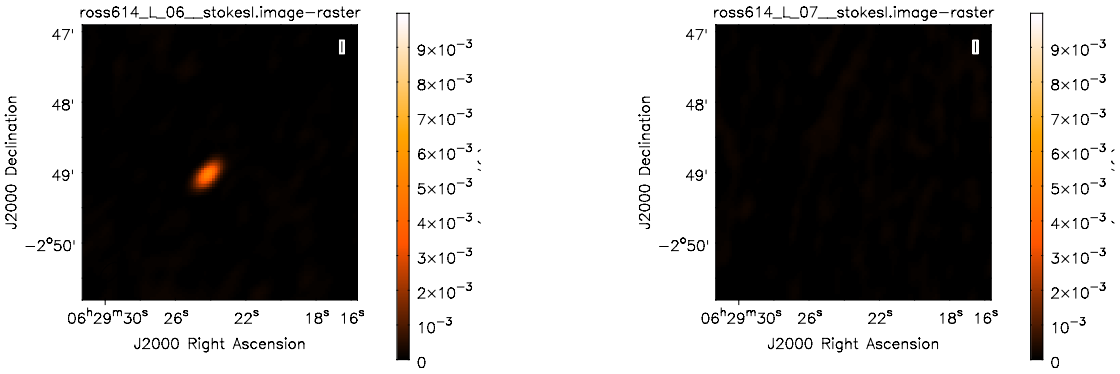

(a) March 3, 2016

(b) April 9, 2016

Figure 4-2: Example cleaned images of the Ross 614 AB field. Left panel shows an observation with a clear detection. Right panel shows an observation with no detected flux from the position of Ross 614. Both images are L-band.

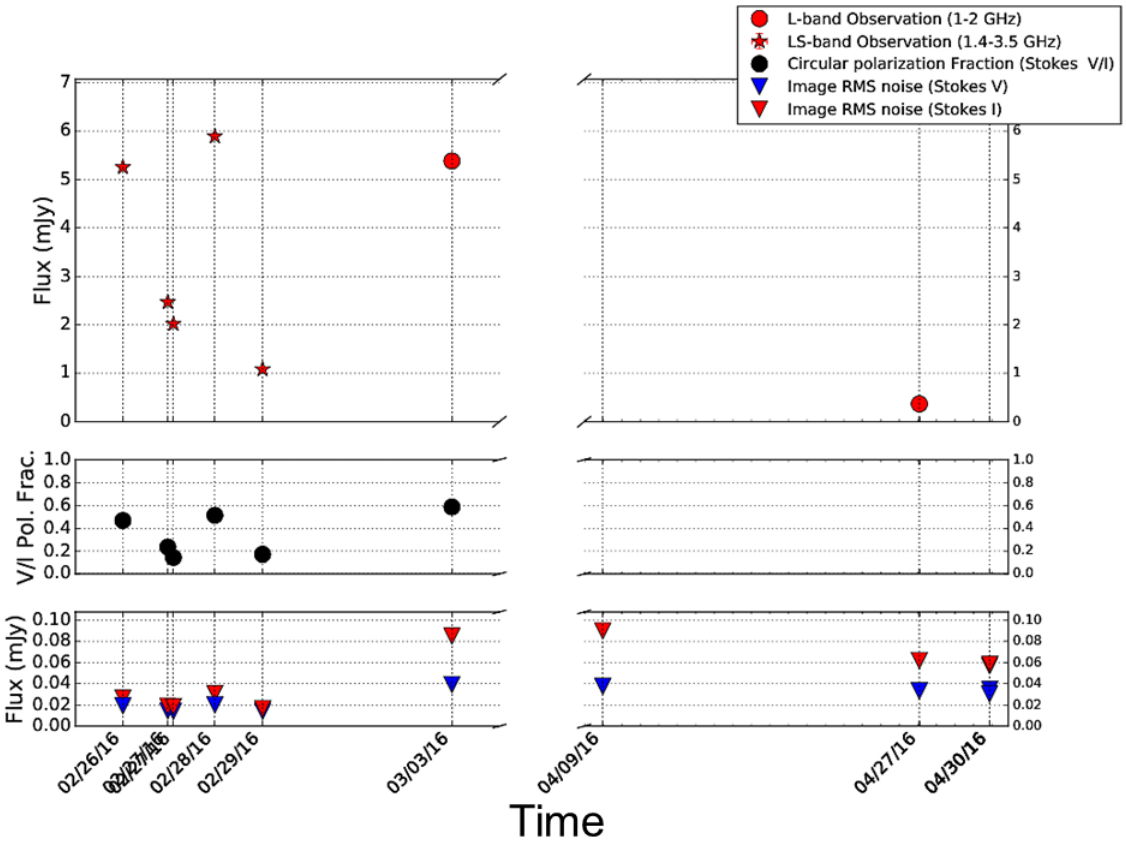

Figure 4-3: Timeseries of Ross 614 AB VLA observations. Top panel shows detected flux vs. time. Spurious detections with large error bars were rejected based on visual inspection of the relevant images. All points in the top and middle panels have error bars, but most error bars are smaller than the markers. The center panel shows polarization fraction for each detection. The bottom panel shows the image RMS level for each observation. There is no polarization fraction for the 4/27/16 observation since no Stokes V source was detected. The Stokes V image RMS is lower than Stokes I, as expected, since there are very few circularly polarized sources in the sky. In two cases (2/27/16, 4/30/16), there was more than one observation on the same day. The data show a week-long period of enhanced but variable radio emission that may be attributable to a long-lived active region.

significant. The higher frequency, wider bandwidth LS-band observations have lower noise than the L-band observations, as expected.

The recovered position of each detected source was compared to the expected current position of Ross 614 AB, accounting for proper motion. All detected sources were consistent with Ross 614 AB within the synthesized beamwidth of the observation (Figure 4-4). The interferometric resolution was not sufficient to spatially separate the binary components, so both stars are within a synthesized beam. There are no known extragalactic sources in close proximity to the current location of Ross 614 AB, so the detected flux is likely from one or both of the stars in the binary.

The spectral behavior of each LS-band observation is shown in Figure 4-5 . The two brightest detections (2/26/16 blue, 2/28/16 orange) show the most interesting spectral behavior. There is no consistent spectral shape across all observations. The polarization fraction (Figure 4-5, bottom panel) stays roughly constant within the error bars. Stellar radio emission is commonly interpreted on a dynamic spectrum plot (time vs. frequency), but the short duration of the observations in this campaign preclude typical dynamic spectrum analysis. Stellar radio bursts show complex, fine time-frequency structure throughout their evolution, so it is unsurprising that the spectra of the Ross 614 AB flare observations vary relative to one another.

Radio Emission Source and Mechanism

The high degree of polarization effectively rules out background sources or thermal emission, since neither are typically highly circularly polarized. The remaining candidates are stellar or planetary non-thermal emission. Stellar non-thermal emission can be generated coherently by the electron cyclotron instability mechanism, plasma emission (as in type II/III solar radio bursts), or incoherent gyrosynchrotron emission [16].

Planetary radio emission in the solar system is exclusively an electron cyclotron/synchrotron maser process [331]. Planetary electron cyclotron maser emission (involving non-relativistic electrons) is highly (>90%) circularly polarized. Detected radio emission from brown dwarfs is also very highly polarized [127]. The moderate degree of polar-

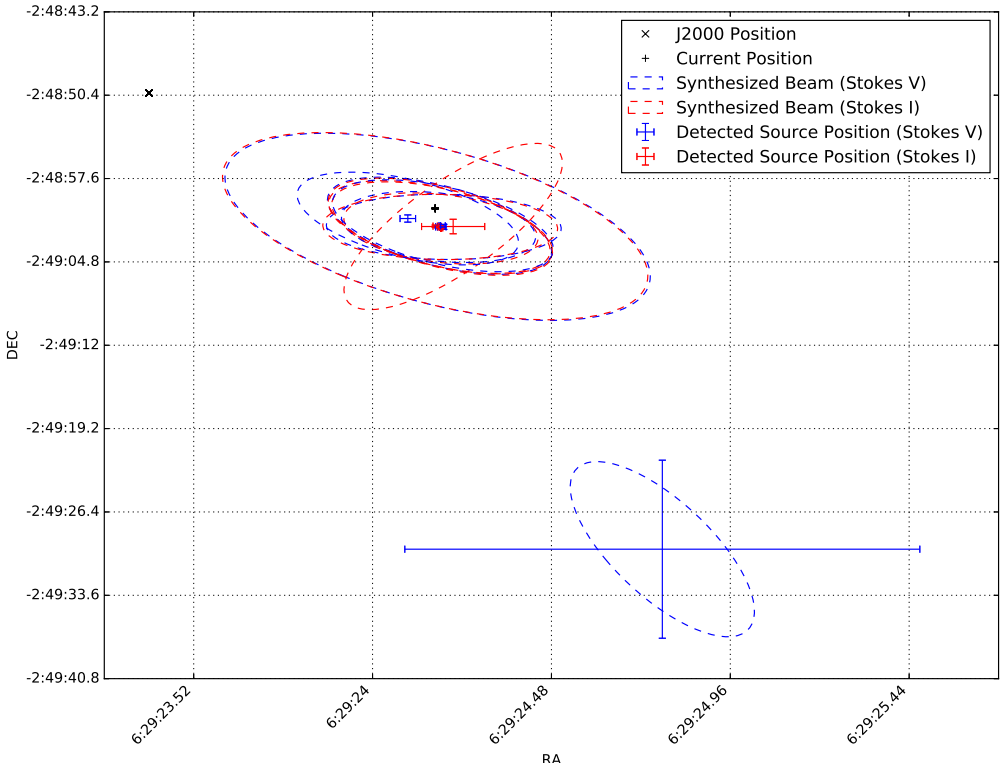

Figure 4-4: Locations of detected sources near Ross 614 AB. Stokes I (red) and Stokes V (blue) source locations are plotted with error bars reported by the source fitting tool. Each detected source is plotted with the synthesized beam ellipse (red and blue, dashed) that is relevant for each observation. The position of Ross 614 AB at the time of each observation is marked with a black cross. Ross 614 AB's J2000 position and the phase center of each observation is indicated by a black X. All but one of the detected sources are consistent with the current location of Ross 614 AB. The outlier source in the lower right corner is likely a sidelobe that was fit by mistake based on a visual inspection of image. Aside from the outlier, all detections are consistent with the location of the Ross 614 and may be confidently attributed to the system rather than a background source.

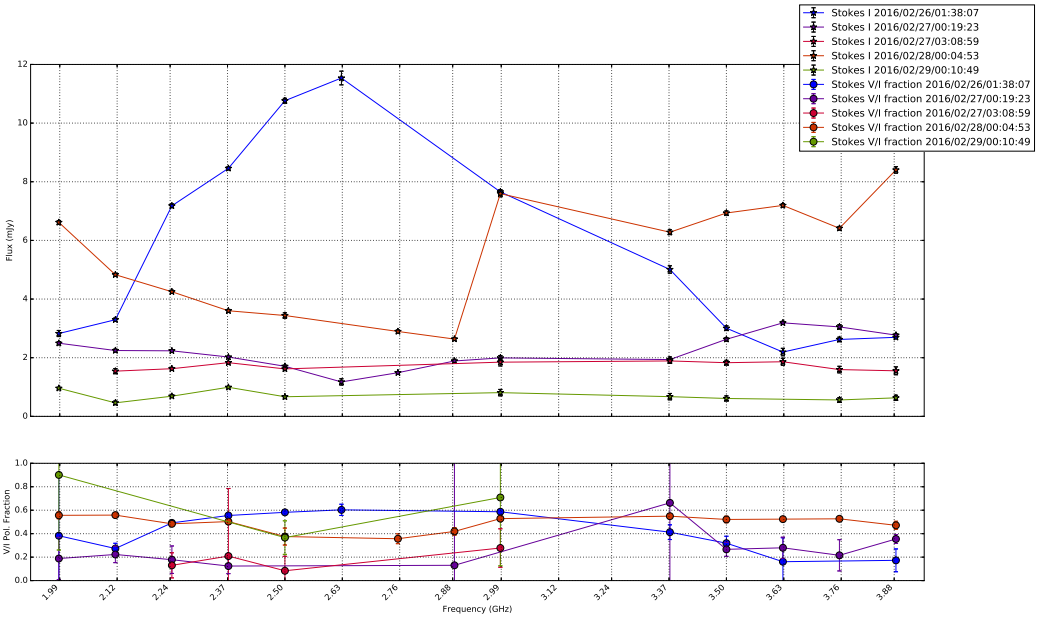

Figure 4-5: Spectra from five LS-band observations of Ross 614 AB. Top panel shows Stokes I flux as a function of frequency. Bottom panel shows circular polarization fraction as a function of frequency.

ization seen in the Ross 614 AB observations is more consistent with stellar activity (likely a flare or series of flares) than planetary emission. The recurrence of flare-like emission over several days is suggestive of a very active region rotating in and out of view. The isolated, weak detection on 4/27/16) could either be slightly elevated quiescent emission, a weaker flare, or the declining phase of a large flare.

The polarization fraction observed generally agrees with higher frequency observations of flares on late-type stars in Berger (2002) [21]. Following the analysis in [21], the emission brightness temperatures range from $\sim 10^9$ - 10^{10} if the flare emission is assumed to come from the whole corona ($\sim 0.1\ R_{star}$) to $\sim 10^{11}$ - 10^{12} if the energy comes from a coronal loop ($\sim 0.1\ R_{star}$). Since the observing frequencies are well below 10 GHz, the stellar emission is likely coherent (CMI or plasma emission) [16]. Without a high resolution dynamic spectrum, it is difficult to determine which mechanism is at work. If the mechanism is electron cyclotron maser instability, the magnetic field of Ross 614 AB (or a large active region on one of the stars) is >1400 G since no frequency cut-off was observed. If the emission from a plasma process,

the emission frequency is either the local plasma frequency or a low order harmonic of it. The plasma density that corresponds to a plasma frequency of 4 GHz is $4 \cdot 10^{11}$ cm^{-3}. If the cyclotron frequency is assumed to be less than half of the plasma frequency, then the implied magnetic field would be ≤ 700 G. The B-field calculated assuming an electron cyclotron mechanism is in better agreement with the literature estimate for Ross 614 A (2.75 kG), though it is not possible to rule out either of the other two emission mechanisms definitely. It is also not possible to determine which star hosted the detected flares, or whether all the flares came from the same star.

Conclusions

We report six strong, circularly polarized detections of radio emission from the M-dwarf binary Ross 614 AB over two weeks using the VLA LS and L-band. The most likely source of the detected radio emission is a series of stellar flares, perhaps from a large active region on the surface of one of the stars. It is not possible to rule out planetary radio emission or planetary influence on stellar emission with the available data. Longer individual observations as well as good temporal coverage over several weeks (to cover several 8-day stellar rotation periods) are required to determine whether the intermittent radio emission is periodic. High resolution dynamic spectra would be useful in ruling out type II/II bursts, while simultaneous optical monitoring could indicate whether flares are indeed the source of emission for this system.

It was not possible to determine which component of the binary was responsible for the flare activity since the components were not resolved with the VLA. VLBI observations could easily separate the two stars and attribute any flares during the observation to one or the other. Multi-wavelength campaigns are the gold standard for stellar flare research since they detect energy release across the spectrum and probe different heights in the stellar atmosphere as well as different energetic particle populations (see [225] for a multi-wavelength campaign targeting EV Lac). A multi-wavelength campaign combined with VLBI observations would offer the best chance of attributing flares to individual binary components and of determining the emission mechanism. The addition of Zeeman doppler imaging (ZDI) would provide a map of

the magnetic field and perhaps even allow tentative localization of flare events.

4.4.3 Survey Results

The goal of the Nearest Stars survey was to set physically meaningful upper limits on radio emission from stars or substellar companions in the solar neighborhood. Though we set out to search for exoplanetary radio emission, the survey has turned out to be perhaps even more useful for constraining radio emission from nearby cool stars. There are few measurements of stellar radio emission (or limits) in L-band or S-band in the literature; this work has contributed the first limits in these bands for the stars surveyed (other than Ross 614). Figure 4-6 shows the flux and luminosity upper limits that result from non-detections in this work. Figure 4-6 also shows limit values from literature and from surveys (Chapter 3) for these objects. Table 4.4.3 summarizes flux and luminosity limits (Stokes I) from this survey and literature. Stokes V limits from this work are shown in 4.4.3. See Section 8.2 for a discussion of the limitations of these upper limits.

This survey rules out substellar companions with B-fields >350-1400 G with quiescent emission in the cyclotron maser mode. The limits also place strong constraints on the magnetic fields of these stars. The 3-σ limits obtained are within a factor of 5 of Jovian radio luminosity and on par with, or lower than, stellar radio luminosities measured at higher frequencies. Future work on the P-band and LOFAR data from this survey may reveal radio emission from weaker B-fields, or further constrain allowed field strengths.

Substellar companion non-detections notwithstanding, radio observations of stellar radio emission are a useful tool for assessing the space weather conditions for stars with known planets. Gl 411 and Lutyen's Star now fall into that category, although unfortunately neither was observed by the VLA. Measuring stellar magnetic fields and placing constraints on flare rates and flare energies are critical for modeling exoplanet atmosphere evolution for individual planets.

Table 4.5. Radio detections and limits

	Procyon		GJ 725		GJ 1111		UGPS	
	Flux (μJy)	L_ν (10^{12} erg s^{-1} Hz^{-1})	Flux (μJy)	L_ν (10^{12} erg) s^{-1} Hz^{-1})	Flux (μJy)	L_ν (10^{12} erg s^{-1} Hz^{-1})	Flux (μJy)	L_ν (10^{12} erg s^{-1} Hz^{-1})
74 MHz[a]	$<2.61\cdot10^5$	<3853	$<2.34\cdot10^5$	<3572	$<2.32\cdot10^5$	<3650	$<3.93\cdot10^5$	<7767
150 MHz[a]	$<6.71\cdot10^3$	<99.1	$<1.10\cdot10^4$	<162.6	$<9.41\cdot10^3$	<148.0	$<7.62\cdot10^3$	<150.7
1-2 GHz	<182	<2.69	<338	<5.16	<225	<3.54	<321	<6.35
2-4 GHz	<44	<0.66	—	—	—	—	—	—
4-8 GHz	<90[c]	<1.3[c]	<141[d]	<2.15[d]	<23[e]	<0.36[e]	—	—
8-12 GHz	33[f]	0.48[f]	—	—	—	—	—	—
	115[f]	1.7[f]	—	—	—	—	—	—

Note. — Limits are from this work except where otherwise specified. Limits from this work (including Ch. 3) are 3-σ, Stokes I. See Table 4.4.3 for Stokes V limits.

[a]VLSSr, Ch. 3

[b]TGSS ADR1, Ch. 3

[c][28]

[d][31]

[e][317]

[f][78]

Table 4.6. Stokes V flux and luminosity limits

	Procyon		GJ 725		GJ 1111		UGPS	
	Flux (μJy)	L_ν (10^{12} erg s^{-1} Hz^{-1})	Flux (μJy)	L_ν (10^{12} erg) s^{-1} Hz^{-1})	Flux (μJy)	L_ν (10^{12} erg s^{-1} Hz^{-1})	Flux (μJy)	L_ν (10^{12} erg s^{-1} Hz^{-1})
1-2 GHz	<90	<1.32	<105	<1.61	<101	<1.60	<124	<2.46
2-4 GHz	<43	<0.64	—	—	—	—	—	—

Note. — Limits are 3-σ, Stokes V. See Table 4.4.3 for Stokes I limits.

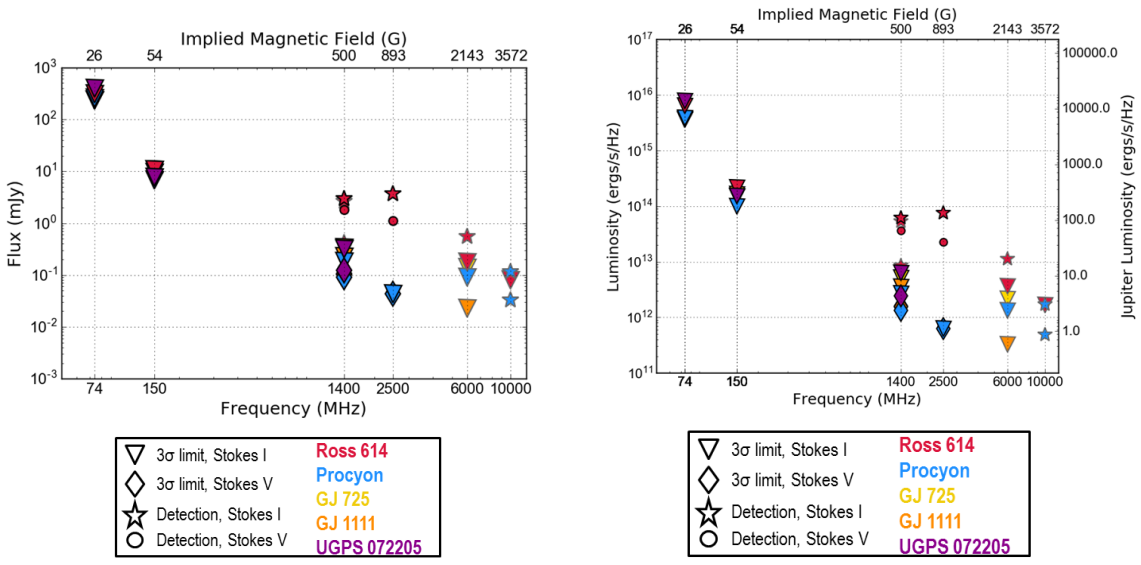

(a) Flux limits

(b) Luminosity limits

Figure 4-6: Flux (a) and luminosity (b) limits and detections for VLA Nearest Stars observations. Marker shapes represent the type of limit or detection; marker colors indicate the object observed. Limits for 74 and 150 MHz are derived from the archival search described in Chapter 3. Limits and detections for 1.4 and 2.5 GHz are from this work and from literature (see Tables 4.4.3, 4.4.3). All higher frequency detections/limits are from literature.

4.5 Discussion

The limits obtained by this survey are such that we would have detected any planet with 10x Jovian luminosity *if* it was emitting while we were observing and *if* the emission was beamed toward the Earth (see Figure 4-7). This survey did not have sufficient time coverage to detect periodic modulation of stellar radio emission due to stellar rotation, magnetic cycles, or magnetic interactions between the stellar magnetic field and a planet (Jupiter-Io type interaction). Targeted observations of known planets are best suited to detecting star-planet interaction since such observations can either follow the planet for multiple orbits (if the period is sufficiently short), or observe multiple phase points in the planets orbit in order to compare radio flux at each point (Io-related Jovian emission is strongly Io-phase dependent). A future survey could search for star-planet interaction by targeting one star at a time and observing it continuously for as long as possible. Planets moving fast relative to the

co-rotation of the stellar magnetic field are most likely to drive radio emission [334], so continuous observations could be limited to a few days. Targets that are circumpolar are best suited to this search strategy.

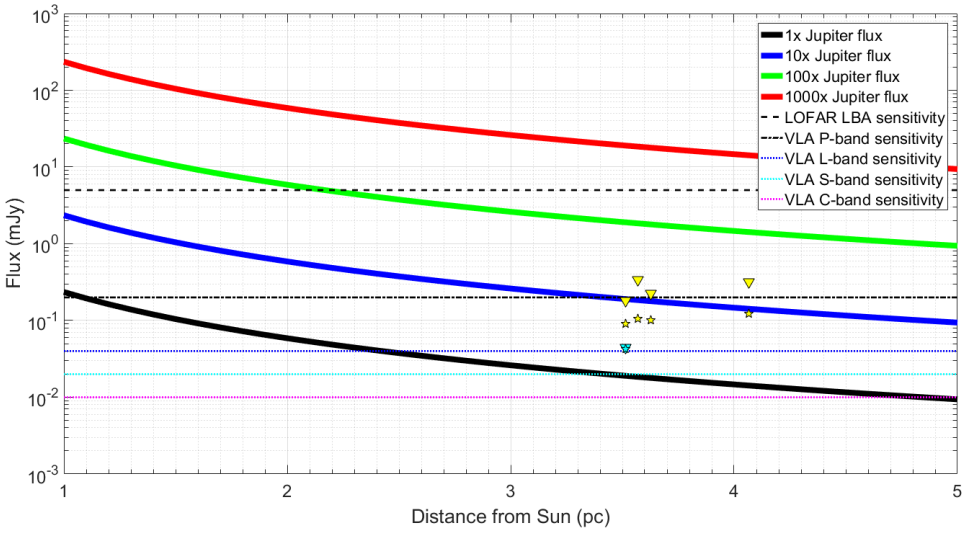

Figure 4-7: Limits obtained compared to scaled Jovian flux. Yellow downward triangles and stars are L-band and LS-band Stokes I 3-σ limits, respectively (Table 4.4.3). cyan downward triangles and stars are L-band and LS-band Stokes V limits, respectively (Table 4.4.3). Any planet or star with flux ∼10x Jupiter *that was emitting in the direction of Earth during the observation* would have been detected.

The observing strategy for star-planet interaction in systems with known planets is distinct from the observing strategy for searching for as-yet unknown companions of nearby stars. In the first case ('characterization'), observations can be organized around the period of the planet and perhaps focused on certain orbital phases of the planet (Ch. 5). The rotational period of the star, if known, should also be taken into account. In the second case ('detection'), there is no known planetary period to guide observations. In the detection case, observing continuously over a long period of time is ideal because there is no way to predict when a planet in the system might emit a bright burst of radio emission either in response to a stellar event or to a transient event within the planet's magnetosphere (e.g. a major volcanic eruption on a moon injecting extra plasma into the magnetosphere). The Owens Valley LWA, which is capable of observing the entire sky continuously with high time resolution,

is conducting just such a survey [5]. Distinguishing stellar bursty emission from planetary emission is a problem, but any detection at all can be used to justify follow-up observations with other instruments, preferably over a wider frequency range.

Instruments that cannot observe the whole sky all time time (VLA, LOFAR, VLBA) can also be used for 'detection' surveys, though they are better suited to targeted 'characterization' work. Pointed instruments can be effective for small surveys where their formidable collecting area, bandwidth, and angular resolution are trained on a small set of targets (as in this survey). The next iteration of this survey would benefit from longer observations of each target to look for periodic behavior and/or random energetic events. The time occupancy of the brightest solar system events is low because those events are highly energetic and therefore rare. The time coverage needed to 'guarantee' detection of a planet, if it exists, is difficult, if not impossible, to determine. Given the constraints on oversubscribed pointed instruments and the physical constraints of being on the Earth's surface (horizon), pointed instruments cannot observe a single target indefinitely. Upper limits derived from targeted 'detection' surveys come with the asterisk that there may be radio emission from target systems, but it was missed due to breaks in temporal coverage. Nevertheless, planets around nearby stars are highly valuable since they can be most easily characterized. Searching for these planets by any and all observational means available increases the chance of finding high value follow-up targets.

Chapter 5

Radio Observations of HD 80606 b: An Eccentric Hot Jupiter

Eccentric giant planets that pass close to their host star during periastron present a unique opportunity for radio detection. Exoplanet radio detection is riddled with uncertainties (see Section 1.2.2, 1.3.3); above all, the bursty nature of radio emission observed from solar system planets makes it difficult if not impossible to predict when an exoplanet should be emitting strongly enough to be detected. Eccentric giant planets, however, are predicted to be brightest in the radio (assuming they emit at all) during their periastron passage when stellar wind intensity incident on the planet's magnetosphere is at maximum (see Section 1.2.3). This chapter describes two observational campaigns that focus on periastron passage of HD 80606 b, an extremely eccentric massive planet that passes within 6 $R_\star$of its host.

5.1 HD 80606 System

HD 80606 is a main sequence G5 star (V-mag = 9.1) that hosts a highly eccentric (e = 0.934 $\pm$ 0.003) giant planet, HD 80606 b (M sin i = 3.89 $\pm$ 0.188 M_J) [210]. HD 80606 b transits its host star and has a measured radius of 1.029 R_J[204]. It has been suggested that HD 80606 b's tight, highly eccentric orbit may be a result of interaction with HD 80606's distant binary companion, HD 80607 [327]. This system

is a valuable target for radio observations because its highly eccentric orbit exposes the planet to a wide range of stellar wind intensities. Assuming that the planet has a magnetosphere and that the strength of its magnetospheric radio emission is driven by the incident stellar wind (as is the case with the Earth), the radio flux from HD 80606 b should increase dramatically as it approaches and passes through periastron. This predictable periodicity is helpful for disentangling other effects, such as planetary rotation and stellar rotation. The goal is to use the contrast between flux at apastron and periastron to constrain the field strength as well as the amplification due to the stellar wind. See Figure 5-1 for a schematic of HD 80606 b's periastron passage.

HD 80606 has been observed using the VLA at 1425 MHz and 325 MHz by Lazio et al. (2010) [170]. No emission was observed and upper limits on planetary luminosity were determined to be $2.7 \cdot 10^{23}$ ergs/s (1425 MHz) and $2.3 \cdot 10^{24}$ ergs/s (325 MHz). These values are several orders of magnitude greater than the luminosity of Jupiter at 40 MHz ($2 \cdot 10^{18}$ ergs/s). There are various explanations for the non-detection in the VLA observations. Radio emission from planetary magnetospheres is often strongly beamed and the beam angle and direction depend on the planets rotation axis as well as the structure of the magnetic field. If Earth is not within HD 80606 b's emission cone, no radio emission will be detected no matter how strongly the planet may be emitting. Another possible explanation is that the planet's radio emission cuts off at a lower frequency than the observed frequency. The LOFAR observations are intended to probe a lower frequency regime to address this issue. Finally, the system is fairly far away (58 pc), so the sensitivity of the VLA may not have been high enough to make a detection.

HD 80606 b radio detection is something of a long shot given its distance (58 pc [37]), but at the time of the original LOFAR proposal it was the only known massive, highly eccentric planet that could be observed with LOFAR to test the theory of extreme solar wind radio flux enhancement. The radio signal from HD 80606 b is expected to be very faint (mJy) if it is present at all. A naïve estimate for the flux from HD 80606 b can be obtained by simply scaling the luminosity of Jupiter to the distance of HD 80606. This yields a flux density of 70 nJy, well beyond the capabilities

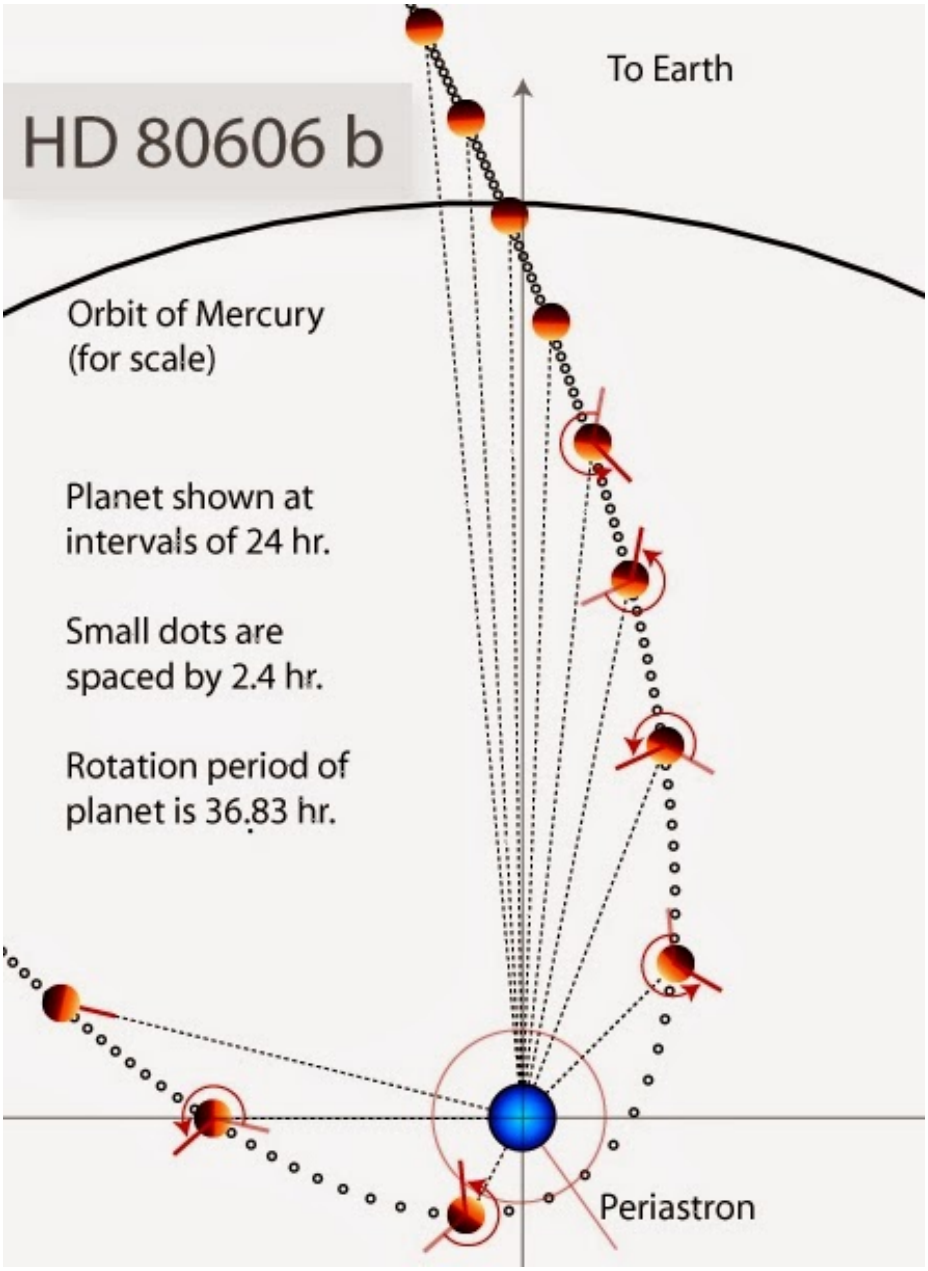

Figure 5-1: HD 80606 b periastron passage schematic. HD 80606 b passes $\sim$6 $R_\star$from its host at closest approach. Image credit: G. Laughlin.

Table 5.1. LOFAR Cycle 0 observations of HD 80606 b

Epoch	Date Observed	HD 80606b Orbit Location	Comment
Epoch 0	March 2013	Near apastron	Serves as baseline for other observations
Epoch 1	January 24, 2013	48 hours pre-periastron	
Epoch 2	January 25, 2013	18 hours pre-periastron	
Epoch 3	January 27, 2013	18 hours post-periastron	
Epoch 4	January 28, 2013	48 hours post-periastron	

of LOFAR or any other existing low frequency telescope. Scaling the flux by a factor of 3000 to account for the higher density solar wind at HD 80606 b's periastron passage increases the predicted flux to 200 μJy [170]. These estimates assume a planet identical to Jupiter; if HD 80606 b is intrinsically, say, 10x more luminous in the radio than Jupiter, the expected flux at periastron passage rises to 2 mJy, a value that is close to the current detection thresholds of existing telescopes like LOFAR. The unknown HD 80606 b magnetic field strength as well as the unknown stellar wind intensity and variability increase the uncertainty of these estimates. LOFAR observations can, at minimum, rule out the most extreme scenarios for radio emission from this system.

5.2 Data[1]

J. Lazio, D. Winterhalter and collaborators requested and received 30 hours of LOFAR Cycle 0 time on HD 80606. The time was divided into five 6-hour observations. The first four observations (designated Epochs 1-4) were collected around the 12/27/13 periastron passage of HD 80606b (see Table 5.2). This section focuses on Epoch 1 which was observed approximately 48 hours before periastron passage. Epoch 2 was observed 18 hours before periastron passage, Epoch 3, 18 hours after periastron, and Epoch 4, 48 hours after periastron. Epoch 0 was observed two months later when HD 80606b was close to apastron. Observations at or very near to periastron were avoided due to concerns that the plasma frequency of the dense stellar wind plasma near the star might block the transmission of planetary radio emission at low frequency.

[1]Some of this work was presented as Project 2 for the EAPS General Exam.

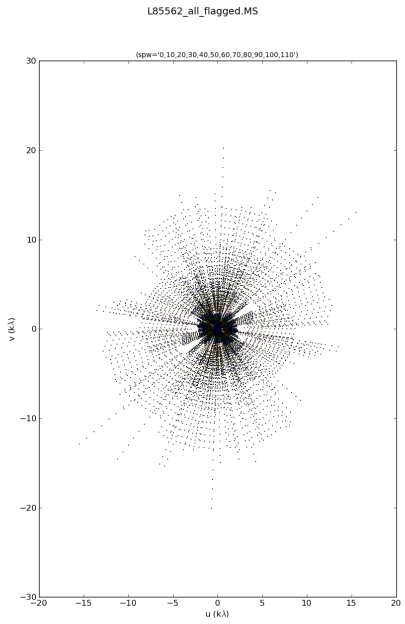

Figure 5-2: UV plane coverage for Epoch 1 observation. 'U' is the horizontal axis and 'V' is the vertical axis. Both axes have units of kλ. The dense LOFAR core accounts for the dense coverage at short baselines. For clarity, only 1 out of every 10 channels is plotted. See Chapter 2 for details on LOFAR's layout and station architecture.

All five observations were made using LOFAR's Low Band Array (LBA, see Section 2.4). The LBA is capable of observations from 10-90 MHz, but the 30-75MHz filter was used for the HD 80606 observation. The use of this narrower filter improves noise rejection at the top and bottom of the bandpass. LOFAR is built in a hierarchical structure. Each LOFAR 'station' is the equivalent of a single parabolic dish in higher frequency arrays like the VLA. An LBA station is composed of 96 crossed dipole antennas, although only 48 can be beamformed at the same time. The inner 48 or outer 48 antennas may be selected depending on the needed primary beam size and sidelobe level requirements. The 'LBA Outer' configuration was used for this observation. The beamformed observations from each station are then cross correlated in typical interferometric fashion. All five observations used the full Netherlands array (37 stations). Figure 5-2 shows (u, v) coverage for the Epoch 1 observation.

Calibration sources are observed simultaneously with the target source. Parabolic dish interferometers (VLA, ALMA, GMRT) typically switch back and forth between

a target field and a calibrator field. Simultaneous observation of the calibrator and target improves the quality of the calibration, particularly for fast variations in ionospheric conditions. The LBA stations can form multiple beams, so a typical observation set-up has one beam on the main target field and one beam on the calibrator field. For the HD 80606 b observations, half of the bandwidth (every other one of the 256 195 kHz sub-channels) was devoted to the calibrator and the remaining half to the HD 80606 field. This means that the actual bandwidth on the target is $1/2$ of the 45 MHz implied by the width of the filter. Standard data cleaning and calibration procedures, including RFI flagging, flux, phase, and gain calibration, and time domain averaging, were performed by the observatory using the LOFAR standard calibration pipeline. The resulting data product was packaged as a Measurement Set (MS) and delivered to the proposers. The MS file contains the calibrated complex visibilities for the full 6-hour observation. There are 4 complex numbers (polarization products XX, YY, XY, YX) at each time point (10 seconds) in each of the 120 subbands. In theory, calibrated data is "image ready" and should be immediately usable for analysis. In practice, some additional flagging was required to remove bad data points before imaging could proceed.

5.3 Imaging

The primary challenge in searching for exoplanetary radio emission is that the structure of the signal is unknown in both time and frequency. Observations of solar system planets show that planetary radio emission can vary dramatically over timescales ranging from seconds to days or months [147]. The observed spectrum can vary also. Additionally, it is not possible to estimate the planetary magnetic field of HD 80606 b with confidence, so the expected cut-off frequency is not known either.

The fundamental trade-off in the analysis of this data is between time/frequency resolution and sensitivity. Increasing the integration time or bandwidth will improve the signal to noise ratio, but transient bursts might be averaged out. The data was therefore imaged at a range of resolutions in time and frequency to provide the best

Table 5.2. Time and frequency divisions used for imaging

	Step sizes	Number of images for each step size
Time division	5:37.5, 11:15, 15:00, 22:30, 30:00, 45:00, 60:00, 90:00, 120:00, 180:00 minutes	64, 32 ,24, 16, 12 ,8, 6, 4, 3, 2
Time division	1, 2, 4, 8, 15, 16*, 30, 60 sub-bands	120, 60, 30, 15, 8, 8*, 4, 2

Note. — Time and frequency divisions used for imaging. Subbands are 195 kHz wide.

chance of detecting a signal if it is present. The dataset was broken up into chunks in both time and frequency and imaged. The first set of images was intended to produce a time series "light curve" by binning the data in time. The second set binned the data in frequency to produce a rough spectrum. The binning started with small chunks of data and then progressively doubled the size of the chunks until they were 1/2 of the full dataset (Table 5.3, Figure 5-3). The time series analysis used the center 75% of the bandwidth (SB 15-105). The spectral analysis used the full 6 hour time range. A set of 12 reference objects from the 4C [233] catalog were selected in order to remove systematic trends (Table 5.3). The approach is similar to the use of an ensemble of standard, non-variable stars for precision photometry in optical astronomy.

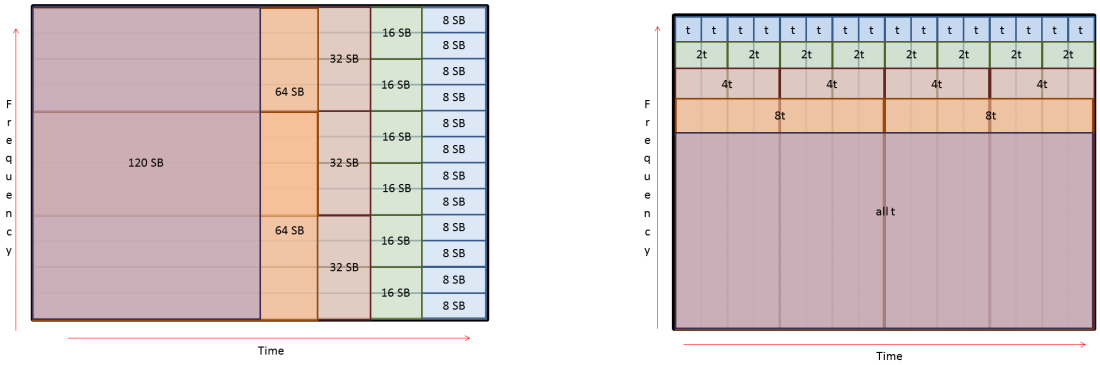

(a) Frequency division

(b) Time division

Figure 5-3: Schematic illustrating the time/frequency division concept for imaging. The left chart shows division by sub-bands (SB) to generate a coarse spectrum. The right figure illustrates binning by increasing time intervals to generate a light curve.

All flagging, imaging, and fitting was performed using CASA [194], a software

Table 5.3. Reference sources from 4C catalog.

Source Name	RA1950 h:m:s	DE1950 d:m:s	4C Flux (178 MHz) Jy	VLSS Flux (74 MHz) Jy	VLSS Flux Err Jy	Spectral Index	Flux 74 MHz (calc) Jy	Flux 52 MHz (calc) Jy	Flux 178 MHz (calc) Jy
4C47.3	09 14 05.0	+47 34.3	2	5.32	0.57	-1.054	10.075	14.611	3.996
4C48.23	08 58 15.3	+48 53.9	2.9	1.91	0.2	-0.819	2.284	3.050	1.113
4C48.24	09 11 18.4	+48 52.2	3.8	5.14	0.52	-0.736	7.094	9.198	3.718
4C48.25	09 26 56.9	+48 43.9	2.8	5.88	0.59	-0.724	6.210	8.017	3.290
4C48.26*	09 28 14.9	+48 03.1	2.9	1.62	0.18	-0.778	5.431	7.148	2.742
				3.57	0.39				
4C50.28	09 00 19.6	+50 26.4	2.9	6.81	0.68	-0.729	8.055	10.419	4.247
4C50.29	09 14 11.4	+50 17.9	2.8	5.22	0.52	-0.911	7.216	9.950	3.244
4C51.27	08 57 24.5	+51 16.7	2	1.12	0.13	-1.018	4.020	5.756	1.645
4C52.2	09 08 37.8	+52 51.8	3.6	7.35	0.8	-1.101	11.918	17.577	4.534
4C52.21	09 23 21.6	+52 17.7	2.3	8.06	0.83	-1.086	7.938	11.645	3.060
4C53.18	09 19 19.8	+53 13.8	7.4	16.16	1.65	-0.840	17.107	23.009	8.184
4C53.19	09 24 53.1	+53 27.4	3.8	13.26	1.35	-1.238	14.253	22.059	4.808

Note. — Fluxes from 4C and VLSS as well as spectral fits from SPECFIND [301] are included. The spectral fits were used to calculate the expected flux at three frequencies (right 3 columns).

*Source 4C48.26 (starred) has two corresponding entries in VLSS.

package developed by the National Radio Astronomy Observatory (NRAO). Significant effort was devoted to determining the optimal parameters to the CLEAN algorithm. The final parameters are listed in Table 5.3. These parameters were determined by trial and error testing of a range of values and comparison of the noise level and overall appearance of the CLEANed image. A two-step cleaning approach was implemented. The first round of cleaning ran for 7500 iterations and used a mask to focus on regions with known VLSS [53, 166] sources as well as the center of the image where HD 80606 lies. Using a mask during CLEANing restricts the algorithm to look for flux only in the masked areas. The second stage ran for 2000 iterations and used no mask so that any additional flux outside of the areas with known sources could be cleaned. Initial imaging was done for Stokes I only, although future work will include extensive Stokes V imaging as well, since planetary radio emission is expected to be highly circularly polarized. Test Stokes V images showed no features and appeared to be entirely noise, but this may be a result of issues with the calibration pipeline during Cycle 0.

Additional effort was required to ensure that CLEAN would run in a reasonable amount of time. The LOFAR field of view is very large (6-10° depending on

Table 5.4. Key `CLEAN` parameters for imaging

Weighting	Robust	Image size (pixels)	Pixel size (arcsec)	Gain	W-planes	Algorithm	Primary beam correction
Briggs	0.75	2048x2048	Set to the estimated synthesized beam size for the center frequency	0.1	512	Clark	Off

Note. — Time range and frequency range varied depending on the binning of each image. All other parameters were left at default values.

frequency), so w-projection [57] with many w-planes was required. W-projection is computationally efficient, but requires a large amount of RAM. Attempts to image significant fractions of the full 6-hour dataset on quad core desktop machines were unsuccessful either due to RAM-related crashes or unacceptably long runtimes of many hours to days for a single image. An Amazon Web Services (AWS) cloud machine optimized for RAM-intensive processing and equipped with up to 240 GB of RAM and multiple cores was used instead with much better results. CASAs `pclean()` parallelized algorithm was used rather than the typical `clean()` in order to take full advantage of the multiple cores (up to 32) available on the AWS machine.

5.4 Analysis

Completed images were analyzed using a custom script that retrieved the full image residual RMS, CLEAN beam size, and other statistics. Subimages 15 x 15 beamwidths square were centered on the 12 brightest VLSS/4C sources (Table 5.3) as well as the HD 80606 field. CASAs `imfit()` function was used to fit 2D Gaussians to each subimage in order to measure the flux of each source. The positions and position errors for each fitted source were also recorded to give a rough estimate of image quality and also highlight ionosphere-induced position shifts. Fits with errors larger than 50% were discarded.

A total of 417 full field images, 171 time series images and 246 frequency division images were produced using scripted `pclean()` commands. These images were run

through an analysis pipeline as described in the previous section. The key outputs of the analysis pipeline are RMS values for each image and flux values from fitting of known sources as well as the target field. Sample images for time and frequency binning are shown in Figure 5-4. The features of these images are discussed in detail in the next two sections.

5.4.1 Light Curve (Time Binning)

The first check of the image quality was whether RMS noise decreases as $1/\sqrt{n}$ as the time bin size (integration time) increased. The results for the time binning experiments are shown in Figure 5-5. The RMS value of the image residual was calculated for each full image as well as for a 15 x 15 beam subimage centered at the location of HD 80606 (also the phase center of the image). The RMS of this small subimage (shown in red in Figure 5-5) was generally higher than the RMS of the full image. For short integration times, the RMS noise does decrease with a slope of approximately $-1/2$ in logspace as expected. At longer integration times, the noise levels diverge from the ideal curve (black dashed line). This indicates that there are non-Gaussian components to the image noise. Spikes emanating from bright sources (see Figure 11, bottom right) in the time series images are likely caused by direction dependent ionospheric effects. This analysis shows that a noise level of 10 mJy can be achieved in approximately 1 hour and the full integration time yields a noise level of $\sim$6 mJy.

Next, the RMS data were plotted as a function of time (Figure 5-6) to determine whether observing conditions or instrumental effects were significant contributors to the image noise levels. The observation was performed from approximately 9:30 pm on January 24th to 3:30 am the next day (LOFAR local time). The most obvious feature in Figure 13 is a dip in the RMS level that occurs around midnight. Otherwise, there is a slight increase in noise at the beginning and end of the observation. The origin of the midnight feature is unknown, but one possibility is that it is a result of the ionospheric 'midnight wedge' passing over the telescope [150].

Analysis of the image residuals indicates relatively well-behaved data. Visual examination of the time series images, however, tells a different story. First, a zoom-

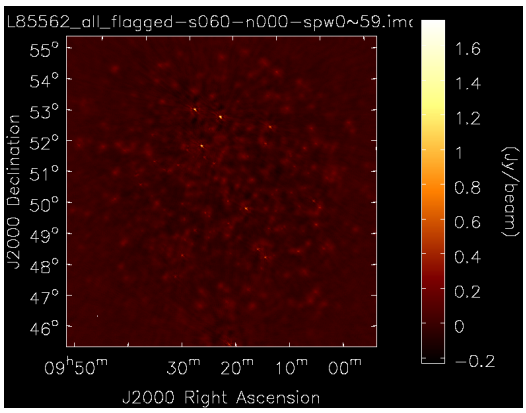

(a) Frequency split, 1/2 bandwidth (image)

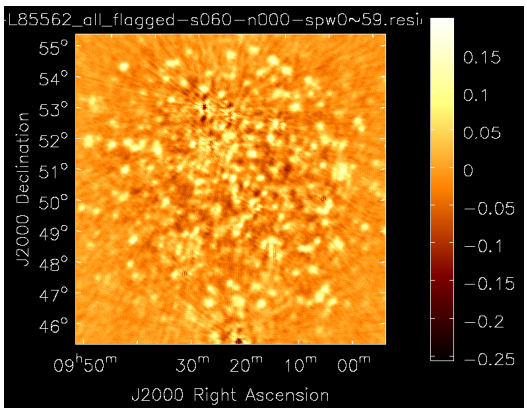

(b) Frequency split, 1/2 bandwidth (residual)

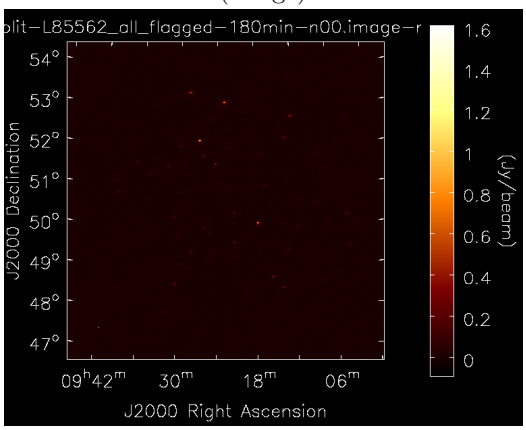

(c) Time split, 1/2 bandwidth (image)

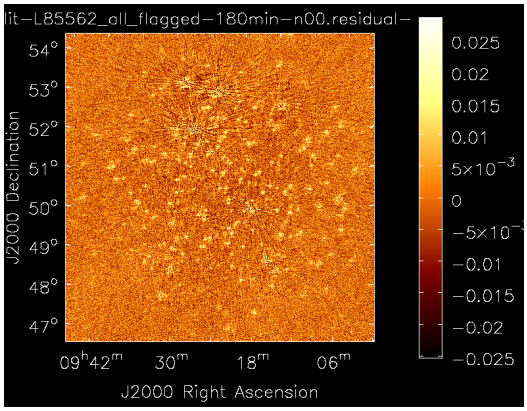

(d) Time split, 1/2 bandwidth (residual)

Figure 5-4: Sample images and residuals. The top set of image (left) and residual (right) are from the frequency binning experiment. The first 1/2 of the bandwith is imaged in this sample. The bottom image and residual are from the time binning experiment. The first 1/2 of the 6 hour observation is imaged in this sample.

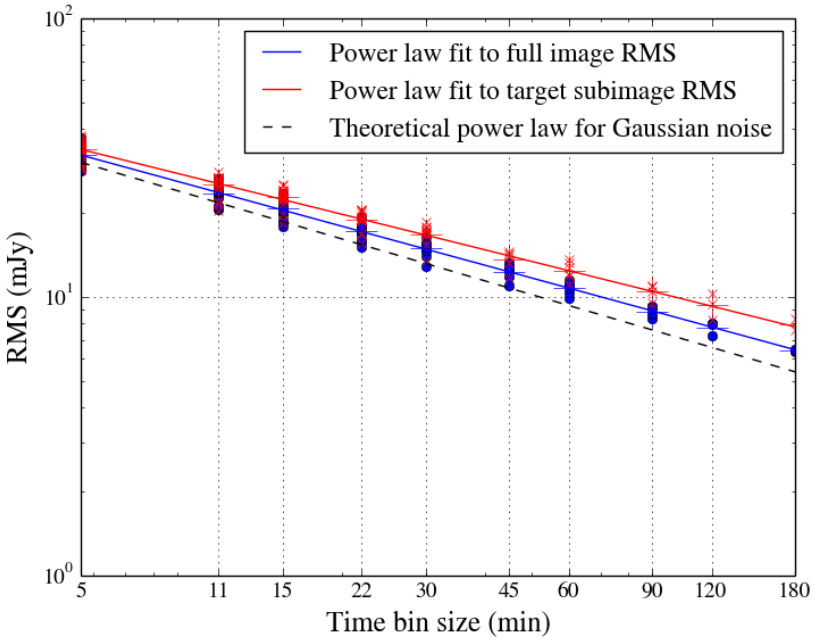

Figure 5-5: RMS for full image and center subimage as a function of time binning. The red points are the RMS value for the small subimage (15x15 beams) at the center of the image (where HD 80606 should be). The blue points are the RMS for the full image (2048 x 2048 pixels, 7 degrees). The large + markers represent the average of each cluster. The solid lines represent power law fits to the data and the dashed line is a theoretical power law fit for Gaussian noise (slope = -0.5).

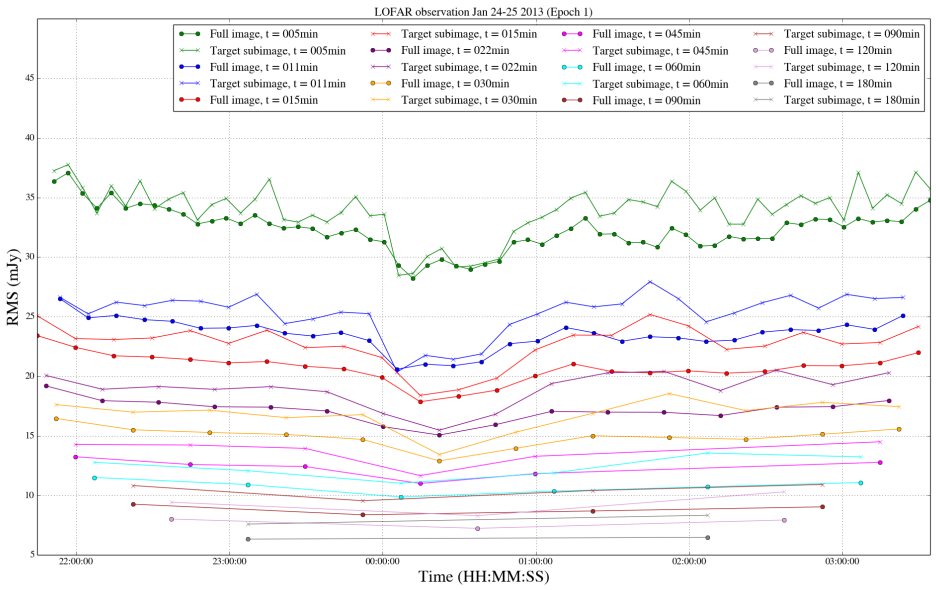

Figure 5-6: Timeseries of RMS values for full image (o markers) and center subimage (x markers). Different time binning values are represented by different colors. Points are located at the center of the time bin. Times are local LOFAR times during observation.

in of the center of the field shows a source very close to the location of HD80606. This source is identified in the VLSS catalog [166] as VLSS0922.6+5035 and has a flux density of 0.46 ± 0.08 Jy. This source is likely a background radio galaxy based on its spectrum (Figure 5-7b) [301]. The spectral index of this source is ∼-0.8, which is consistent with a typical background radio galaxy. Unfortunately, it is very close to the position of HD 80606 (0.69 arcminutes) and therefore blended with any emission coming from HD 80606 b. If the source position and shape is stable from one image to the next, the presumably constant extragalactic source could be subtracted out by differencing adjacent images or peeling the source from the visibilities. The lack of proper ionospheric calibration makes this impossible at present. As shown in Figure 5-8, even the brightest source in the field of view (4C53.18) changes both shape and position significantly over short times (5 minutes in this case).

The fitting routine was applied to the subfield at the center of the image, which contains HD 80606 as well as the nearby extragalactic source. It is assumed that the

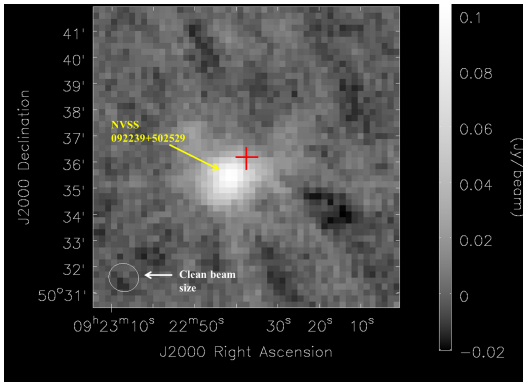

(a) Extragalactic source near the location of HD 80606

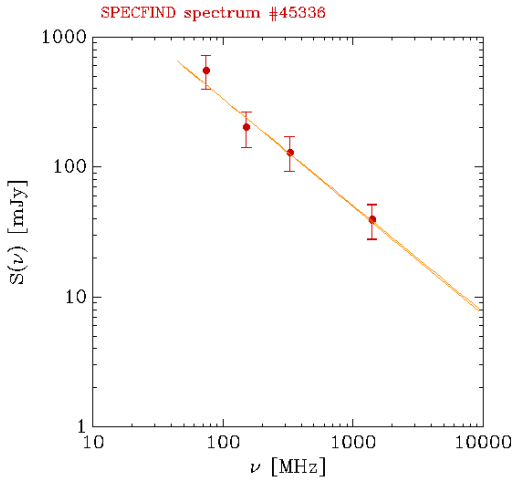

(b) Spectrum of extragalactic source

Figure 5-7: HD 80606 field with nearby extragalactic source (left). The red crosshair indicates the location of HD 80606. The beamsize is indicated in the lower left of the image. Spectrum for VLSS0922.6+5035 (right). The measurements are from FIRST/NVSS (1400 MHz), WN (325 MHz), 7C (151 MHz), and VLSS (74 MHz).

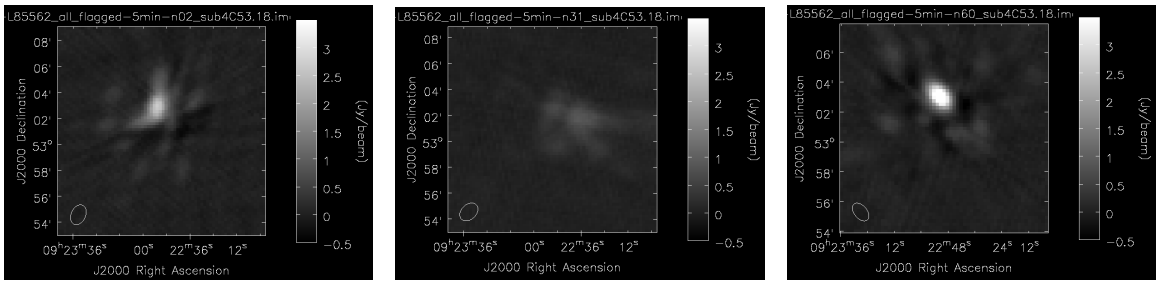

Figure 5-8: Example images of a bright source (4C53.18) at three different time intervals. The oval at the bottom left corner of each image represents the beam shape and size. The shape, position, and brightness of the source change significantly.

fit will center on the extragalactic source, but may include a contribution from HD 80606. The results for all integration times are shown in Figure 5-9. There are some gaps in this 'light curve' since some fit attempts did not converge and others were excluded if the reported errors were larger than 50% of the fit flux value. There is a sizable gap around midnight and a set of anomalously high fluxes with large error bars around 23:00. The rest of the light curve is generally below the expected flux for the extragalactic source. This is consistent with the low fluxes seen for the reference sources. There is no evidence of excess emission due to HD 80606 b. An example of a light curve using only one integration time (5 minutes) is shown in Figure 5-10.

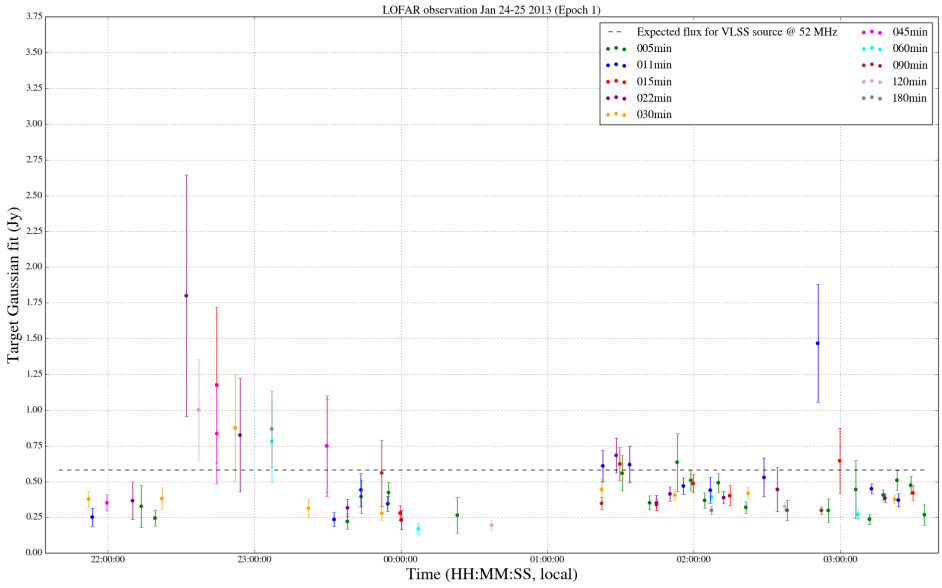

Figure 5-9: Flux values derived from 2D Gaussian fits of the HD 80606 region. Results from all integration times are combined on this plot. The dashed line is the expected flux from the VLSS extragalactic source. The feature near 23:00:00 is likely due to ionospheric effects rather than enhanced flux from HD 80606 (based on examination of individual images).

The fits to the images provided positions for the sources as well as flux values. Figure 5-11 shows the positions for the source in the center subimage. There is considerable spread in the calculated position relative to the known location of HD 80606 and HD 80607 (the binary companion of HD 80606) and the extragalactic source. The cause of these position shifts is the changing refractive index of the

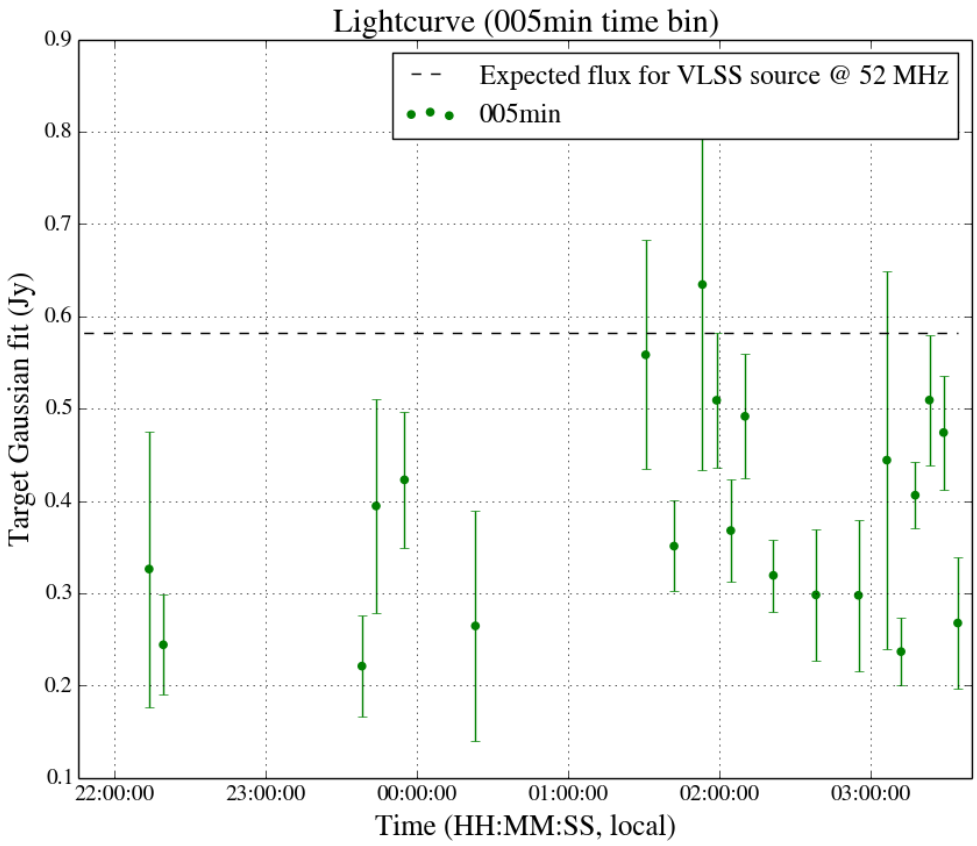

Figure 5-10: Light curve with 5 minute integration times. Dashed line is the expected flux at 52 MHz from the nearby extragalactic source.

ionosphere during the observation. Seeing, or the twinkling of stars in the optical regime, is a similar effect due to turbulence in the troposphere. The ionosphere also distorts the shape of the sources, so large error bars are probably indications of very non-Gaussian source shapes.

Finally, the shape of the beam (as calculated by CASA during cleaning) changes throughout the observation. The beam is represented by an ellipse and Figure 5-12 shows the major (blue) and minor (red) axes of the ellipse in arcseconds as a function of time. The position angle in degrees is also shown (green). The orientation of the beam flips at approximately 01:30. It is unclear what causes this flip, but a likely explanation is the changing position of the target field with time. The change in beam shape and position can also be seen the reference beam outlines in the lower

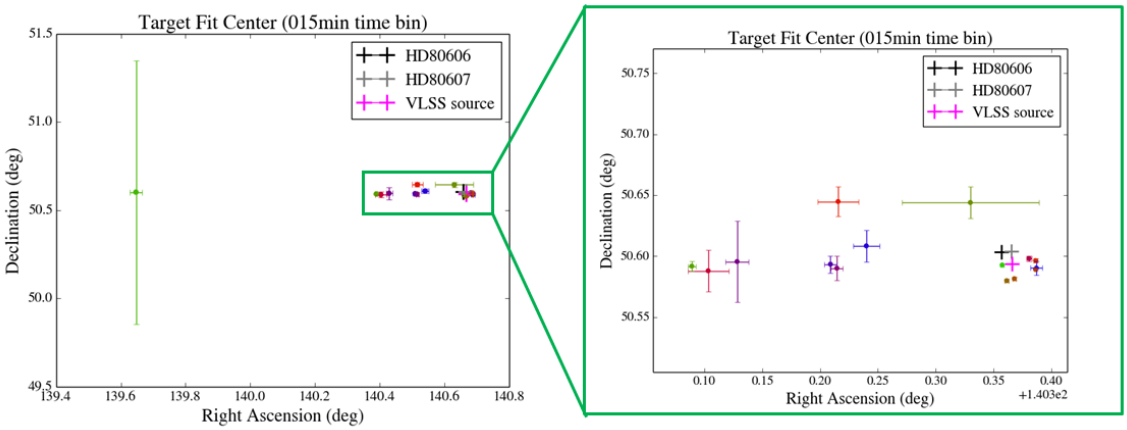

Figure 5-11: Fit positions for 15 minute integrations. Left panel shows all fits for this integration time, right panel is a zoom-in to the green box shown on the left image. The color of the fits represents the relative time of the image that they are derived from blue at the early part of the observation, green toward the middle, and red towards the end. Positions of HD 80606, HD 80607, the binary companion of HD 80606, and the VLSS extragalactic source are shown with '+' markers for reference.

left corner of each image in Figure 5-8.

5.4.2 Spectrum (Frequency Binning)

The images generated by binning increasing numbers of subbands were processed using the same procedure as the time binned images. Figures 5-4b, 5-4b show an example of a frequency binned image and residual. The image RMS results for the frequency binning experiment are shown in Figure 5-13. The frequency binning results show a shallower slope than the time binning experiment. The likely cause is 'smearing' in the residuals caused by the jittery motion of the sources due to the ionosphere (see Figure 5-4b). The large motions of sources over the 6 hour integration leaves large scale structure ('blobs') in the residuals that cannot be removed with further cleaning. Additional ionospheric corrections are needed to remove this effect. The 'blobs' are more pronounced in the frequency binning images because the full 6 hour observation is imaged, while the time binned images only use at most 3 hours of the observation. Less integration time allows less time for the ionosphere to smear sources.

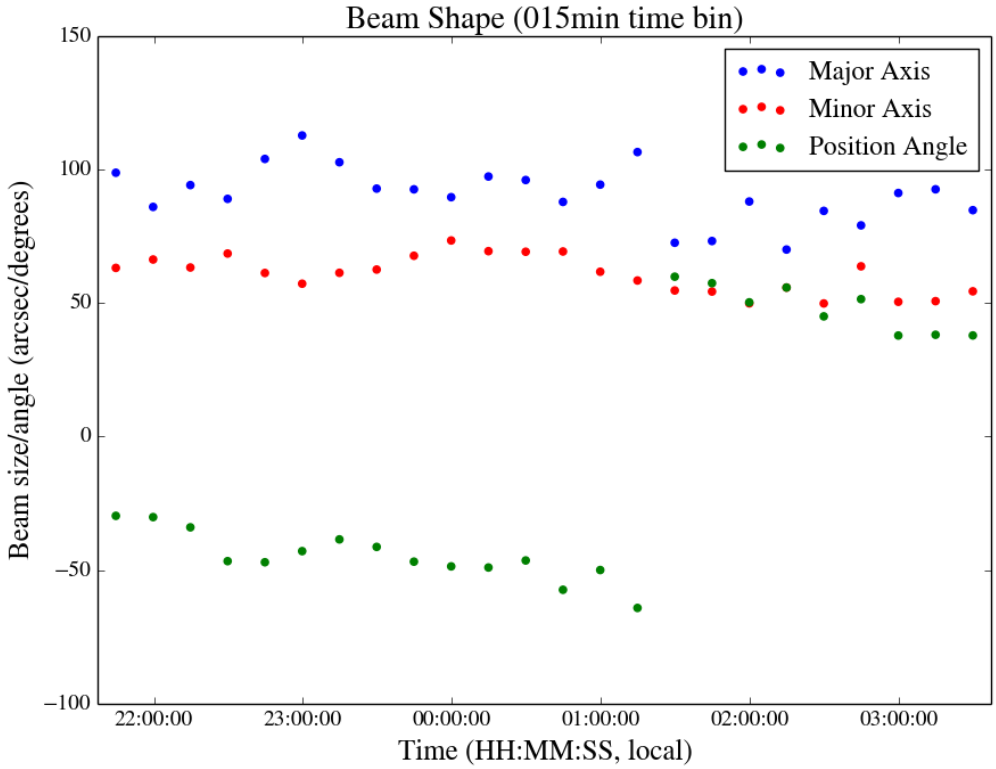

Figure 5-12: Beam shape parameters as a function of time. The vertical axis represents arcseconds for the major and minor axes and degrees for the position angle.

The flux values from fits to the image center subimage (which contains HD 80606-7 and the VLSS extragalactic source) seen in Figure 5-14. Estimated flux values climb very quickly below 45 MHz. Examination of images of this region show that the rapid increase in flux toward low frequencies is not real. It is likely due to increased noise in the low frequency images and poorer fits due to non-Gaussian source shapes. There is interesting structure present in the spectrum, however. A set of three peaks appears between 45 and 65 MHz. The source of this structure is unknown, but it will be interesting to see if this structure persists when proper ionospheric calibration and bandpass fitting are applied.

The positions of the fitted sources are not as widely scattered as in the time binning case (Figure 5-15). All of the frequency binned imaged used the full 6-hour observation, so this averaging effect is likely responsible for the improved clustering. While there are still outliers, the estimated positions cluster much closer to the VLSS

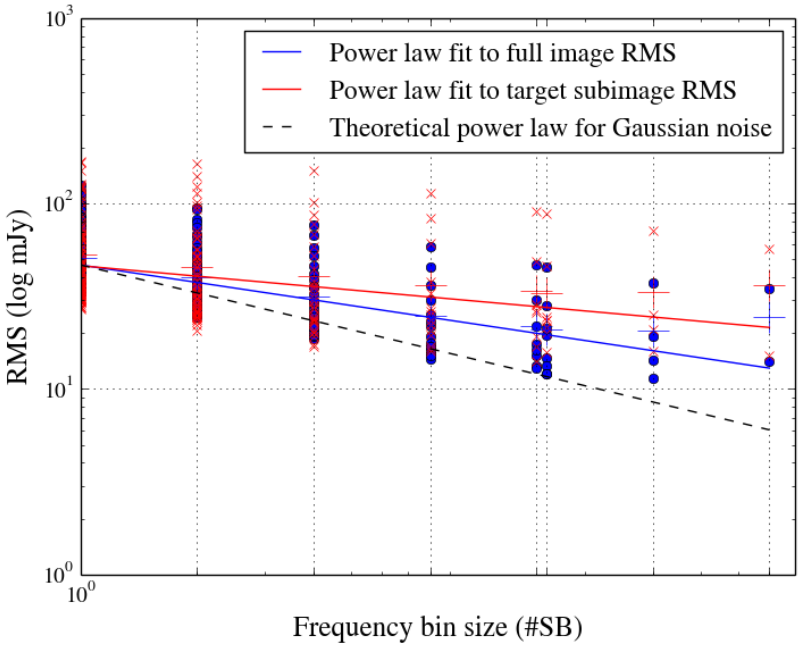

Figure 5-13: RMS values for frequency binned images. The red points are the RMS value for the small subimage (15 x 15 beams) at the center of the image (where HD 80606 should be). The blue points are the RMS for the full image (2048 x 2048 pixels, ∼7 degrees). The large "+" markers represent the average of each cluster. The solid lines represent power law fits to the data and the dashed line is a theoretical power law fit for Gaussian noise (slope = -0.5).

position of the extragalactic source (indicated by pink +).

5.5 Results

5.5.1 Upper Limit on HD 80606 b Radio Luminosity

We obtain an upper limit of $5.6 \cdot 10^{23}$ ergs/s on the radio luminosity of HD 80606 b at 52 MHz for Epoch 1 (48 hours pre-periastron). This value is derived from the noise level obtained using the full time and bandwidth of the observation (6 mJy). Jupiters luminosity is about $2{\cdot}10^{18}$ ergs/s, assuming bandwidth ∼40 MHz ($\sim 5.6{\cdot}10^{11}$ ergs/s/Hz). Even assuming that HD80606 would be brighter than Jupiter by a factor of 3000 because of the increased stellar wind flux during HD 80606bs periastron passage [170], the upper limit is still two orders of magnitude brighter than the planet

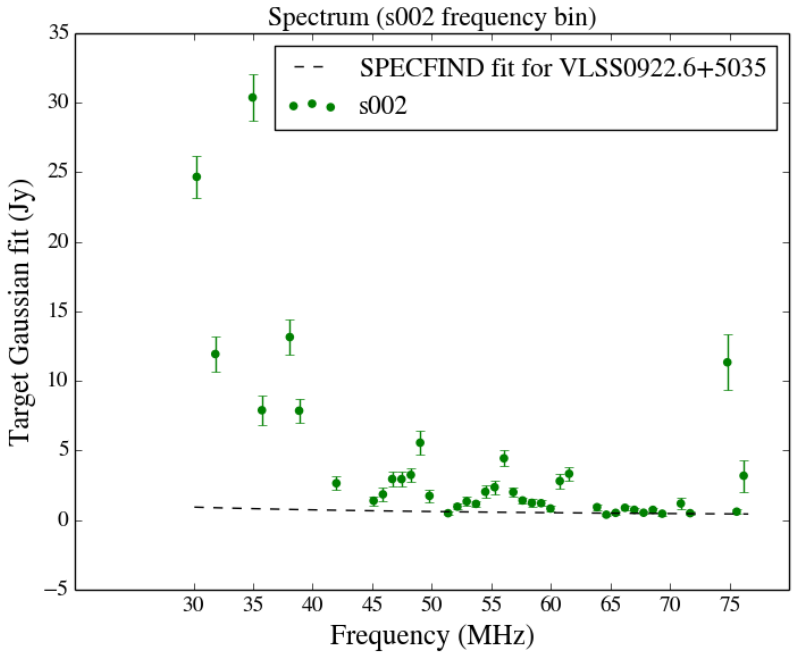

Figure 5-14: Spectrum of central subimage using 2 subband binning. Expected spectrum for VLSS extragalactic source is shown as a dashed curve.

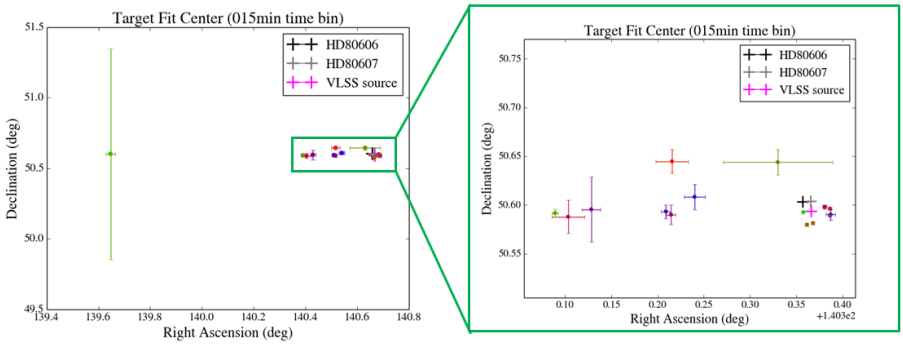

Figure 5-15: Source positions for 2 subband frequency binning. The left image shows all fits across the spectrum. The right image is a zoom-in of the green box on the left image. The color of the fits represents the frequency of the image that they are derived from blue at the low frequency end of the spectrum, green toward the center, and red at the high frequency end. Positions of HD 80606, HD 80607, the binary companion of HD 80606, and the VLSS extragalactic source are shown with + markers for reference.

is expected to be. Nevertheless, this limit is the lowest limit to date at this frequency.

5.5.2 Limit on HD 80606 b Magnetic Field Strength

Since we made no detection of planetary radio emission, we can only set upper limits on HD 80606 b's magnetic field strength and radio flux/luminosity (Figure 5-16). The central frequency of the observation, 52 MHz, corresponds to a magnetic field strength of 18.6 Gauss (see Eq. 1.1). This is only slightly larger than Jupiters magnetic field strength (14 G, as calculated from Jupiter's cut-off frequency of about 40 MHz). Without a detection, it is impossible to say if HD 80606 b's magnetic field is weaker than this value and there is no emission in our observational band, or if its luminosity is simply too small to be detected in this observation.

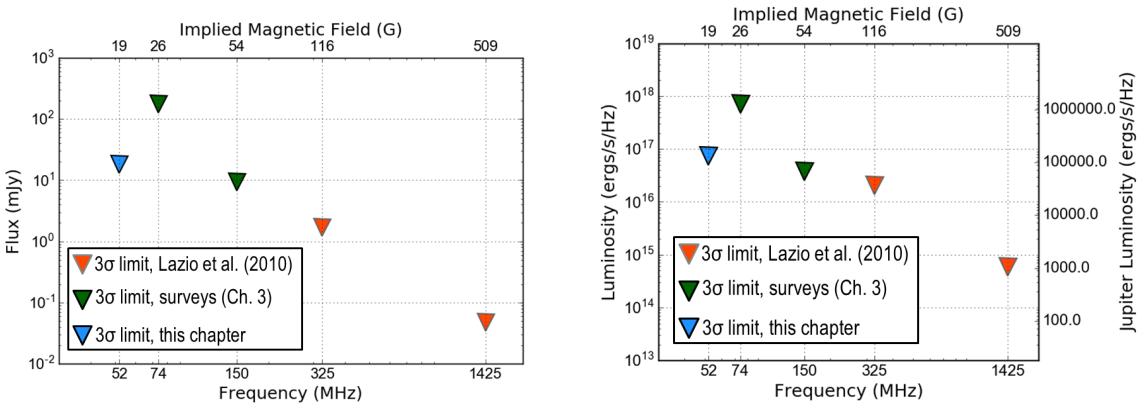

(a) Flux limits

(b) Luminosity limits

Figure 5-16: Flux (a) and luminosity (b) limits for HD 80606. Red downward triangles represent limits from VLA measurements by Lazio et al. (2010) [170], green downward triangles represent limits derived from survey data (Chapter 3), and the blue downward triangle represents the limit obtained from LOFAR data as described in this chapter. The top horizontal axis on both plots indicates the magnetic field strength implied by the observing frequency assuming that emission is at the cyclotron frequency (see Equation 1.1). The right hand vertical axis on panel b compares the luminosity values on the left vertical axis with Jupiter's luminosity at ∼30 MHz.

5.5.3 Time and Frequency Variability

We detected no time or frequency variability in the region containing HD 80606 b and the contaminating background source.

5.6 Discussion

5.6.1 Interpretation of Non-detection

There are several explanations for non-detection that must be considered. Solar system examples of CMI emission are strongly beamed, so the emission beam from HD 80606 b may not cross Earth's line of sight. Alternatively, HD 80606 b may have a much weaker magnetic field than expected, so the peak emission frequency would lie below the observation band. The stellar corona could conceivably absorb any planetary radio emission since HD 80606 b was headed toward occultation during this epoch. Finally, it is possible that even with a strong magnetic field and favorable beaming, conversion of stellar wind kinetic/magnetic energy to planetary radio emission is very inefficient and results in a signal that is below the noise floor of this observation.

We can conclude that, during Epoch 1, HD 80606 b did not exhibit extreme radio luminosity that would correspond to an intrinsic radio luminosity >10x Jupiter's enhanced by several orders of magnitude by high density stellar wind. As mentioned in Section 5.3, extreme conditions must be invoked for HD 80606 b to even get close to a predicted flux that would be detectable by LOFAR. Though the limits set in this work are the lowest obtained to date at the frequencies considered, they are not low enough to rule out a magnetic field for HD 80606 b or constrain the effect of close periastron passage on planetary radio emission. The distance to HD 80606 is the biggest problem, suggesting that closer systems should be observed.

5.6.2 Ongoing and Future Work

There are several Jupiter-mass planets with high eccentricity in the Northern sky (although none as eccentric as HD 80606). HD 17156 [12] and HD 156279 [75] are the top choices for LOFAR observations. HD 156279b is larger than HD 80606 b and also closer, although it does not transit. Both its size and distance make HD 156279 b the most promising candidate for observing enhanced radio emission during periastron.

HD 17156 b is a very close analog to HD 80606; it has nearly the same mass and radius (observed via transit), but it is farther away. Neither of these systems has known background sources within 10 arcmin in VLSSr, eliminating the problem of a contaminating background source.

We[2] proposed for and received 90 hours of LOFAR time in Cycle 4 to observe these two targets and to reobserve HD 80606 b. HD 80606 was included despite its distance and the background source because many of the LOFAR issues that reduced sensitivity in the Cycle 0 data discussed above have since been mitigated, allowing for improved limits with new data. Each target was observed for five 6-hour epochs. As with the Cycle 0 HD 80606 b observations, four of the five epochs were concentrated around periastron (two before, two after) and one epoch was near apastron. Some HD 80606 b observations were broken into pieces to accommodate other scheduled observations. Data analysis for the Cycle 4 campaign is in progress. Initial results from the PiLL pipeline (see Chapter 2) for a sample 2 hour observation reach an RMS of 6 mJy at the center of the image, slightly better than the two hour blocks of Cycle 0 data.

The raw data from the Cycle 0 campaign was fortuitously discovered in the LOFAR Long Term Archive (LTA). Both calibrator and target observations are available, allowing for reprocessing using new tools and the benefit of several years of LOFAR data experience. The raw data has been preprocessed to remove the contribution of bright A-team sources and flag the data comprehensively. The re-preprocessed observations are also being processed using the PiLL pipeline. All of the eccentric planet data will be processed in the manner described above once preprocessing and calibration are finished. Additionally, imaging and post-processing will be done in Stokes V (circular polarization).

[2] J. Lazio (PI), M. Knapp, D. Winterhalter, W. Farrell

5.7 Conclusion

HD 80606 b, a highly eccentric hot Jupiter at 58 pc, has been observed before and after periastron with the LOFAR LBA telescope from 30–75 MHz. Analysis of one 6-hour epoch out of five observation epochs (48 hours pre-periastron) detected no radio emission from HD 80606 b. A novel time/frequency splitting approach was used to search for time-variable planetary radio emission. RMS image noise for the full integration time and bandwidth was 6 mJy, setting a 1-σ upper limit on HD 80606 b's radio luminosity of $5.6 \cdot 10^{23}$. Though this limit is the lowest to date at 30–75 MHz, it is still $\sim$2 orders of magnitude higher than the predicted luminosity of HD 80606 b during periastron passage. The most likely explanation for the non-detection of HD 80606 b is that its distance is too great to allow for detection with current ground-based observatories. A new observing program has been designed and carried out to observe an analog of HD 80606 b (HD 156279 b) that is a factor of $\sim$2 closer to the Earth, increasing the chances of a detection or more constraining upper limits. Reduction of these new observations as well as re-processed Cycle 0 data are currently underway.

Chapter 6

TRAPPIST-1: Radio Observation Strategy and Thermal Evolution Modeling

The TRAPPIST-1 (T1) system is the best opportunity to date for detecting the magnetic fields of Earth-sized planets, either directly or indirectly, and adding to the small sample of measured magnetic fields of terrestrial bodies. This chapter describes an observing strategy for T1 that could also be applied to similar nearby systems that are likely to be discovered in the near future. Section 6.3 describes the first steps on the path toward theoretical predictions for rocky planet magnetic fields that can be tested with observations of these nearby systems.

6.1 TRAPPIST-1 System

The recently discovered TRAPPIST-1 system [110, 111] is extraordinary in a number of ways. First, it is nearby (12 pc) compared to most other known exoplanet systems, enabling detailed follow-up across the EM spectrum. Proximity is especially important for radio observations since the expected signal strengths from planetary or star-planet interactions are weak (see Section 1.3.3. Second, all the planets in the system (so far) are close to Earth-sized (see Table 6.1), providing a laboratory for

studying the formation and evolution of Earth-sized, potentially rocky planets at a range of stellar distances and insolations. Three of the TRAPPIST-1 planets (e, f, g) are in the 'habitable zone', defined as the range of planetary equilibrium temperatures that would permit surface liquid water [151]. Third, the TRAPPIST-1 system resembles the Galilean moon system of Jupiter in several important ways.

The orbits of T1-b and T1-c, the innermost two planets, resemble the inner two Galilean moons (Io and Europa) in that the planets/moons are just outside the corotation point (vertical dashed line in Figure 6-1) with their parent body, so the parent body's magnetic field drags across the planets/moons. The mass ratios between the parent and satellites are similar as well. Most importantly, T1-b and T1-c may experience significant tidal heating like Io and Europa [183]. If the tidal heating calculations for T1-b and T1-c are correct, one or both may be volcanically active like Io. As described in Section 1.2.4, Io's volcanic outflow adds a large volume of plasma to Jupiter's magnetosphere and drives a major component of Jupiter's radio emission via the Io flux tube. Zarka (2007) [334] describes in detail how either an 'unmagnetized' planet (no intrinsic, global magnetic field) or a magnetized planet (global, dynamo magnetic field) could enhance and modulate the radio emission of the host star. In the case of TRAPPIST-1, a M8 dwarf with a magnetic field of 600±200 Gauss [243], stellar radio emission via the electron cyclotron maser instability (CMI) mechanism, would be detectable by ground-based telescopes at frequencies ranging from ∼30-300 MHz, depending on where the radio emission originates in the stellar corona.

This chapter describes an observational strategy aimed at detecting (or setting limits on) the magnetic fields of the inner two TRAPPIST-1 planets (T1-b and T1-c, see Section 6.2). The observational program is designed to search for either planet-modulated stellar radio emission or emission from the planets directly. Section 6.3 describes thermal evolution modeling of T1-b and T1-c to investigate the thermal history parameter space of these two planets and attempt to constrain when in their history a thermal dynamo magnetic field was most likely. The estimated tidal heating for both planets is added to the baseline thermal evolution model to examine what effect extra internal heat would have on thermal dynamo generation.

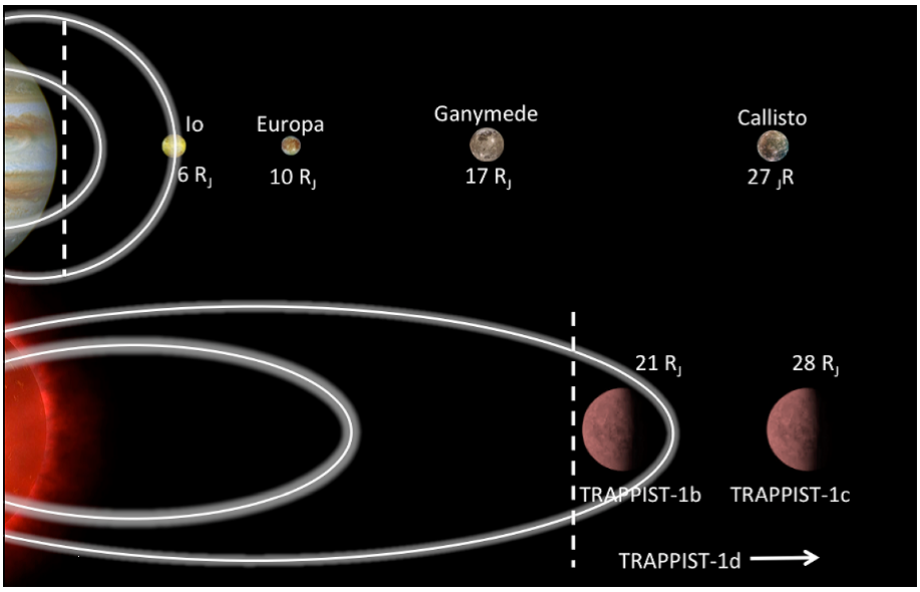

Figure 6-1: Comparison of the Galilean moon system of Jupiter to TRAPPIST-1b, c. Figure credit: Adam Burgasser

Table 6.1. TRAPPIST-1 planet properties

Planet	Period (days)	Radius ($R_\oplus$)	Mass ($M_\oplus$)	Bulk Density ($\rho_\oplus$)	Semi-major axis (10^{-3} AU, $R_\star$)	Irradiation ($S_\oplus$)	Equil. Temp. (K)	Incl. (°)	Ecc.
b	1.51087081 $\pm 0.6\cdot10^{-6}$	1.086 ±0.035	0.85 ±0.72	0.66 ±0.56	11.11 ± 0.34, $20.50^{+0.16}_{-0.31}$	4.25 ±0.33	400.1 ±7.7	89.65 $^{+0.22}_{-0.27}$	<0.081
c	2.4218233 $\pm0.17\cdot10^{-5}$	1.056 ±0.035	1.38 ±0.61	1.17 ±0.53	15.21 ± 0.47, $28.08^{+0.22}_{-0.42}$	2.27 ±0.18	341.9 ±6.6	89.67 ±0.17	<0.083
d	4.049610 $\pm0.63\cdot10^{-4}$	0.772 ±0.030	0.41 ±0.27	0.89 ±0.60	$21.44^{+0.66}_{-0.63}$, $39.55^{+0.30}_{-0.59}$	1.143 ±0.088	288.0 ±5.6	89.75 ±0.16	<0.070
e	6.099615 $\pm0.11\cdot10^{-4}$	0.918 ±0.039	0.62 ±0.58	0.80 ±0.76	$28.17^{+0.83}_{-0.87}$, $59.97^{+0.40}_{-0.77}$	0.662 ±0.051	251.3 ±4.9	89.86 $^{+0.10}_{-0.12}$	<0.085
f	9.206690 $\pm0.15\cdot10^{-4}$	1.045 ±0.038	0.68 ±0.18	0.60 ±0.17	37.1 ± 1.1, $68.4^{+0.5}_{-1.0}$	0.382 ±0.030	219.0 ±4.2	89.680 ±0.034	<0.063
g	12.35294 $\pm0.12\cdot10^{-3}$	1.127 ±0.041	1.34 ±0.88	0.94 ±0.63	45.1 ± 1.4, $83.2^{+0.6}_{-1.2}$	0.258 ±0.020	198.6 ±3.8	89.710 ±0.025	<0.061
h	18.764 $^{+0.008}_{-0.009}$	0.715 $^{+0.047}_{-0.043}$	—	—	63^{+27}_{-13}, 114 ± 5	0.131 $^{+0.081}_{-0.067}$	169 ±4	89.8 ±0.3	—

Note. — Table reproduced from [111], data for TRAPPIST-1h updated from [183].

6.2 LOFAR Observations[1]

The TRAPPIST-1 system is an appealing target for radio observations given its proximity, bounty of planets, and strong, active stellar magnetic field. The potential for Io-Jupiter type interaction increases the chances of detectable planetary signatures significantly since the star's radio emission, which would be modulated by the planet(s), should be well within the observable frequency range for ground-based low frequency instruments like LOFAR. We[2] proposed for and were awarded 73 hours of LOFAR Cycle 6 LBA and HBA time to observe the TRAPPIST-1 system as part of a multi-wavelength follow-up campaign. The observational motivation and strategy are discussed below. Data reduction is in progress, but not far enough along to report fully here.

The T1 LOFAR observing campaign has three goals:

1. Search for Io-Jupiter analog star-planet interaction

2. Search for auroral cyclotron radio emission from any of the T1 planets

3. Characterize the host star and interplanetary medium via detection of radio flares and/or Type II radio bursts, which are correlated with coronal mass ejections (CMEs)

The experiment design is motivated by the first goal. In the case of non-detection, the observations can be used to set physically meaningful limits on radio emission from T1 and any planets in the system. The broad frequency coverage of LOFAR LBA+HBA (30–75 MHz, 110-185 MHz) corresponds to cyclotron emission from magnetic fields ranging from 10–68 G. This range covers Jupiter-like magnetic fields to stellar magnetic fields.

[1] Some text in this section was adapted from LOFAR proposal LC6_007 (PI: M. Knapp)

[2] M. Knapp (PI), A. Burgasser, M. Gillon, J. de Wit, D. Queloz, B. Demory, E. Jahin, S. Lederer, L. Delrez, A. Burdanov, V. van Grootel, A. Triaud, P. Magain, C. Melis

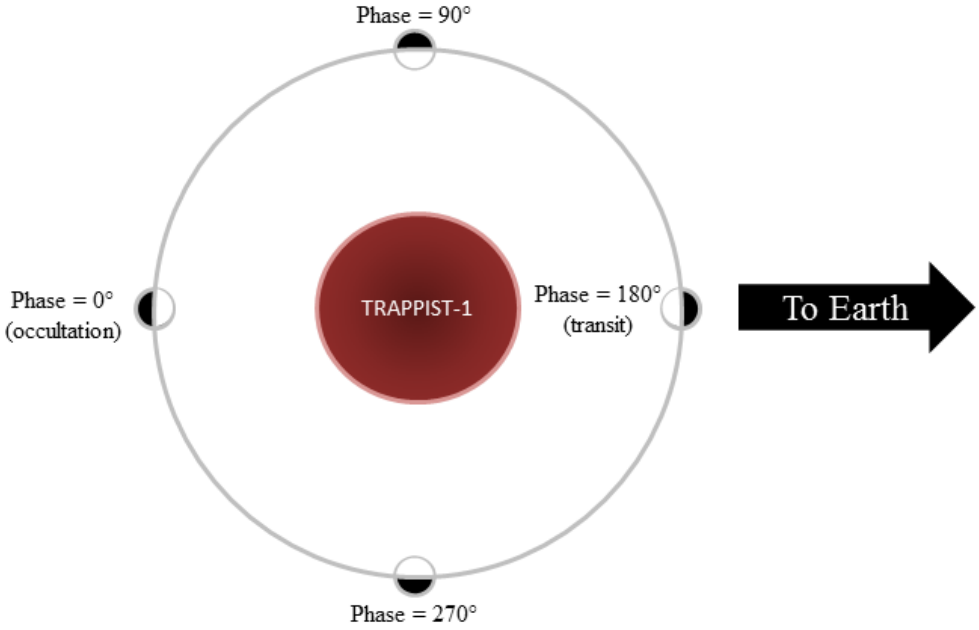

Figure 6-2: Phase point observations for TRAPPIST-1 b or c (not to scale).

6.2.1 Observational Strategy for Detecting Star-Planet Interaction (Io-Jupiter Type)

Planet-modulated stellar radio emission (Io-Jupiter type) offers the best chance of indirectly constraining planetary magnetic fields. The key is that only the stellar radio emission must be detected, not the (presumably weaker and lower frequency) planetary radio emission. Any planet, whether it has a global dynamo magnetic field or not, can alter the radio emission of the host star through either the 'bipolar inductor' or 'unipolar inductor' interaction modes (see Section 1.2.4). The cross-section of the body and its distance from the host star determine the size of the stellar radio emission modulation [334]. A magnetosphere generated by an intrinsic dynamo magnetic field would be a larger obstacle than the planet's solid radius alone would predict, yielding an anomalously large effect on stellar radio emission. Given the known radii and orbits of the T1 planets, such an anomaly would be straightforward to detect if stellar radio emission is found to be modulated at one or more of the T1 planet periods.

We observed the T1 system at four phase points the orbits of T1-b and T1-c: occultation (phase = 0°), phase = 90°, transit (phase = 180°), and phase = 270° (see Figure 6-2). Io-related Jovian emission shows a strong dependence on Io-phase, so *variations in emission as a function of phase will be indicative of star-planet interaction as the source.* Observations during occultation (phase=0) are longer (3 hrs LBA, 1 hr HBA) in order to isolate the contribution from the planetary dayside. Lecavelier des Etangs et al. (2013) [173] used the occultation method to search for auroral radio emission from HAT-P-11 using GMRT at 150 MHz and obtained intriguing but low significance results. The other three phase points (90°, 180°, 270°) are observed for 2 hours (LBA) and 30 minutes (HBA) each. The same sequence of observations were performed at the four phase points for both TRAPPIST-1b and TRAPPIST-1c. Since all four of the Galilean satellites influence Jupiters radio emission, it is reasonable to assume that at least the inner two planets of the TRAPPIST-1 system may contribute to star-planet interaction-related radio emission. We are not aware of any other radio exoplanet observations that have used this phase-targeted observation strategy to look for star-planet interaction. This strategy is an optimal compromise between the uninterrupted full orbit coverage that is desirable and the constraints of oversubscribed observatories and the rising/setting of this low declination target.

6.2.2 Prospects for Direct Planetary Radio Detection

The second goal of the LOFAR T1 is to search for planetary cyclotron emission directly. If one or more of the planets has a particularly strong magnetic field (on the same order as Jupiters surface field strength, ∼10 G), it will exhibit auroral cyclotron-type radio emission as a result of stellar wind-magnetosphere interaction at a frequency detectable from the ground [17]. The intensity of auroral radio emission should be significantly enhanced by the high kinetic and magnetic stellar wind flux at ∼20–30 stellar radii according to the radiometric Bode's law (Section 1.2.3), which scales emitted radio power as $(d/d_{Jup})^{-1.6}$, where d is the planets semi-major axis and d_{Jup} is Jupiters semi-major axis of 5 AU. Assuming a magnetic field strength similar to Jupiter, the radiometric Bode's law plus scaling for distance to T1 (12 pc) predicts

a flux at Earth of 6 mJy for T1-b. Flux of 6 mJy would be difficult to detect with the LOFAR LBA since current work has only achieved noise levels of a few mJy in the best cases, but detection at this level is within the realm of possible, especially with better ionospheric removal. This calculation assumes the host star is the Sun, so the much larger magnetic field and stellar wind of T1 could cause the flux to increase by an order of magnitude or more, allowing for more robust detection with LOFAR LBA.

The observational signature of auroral radio emission is a relatively flat spectrum ending in an abrupt cut-off corresponding to the local electron cyclotron plasma frequency in the emission region (see Figure 1-1). Even if the magnetic fields of the T1 planets are too weak to emit at frequencies accessible from the ground, LOFAR LBA observations will set physically meaningful upper limits on their radio luminosity and magnetic field strength. The nearness of this system, strong tidal heating of the planets, 'equator on' orientation of the system, and high density stellar wind at the location of the planets all suggest that the T1 system may offer one of the best chances yet to detect the magnetic field of an Earth-sized exoplanet via radio emission.

6.2.3 Prospects for Observing Stellar Flares

The proposed observations will also indirectly probe the interplanetary medium of the TRAPPIST-1 system. Optical flares have been detected at a rate of 1 per 50 hrs [110], later refined with K2 data to 0.38 per day [183]. One massive K2 flare briefly doubled the brightness of the star. If a flare happens during the observations, it may be possible to detect analogs to Type II or Type III solar bursts. This would, by itself, be a significant discovery since there has not yet been a detection of a Type II/III burst or CME from any star but the Sun. Type II bursts, in particular, are thought to trace the path of a CME-driven shock as it propagates outward through the interplanetary medium [115]. The rate and strength of flares and CMEs is critical for understanding atmospheric evolution and photochemistry of the TRAPPIST-1 planets [153, 258]. Disentangling stellar radio emission from planetary radio emission is a key challenge. We will use a combination of polarimetry, orbital phasing, and

timing/periodicity to sort out various sources of radio emission. Any radio detection from the TRAPPIST- 1 system would be a significant result, since low frequency radio emission from late-M-dwarfs is poorly studied and no radio emission from an exoplanet, Earth-sized or larger, has been detected to date.

6.3 Influence of Tidal Heating on Dynamo Initiation and Maintenance[3]

6.3.1 Tidal Heating in the Solar System

The effect of a non-homogeneous planet/moon interior on tidal heating was investigated by Peale & Cassen (1978) [230]. Peale & Cassen used a two-layer model with a 'soft' lunar core (low rigidity μ) and a 'hard' lunar mantle (high rigidity). Dissipation in the inner 'soft' or liquid (low rigidity, low viscosity) region was found to be negligible compared to dissipation in the 'hard' outer shell. They found that there was significantly higher dissipation ($\sim$3–15x) in the two-layer case than the homogeneous case even though the total volume being heated (the outer mantle) was smaller. The enhancement in dissipation grows as the thickness of the outer layer shrinks. Peele & Cassen suggested that a melting run-away could occur if the hot bottom of the mantle melted due to high tidal dissipation, shrinking the mantle and increasing dissipation in the now-thinner mantle. They suggest that such an effect could have melted the whole lunar mantle and caused widespread volcanism. In a subsequent paper [231], they predicted (correctly) that Io's extreme tidal forcing gives rise to extensive volcanism due to melting in the mantle.

The two-layer interior model assumes that rheological parameters do not vary across the layer, which is unphysical. Density (ρ), viscosity (η), and shear modulus (μ) vary with temperature and pressure and therefore with depth. More recent multi-layer modeling of the Moon [130] has suggested that most tidal dissipation in the present-day Moon is confined to a thin, relatively low viscosity layer at the bottom of

[3]This work was done in collaboration with Vlada Stamenkovic

the mantle. In the case of the Moon, this layer may be acting as a "thermal blanket", slowing lunar core cooling. A similar effect may be at work in Io's asthenosphere [257]. In layers like Io's aesthenosphere or the bottom of the lunar mantle, there may be a stable equilibrium point where heat transport via convection or melt movement balances temperature/viscosity-dependent tidal dissipation [257, 95, 314, 201].

Henning & Hurford (2014) [133], using multi-layer models, demonstrated that "viscosity maxima translate into dissipation minima". The converse, that viscosity minima in *solid* layers correspond to dissipation maxima, is also true. Soft, lower viscosity solid layers dominate the total dissipation in an Earth-like layered planet. Liquid or mostly melted[4], layers have essentially no dissipation. Figure 4 from [133], reproduced here as Figure 6-3, shows strong peaks in dissipation in lower density solid regions, particularly the D'' layer above the liquid outer core and the lower viscosity upper mantle. Dissipation is higher for the multi-layer models than the homogeneous case (solid black curve).

In the work described below, we take the insights gained from observation of tides in Solar System bodies and multi-layer tidal dissipation modeling and apply them to the TRAPPIST-1 planets. We confine our modeling to the inner two planets, T1-b, T1c, and assume that these planets do not have a significant water ice shell or deep oceans. Surface oceans and ice shells will significantly reduce the tidal dissipation in the silicate part of a planet [133]. We assume that TRAPPIST-1b–c are Earth-like in composition (silicate mantle, iron core) and relatively dry with no significant surface oceans, though we do not rule out hydrated minerals in the mantles.

6.3.2 Necessary Conditions for a Dynamo

Magnetic dynamos in rocky, Earth-like planets are generated in the electrically conducting liquid metal (usually iron) core. A dynamo is the steady-state amplification of a seed magnetic field via magnetic induction due to the organized helical motion of

[4]According to Henning & Hurford and references therein, silicates behave like a solid in terms of viscosity and shear modulus until reaching a temperature about halfway between the solidus and liquidus temperatures. Once a silicate reaches 40%–60% melt fraction, it begins to behave like a liquid for the purposes of tidal dissipation.

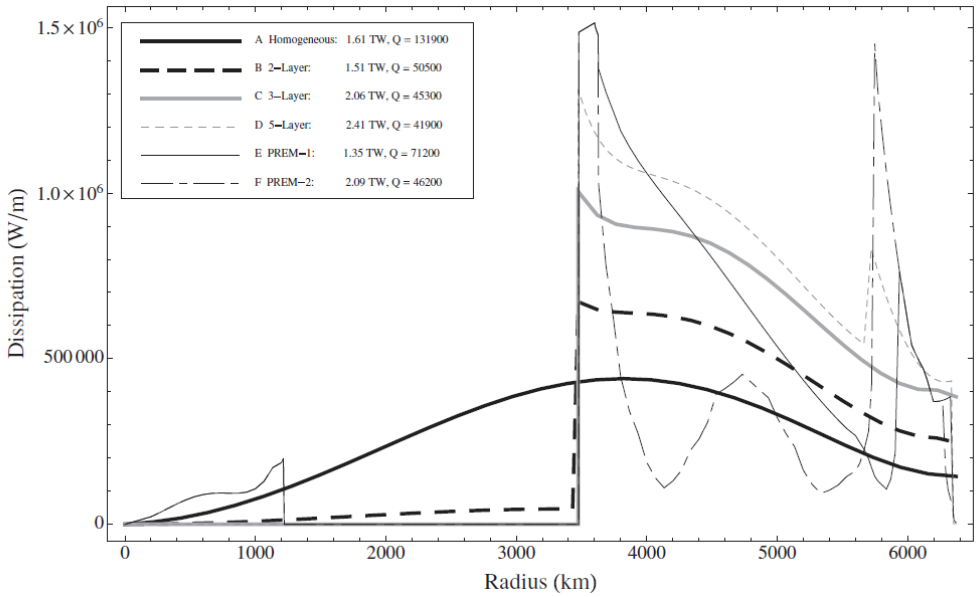

Figure 6-3: Tidal dissipation in a multi-layered Earth-like planet. Lower density solid layers, like the D'' layer above the Earth's outer core, dominate tidal dissipation. Reproduced from [133], Fig. 4

an electrically conductive fluid caused by convection paired with rotation [227, 112]. The rotational motion is imposed on the liquid metal core by planetary rotation. Rotation is not required to be fast for a planet with a liquid core to have a dynamo; even Venus's slow rotation is sufficient to sustain a dynamo *if* the core is also convecting [277]. See [50, 224, 51] for a discussion of the role of rotation on magnetic field topology and strength. Convection, the second ingredient necessary for a dynamo, can be driven thermally or compositionally. Thermal convection is driven by the buoyancy of hot material and is favored when the thermal gradient is sufficiently steep that the density stratification in the fluid becomes unstable. The dimensionless Rayleigh number is used as a proxy to determine whether a layer is unstable to convection. See [273], Eq. 25 for the critical Rayleigh number which determines whether a layer in the thermal evolution model is convecting or not.

Compositional convection is driven by composition-dependent buoyancy and can be driven either 'bottom up' (Earth) or 'top down' (Ganymede). In the 'bottom up' case, which is believed to be relevant to the Earth's core and possibly other Earth-sized bodies, heavy elements (iron, nickle) crystallize onto the inner core as the outer

core cools, leaving lighter, more buoyant material (sulfur) behind at the bottom of the outer core that tends to rise (see [277], references therein). In the 'top down' case, relevant to smaller planets/moons like Ganymede, iron condenses out of the Fe-S solution near the CMB and precipitates downward where it eventually remelts and mixes convectionally with the Fe-S solution in the deep core [249]. The amount of sulfur in solution with iron in the core as well as the relative slopes of the temperature gradient and the iron melting point gradient, which is pressure-dependent, determine whether 'top down' compositional convection is possible [49].

In this work, we focus on identifying the conditions in the core that favor or disfavor thermally driven dynamos only. As long as the core is cooling (DI>-1, see below), however, a compositional dynamo *may* be active. We do not make any predictions about compositional dynamos beyond identifying the conditions under which it is physically possible for one to exist.

6.3.3 1D Thermal Evolution Model

The thermal evolution model used to investigate the effect of tidal heating on T1-b and T1-c was developed by Vlada Stamenkovic [272, 273]. The Stamenkovic model is a 1D parameterized convection model that has been validated against a 2D spherical shell convection model. The advantage of a 1D parameterized model is that it runs very quickly, allowing for fast filling of the input parameter space and long evolution times. The model evolves forward in time from initial conditions of mantle temperature and core temperature. The planet is assumed to be differentiated at the beginning of model time and its core fraction (by mass) is set. The planetary radius and core radius are derived from the input planet mass according to [291]. The model allows for either a 'stagnant lid' (SL) lithosphere with no moving plates or a 'plate tectonics' (PT) lithosphere. This choice controls the heat flow out of the mantle and therefore out of the core. The model input parameters are listed in Table 6.3.3. Another key feature of this model is the option to use a pressure- and temperature-dependent rheology (set by V^*_{eff}) [272], which has a large effect on mantle viscosity with depth and therefore ability to convect and remove heat from the core. If viscosity depends only

Table 6.2. Thermal evolution model parameters

Parameter	Description	Range	Units	Earth Value
M	Planet mass	0.5, 1, 1.5, 2	$M_\oplus$	1
T_{evolve}	Evolution run time	8000	Myr	4600
STRUCTURE	Planet structural type	ELSE*	—	ELSE
F_Q	Radiogenic heat flux rel. to Earth	1	1	
T_S	Surface temperature	400 (T1-b), 342 (T1-c)	K	288
MODE	Tectonic mode	PT, SL	—	PT
MELT	Mantle melt generation on/off	ON	—	ON
$T_m(0)$	Initial mantle temperature	Melt	K	??
$T_c(0)$	Initial core temperature	Melt	K	??
η_0	Reference viscosity (T=1600 K, P=0)	10^{19}, 10^{21}	Pa s	10^{21}
A	Activation energy	240, 300	kJ mol^{-1}	300
V^*_{eff}	Activation volume for upper mantle (sets pressure dependence of viscosity)	0, 2.5	cm^3 mol^{-1}	??
Fk_m	Mantle thermal conductivity scaling factor	1	—	1
$F\alpha_m$	Mantle thermal expansivity scaling factor	1	—	1
Fc_m	Mantle heat capacity scaling factor	1	—	1
Q_{tide}	Tidal heat input	10, 1, 0.1, 0	W m^{-2}	

Note. — Some values adapted from [274], Table 1 (see for additional references). The Range column indicates the values used in the TRAPPIST-1 evolution models.

*'Earth-Like Super Earth', a structure with the same core/mantle fractions as the Earth.

on temperature, the mantle becomes less viscous with increasing depth. If viscosity is also pressure-dependent, the opposite is true. Additional details can be found in [273].

The Stamenkovic thermal evolution code calculates a 'Dynamo Index' (DI) at each timestep. The dynamo index is a measure of whether thermally driven convection is expected in the core. Thermal convection is expected if the heat flux through the CMB exceeds a critical value (see [273], Eq. 2). If this condition is met, the dynamo index is 1, meaning that a thermally driven dynamo is expected. No calculation of the expected magnetic field strength or topology is made. If the heat flux is below the critical value but still positive (the core is cooling), the dynamo index is 0. A DI of 0 means that a thermal dynamo is disfavored, but a composition-driven dynamo is still possible. The model used for this work does not consider inner core nucleation or growth through crystallization. In the final case, DI=-1, the core is heating rather than cooling, so no dynamo of either type is possible.

The Stamenkovic model was used to calculate the dynamo index as a function of time and planet mass for several sets of conditions with varying tidal heating

values. Tidal heating was added to the mantle as an extra heat source similar to radiogenic heating, though constant through time. We assumed that, even if tidal heat deposition takes place in a thin layer of minimum solid viscosity, mantle convection will distribute the tidal heat throughout the mantle relatively quickly. Limitations of that assumption are discussed in Section 6.4. Each model was evolved from initial conditions to 8 Gyr[5].

The set of parameters varied in the thermal evolution models was restricted to focus on the effect of tidal heating specifically. All parameters were fixed at Earth-like values (Table 6.3.3) except for mass and η_0, which approximates whether the mantle is contains hydrated minerals or not ('wet' vs. 'dry'). The activation volume V^*_{eff}, which represents the pressure dependence of viscosity, was fixed at $V^*_{eff} = 2.5$, which yields a moderately temperature- *and* pressure-dependent viscosity (see [273], Eq. 7). The pressure- and temperature-dependent case was chosen because it is more likely to be physically realistic and because it is more compatible with the simplifying assumption that tidal heat is evenly distributed throughout the mantle.

Three masses were chosen from within the error bars of the transit timing variation (TTV) masses in [111]. M=0.5, 1.0, and 1.5$M_\oplus$were used for T1-b; M=1, 1.5, and 2.0$M_\oplus$for T1-c. Recent reanalysis of the TTVs has lowered the mass estimates for some of the planets [305], but the masses tested are still appropriate for T1-b and T1-c. The surface temperature for each planet is the equilibrium temperature listed in Table 6.1. A range of tidal heat fluxes are considered based on [183], Figure 7. The highest tidal heat flux modeled, 10 W m^{-2}, is comparable to that of Io ($\sim$3 W m^{-2}).

Figure 6-4 shows the results of a thermal evolution model run with all Earth-like parameters for 6 Gyr for reference in interpreting the results in Figures 6-6, 6-7. The left panel shows the core and mantle temperatures as a function of time and the right panel shows the dynamo index over the same period. The dynamo index falls to 0 slightly before 4 Gyr, indicating that Earth's present-day dynamo may be more

[5]The age of the TRAPPIST-1 system is uncertain. The discovery paper constrained the age to >500 Myr, but very recent work has suggested that TRAPPIST-1 may be much older, 7.6±2.2 Gyr [39]

compositionally driven than thermally driven [277]. Figure 6-5 shows a similar model, but with the stagnant lid (SL) tectonic mode instead of the plate tectonics (PT) mode. DI drops to 0 faster in the SL case because the mantle cools less efficiently, causing the core heat flux to drop below the critical value sooner.

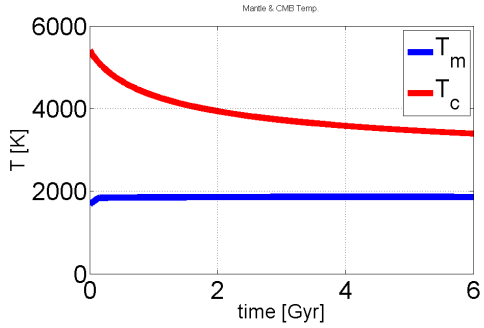

(a) Mantle and core thermal evolution for Earth with plate tectonics

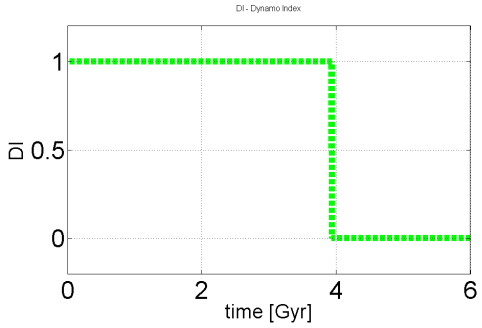

(b) Dynamo index (DI) evolution for Earth with plate tectonics

Figure 6-4: Thermal evolution for Earth with plate tectonics

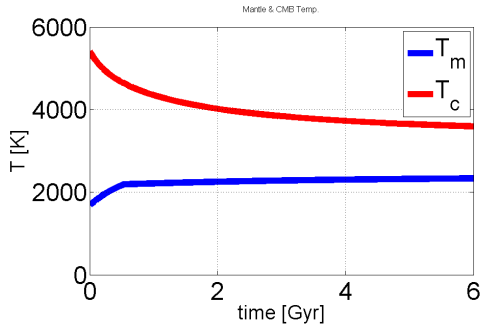

(a) Mantle and core thermal evolution for Earth with stagnant lid

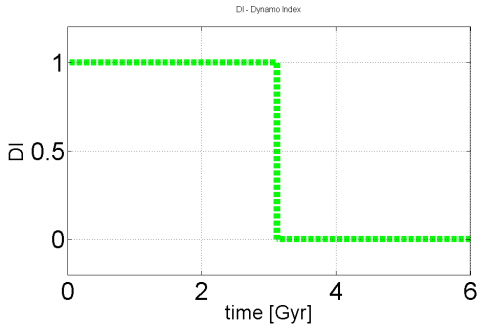

(b) Dynamo index (DI) evolution for Earth with stagnant lid

Figure 6-5: Thermal evolution for Earth with a stagnant lid lithosphere (no plate tectonics).

6.4 Results and Future Work

6.4.1 Results

Thermal evolution modeling showed little dependence on tidal heating, at least for the heating rates studied. Differences in tidal heating did not shift the thermal

dynamo cutoff point (DI=1 $\rightarrow$ DI=0) by more than 1 Gyr in any case. Smaller planets cool faster, causing an earlier thermal dynamo cutoff. Tidal heating has the most influence on the dynamo evolution of stagnant lid planets. This may be because planets with plate tectonics are efficient at removing heat from their mantles already, so the addition of extra heat makes little difference. The addition of extra tidal heat to stagnant lid planets, however, makes their mantles slightly less viscous and allows for more efficient convection. Extra tidal heat may also drive extra melt formation which also extracts heat from the mantle and delivers it to the surface via volcanism. For stagnant lid planets, the addition of tidal heat prolongs the lifetime of a thermal dynamo.

The thermal dynamo cuts off before $\sim$4 Gyr in all cases tested. This is consistent with thermal evolution for the Earth, where compositional buoyancy may be providing at least some of the convection needed to sustain the present-day dynamo. Whether a compositionally driven dynamo could take over from the thermally driven dynamo in the T1 planets depends on the composition of those planets and is beyond the scope of this work. These results highlight the importance of system age when trying to predict whether a rocky planet will have a dynamo. If the T1 system is indeed $\sim$7–8 Gyr old as suggested in [39], this thermal modeling suggests the planets are unlikely to still have dynamo magnetic fields.

6.4.2 Future Work

There are two key additions to the thermal modeling presented here that will be the subject of future work:

1. Improved tidal heating modeling, including coupling the dynamical evolution modeling to evolving interior properties

2. Adding inner core growth and exploring a range of core mass fractions

The tidal heating estimates for the T1 planets assume that each planet is a homogeneous sphere of constant density and viscosity. This simplification is necessary

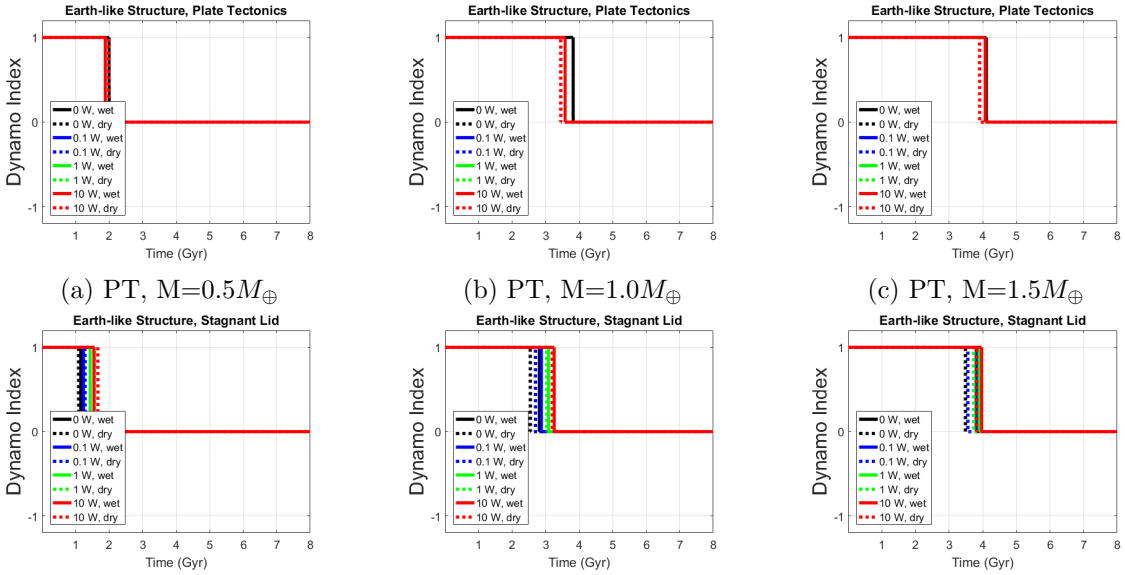

(a) PT, M=0.5$M_\oplus$ (b) PT, M=1.0$M_\oplus$ (c) PT, M=1.5$M_\oplus$

(d) SL, M=0.5$M_\oplus$ (e) SL, M=1.0$M_\oplus$ (f) SL, M=1.5$M_\oplus$

Figure 6-6: Thermal evolution dynamo results for T1-b. Mass increases left to right from 0.5$M_\oplus$to 1.5$M_\oplus$. The top row shows the results for PT tectonic mode, the bottom row shows results for SL tectonic mode. Colored solid lines show DI vs time for a wet mantle, dashed lines show a wet mantle. Tidal heat had a very small effect on the time of thermal dynamo cutoff; the mass and tectonic mode had much larger effects.

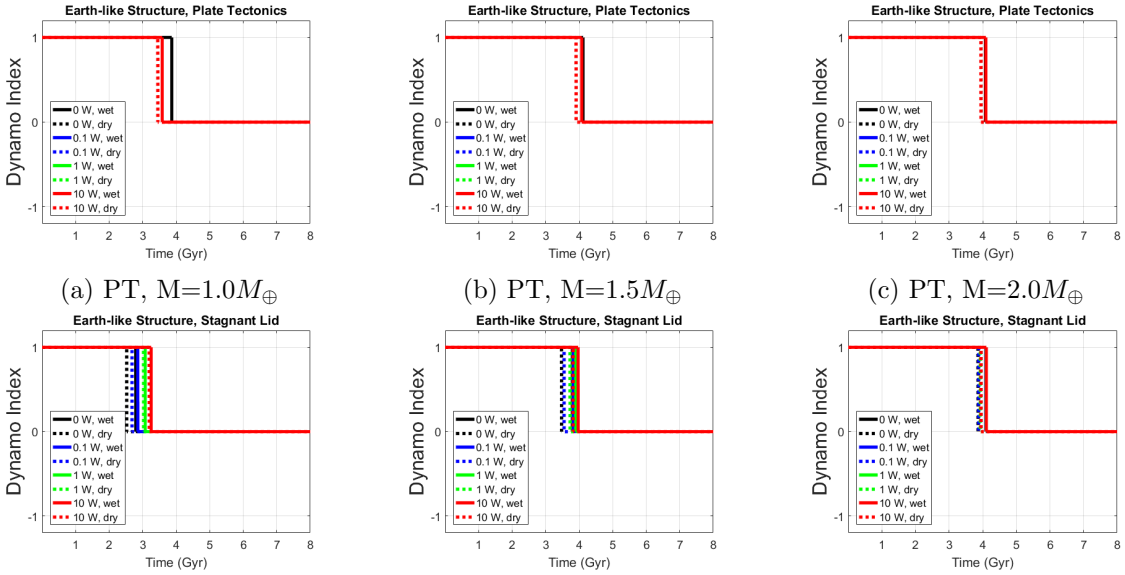

(a) PT, M=1.0$M_\oplus$ (b) PT, M=1.5$M_\oplus$ (c) PT, M=2.0$M_\oplus$

(d) SL, M=1.0$M_\oplus$ (e) SL, M=1.5$M_\oplus$ (f) SL, M=2.0$M_\oplus$

Figure 6-7: Thermal evolution dynamo results for T1-b. Mass increases left to right from 1.0$M_\oplus$to 2.0$M_\oplus$. The top row shows the results for PT tectonic mode, the bottom row shows results for SL tectonic mode. Colored solid lines show DI vs time for a wet mantle, dashed lines show a dry mantle. Tidal heat had a very small effect on the time of thermal dynamo cutoff; the mass and tectonic mode had much larger effects.

to make long dynamical evolution runs tractable in terms of computation time, but it leaves out the effect of rheology changes on the distribution of tidal heat. This approach also does not take into account feedback between the depostion of heat (which depends on the rigidity of the body) and the effect of added heat on the material properties of the body. The location of tidal heat deposition is also not accounted for in either the dynamical evolution modeling or this thermal evolution work. The impact of heat deposition location depends strongly on whether a temperature-only dependent visocsity is used vs. a pressure- and temperature-dependent viscosity. In the case where viscosity only depends on temperature, the lowest viscosity layer will be close to the CMB. If tidal heat is preferentially deposited there, this layer could act like a thermal blanket on the core, impeding cooling. In the pressure- and temperature-dependent viscosity case, the low viscosity layer where tidal heat is deposited will be near the top of the mantle. Here, tidal heat dissipation may drive surface volcanism but will have less effect on core cooling. A pressure- and temperature-dependent viscosity is the more likely physical case, but exploring both options and their effect on a thermal dynamo will inform testable predictions about whether very strongly tidally heated planets can have thermal (or compositional) dynamos. The results of future observations of rocky exoplanet magnetic fields could therefore help to discriminate between different rheological models of rocky planet interiors.

The planetary interior structure was restricted to an Earth-like core fraction in this work to keep the parameter space manageable. A logical next step in this work is to vary the core fraction for a fixed mass (and eventually for a range of masses) to further explore the available parameter space for the interiors of the T1 inner planets. There are no observational constraints on core size (or existence) for the T1 planets, so the parameter space is unconstrained. Adding inner core growth to the evolution of the planets will set limits on the lifetime of compositional dynamos. There can be no dynamo of any kind if the iron core has solidified entirely.

The parameter space for exoplanet interior modeling and evolution is immense. Further additions to the modeling described in this section could include variable elemental/mineral compositions for the mantle, variable sulfur or other light element

contamination of the iron core, and the addition of water and/or ice layers to the surface of the planet. There is also the possibility of transient extreme tidal heating events due to dynamical migration that could partially or totally 'reset the clock' for thermal dynamos by melting some or all of the mantle [231]. Carefully constrained and limited modeling does offer testable predictions, but ultimately observational data are needed to inform more detailed, meaningful modeling of the TRAPPIST-1 planetary interiors, surfaces, and atmospheres.

Chapter 7

The Next Step: Space-Based Observation

Previous chapters have focused on attempts to detect exoplanetary radio emission via ground-based telescopes. Ground-based telescopes have the obvious advantage of being available for use right now and there are exciting advances in low frequency observation. LOFAR [65], MWA [179], and LWA [82, 126] are breaking new ground in ionospheric calibration, RFI excision, and widefield imaging, all critical to achieving higher sensitivity at low frequencies. SKA-Low [63] will make use of these developments while adding significantly more collecting area, further improving the sensitivity of ground-based low frequency telescopes (see Figure 3-25). Ground-based low frequency telescopes, however, are fundamentally limited in several critical ways. This chapter describes those limitations and how they inhibit exoplanet detection, then makes the case for a space-based observatory as a necessary next step and describes a pathfinder mission for space-based radio interferometry at low frequencies.

7.1 Limitations of Ground-Based Low Frequency Observation

The ionospheric plasma frequency fundamentally limits the spectral range accessible to ground-based telescopes. Electromagnetic waves cannot propagate through an ionized medium if their frequency is lower than the local plasma frequency (Eq. 1.2). If the EM frequency is lower than the plasma frequency, electrons in the plasma can move 'fast' enough to counteract the oscillating electric field of the EM wave, effectively screening out the incoming wave. The ionosphere acts like a mirror for incoming radiation below the plasma frequency, a property that is exploited in short wave communication to 'bounce' signals off of the ionosphere so that they can propagate beyond the transmitter's horizon. While useful for communication, the opacity of the ionosphere below the plasma frequency is a low frequency cut-off for astrophysical signals.

The plasma frequency, or cut-off frequency, of the Earth's ionosphere varies temporally and spatially. Generally, the plasma frequency is higher during daytime when the sun is actively ionizing the upper atmosphere and at lower latitudes. The ionospheric cut-off frequency ranges from ∼2–15 MHz depending on location and conditions. Even under the best ionospheric conditions, the radio sky below 1 MHz is inaccessible from the Earth's surface.

Plasma is a dispersive medium - the index of refraction is frequency dependent. Incoming radiation at frequencies approaching the local plasma frequency is strongly refracted. Radio observations slightly above the ionospheric cut-off frequency are therefore possible in theory but extremely challenging in practice (see Section 2.5). The ionosphere is a turbulent medium, so random phase shifts and are imposed on incoming radiation in a frequency-dependent manner. These phase shifts and refractive effects could be corrected if the 3D electron distribution of the ionosphere over an observatory was known as a function of time, but such data are rarely, if ever, available for existing radio telescopes. If the locations and fluxes of many point radio sources are known, the interferometric data can be used to fit a phase screen

for the ionosphere based on the phase errors between the 'model' source positions and measured source positions. This technique is in use at existing low frequency observatories, but requires many bright calibrator sources spread evenly across the sky. Higher sensitivity low frequency telescopes, like LOFAR 2.0 or SKA-Low, will be better able to use this calibration strategy than existing telescopes.

In practice, especially at LOFAR LBA, there are not enough bright calibrators with sufficient signal-to-noise (SNR) in the short time intervals required for calibration of the time-varying ionosphere. If LOFAR LBA sensitivity was increased through the addition of additional stations or expansion of existing stations, the calibration situation would improve, though it would remain computationally expensive. The effect of incomplete or insufficient direction-dependent ionospheric calibration on interferometric images is source position shifts, source shape changes, and higher background noise as a result of uncorrected phase errors. The effects are time variable and behaves like atmospheric 'seeing' at visible wavelengths. Recent work by F. de Gasperin has demonstrated that ionospheric scintillation causes amplitude errors as well as phase errors[1].

In summary, ionosphere-induced errors are very difficult to fully correct for existing arrays using state-of-the-art calibration techniques. This is an active area of research and techniques will likely improve with time, but the ionosphere remains a major barrier to sky-noise limited high sensitivity, high dynamic range low frequency imaging. For example, the theoretical image noise for full bandwidth, 6-hour integration with LOFAR LBA is $\sim$0.5 mJy[2], but the achievable image noise (with current techniques) is 10x the theoretical value. Imperfect ionospheric calibration (and RFI losses) puts even a 100x Jupiter flux planet at 2 pc out of reach (1-σ) for LBA frequencies.

[1] Private communication. Also see Figure 2-3

[2] See https://support.astron.nl/ImageNoiseCalculator/sens.php

7.2 The Promise of Space-Based Radio Interferometry

Observations from space, above the ionospheric peak, would not suffer from ionospheric effects and would not be limited by the ionospheric cut-off frequency. Space-based radio interferometry is therefore the next frontier. A space-based interferometric observatory would open up the last unexplored window of the EM spectrum, enabling a range of science cases from solar flares to the origin of galactic cosmic rays. Most importantly for this work, space-based radio interferometry is necessary to detect Earth-strength exoplanetary magnetic fields. As described in Chapter 1, only Jupiter's magnetic field is strong enough to produce cyclotron emission at frequencies above the Earth's ionospheric cut-off. Detection of radio emission from other solar system planets (Saturn, Uranus, Neptune) requires space-based measurement and was achieved by various spacecraft including Voyager 2 [332].

The only existing maps of the sky below 10 MHz come from the RAE-2 spacecraft in 1973 [308, 121]. This single spacecraft was placed in orbit around the Moon to avoid terrestrial noise, both natural and man-made. RAE-2 data were used to construct a partial map of the sky at several frequencies with a resolution of $\sim$60 degrees at its lowest frequencies [3]. There have been numerous proposals to design and build a multi-element interferometric array to map the sky at higher resolution (e.g. [146, 187, 43]), but none of these projects have yet been built and launched due to cost and complexity. Lowering the cost and complexity of such missions would help enable a wide range of new scientific investigations.

Large space-based interferometric arrays have been proposed [146, 187, 219, 157, 20] and (with luck) may be funded and launched in the not-too-distant future. The number of spacecraft needed to construct such an instrument will likely drive the array cost. Very sensitive measurements, like those required to detect Earth-like auroral magnetospheric emission from exoplanets, will require thousands of spacecraft [145] to achieve the required sensitivity. See Section 8.3.2 for a detailed discussion of the requirements for detecting Earth-strength magnetic fields. Reducing the number of

interferometric elements needed without sacrificing sensitivity would therefore lower the costs of such an array. The next section describes a collaborative research effort to develop a better antenna for space-based interferometry [158] that will offer a significant improvement over 'traditional' dipoles or tripoles (dipole triads).

The advent of CubeSats has changed the landscape and increased the feasibility of a multi-spacecraft interferometric array. Such arrays have been proposed (e.g. [20, 219, 160]) and are a key step to lowering mission costs. It is still critical, however, to minimize the number of spacecraft required for such an array in order to keep costs and logistics reasonable. The vector sensor described in this work offers a more capable array element than the crossed dipoles typically used for ground-based low frequency interferometric arrays or the tripole antennas (dipole triads) often considered for space based arrays. When combined with appropriate signal processing, the extra degrees of freedom that the vector sensor provides will reduce the number of spacecraft needed for mapping the sky below 10 MHz both by increasing the sensitivity of each interferometric array element and by improving rejection of interfering sources. The potential for utilizing the vector sensor to provide characterization of strong interfering sources also opens the possibility of using these degrees of freedom to provide spatial pre-whitening. This may enable astronomically useful observations much closer to Earth than previously proposed missions, which often select Lunar orbits or surface installations to exploit the radio shadow of the Moon [145].

7.3 Vector Sensor: An Optimal Antenna for Low Frequency Space-Based Interferometry[3]

A vector sensor is composed of three orthogonal dipole elements and three orthogonal loop elements that share a common phase center [323, 215]. Figure 7-1 shows a vector sensor designed by the Naval Research Laboratory (NRL) [174]; the three loop elements and three dipole elements are clearly visible. Two out of the three dipole elements shown comprise a crossed dipole; all three dipoles form a tripole. Crossed

[3]This work was published in [158, 245, 159]

dipoles and tripoles have been proposed as the fundamental antenna element for various space-based low frequency interferometric arrays (see previous section).

The six elements of the vector sensor allow it to measure the full E-field and B-field of incident electromagnetic radiation. This allows the vector sensor to determine direction of arrival as well as polarization of an incoming signal in a single measurement. While vector sensors have not previously been used for radio astronomy, they offer significant benefits in both sensitivity and interference nulling [226] over the more traditional crossed dipoles or dipole triads currently used in interferometric arrays. These benefits suggest that vector sensors would make more capable interferometric elements for a future space-based array and allow for a reduced number of elements with no loss in performance. Development of the vector sensor as a radio astronomy instrument is ongoing as part of a collaboration between myself, MIT Haystack Observatory, and Lincoln Laboratory. My work on the project was focused on developing imaging algorithms for individual vector sensors as well as small interferometric arrays of vector sensors.

Vector sensors have three key advantages:

1. Vector sensors are able to determine direction of arrival of sources [325] without resorting to multiple poses as required for a triad.

2. Vector sensors maximize the statistics collected from a single point in space. This maximizes the utility of a single satellite short of deploying a spatial array and will provide a more capable interferometer with fewer spacecraft. While the final constellation is expected to contain multiple satellites, the ability to collect these statistics with a vector sensor allows radiometric imaging to be performed with a single spacecraft.

3. Vector sensors can null or isolate specific sources [247]. This potentially is of benefit in the near earth environment where background signal due to terrestrial sources can require measurements with extraordinary dynamic range.

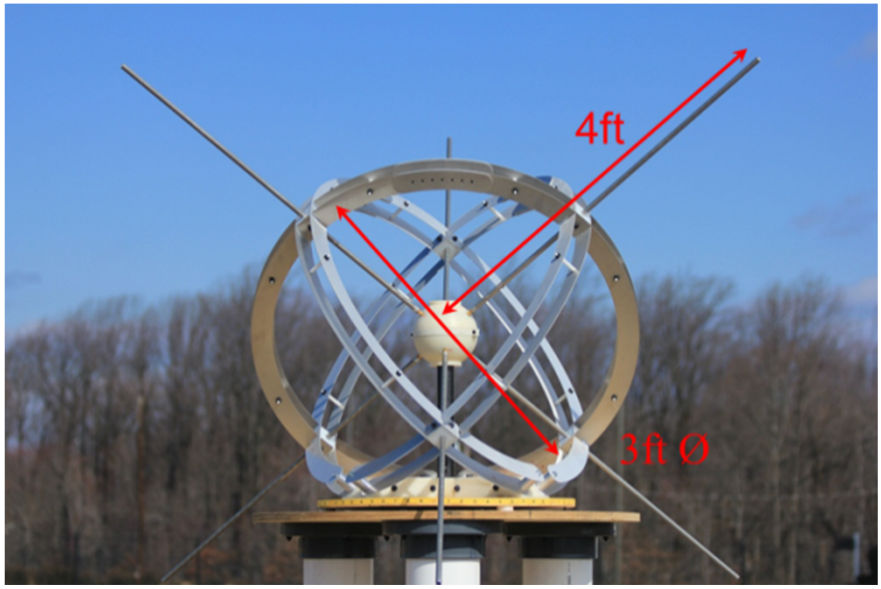

Figure 7-1: Vector sensor designed by NRL [174]. The three mutually perpendicular loop elements and three dipole elements are clearly visible. Dimensions of the loops and dipoles are indicated in red.

7.3.1 Vector Sensor Data Model

The response of the vector sensor as a function of spatial position (θ, ϕ) and polarization (α, δ), from Wong et al. (2000) [326] and separately derived by Alan Fenn:

$$\mathbf{y} = \beta\mathbf{a} \tag{7.1}$$

$$\mathbf{a} \equiv \mathbf{a}(\theta, \phi, \alpha, \delta) \equiv \begin{pmatrix} e_x \\ e_y \\ e_z \\ h_x \\ h_y \\ h_z \end{pmatrix} = \tag{7.2}$$

$$\begin{pmatrix} \cos(\theta)\cos(\phi) & -\sin(\phi) \\ \cos(\theta)\sin(\phi) & \cos(\phi) \\ -\sin(\theta) & 0 \\ -\sin(\phi) & -\cos(\theta)\cos(\phi) \\ \cos(\phi) & -\cos(\theta)\sin(\phi) \\ 0 & \sin(\theta) \end{pmatrix} \cdot \begin{pmatrix} e^{i\delta}\sin(\alpha) \\ \cos(\alpha) \end{pmatrix} = \begin{pmatrix} e^{i\delta}\cos(\theta)\cos(\phi)\sin(\alpha) - \cos(\alpha)\sin(\phi) \\ \cos(\alpha)\cos(\phi) + e^{i\delta}\cos(\theta)\sin(\alpha)\sin(\phi) \\ -e^{i\delta}\sin(\alpha)\sin(\theta) \\ -\cos(\alpha)\cos(\theta)\cos(\phi) - e^{i\delta}\sin(\alpha)\sin(\phi) \\ e^{i\delta}\cos(\phi)\sin(\alpha) - \cos(\alpha)\cos(\theta)\sin(\phi) \\ \cos(\alpha)\sin(\theta) \end{pmatrix} \tag{7.3}$$

The amplitude-weighted vector sensor array response is $\mathbf{y}$ and β is a scalar amplitude. The six elements of $\mathbf{a}$ correspond to the three dipoles (e_x, e_y, e_z) and three loops (h_x, h_y, h_z). The right-hand side of Equation 7.3 is a column vector of six vector sensor steering vectors. These steering vectors represent the ideal output of each vector sensor element (amplitude and phase) as a function of incoming radiation properties (θ, ϕ, α, δ).

The alternative formulation from Nehorai et al. (1999) [214] uses polarization

orientation angle (ψ) and ellipticity (χ) instead of α and δ.

$$\mathbf{B} = \begin{pmatrix} -\sin(\phi) & -\cos(\phi)\sin(\theta) \\ \cos(\phi) & -\sin(\theta)\sin(\phi) \\ 0 & \cos(\theta) \\ -\cos(\phi)\sin(\theta) & \sin(\phi) \\ -\sin(\theta)\sin(\phi) & -\cos(\phi) \\ \cos(\theta) & 0 \end{pmatrix} \tag{7.4}$$

$$\mathbf{Q} = \begin{pmatrix} \cos(\psi) & \sin(\psi) \\ -\sin(\psi) & \cos(\psi) \end{pmatrix} \tag{7.5}$$

$$h = \begin{pmatrix} \cos(\chi) \\ i\sin(\chi) \end{pmatrix} \tag{7.6}$$

$$\mathbf{B}\cdot\mathbf{Q}\cdot h = \begin{pmatrix} \cos(\chi)(\cos(\phi)\sin(\theta)\sin(\psi) - \cos(\psi)\sin(\phi)) + i\sin(\chi)(-\cos(\phi)\cos(\psi)\sin(\theta) - \sin(\phi)\sin(\psi)) \\ i\sin(\chi)(\cos(\phi)\sin(\psi) - \cos(\psi)\sin(\theta)\sin(\phi)) + \cos(\chi)(\cos(\phi)\cos(\psi) + \sin(\theta)\sin(\phi)\sin(\psi)) \\ i\cos(\theta)\cos(\psi)\sin(\chi) - \cos(\theta)\cos(\chi)\sin(\psi) \\ i\sin(\chi)(\cos(\psi)\sin(\phi) - \cos(\phi)\sin(\theta)\sin(\psi)) + \cos(\chi)(-\cos(\phi)\cos(\psi)\sin(\theta) - \sin(\phi)\sin(\psi)) \\ \cos(\chi)(\cos(\phi)\sin(\psi) - \cos(\psi)\sin(\theta)\sin(\phi)) + i\sin(\chi)(-\cos(\phi)\cos(\psi) - \sin(\theta)\sin(\phi)\sin(\psi)) \\ \cos(\theta)\cos(\chi)\cos(\psi) + i\cos(\theta)\sin(\chi)\sin(\psi) \end{pmatrix} \tag{7.7}$$

The right-hand side of Equation 7.7 represents the same six steering vectors as Equation 7.3, but using a different polarization basis. In either polarization formulation, the vector sensor response to multiple sources at different locations with different polarizations is the sum of the steering vector for each source. An inversion technique is required to recover the location and polarization of sources from the 6-element column vector representing the phase and amplitude of each vector sensor channel output.

7.3.2 Expectation Maximization for the Vector Sensor[4]

I tested variety of inversion algorithms during the vector sensor development effort. Detailed algorithm descriptions and comparisons can be found in [302]. I will briefly outline the Expectation Maximization (EM) algorithm [67, 200] that is used on sim-

[4]Adapted from [158], Section 2

ulated data in subsequent sections. The application of the EM algorithm to vector sensors is described in detail in [246].

For simplicity, the full 4π steradian sphere from which the vector sensor can receive signals (assuming it is in space) is discretized into I pixels using HEALpix [116]. We consider K temporal samples from N vector sensor elements ($N = 6$). Initially, two polarization bases were used (horizontal and vertical linear polarization or right and left circular polarization), but a full Stokes polarization basis is necessary when working in the higher order covariance space of the EM algorithm. Steering vectors are generated for every spatial pixel in each Stokes component. The full array of steering vectors $\mathbf{A}$ is indexed $i = 1...I$. Radiation from each spatial/polarization cell is assumed to approximate a complex white Gaussian process. The vector sensor output $\mathbf{z}[k]$ for each temporal sample is given by

$$\mathbf{z}[k] = \sum_{i=1}^{I} c_i[k]\mathbf{a_i} + \mathbf{n}[k] \tag{7.8}$$

where $\mathbf{n}[k]$ is the receiver noise, also a complex white zero-mean Gaussian process. The columns of $\mathbf{A}$ are $\mathbf{a_i}$ and $c_i[k]$ represent the signal from each spatial/polarization cell. In matrix form,

$$\mathbf{Z} = \mathbf{AC} + \mathbf{N} \tag{7.9}$$

where $\mathbf{Z}$ has columns $\mathbf{z}[k]$, $\mathbf{A}$ has columns $\mathbf{a_i}$, $\mathbf{C}$ has columns $c_i[k]$, and $\mathbf{N}$ has columns $\mathbf{n}[k]$. The sample covariance matrix $\mathbf{S}$ is therefore

$$\mathbf{S} = \frac{1}{K}\mathbf{Z}\mathbf{Z}^H \tag{7.10}$$

The steps of the EM algorithm are as follows:

1. Initialize the complete data spectral estimates $\widehat{\mathbf{\Sigma}}^1$ and covariance matrix $\widehat{\mathbf{R}}^1$:

$$\widehat{\mathbf{R}}^1 = \mathbf{A}\widehat{\mathbf{\Sigma}}^1\mathbf{A}^H + \mathbf{R}_n \tag{7.11}$$

2. Iterate until convergence criteria met or maximum iterations P exceeded ($p =$

$1 \ldots P$)

$$\widehat{\mathbf{\Sigma}}^{p+1} = diag(\widehat{\mathbf{\Sigma}}^{p} + \widehat{\mathbf{\Sigma}}^{p}\mathbf{A}^{H}(\widehat{\mathbf{R}^{p}}^{-1}\mathbf{S}\widehat{\mathbf{R}^{p}}^{-1} - \widehat{\mathbf{R}^{p}}^{-1})\mathbf{A}\widehat{\mathbf{\Sigma}}^{p}) \tag{7.12}$$

$$\widehat{\mathbf{R}}^{p+1} = \mathbf{A}\widehat{\mathbf{\Sigma}}^{p+1}\mathbf{A}^{H} + \mathbf{R}_{n} \tag{7.13}$$

$\mathbf{R}_n$ is the noise covariance matrix. The superscript ^{H} represents a hermitian transpose and the superscript $^{-1}$ represents a matrix inversion. The estimates for signal amplitude for each spatial/polarization pixel at iteration p are the elements of the column vector $\widehat{\mathbf{\Sigma}}^{p}$.

7.3.3 Simulated All-Sky Imaging with the Vector Sensor[5]

This section describes simulated imaging results using the EM algorithm described in the previous section. The work described below was carried out in `MATLAB`.

Simulated sky maps and test patterns were generated using equal area sampling of a sphere rather than a regular grid in spherical coordinates. A grid with equal spacing in elevation and azimuth oversamples the poles and undersamples the equatorial region, leading to poor convergence and distortions in the resulting images. A `MATLAB` implementation of the HEALPix [116] library developed by JPL was used to generate a list of sample points that are equally spaced over 4π steradians. Fairly coarse sampling was used for the simulations presented here (3072 pixels over the sphere, each pixel is approximately 13 square degrees) in the interest of reasonable simulation runtimes. Tests with higher resolution indicated that there was little loss of fidelity due to the decreased simulation resolution.

As illustrated in Figure 7-2, discrete sources, representing unresolved bright radio sources, were modeled either as single bright pixels or as low variance bi-variate Gaussian distributions. Spatially distributed sources (e.g. the galactic plane or other bright resolved object) were modeled as Kent (FB5) [152] distributions. A Kent distribution is a bi-variate Gaussian distribution recast onto the surface of the unit sphere. A small Gaussian noise component was added to each pixel of the simulated

[5]This section is reproduced from [158], Section 4

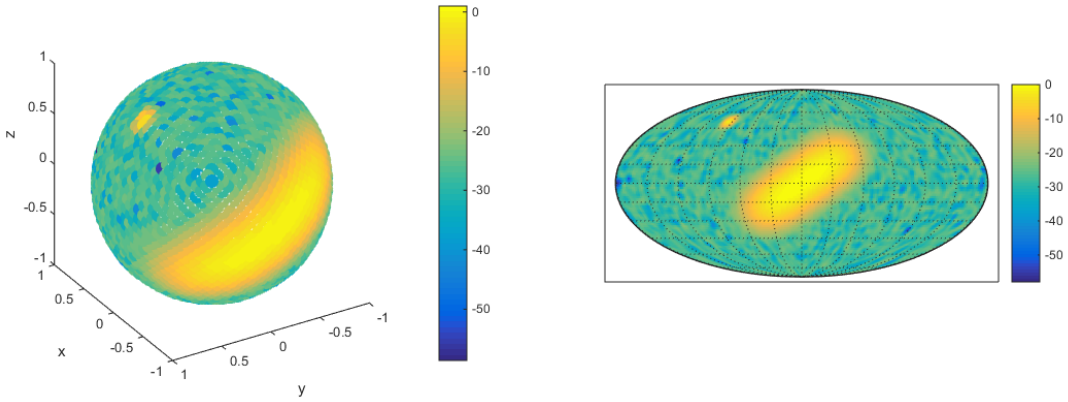

(a) Simple simulated sky, 3D sphere (b) Simple simulated sky, Mollweide projection

Figure 7-2: Simulated sky maps using HEALpix sampling. The simulated point and distributed sources shown were used to generate simulated input for EM algorithm testing. The pixel values are normalized and the colorscale represents intensity in dB. Figure 7-2a view shows the model sky on a sphere. Individual pixels are visible. Figure 7-2b view is a smoothed Mollweide projection of the same simulated sky.

sky map. All pixel values in the map were constrained to be positive. Running the EM algorithm on the simulated sky in Figure 7-2 produced the estimated brightness distribution in Figure 7-3. The EM algorithm is 'tuned' to produce point-like 'peaky' results, so the distributed source in the input image has become a set of point sources over a brighter background. Alternative algorithms or smoothing penalties may improve the recovery of distributed sources and this will be a topic for future algorithm refinement.

The dimensionality argument from [158], Section 2, indicates that the vector sensor should be able to resolve up to 19 sources if higher order statistics are exploited correctly. In order to test this assertion, point sources of varying intensity were scattered randomly across a sphere. This model sky was sampled many times to produce a time series input to the EM algorithm. When the point sources were modeled as white Gaussian processes across the full time range of the simulation, up to 5 sources could be resolved when a uniform distribution of energy was used to initialize the estimation algorithms (Figure 7-4, (a), (c), (e)). This limit on resolution was almost certainly due to local maxima in the log-likelihood since initializing the algorithms with a solution that was close to the truth and with more sources than

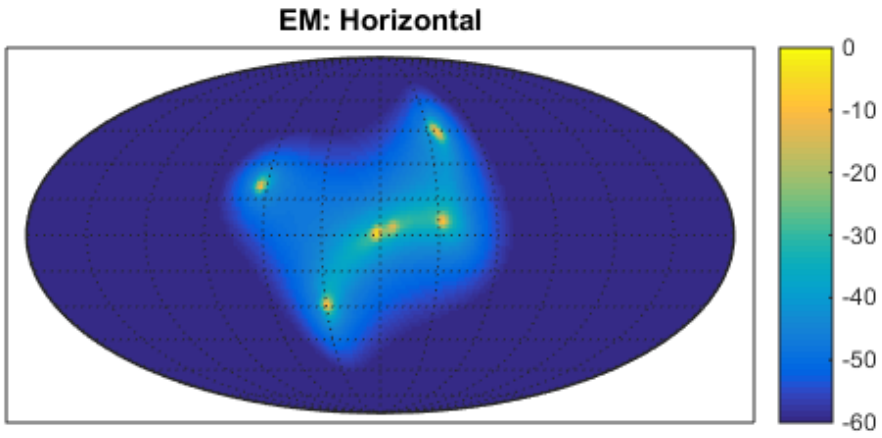

Figure 7-3: EM algorithm estimate for all-sky brightness distribution. This result was generated from a single time 'snapshot' of the sky model. The image is normalized and the colorscale represents dB. The EM algorithm is somewhat biased toward finding peaks, so various smoothing penalties are being investigated to improve imaging of spatially distributed sources.

5 would converge. When the sources were instead impulsive, meaning each source appears only once in the time series, up to 18 sources could be resolved (Figure 7-4, (b), (d), (f)) even with the uniform distribution for initializing the estimators. This approaches the theoretical number of sources that we expect to resolve when fully exploiting higher order statistics.

While the current algorithm performance for true Gaussian sources is below what is theoretically possible, the vector sensor is still able to detect the direction and polarization of multiple sources from a single pose. Algorithmic development is ongoing to improve performance for truly Gaussian sources. The ease with which the algorithm detects impulsive, non-Gaussian sources maybe of use for detecting and nulling interfering terrestrial signals. Indeed, the primary relevance of source detection for the vector sensor in the context of a space-based interferometric array is nulling unwanted interfering sources.

7.3.4 Vector Sensor Sensitivity

The vector sensor's nulling capability provides an advantage over alternative antennas for a space-based interferometer (dipole, tripole). Another key advantage of the vec-

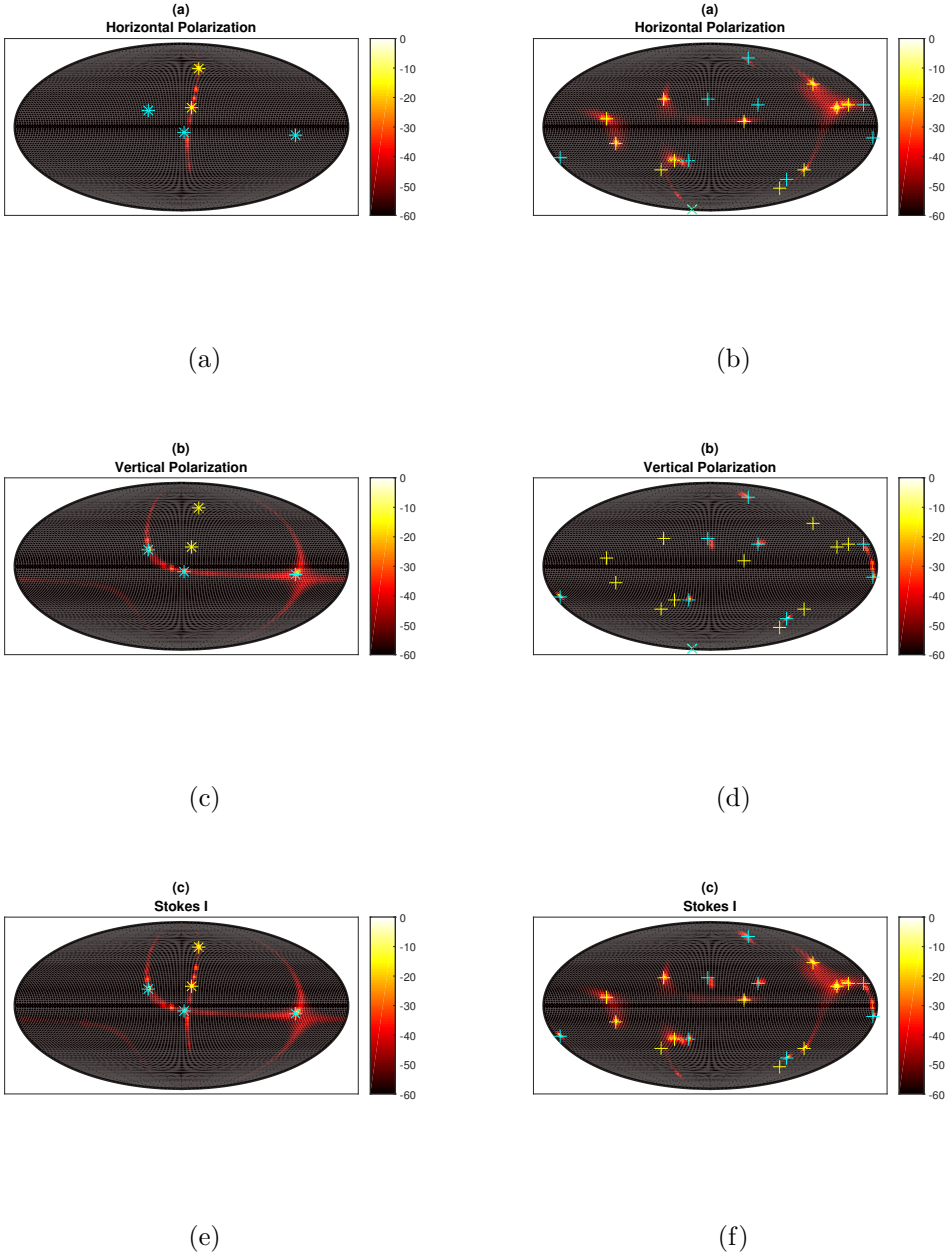

Figure 7-4: Results from point source detection tests. The left column (a, c, e) shows the results for a simulation using five white Gaussian sources. The right column (b, d, f) shows results from a simulation using 19 impulsive 'lightning-like' sources. The top row of images (a, b) shows the horizontal polarization map, the middle row (c, d) shows vertical polarization, and the bottom row (e, f) shows total intensity (Stokes I). The yellow markers ('*' for Gaussian sources, '+' for impulsive sources) indicate the true position of horizontally polarized sources while the cyan markers indicate the true position of vertically polarized sources. The colorscale is the same for each image and is in units of dB. These examples demonstrate that a single vector sensor can successfully detect and determine the polarization of up to 18 point sources.

tor sensor is increased sensitivity per interferometer element. A detailed calculation of signal-to-interference plus noise ratio (SINR) for a vector sensor and dipole triad (tripole) can be found in [158], Section 2[6]. The results are reproduced here in Figure 7-5. In the general case, the vector sensor is 2x (3 dB) more sensitive than a tripole of equal dimensions. In the case of interfering sources, the sensitivity improvement provided by the vector sensor is a function of angular distance from the interfering source. This is illustrated clearly in Figure 7-5a, where the sensitivity to vertically polarized sources is shown as a function of angle when a bright vertically polarized interfering (or 'nuisance') source is placed at the center of the map. The vector sensor sensitivity advantage ranges from 1 dB to 6 dB for this case. One reason the vector sensor is more sensitive than a similarly sized tripole is that the extra elements remove any angular ambiguity in source position. The increased sensitivity of the vector sensor vs. a dipole triad means that ***an interferometric array composed of vector sensors would need only half as many elements to achieve a set sensitivity requirement when compared to an array composed of dipole triad elements.***

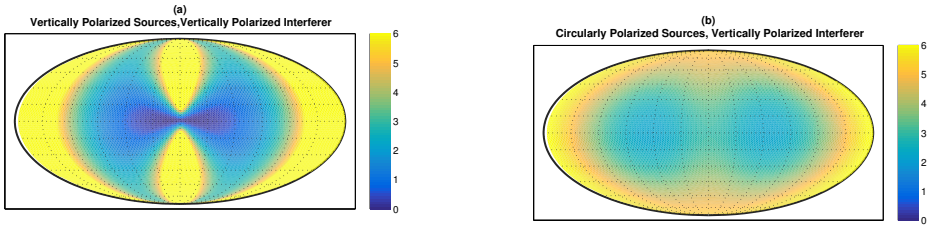

(a) (b)

Figure 7-5: Comparison of the SINR (dB) of a vector antenna vs. a tripole antenna for a high interference-to-noise power ratio. The simulation is of a single interfering source and the relative SINR plotted shows the improvement provided as a function of the angle in space. The interfering source is at the center of the image and is vertically polarized. Plot (a) illustrates the gain for observing vertically polarized sources. Plot (b) shows the gain for right-circularly polarized sources.

[6]Frank Robey did the SINR analysis and Ryan Volz provided the simulated images

7.3.5 Vector Sensor for CubeSats

Lincoln Laboratory designed, manufactured, and tested several vector sensors for testing as part of the vector sensor project. The CubeSat-compatible deployable vector sensor (DEVS) is shown in Figure 7-6. The vector sensor stows into a 1 U (10 x 10 x 10 cm) volume. It deploys in two stages. First, the top of the container expands upward to increase the available loop area of the loop elements. Second, the orthogonal rectangular loop arms uncoil from the central spool. The rectangular loops are currently made from spring steel (tape spring), but lighter weight materials are being considered. The orthogonal rectangular loops are both loop antennas and dipoles through the use of a hybrid modeformer, so they comprise four out of the six vector sensor elements. The third loop antenna is strung around the perimeter of the rectangular loops and the last element is a monopole that extends up from the circular canister at the top of the deployer. Each loop-dipole is 4 m tip-to-tip and the monopole is 2 m long. Details of the DEVS design and testing can be found in [245].

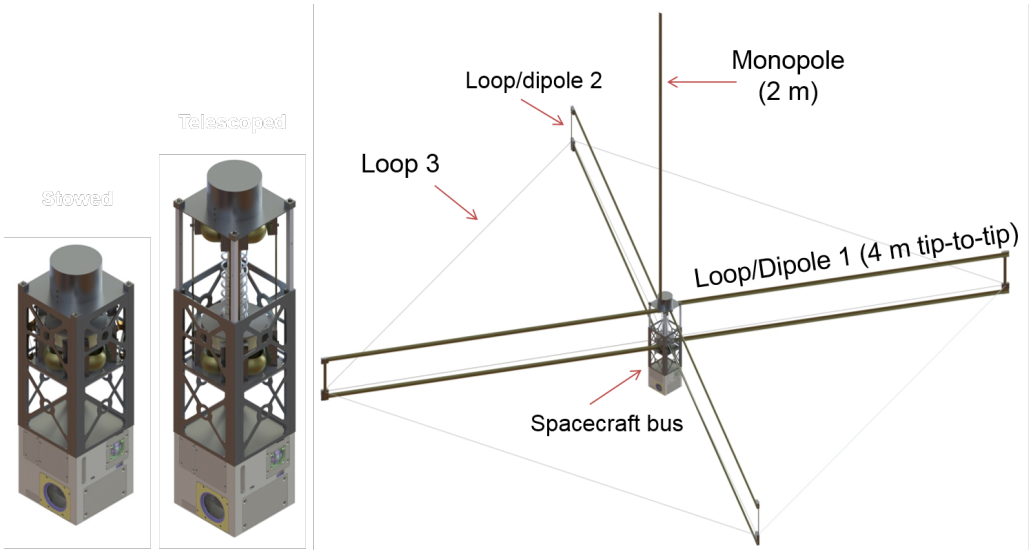

Figure 7-6: DEVS deployable vector sensor. The vector sensor deploys in two stages. The stowed configuration is shown on the left. The first stage of deployment is shown in the center (deployer top extends upward). The final deployed configuration is shown on the right.

7.4 HeRO: A First Step[7]

No space-based interferometric observatory has been funded or flown to date. This initial hurdle must be overcome before an instrument capable of detecting Earth-strength magnetic fields can be proposed. HeRO (**He**liophysics **R**adio **O**bserver), led by PI Dale Gary of NJIT, is a proposed small 'Mission of Opportunity' submitted to NASA Heliophysics for consideration. HeRO, if funded, is a critical first step towards a larger future exoplanet-capable space-based interferometer because it will demonstrate the technology, algorithms, and operational strategy necessary for space-based radio interferometry.

7.4.1 Science Objectives

HeRO's science case focuses on solar radio bursts, specifically type II and type III bursts. Solar radio bursts are an attractive target for the first space-based interferometric mission because they are very bright (10^3 - 10^8 Jy) [254, 161, 320] and occur often, especially during solar maximum. Type II solar bursts are thought to originate from plasma shocks, often driven by coronal mass ejections (CMEs) [113, 114]. Type III solar bursts are associated with relativistic electron beams propagating along solar magnetic field lines [286]. HeRO will measure the precise position of radio emission from type II and III radio bursts as a function of time, frequency, and polarization. The frequency of emission depends on the local plasma frequency, so these measurements will trace out the density structure of the solar coronal and interplanetary medium as disturbances propagate out from the sun.

HeRO seeks to answer three key questions:

1. What are the shapes and properties of CME shock fronts?

2. What are the sites and conditions for efficient particle acceleration in coronal

[7]Some of this material is used in "HeRO: A Space-Based Low Frequency Interferometic Observatory for Heliophysics Enabled by Novel Vector Sensor Technology" by M. Knapp, D. Gary, M. Hecht, C. Lonsdale, F. D. Lind, F. C. Robey, L. Fuhrman, B. Chen, A. Fenn, and the HeRO Team. This is a reviewed proceeding paper for the 8th International Workshop on Planetary, Solar and Heliospheric Radio Emissions (PRE VIII). The paper is currently in review.

and interplanetary shocks?

3. What is the topology of magnetic fields from the Sun into the heliosphere?

Currently, coronagraphs in Earth orbit or 1 AU heliocentric orbits can track CMEs as they erupt from the sun, but are limited in their ability to trace CMEs as they propagate beyond the corona. HeRO will track CMEs as they evolve from the Sun to the Earth via type II radio bursts, potentially improving space weather forecasting. Similarly, the interplanetary magnetic field is simulated starting with boundary conditions at the sun based on magnetographs and at the Earth based on in-situ satellite measurements [228]. There are no direct measurements of the interplanetary magnetic field between the solar corona and the Earth. Tracing type III bursts with HeRO will fill in this observational gap.

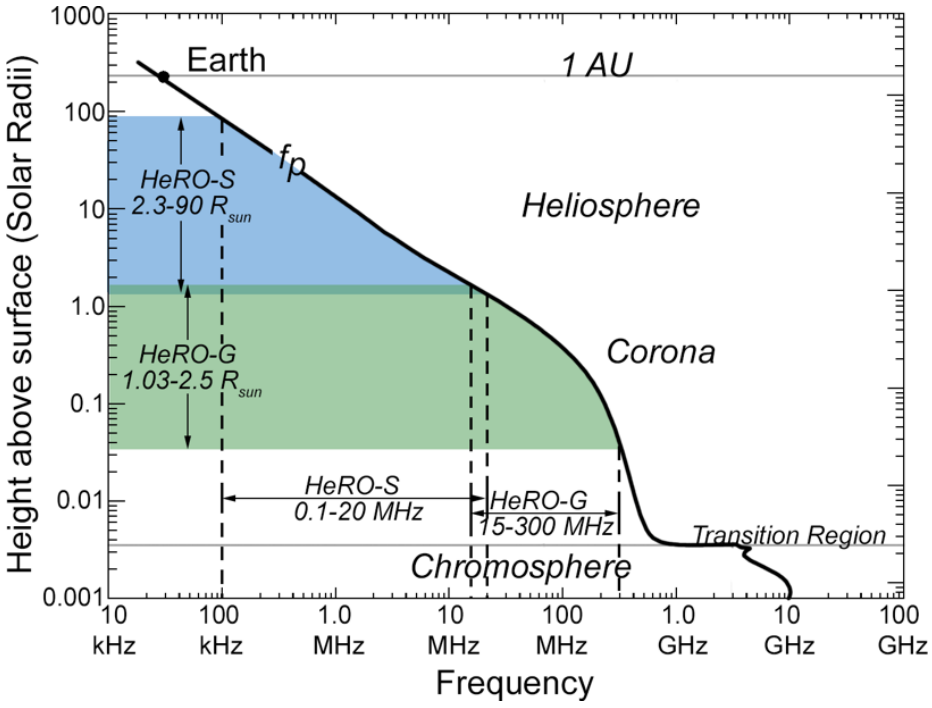

Figure 7-7: HeRO coverage in solar distance and frequency. The solid black curve shows plasma frequency (fundamental) as a function of distance from the sun. The blue shaded area shows HeRO-G's frequency coverage and corresponding solar distance coverage. The blue shaded area shows HeRO-S's coverage. HeRO coveres 100 kHz – 300 MHz in frequency and 1.03–90 R_{Sun}. Figure by D. Gary (NJIT).

HeRO is a composite instrument with a space-based component (HeRO-S, Section 7.4.2) and a ground-based component (HeRO-G, Section 7.4.2). Splitting the

instrument into ground and space components increases frequency coverage while minimizing cost. Observations above the ionospheric cut-off frequency can be conducted on the ground, so HeRO-G can take advantage of significantly lower operating costs vs. spacecraft as well as increased flexibility, ease of maintenance, larger available data storage and increased processing resources. HeRO-S covers the portion of the spectrum that is impossible to observe from the Earth's surface and allows HeRO to track radio bursts from 2 solar radii to 0.5 AU (see Figure 7-7). Together, HeRO-S and HeRO-G provide 100 kHz–300 MHz frequency coverage. HeRO-S and HeRO-G overlap between 15–20 MHz, allowing for cross-instrument calibration.

7.4.2 HeRO Instrument Description

HeRO-S

HeRO-S(pace) comprises a flock of 6 identical 6U (30 x 20 x 10 cm) CubeSats, each with antenna, receiver, position and timing synchronization, precision clock, and memory management. For interferometry of solar radio bursts, the 6 spacecraft are positioned such that the baselines range from 0.5–10 km, in an optimized 3D arrangement that is insensitive to slow variations with time (see Section 7.4.3). For transient sources like solar radio bursts, traditional aperture synthesis based on evolving baseline projections is not possible, but 'snap-shot' interferometry allows precision metrology of centroids for single, compact sources, from which spot maps can be generated as a function of time and frequency.

HeRO-S uses a vector sensor as its antenna. The directivity of the HeRO-S Vector Sensor (VS) (Section 7.3) provides the capability to determine the direction of arrival and the polarization sense of incoming waves, allowing spatial and polarization steering of the antenna beam or nulling of interference sources. This allows HeRO-S to adaptively suppress noise from terrestrial sources by an estimated 30 dB compared to conventional methods, such that solar radio bursts will dominate the result [158]. Without such nulling capabilities, avoidance of strong terrestrial emissions of both natural and artificial origin would require deployment to a distant location

(e.g. Lagrange point or lunar orbit), severely limiting data downlink rates. Positioning HeRO-S above the plasmapause minimizes plasmaspheric masking and distortion over the entire 0.1–20 MHz frequency range while remaining close enough to the Earth for efficient high data rate communication.

HeRO-S CubeSats will fly in loose flock in an elliptical, slightly skewed geosynchronous (S-GEO) orbit. The S-GEO orbit[8] is both slightly eccentric and slightly inclined so it provides the benefits of a GEO orbit (reliable communications, observations above the ionosphere) while never transiting the crowded GEO belt. Requirements for stationkeeping of the spacecraft are not stringent. Knowledge of relative spacecraft position is sufficient to establish array coherence, and can be refined to high accuracy by the interferometry itself. Position knowledge to $1/10$–$1/16$ of a wavelength is generally considered sufficient for interferometric baselines, so HeRO-S's position knowledge requirement is 1–1.5 m at 20 MHz — well within the capability of standard ranging systems. Each spacecraft carries a chip-scale atomic clock for precision timing and has a small electric propulsion system for initial orbit adjustment, stationkeeping, reaction wheel desaturation, and disposal at end of life. The stationkeeping requirements for the S-GEO orbit are minimal ($\sim$64 m/s ΔV).

To date, most CubeSats have been launched into low Earth orbits (LEO), but LEO orbits are still within the ionosphere and are thus unsuitable for HeRO. Atmospheric drag in LEO would make maintaining the 'flock' much more difficult as well. There are rideshare opportunities to orbits beyond LEO and the most important consideration for CubeSats beyond GEO is improved radiation tolerance.

HeRO-S will observe the sun for 16 hours per day and store raw voltages in a ring buffer which can hold up to 32 hours of raw data. During the remaining 8 hours, when the Earth and plasmasphere are between the HeRO-S flock and the Sun, HeRO-S will downlink data that has been flagged as containing an event based on ground-in-the-loop examination of summary dynamic spectra from each node. HeRO-S will use a large dedicated X-band ground station to downlink decimated raw data for correlation on the ground rather than cross-correlating in space and downlink

[8]Developed by Arthur Lue at MIT Lincoln Laboratory.

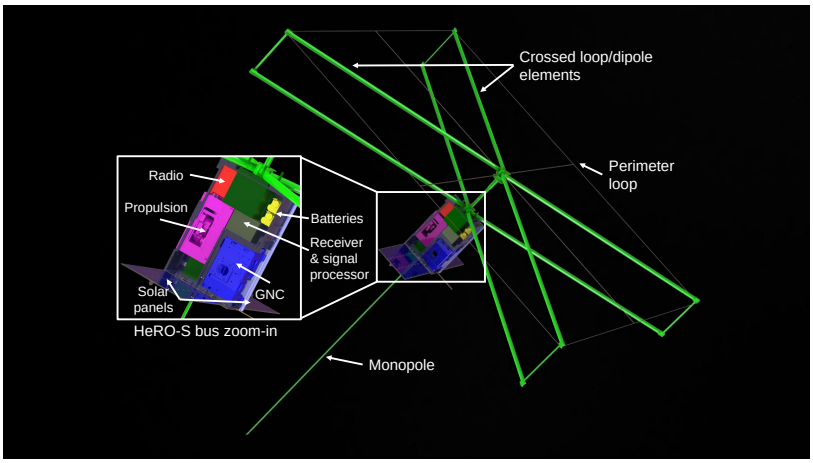

Figure 7-8: The 6U HeRO-S spacecraft. The vector sensor is composed of two crossed loop/dipole arms, a perimeter loop around the tips of the loop/dipoles, and a monopole. False colors are used to highlight key subsystems. CAD model by M. Silver.

the visibilities. Retaining the raw data enables iterative tuning and adjustment of the correlation process for a particular observation, and allows iterative estimation of instrumental calibration parameters. In this respect, the data from both HeRO-S and HeRO-G will allow more processing flexibility than the visibility-only data that is produced by most major observatories.

HeRO-S will be calibrated using a stable NIST-traceable noise diode or comb generator to provide on platform amplitude, frequency, and phase calibration. The calibration signal will be injected into the six antenna inputs [76, 195] to determine channel-to-channel gain and phase differences as well as the absolute gain of the receiver system. The VS antenna element gains as a function of angle are measured by rotation of the spacecraft while observing a known reference such as a ground-based source. Traditional radio interferometry techniques like self-calibration will be used in post-processing on the ground after correlation. To suppress self-electromagnetic interference (EMI), all HeRO subsystems will be selected for low noise and shielded where necessary. Several spacecraft subsystems, including propulsion and communication, will be turned off during data acquisition. The EMI spectrum will be evaluated throughout development and any affected frequency ranges affected will be constrained where EMI cannot be eliminated entirely.

HeRO-G

HeRO-G(round) is the ground-based component of HeRO (15–300 MHz). HeRO-G is composed of two geographically separated 'stations', each containing 25 HeRO-G nodes with UV coverage optimized for solar observing (Figure 7-9b). Together, the two HeRO-G stations will provide 16+ hours of solar observation per day. The HeRO-G nodes are based on the RAPID (**R**adio **A**rray of **P**ortable **I**nterferometric **D**etectors) node design [178]. RAPID is currently under development at MIT Haystack Observatory in collaboration with Cambridge University and NASA JPL. Each RAPID node is physically independent, equipped with a high performance direct digitization receiver, hot-swappable solid state disk (SSD) storage, precision clock, solar and battery power, and optional wireless interconnection.

(a) RAPID Field Unit with SKALA antenna.

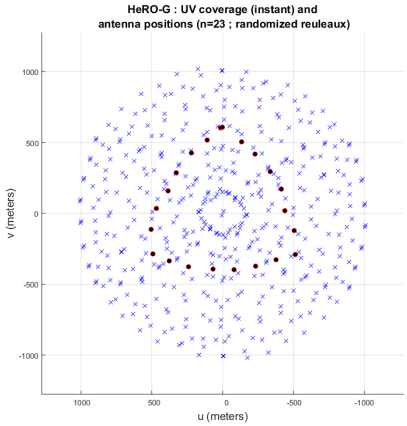

(b) Antenna positions and instantaneous (u,v) coverage for HeRO-G station

Figure 7-9: RAPID Field Unit, used as the basis for HeRO-G, (a) and HeRO-G station layout and UV coverage (b). There are 25 HeRO-G units per station, arranged in a randomized Reuleaux triangle (red dots) to achieve uniform (u,v) plane filling (blue x). Baseline lengths range from 100 m – 10 km.

Each HeRO-G node will use a variant of the SKALA antenna [64] for 50–300 MHz (Figure 7-9a) and a modified LWA antenna [83] for 10–70 MHz. Both antennas will operate simultaneously using a common field unit base. Raw voltage signals from

HeRO-G antennas are captured, filtered, decimated, compressed, and time-tagged before being transferred to the SSD ring buffer in the HeRO-G base unit.

A subset of HeRO-G nodes will be used as a triggering system that semi-autonomously identifies solar bursts from their compact, transient, and spectrally narrow features and their angular location relative to the solar position. A successful detection causes raw data to be retained locally and a trigger to be sent to the outlying, unconnected nodes via Iridium or other satellite provider. Data are collected manually by swapping the solid state disks and transferring them to a centralized cloud computing facility.

7.4.3 HeRO Simulation

This section describes HeRO sensitivity calculations and simulation of HeRO UV coverage, PSF, and spot mapping observations.

HeRO Sensitivity

HeRO's sensitivity depends on:

- Galactic background noise
- Antenna and receiver (RF chain) noise
- Bandwidth
- Integration time
- Number of antennas

The sensitivity calculations are slightly different for HeRO-S vs. HeRO-G since every HeRO-S antenna sees all of the sky (4π sr) while HeRO-G antennas see only half of the sky (2π sr). Figure 7-10 shows HeRO's sensitivity compared to typical type II and III radio bursts.

For HeRO-S, galactic background noise and antenna/receiver noise are summed to attain the noise floor (1-σ sensitivity) of system-equivalent flux density (SEFD). The antenna noise was provided by Kerry Johnson (MIT Lincoln Laboratory) based

on a performance simulation. The antenna/receiver noise was reported in units of $\mathrm{V/m/\sqrt{Hz}}$, electric field spectral density. These data were converted to typical radio astronomy units of Jy (10^{-26} $\mathrm{W/m^2/Hz}$), a spectral flux or 'power' unit, according to Equation 7.14:

$$P\left(\frac{W}{m^2 \cdot Hz}\right) = \frac{E^2 \left(\frac{V}{m \cdot \sqrt{Hz}}\right)^2}{R(\Omega)} \tag{7.14}$$

Units for each quantity are shown in parentheses and R is the impedance of free space (377 Ω).

The galactic background noise is a piece-wise power law from [145] given in units of brightness temperature:

$$T_{sky} = \begin{cases} 16.3 \cdot 10^6 \ K \ \left(\frac{\nu}{2 \text{ MHz}}\right)^{-2.53} & \text{at } \nu > \ 2 \text{ MHz} \\ 16.3 \cdot 10^6 \ K \ \left(\frac{\nu}{2 \text{ MHz}}\right)^{-0.3} & \text{at } \nu \leq \ 2 \text{ MHz} \end{cases} \tag{7.15}$$

Brightness temperature T is converted to flux units S (Jy or $\mathrm{W/m^2/Hz}$) using Equation 7.16:

$$S = \frac{2k_B\Omega}{c^2} \cdot T\nu^2 = 3.86084 \cdot 10^{-39} \ T\nu^2 \tag{7.16}$$

where k_B is Boltzmann's constant, c is the speed of light, and ν is frequency in Hz. In order to make this conversion, some solid angle Ω must be used. For interferometers, that is usually the solid angle of the synthesized beam to the half power point ($\Omega_{synth} = \frac{\pi\theta^2}{4 \ ln \ 2}$, where θ is the half-power beamwidth of the synthesized beam). In the case of the individual vector sensor, we can use $\Omega = 4\pi$.

The SEFD for HeRO-S is therefore the quadrature sum of galactic noise and antenna noise. Figure 7-10 shows antenna nosie in dark blue, galactic noise in red, and the quadrature sum in black. The curves have been adjusted downward by a factor of 2 to convert from single antenna to full vector sensor, $\sqrt{2}$ in order to represent a single HeRO-S baseline (2 vector sensors), and $\sqrt{8000}$ for a integration time-bandwidth (BΔt) product of 8000.

HeRO-G uses an LWA-derived antenna [83] for low frequencies and the SKALA antenna [64] for higher frequencies. The SEFD for the LWA antenna/receiver was

calculated by fitting a power law to data available in [83], Fig. 3. The SEFD for the SKALA antenna was provided by Eloy de Lera Acedo[9]. The same BΔt shift was applied to the LWA and SKALA SEFD. The LWA SEFD/sensitivity curve is shown in dotted green and the SKALA curve in dotted cyan in Figure 7-10. Each curve represents a single baseline (2 antennas).

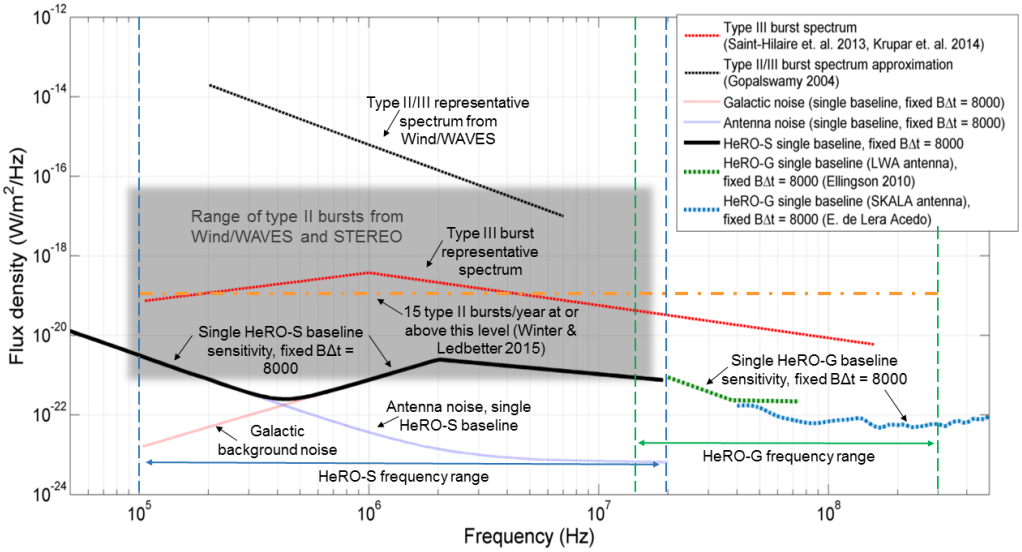

Figure 7-10: HeRO Sensitivity compared with expected solar radio burst flux. A single baseline of HeRO-S or HeRO-G will detect type II and III solar bursts over several decades of intensity and frequency. Shown for comparison are an average type III burst spectrum, scaled to an occurrence rate of 3 bursts per day (red) [161, 254]; the range of type II bursts recorded by Wind/WAVES and STEREO over several years (gray box) [320]; the intensity of both type II and type II bursts observed by Wind/WAVES (black dashed) [113]; HeRO-S SEFD (solid black), the quadrature sum of antenna noise (dotted blue) and galactic background (dotted red) assuming a time-bandwidth product BΔt= 8000; HeRO-G SEFD for LWA antenna (green [83]) and SKALA antenna (cyan [64]). HeRO-G sees substantially less galactic noise than HeRO-S because of the limited field of view.

The HeRO sensitvity plot (Figure 7-10 also shows a range of estimates for the flux of type II and III radio bursts. The large gray shaded box represents the range of frequency and intensity of type II radio bursts observed by Wind/WAVES and STEREO [254]. Spectral information was not available for the data in [254]. An average spectrum of type III radio bursts was generated from data in [161] (red

[9]Private communication, 10/10/16.

dotted curve). Krupar et al. (2014) [161] also provided occurrence rate statistics for type III radio bursts. The flux level of the red dotted curve is consistent with an occurrence rate of 3 per day. The orange curve shows the average flux level for type II bursts with an occurrence rate of 15 per year [320]. The final curve (dotted black) is a spectrum of type II/III bursts found in [113], Fig. 15.1. This curve disagrees with the flux levels of a large sample of type II bursts indicated by the gray box. Multiple attempts to contact the author and determine the source of the disagreement were unsuccessful, so the curve has been included for completeness.

HeRO will be able to provide additional statistics on the occurrence rates, occurrence vs. intensity, and spectral characteristics of type II and III radio bursts. HeRO will able to detect nearly all type II and III radio bursts represented in Figure 7-10 over their entire frequency range. HeRO will have a single baseline SNR of at least 30 for all frequencies for type III radio bursts represented by the average spectrum (red dotted curve) if a $B\Delta t$ product is maintained. The bandwidth and integration time for $B\Delta t = 8000$ at 20 MHz are 40 kHz and 0.2 sec (maintaining a 0.2% fractional bandwidth). At 100 kHz, B = 200 Hz and $\Delta t = 40$ sec. Larger fractional bandwidths may be allowed at lower frequencies.

Interferometric Simulation

This section describes interferometric modeling for HeRO-S. Some of the modeling tools were modified from work described in [160]. HeRO-S orbit design was done by Arthur Lue of MIT Lincoln Laboratory. Here I have simulated the HeRO-S orbits in STK [10] based on orbital elements provided by A. Lue. The orbit configuration is referred to as skew-GEO (geostationary). The orbits are slightly inclined relative to the equatorial plane as well as slightly eccentric to avoid crossing the heavily populated GEO belt, which is home to many commercial and government spacecraft. The HeRO-S orbits therefore have the stability and stationarity of traditional GEO orbits without the regulatory burden of operating safely in the GEO belt.

Given orbital parameters, STK evolves the orbits through time and reports po-

[10]System Tool Kit by AGI. See https://www.agi.com/products/engineering-tools

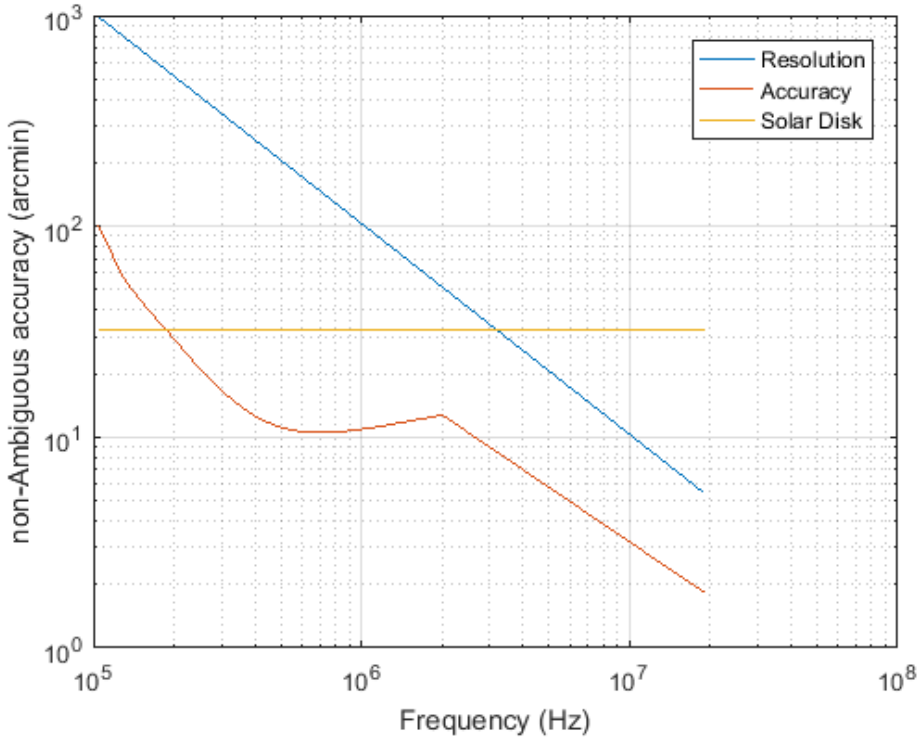

Figure 7-11: HeRO spot map accuracy as a function of frequency. Spot map accuracy depends on signal-to-noise ratio (SNR), so the red curve varies according to the difference between HeRO-S SEFD (Figure 7-10, black curve) and the average type III burst spectrum (Figure 7-10, red dotted curve). The resolution is simply λ/D for the array, assuming the maximum baseline (D) is 10 km.

sitions in cartesian coordinates. I imported those coordinates into MATLAB, transformed them into a coordinate system centered in the HeRO-S array, and computed (u, v, w) coordinates for each timestep. I then flattened the (u, v, w) coordinates into (u, v) coordinates in a plane perpendicular to the direction of the Sun. Instantaneous (u,v) positions of HeRO-S at 20 MHz are shown in Figure 7-12; (u,v) coverage for HeRO-S at 20 MHz over 24 hours is shown in Figure 7-13. Reducing the number of active HeRO-S satellites degrades the PSF and introduces additional ambiguities. Figure 7-14 shows the PSF resulting from instantaneous (u,v) positions of 4 HeRO-S satellites; Figure 7-15 shows the improved PSF when all 6 satellites are used.

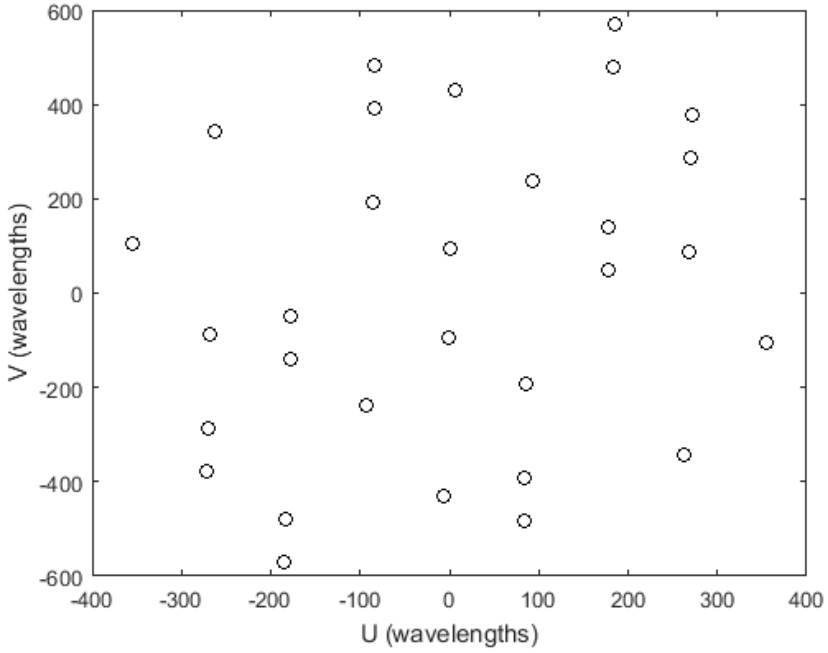

Figure 7-12: UV plane coverage (instantaneous) for HeRO-S at 20 MHz

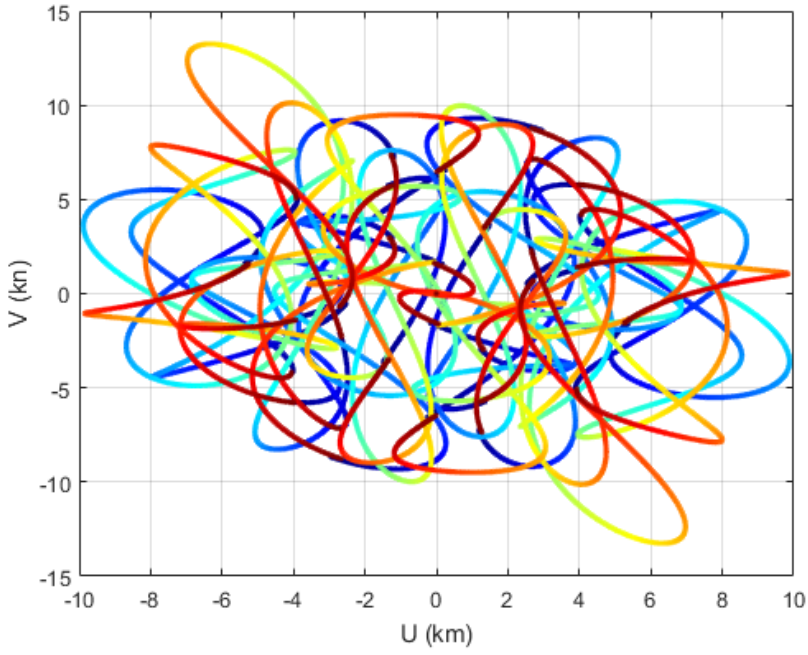

Figure 7-13: UV coverage over 24 hours (20 MHz)

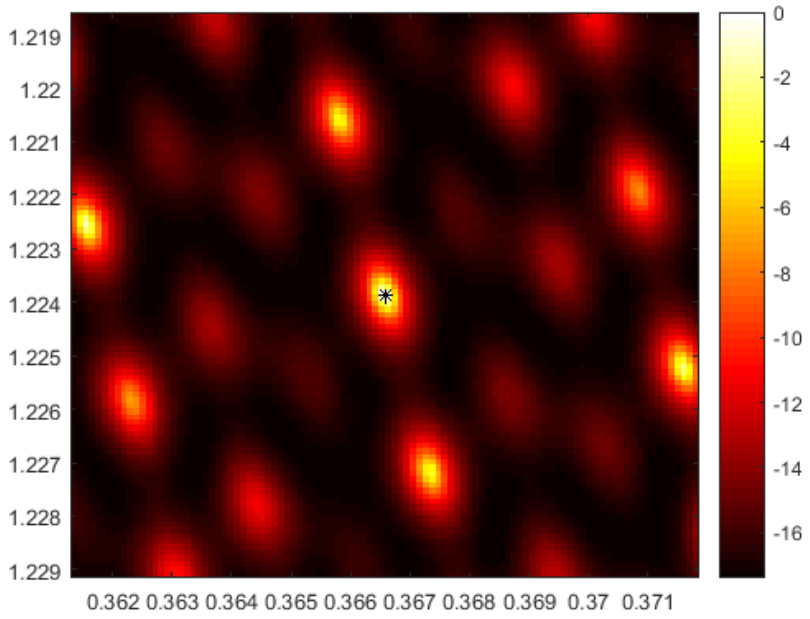

Figure 7-14: HeRO-S PSF, 4 satellites

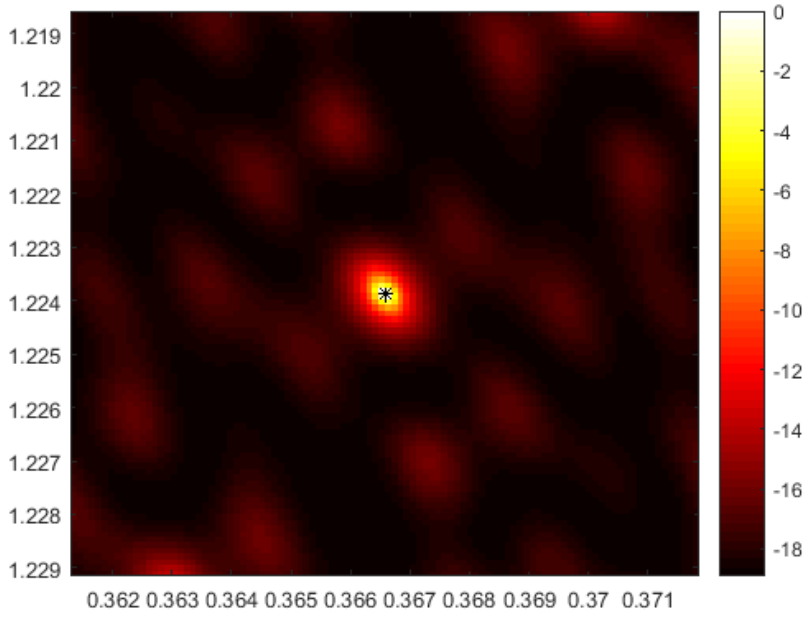

Figure 7-15: HeRO-S PSF, 6 satellites

7.4.4 HeRO Secondary Science Goals

HeRO's primary mission is focused on heliophysics, but this novel instrument presents an opportunity to do other solar system radio science as well. Since each HeRO

element sees the whole sky all the time, it can be digitally 'pointed' at any target during calibration on the ground. Below are two secondary science goals for HeRO.

Studying radio emissions from Jupiter and the other outer planets. Jupiter's radio flux is often within an order of magnitude of solar bursts [117], and readily observable with HeRO. HeRO has the unique capability to observe remotely both the initiation of IPM disturbances (via type II bursts) propagating toward Jupiter and the resulting radio emission when the disturbances interact with Jupiter's magnetosphere.

Saturn's radio emission has been monitored by Cassini for over a decade, revealing intriguing variations in the modulation periods of kilometric radiation from the northern and southern magnetic poles [124]. When Cassini completes its 'Grand Finale' and dives into Saturn, there will be no instrument monitoring the continuing evolution of SKR periodicity.

Imaging of the galactic synchrotron background, and the absorption structures at HF frequencies. Since the structures are static, both sensitivity and (u, v) coverage can be built up over time during the spacecraft orbit, and as the orbits slowly evolve. All-sky mapping at HeRO's frequency range would provide the first such maps with resolution greater than 60°. Such maps offer the tantalizing possibility of serendipitous discoveries, a feature of all past mapping efforts that opened up a new window in the electromagnetic spectrum. In more practical terms, HeRO's all-sky maps would provide important constraints on scattering and absorption in the interstellar and interplanetary medium (ISM/IPM). Measuring the effects of the ISM/IPM on sources outside the solar system will inform the design of larger space-based low frequency interferometers.

7.5 Conclusions and Next Steps

HeRO is not sufficiently sensitive to detect exoplanetary radio emission, though it may be useful for solar system planetary radio emission, particularly for Jupiter and Saturn (see above). It is a stepping stone, however, to larger space-based arrays that could be capable of detecting radio emission from nearby exoplanets. The most

important feature of the vector sensor described above is that it is twice as sensitive as a comparable crossed dipole, meaning that an array of vector sensors requires half the number of elements for a given sensitivity. As shown in Figure 1-5, the entire population of exoplanets with magnetic field weaker than Jupiter's (assuming such exoplanets exist, as they do in the Solar System) will be left out if they are not suitably situated to modulate the radio emission of their host stars. To access this population, and learn about the magnetic fields of terrestrial planets from a larger sample than the solar system can provide, space-based observation is the only way forward. The requirements for a space-based array capable of detecting Earth-like magnetic fields is discussed in the next chapter, section 8.3.2.

Chapter 8

Summary and Conclusions

8.1 Contributions to Exoplanetary Radio Astronomy

Three different approaches were used in this work in an effort to detect radio emission from exoplanets. Chapter 3 described a systematic approach to searching for exoplanetary (or stellar) radio emission from nearby systems in archival radio survey data. The limits obtained are shown in Figure 8-1. The key contribution of the work described in Chapter 3 was a flexible tool that can be used on any radio (or other wavelength) survey for which images are available. As an example, the framework developed for radio exoplanet searches has been used to look for 'Planet 9' [18] across radio, IR, and optical catalogs[1]. Fully utilizing survey image data rather than just source catalogs highlights systems that require follow-up and can also be used to identify problematic systems for targeted observations, such as systems with a bright radio source nearby.

Chapters 4 and 5 focus on targeted observations. Chapter 4 describes a survey that set stringent limits on radio flux at 1-4 GHz from the nearest star systems. The original goal of the Nearest Stars survey was to search for and set limits on radio emission from yet-unknown exoplanets with no preconceptions about which stars were

[1]Work carried out by C. Minsky (UROP) under supervision of M. Knapp and B. Weiss.

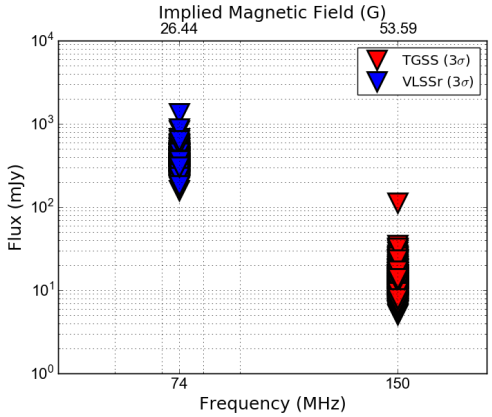

(a) Flux upper limits for nearby exoplanets

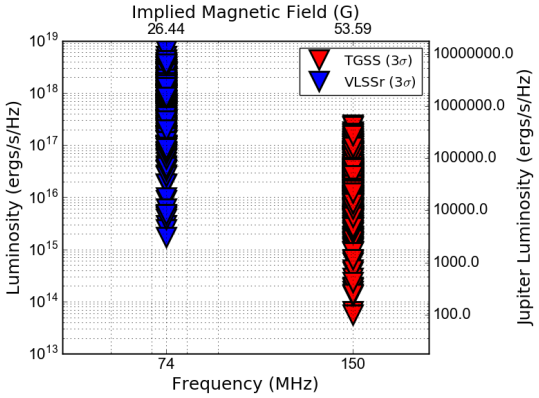

(b) Luminosity upper limits for nearby exoplanets

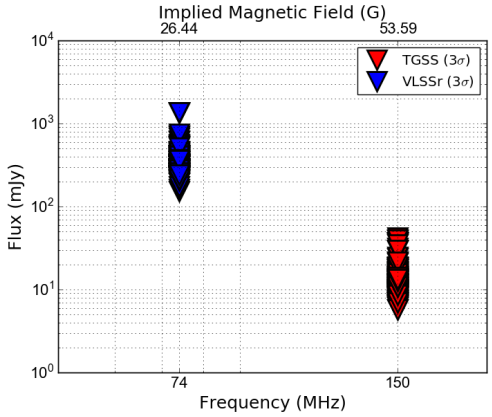

(c) Flux upper limits for stars within 8 pc

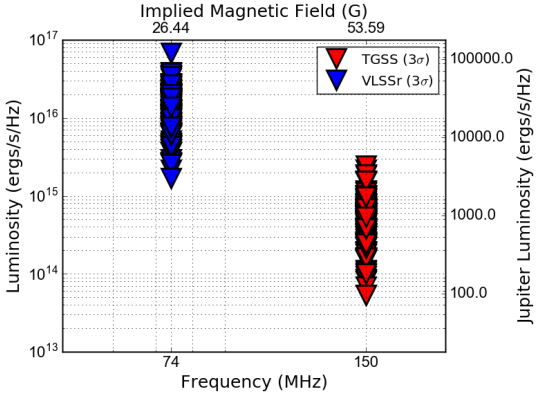

(d) Luminosity upper limits for stars within 8 pc

Figure 8-1: Upper limits on radio flux (left) and luminosity (right) from archival survey data (reproduced from Chapter 3, Figures 3-24 and 3-10). Panels a and b show limits for the 100 pc exoplanet host sample; panels c and d show limits obtained for the 8 pc nearby stars sample. Blue downward triangles represent 3σ limits at 74 MHz derived from VLSSr. Red downward triangles represent 3σ limits at 150 MHz derived from TGSS ADR1. The top horizontal axis on all plots indicates the magnetic field strength implied by the observing frequency assuming that emission is at the cyclotron frequency (see Equation 1.1). The right hand vertical axis on panels b and b compares the luminosity values on the left vertical axis with Jupiter's luminosity at $\sim$30 MHz.

most likely to host planets. The survey produced limits on quiescent stellar flux for four objects, several of which had no published limits at 1–4 GHz. Limits for the five objects observed with the VLA are summarized in Figure 8-2. The limits obtained also ruled out radio emission greater than 10x Jupiter's flux for any substellar companions, at least during the observations. One of the objects for which limits were set was

a very recently discovered low mass (T9) brown dwarf with no previously reported radio observations at any frequency. A series of bright radio flares was detected from the M dwarf binary system Ross 614. Additional survey data from LOFAR and VLA P-band will add to the comprehensive limits compiled for the survey objects. Future survey observations will be longer to increase the chances of detecting periodic radio emission.

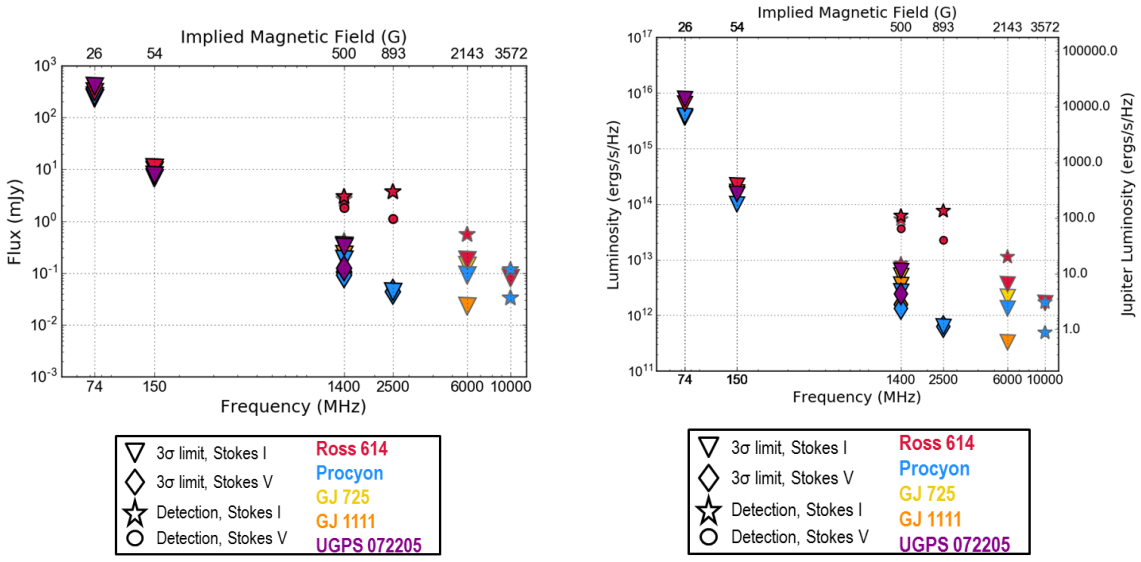

(a) Flux limits and detections

(b) Luminosity limits and detections

Figure 8-2: Upper limits on radio flux (left) and luminosity (right) for five nearby stars derived from VLA observations (Ch. 4), survey data (Ch. 3), and literature (reproduced from Chapter 4, Figure 4-6). Marker shapes represent the type of limit or detection; marker colors indicate the object observed. Limits for 74 and 150 MHz are derived from the archival search described in Chapter 3. Limits and detections for 1.4 and 2.5 GHz are from this work and from literature (see Tables 4.4.3, 4.4.3). All higher frequency detections/limits are from literature.

Observations of eccentric hot Jupiter HD 80606 b introduced yet another observation strategy: orbital phase targeting. This strategy addresses the challenge of optimizing observations to times (orbital phases) when exoplanetary radio emission is expected to be at a maximum. In the case of eccentric planets, that time is before, during, and after periastron when the stellar wind is most intense. LOFAR LBA observations of HD 80606 b near planetary periastron produced the lowest limits ever at LBA frequencies. All available limits for HD 80606, including from this work,

are summarized in Figure 8-3. The challenges of ionospheric calibration encountered while reducing the LOFAR LBA HD 80606 b data highlight the need for innovative approaches to ionospheric calibration. New observations of a recently discovered HD 80606 b analog (HD 156279 b) that is much closer to the Solar System have been carried out and data reduction on this promising system is in progress. HD 156279 b offers the opportunity to set more tightly constraining limits on physical processes than is possible for the more distant HD 80606 b.

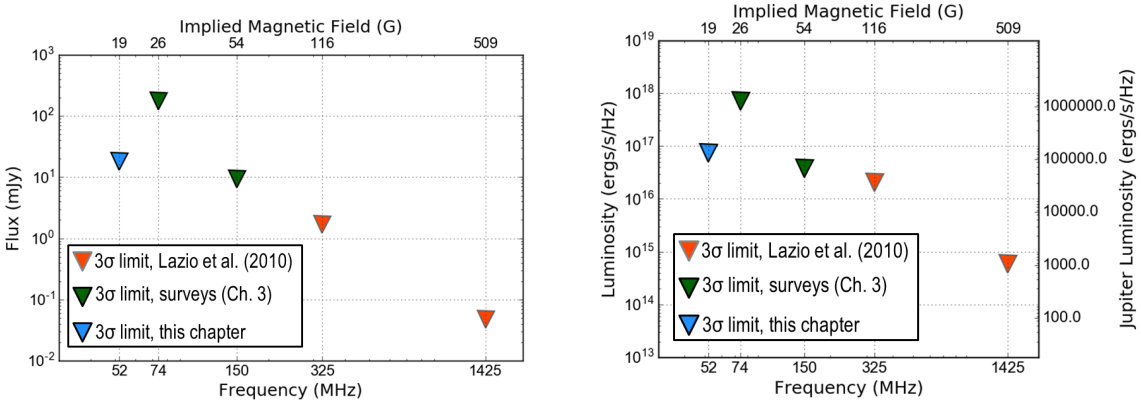

(a) Flux limits

(b) Luminosity limits

Figure 8-3: Flux (a) and luminosity (b) limits for HD 80606 (reproduced from Chapter 5, Figure 5-16). Red downward triangles represent limits from VLA measurements by Lazio et al. (2010) [170], green downward triangles represent limits derived from survey data (Chapter 3), and the blue downward triangle represents the limit obtained from LOFAR data as described in Chapter 5.

Looking to the future, Chapter 6 describes an exciting newly discovered multi-planet system, TRAPPIST-1, that offers the best opportunity to date to constrain the magnetic fields of small, Earth-sized planets. Detecting the Earth's magnetic field scaled to the distance of TRAPPIST-1, is difficult; perhaps impossible (see Section 8.3.2). The alternative is to detect planetary magnetic fields indirectly via planet-induced modulation of stellar radio emission. This Io-Jupiter type interaction seems plausible for the inner two TRAPPIST-1 planets (b, c) and has several advantages for observations. The radio emission that must be detected is the star's rather than the planet's, so it is likely to appear at higher frequencies due to the strong magnetic field of the star (Eq. 1.1). The phases at which planet-modulated/enhanced stellar

emission is most likely to be visible from Earth are also predictable, leading to another orbital phase targeting strategy developed in this work. The observation strategy developed for the TRAPPIST-1 system is also applicable to other M dwarf planetary systems, especially active M dwarfs with strong magnetic fields. Chapter 6 also lays the groundwork for thermal evolution modeling that can be used to make testable predictions about which planets are likely to have thermally driven dynamos in their cores. If radio detections of exoplanets (or limits) are to be useful, they should be used to constrain interior models and to extract information about the structure and history of the planet. This is a major area of future work in this field.

The future of low frequency radio instrumentation is explored in Chapter 7. The highly capable vector sensor is introduced as an alternative array element to the traditional crossed dipoles. The key contribution in Section 7.3 is the development and testing (in simulation and the field) of all-sky imaging algorithms for a single vector sensor that can be applied to astronomical observations. Chapter 7 also describes a proposed space mission using the vector sensor that will both perform novel tracking of solar radio bursts as they traverse the heliosphere and will serve as a pathfinder toward larger space-based low frequency interferometers applicable to exoplanet searches.

8.2 Limitations of upper limits

The flux and luminosity upper limits presented here, though the best available for most objects studied, are limited in several important ways. Note that non-detections in radio are translated into upper limits on planetary magnetic field (as in Figure 8-4) by assuming that the reason for the non-detection is that the observing frequency is above the cut-off frequency of the planet's CMI emission. Flux and luminosity limits, on the other hand, require no such assumption and simply state an upper limit on radio flux from a region around an exoplanetary system.

First, upper limits on radio emission (and magnetic field) are valid *only during the observations(s).* Assuming exoplanetary radio emission is similar to Solar System planetary radio emission (or even brown dwarf radio emission), it is expected to

be highly variable in time. A non-detection and resulting limit do not conclusively rule out radio emission from the observed system; only continuous monitoring over months to years with high sensitivity can provide a truly constraining limit on radio emission from nearby systems. The combination of high sensitivity and continuous temporal monitoring is not possible with current instruments due to both demands for observing time for other applications and their Earthbound nature — sources cannot be observed when they are below the horizon. Until a high sensitivity space-based array exists, or there are multiple high sensitivity ground-based telescopes distributed in both longitude and latitude, all limits on exoplanetary radio emission will come with the temporal variability caveat.

The second limitation is sensitivity. Figure 8-4 (a) plots all available limits and detections of exoplanets, brown dwarfs and late M dwarfs against mass and average magnetic field. Both the size and color of the symbols indicates how constraining the limit is in terms of Jovian luminosity; larger, lighter colored symbols indicate poorer constraints. The problem is particularly acute for exoplanet systems that are far away, highlighting the need to focus on nearby systems in order to generate the most meaningful limits. Only for nearby systems (or high frequency, were planetary emission is less likely) do the available limits approach Jovian luminosity. A limit that is many orders of magnitude above Jupiter's luminosity constrains the most extreme scenarios for exoplanetary radio emission, but cannot rule out Solar System-like exoplanetary magnetic fields and radio emission. While longer observations and/or stacking many observations can increase sensitivity and therefore improve limits in the case of non-detection, existing arrays are limited at low frequencies either by inability to completely calibrate for ionospheric effects or confusion. The SKA1-Low will be a major step forward in sensitivity and should provide constraints on exoplanetary radio emission for scenarios more closely resembling Solar System planets.

Comparing existing limits to Jovian luminosity is imperfect as well. Comparing non-detection luminosity limits to Jovian luminosity is valid in the regime where the emission mechanism of the planet being observed is expected to be the same as Jupiter's radio emission mechanism (CMI at low frequencies). This assumption

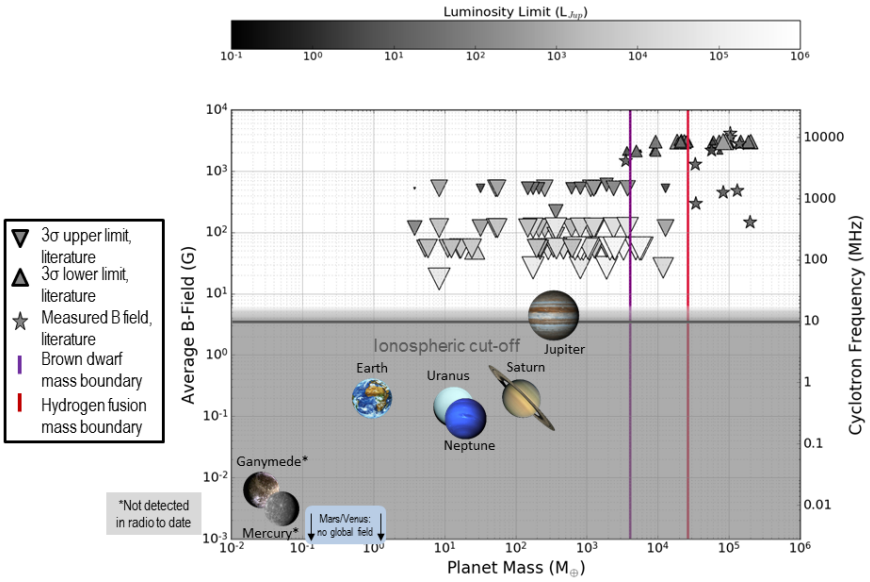

(a) Literature limits

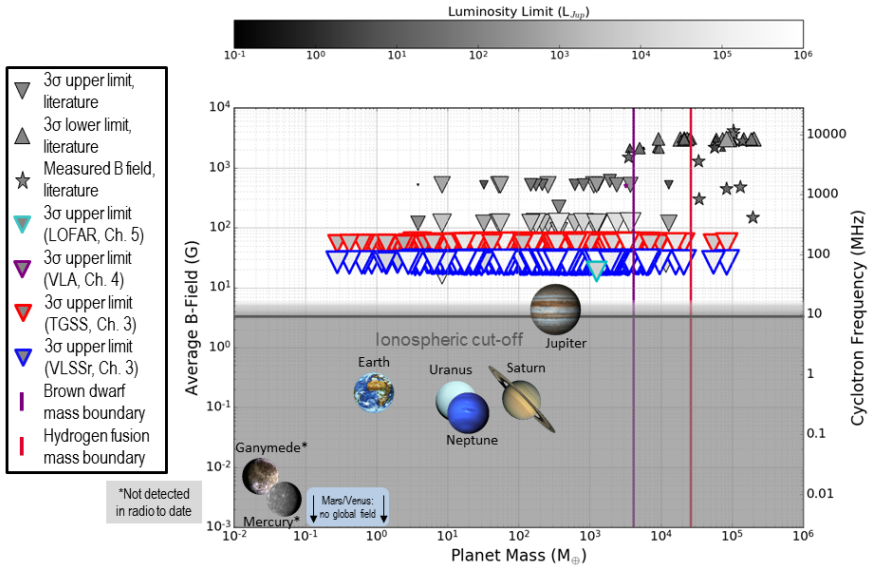

(b) Limits from this work

Figure 8-4: Limits on exoplanet magnetic fields via radio observation from literature (a) and chapters 3, 4, 5 of this work (b). The size and color of the limit/detection symbol indicates how constraining it is in terms of Jovian luminosity. Larger, lighter symbols indicate less constraining limits. Solar System planet magnetic fields are shown for comparison. A sample of brown dwarfs and late M dwarfs with measured magnetic fields are included for context as star symbols. Lower limit symbols (upward triangles) indicate a detection of radio emission from a system, but not a detection of the cut-off frequency. The limits from exoplanet radio observation campaigns shown here are listed in Table 1.3.2. Limits from an MWA exoplanet survey [209] are also included, as well as brown dwarf/M dwarf limits from [149] and [127] and references therein.

may indeed be valid for brown dwarfs [127], though it is unclear how far up the H-R diagram that assumption holds, and whether it is valid for all brown dwarfs. Jupiter's CMI radio emission cuts off sharply above ∼40 MHz (Figure 1-3), so comparing Jovian luminosity to limits from higher frequency observations is perhaps not ideal. Until the luminosity of a planet more massive than Jupiter, but not yet a brown dwarf, is measured, however, there is little else to use for context and comparison.

Finally, there is the problem of multiple potential radio emitters in a single stellar system. The host star, stellar companions, and sub-stellar (planetary) objects are capable of producing radio emission by the CMI or other mechanism. Non-detection limits, therefore, apply to all bodies in a stellar system since low frequency telescopes do not have the angular resolution to separate host stars from their planets. Figure 8-4 contains one symbol for each planet in a stellar system, with the limit for each derived from the same observation. Non-detections are not planet-specific, but there is hope that detections could be. Temporal modulation will be key to determining which body in a stellar system is the source of detected radio emission (see Section 2.2.2). Only with a positive detection can an upper limit (or magnetic field measurement if the cut-off is detected) be assigned to a specific exoplanet or star.

One positive feature of radio observations compared to optical measurements is that background sources are much less likely to contaminate observations of nearby exoplanetary systems. Exoplanetary radio observations are focused on 1) detecting flux from the position of a known star and 2) using temporal modulation of the signal to determine whether it originates from the star or a planet in the system. Background radio sources are much less likely to be variable than stars at visible/IR wavelengths. This is because the vast majority of background radio sources are extra-galactic and effectively constant on short timescales. Foreground sources, like radio emitting stars or supernovae remnants, are rare compared to background stars in visible light. Background radio stars are unlikely to contribute significantly even if they are near the target system since distance dilution will significantly attenuate their flux. Confusion-limited instruments have a constant background level that limits sensitivity, but the fact that the background is *constant* is a boon to the search

for bursty exoplanetary radio emission.

8.3 The Path Forward

No radio exoplanet detections were made in this work despite using a wide range of observing strategies, instruments, and data reduction techniques. The non-detections presented here highlight the magnitude of the challenge that exoplanetary radio emission presents. The difficulties presented by the ionosphere alone beg the question: should we give up on ground-based radio exoplanet searches and focus solely on space? The conclusion from this work is: not yet. One key reason not to give up on ground-based observations just yet is that low-frequency radio astronomy appears to be experiencing a Renaissance, at least as measured by the construction and planning of new observatories. The SKA-Low in particular is very promising *if* the state of the art in ionospheric calibration is sufficiently advanced to reach near-thermal noise levels.

Another promising avenue for ground-based observation is searching for star-planet interaction, using Io-Jupiter as a model. Nearby stars with known planets, like TRAPPIST-1, Prox Cen, GJ 411, and Luyten's Star are prime targets for orbital phase targeted observations. More planets around nearby stars are likely to be discovered in the near future. Radio stars have been detected since the early days of radio astronomy, so searching for periodic modulation in stellar radio emission that matches a known planetary period is not a large leap from current capabilities. The difficulty is obtaining sufficient observing time to detect such periodicity. Orbital phase targeting, modeled after the observing strategy for TRAPPIST-1, is one option for optimizing scarce observing resources.

8.3.1 Optimal Observing Strategy for Radio Detection of Exoplanets

The frequency, intensity, timing, and duration of exoplanetary radio emission (or planet-modulated stellar emission) are difficult to predict. The ideal ground-based observing program would therefore need to cover a wide range of frequencies (30 MHz to ∼10 GHz for planetary through stellar emission) and would continuously monitor the entire sky (or at least the n nearest stars) with very high sensitivity. Such a program would have no chance of missing an event due to temporal or frequency coverage gaps; it would be limited only by sensitivity.

Such a campaign is, of course, not possible for a number of reasons. Continuous frequency coverage over several decades would require multiple telescopes since technical requirements for telescope design vary widely over that range. LOFAR, an instrument designed for low frequencies, cannot observe efficiently at GHz frequencies just as the VLA, designed for GHz+ frequencies, is inefficient and insensitive at LOFAR frequencies. Primary element beam width shrinks when switching from dipoles to dishes for higher frequencies (and continues to shrink as λ/D as frequency increases), making continuous all-sky (or all-hemisphere) coverage at high frequencies impossible. Even continuous frequency observations are not possible at high frequencies since all the needed receivers cannot be at the telescope's focus at the same time. Finally, most large, highly sensitive telescopes have many users and cannot dedicate all of their observing time to a single science goal.

Clearly, low frequency telescopes are better suited to continuous, wideband, all-sky/hemisphere monitoring than higher frequency dish-based telescopes. Fully cross-correlated arrays which can image the full primary beam of the antenna element (usually a dipole) are ideal. Data and computational volumes increase rapidly with the number of antennas, but a large number of antennas are required for high sensitivity. It is for this reason that the largest existing and planned low frequency arrays are hierarchical, beamforming a modest number of antennas into stations with narrower primary beams than their constituent dipoles and then cross-correlating a manage-

able number of stations. Only the relatively small (in number of dipoles) LWA and OVRO LWA are fully cross-correlated all-sky imaging arrays.

All-sky survey telescopes like the OVRO LWA[2] (Hallinan 2014 [126], see also [5]) are critical in the search for exoplanetary radio emission. Targeted observations, though potentially more sensitive if conducted with larger telescopes, are blind to most of the sky. Given the very faint signal from average or quiescent Jovian emission at even a few pc (Figure 4-1), there is a better chance of detecting a nearby planet when it experiences a radio burst and briefly increases in brightness by an order of magnitude or more. Bright bursts, often caused by a massive, fast stellar CME hitting the planetary magnetosphere (Section 1.2.3), are rare. The best way to increase the chance of catching one of these rare events is to monitor the whole sky continuously. The increase in sky area that can be monitored offsets the reduced sensitivity of a smaller telescope. All-sky monitoring therefore has a good chance of producing the all-important first detection of a radio exoplanet.

The advantages and limitations of current and planned low frequency telescopes suggest the following strategic considerations for exoplanet observations:

1. The most sensitive available telescopes should be used (currently LOFAR, eventually SKA-Low) to maximize the opportunity to detect exoplanetary radio emission in the targeted observation regime.

2. The design of large low frequency telescopes like LOFAR require targeted observations of finite duration. The closest stars should be targeted since they offer the best chance of detecting a Jupiter-like flux from an exoplanet (see Figure 4-1).

3. Exoplanets are common, so even nearby systems without currently known exoplanets should be targeted.

4. Systems with known planets should be prioritized, however, since orbital targeting optimizes observing time.

[2] http://www.tauceti.caltech.edu/LWA/

5. Observations should last as long as is practical given the target elevation. Circumpolar targets that stay higher than ∼30 degrees elevation at all times are most valuable since these targets can be observed for as long as the telescope time allocation committee will permit.

6. The exoplanet community should advocate for and support large, fully cross-correlated all-sky imaging low frequency telescopes; an expansion of the OVRO LWA concept with enhanced sensitivity[3] is ideal for radio exoplanet searches.

Higher frequencies (>500 MHz), can only practically be used for either follow-up once a detection is made at low frequency or smaller, targeted surveys with non-continuous temporal coverage (preferably simultaneous with lower frequency observations). One niche where high frequency observations are valuable is the search for star-planet interaction in known exoplanet systems. In this case, it is the modulated stellar emission that we hope to detect, not exoplanetary radio emission directly. Most stars, especially M-dwarfs, have stronger magnetic fields than Solar System planets, so they will emit at higher frequencies than planets. The high sensitivity and relative ease of data reduction at higher frequencies are boons to the search for exoplanetary modulation of stellar radio emission (see Section 1.2.4 and Chapter 6). Observations searching for star-planet interaction should take advantage of orbital targeting while also maximizing the length of each individual observation within the constraints of telescope oversubscription and target elevation. High frequency observations are also useful for detecting stellar flare activity and using it to characterize the interplanetary environment around known planets.

While high frequency observations are optimal primarily for either follow-up or orbital targeting of known systems expected to show star-planet interaction, occasional 'blind' observations of the nearest stars are valuable for seeking the unexpected. Longer observations than the ∼5 minute scans used in Chapter 4 are preferred, even if the number of observations must be reduced in compensation. Only very nearby

[3]One important caveat is that a larger (in physical extent and number of elements) OVRO LWA will require advanced ionospheric measurement and calibration since it will fall solidly into Lonsdale regime 4 (see Figure 2-4).

stars should be observed in this 'blind' manner to maximize the chance of detecting something and avoiding the waste of valuable telescope time. There are only 54 stellar systems within 5 pc, and only ∼30 of those are north of -10° declination, so it is indeed feasible to survey nearby stars 'blindly' over a period of several years.

The above discussion focused on ground-based arrays only. Any future space-based array should be a fully cross-correlated imaging array and will have the advantage of observing the full celestial sphere. Such an array should cover a wide bandwidth that spans the lowest practical frequency given scattering/broadening (see Section 8.3.3) to a high frequency that overlaps with ground-based instruments (perhaps 30 MHz). The low data rates implied by very low frequencies (relative to higher frequency ground-based arrays) should allow near-continuous temporal coverage and full frequency coverage across the band described above. A space-based array, assuming it has enough elements to be sufficiently sensitive, meets nearly all of the wishlist criteria described at the beginning of this section. Coordinated observations with ground-based telescopes whenever possible would fully optimize exoplanetary radio observations with a space-based low frequency telescope.

8.3.2 Requirements to Detect Earth- and Jupiter-Analogs in the Solar Neighborhood

Detecting exoplanetary radio emission with existing ground-based instruments requires that exoplanets are different from Solar System planets in at least one of the following ways:

1. Magnetic field stronger than Jupiter so that radio emission can be detected at higher frequencies where there is higher sensitivity

2. Radio flux is enhanced relative to Jovian flux by stronger forcing from the solar wind

In order to quantify what is required to detect Earth or Jovian analogs in the Solar neighborhood (defined here as 5 pc), it is best to avoid invoking any of the special

conditions above and simply scale the known flux of Earth or Jupiter to 5 pc and derive requirements from those values. Using simple scaling to set requirements ensures that observations will be complete at least to the level of known Solar System planets.

Jupiter's flux scaled to 5 pc is 10 μJy. Earth's radio flux is a factor of $\sim$10 lower than Jupiter's (see Figure 1-2), so the Earth's flux at 10 pc is $\sim$1 μJy. Following the sensitivity calculation in Jester & Falcke (2009), Figure 4 [145], an array of 5×10^5 crossed dipoles (or other electrically small, non-resonant antenna) is required to detect Jupiter (1-σ) at 5 pc and 5×10^6 are required to detect the Earth at the same distance. Even with a more sophisticated antenna like the vector sensor reducing those numbers by a factor of two, a formidable array is required to detect planets out to 5 pc.

Though the numbers are daunting, it is important to note that the SKA is aiming for similar numbers of antennas (2.5×10^5 for SKA1-Low). SKA1-Low, with a minimum observing frequency of 50 MHz, should be capable of detecting planets with magnetic fields just slightly stronger than Jupiter's within 5 pc [335] Whether or not the SKA1-Low detects exoplanets, lessons learned and techniques developed will pave the way for the massive space-based array needed to fully explore exoplanetary radio emission in the solar neighborhood.

The high hurdles to direct detection of Earth-like (or even Jupiter-like) radio emissions from exoplanets themselves suggest that the indirect detection approach (star-planet interaction) should be pursued vigorously. In the indirect case, it is the star's radio emission that is detected, not the planet's. Stars have stronger magnetic fields than (known) planets, and therefore emit at higher frequencies that suffer less from scattering. Stellar radio flux is generally higher as well (Ross 614's flux is >100x Jupiter's). These factors make indirect detection of exoplanetary magnetic fields the most promising path forward.

8.3.3 Fundamental Limitations for Ground- and Space-Based Radio Exoplanet Observations

Ground-based observations are fundamentally limited by the ionospheric cut-off frequency (see Section 1.2.1). For most of the Earth, most of the time, the ionospheric cut-off frequency ranges from 10-30 MHz. The ionospheric cut-off is typically lowest above the auroral ovals, near the poles. There are significant difficulties, however, in building and operating large radio arrays in the arctic/antarctic region, so practical ground-based telescopes are practically limited to a minimum observing frequency of $\sim$20 MHz. Observations at 20-30 MHz (and even above) are severely impacted by the ionosphere (see Section 2.5) due to scintillation, refraction, and scattering. Ground-based low frequency observatories can only approach their theoretical thermal noise sensitivity limit if extensive ionospheric monitoring and calibration are employed. LOFAR, the largest interferometer operating at 20-30+ MHz, has not yet approached its theoretical sensitivity limit due to ionospheric effects, so more work is required before ground-based radio telescopes can perform optimally near the ionospheric cut-off. Future low frequency telescopes like SKA1-Low should be very carefully designed to ensure that ionospheric effects can be mitigated.

For space-based low frequency radio observatories, are additional challenges beyond the sheer number of antennas required (see Section 8.3.2) and associated cost and complexity. First, the sky background noise due to galactic synchrotron emission peaks at 2 MHz. Earth-like magnetic fields will have their strongest auroral radio emission near 1-2 MHz, which is an unfortunate cosmic coincidence. Antennas with some directionality and/or nulling capability, like the vector sensor, will be helpful in the 1-2 MHz range because they can null towards the galactic center, cutting down on sky noise significantly.

At frequencies below 1 MHz, the interplanetary and interstellar medium begin to cause problems similar to ionospheric effects, but without the fast time variability. The ISM/IPM scatters, absorbs, and temporally/spatially broadens emission passing through it, with effects that get worse as the frequency of the radiation passing

through the medium approaches the plasma frequency of the medium. Scattering in the IPM/ISM will limit the longest useful baseline for a space-based array, which effectively limits the sensitivity because it sets the confusion limit.

Confusion is the condition where unresolved background sources below the detection threshold of the instrument set a noise floor above the theoretical thermal noise floor. For a confusion-limited instrument, longer integration times will not improve sensitivity beyond the confusion limit. The cure for confusion is to increase resolution, but scattering in the ISM/IPM will limit the benefit or longer baselines/higher resolution. In summary, if scattering in the ISM is as predicted, there is some fixed number of antennas beyond which adding more will not improve sensitivity any further at a given frequency. Exactly where this breakpoint occurs depends strongly on the actual scattering properties of the ISM, which are currently poorly constrained at low frequencies. HeRO (or a similar small low frequency space-based interferometer) may be able to contribute to refining our understanding of ISM/IPM properties at currently unexplored frequencies. See Jester & Falcke (2009), sections 2.4, 2.5 [145] for further discussion about IPM/ISM scattering and confusion.

All hope of detecting radio exoplanets with solar system-like magnetic fields is not lost, however. The very closest planets, like Proxima Centauri b [6] may rise above the scattering-enforced confusion limit. Also, the calculations above do not take strong bursts into account. Planetary radio bursts driven by solar weather can temporarily increase flux by several orders of magnitude. The benefits of bursts point toward an all-sky monitoring strategy for a space-based array, much like the OVRO LWA planet monitoring campaign [5]. Vector sensors are well suited to all sky monitoring, as are crossed dipoles or tripoles.

Finally, the free-free optical depth of ISM plasma goes to 1 within a few pc at very low frequencies (<100 kHz) [145]. This limits how far out into the galaxy a low frequency space-based instrument could 'see'. It will likely imposes strong limits on the detectability of magnetic fields weaker than the Earth's with peak emission frequencies below 1 MHz. It will also limit the ability to map out the low frequency spectrum of planets with Earth-like magnetic fields; the ISM will cut off the low

frequency end of the spectrum.

8.3.4 Steps Toward Detailed Characterization of an Exoplanetary Magnetic Field

Progress in direct exoplanetary radio detection and magnetic field measurement will likely follow a path similar to that of brown dwarf radio observations.

Step 1: Initial radio detection sets lower bounds on magnetic field strength if no cut-off frequency is detected.

Step 2: Follow-up studies with longer temporal coverage reveal properties like rotation period via repeating pulses of radio emission. Observations at different frequencies from the original detection may be needed to find the cut-off frequency and thereby measure the magnetic field strength of the planet/brown dwarf.

Step 3: Long term monitoring over months to years is then required to determine whether the rotation period measured is consistent and therefore definitely due to planetary rotation. Long term monitoring of the timing and polarization of radio pulses could reveal the topology of the magnetic field as well (dipolar vs. multipolar). Photometric/spectroscopic measurements of the host star's rotation period are critical to isolating the planetary rotation signature from any stellar contribution.

Step 4: A detailed study of polarization as a function of time and frequency as described by Hess & Zarka (2011) [135] (see Section 1.3.1). Detailed magnetic field characterization via polarimetric dynamic spectra will require higher sensitivity than initial detections because the exoplanetary radio emission must be detected (or detectable) in each time-frequency-polarization cell. Previous steps, especially step 1, can take advantage of binning in time and frequency to improve signal to noise, but this step requires at least an order of magnitude increase in sensitivity.

8.4 Final Thoughts

This field needs an unambiguous detection in order to move forward. Once an exoplanetary magnetic field is detected, either directly or indirectly through star-planet interaction, the field will blossom. This has happened before, notably with the first detection of an exoplanet around a Sun-like star [192] and more recently for gravitational waves [1] and multi-messenger astronomy [2]. Like exoplanet detection and gravitational waves, detecting the first radio exoplanet will require a sustained, dogged effort. The steps outlined in Section 8.3.1, based on the best available theory and observational experience, are designed to optimize the chance of making that critical first detection. Once the first detection is made, larger observing programs using ground-based telescopes, as well as steps toward a "B_{Earth}" capable space-based telescope, will become more feasible.

Bibliography

[1] B. P. Abbott and E. Al. Observation of Gravitational Waves from a Binary Black Hole Merger. *Physical Review Letters*, 116(6):061102, 2 2016.

[2] B. P. Abbott and E. Al. Multi-messenger Observations of a Binary Neutron Star Merger. *The Astrophysical Journal Letters*, 848(2):L12, 10 2017.

[3] J. K. Alexander and J. C. Novaco. Survey of the galactic background radiation at 3.93 and 6.55 MHz. *The Astronomical Journal*, 79:777, 7 1974.

[4] F. J. Alonso-Floriano, J. C. Morales, J. A. Caballero, D. Montes, A. Klutsch, R. Mundt, M. Cortes-Contreras, I. Ribas, A. Reiners, P. J. Amado, A. Quirrenbach, and S. V. Jeffers. CARMENES input catalogue of M dwarfs. I. Low-resolution spectroscopy with CAFOS. *Astronomy & Astrophysics, Volume 577, id.A128, 19 pp.*, 577, 2 2015.

[5] M. M. Anderson and G. Hallinan. Monitoring nearly 4000 nearby stellar systems with the OVRO-LWA in search of radio exoplanets. *AASTCS5 Radio Exploration of Planetary Habitability, Proceedings of the conference 7-12 May, 2017 in Palm Springs, CA. Published in Bulletin of the American Astronomical Society, Vol. 49, No. 3, id.401.02*, 49, 2017.

[6] G. Anglada-Escudé, P. J. Amado, J. Barnes, Z. M. Berdiñas, R. P. Butler, G. A. L. Coleman, I. de la Cueva, S. Dreizler, M. Endl, B. Giesers, S. V. Jeffers, J. S. Jenkins, H. R. A. Jones, M. Kiraga, M. Kürster, M. J. López-González, C. J. Marvin, N. Morales, J. Morin, R. P. Nelson, J. L. Ortiz, A. Ofir, S.-J. Paardekooper, A. Reiners, E. Rodríguez, C. Rodrguez-López, L. F. Sarmiento, J. P. Strachan, Y. Tsapras, M. Tuomi, and M. Zechmeister. A terrestrial planet candidate in a temperate orbit around Proxima Centauri. *Nature*, 536(7617):437–440, 8 2016.

[7] N. Astudillo-Defru, X. Delfosse, X. Bonfils, T. Forveille, C. Lovis, and J. Rameau. Magnetic activity in the HARPS M dwarf sample. *Astronomy & Astrophysics*, 600:A13, 4 2017.

[8] N. Astudillo-Defru, T. Forveille, X. Bonfils, D. Ségransan, F. Bouchy, X. Delfosse, C. Lovis, M. Mayor, F. Murgas, F. Pepe, N. C. Santos, S. Udry, and A. Wunsche. The HARPS search for southern extra-solar planets XLI. A

dozen planets around the M dwarfs GJ 3138, GJ 3323, GJ 273, GJ 628, and GJ 3293. *Astronomy & Astrophysics*, 602:A88, 6 2017.

[9] M. Audard, M. Gudel, J. J. Drake, and V. L. Kashyap. ExtremeUltraviolet Flare Activity in LateType Stars. *The Astrophysical Journal*, 541(1):396–409, 9 2000.

[10] H. Avenhaus, H. M. Schmid, and M. R. Meyer. The nearby population of M dwarfs with WISE: A search for warm circumstellar dust. *Astronomy & Astrophysics, Volume 548, id.A105, 15 pp.*, 548, 9 2012.

[11] J. I. Bailey, R. J. White, C. H. Blake, D. Charbonneau, T. S. Barman, A. M. Tanner, and G. Torres. PRECISE INFRARED RADIAL VELOCITIES FROM KECK/NIRSPEC AND THE SEARCH FOR YOUNG PLANETS. *The Astrophysical Journal*, 749(1):16, 4 2012.

[12] M. Barbieri, R. Alonso, S. Desidera, a. Sozzetti, a. F. M. Fiorenzano, J. M. Almenara, M. Cecconi, R. U. Claudi, D. Charbonneau, M. Endl, V. Granata, R. Gratton, G. Laughlin, and B. Loeillet. Characterization of the HD 17156 planetary system. 612:601–612, 2008.

[13] J. R. Barnes, J. S. Jenkins, H. R. A. Jones, S. V. Jeffers, P. Rojo, P. Arriagada, A. Jordan, D. Minniti, M. Tuomi, D. Pinfield, and G. Anglada-Escude. Precision radial velocities of 15 M5-M9 dwarfs. *Monthly Notices of the Royal Astronomical Society*, 439(3):3094–3113, 3 2014.

[14] J. R. Barnes, J. S. Jenkins, H. R. A. Jones, P. Rojo, P. Arriagada, A. Jordán, D. Minniti, M. Tuomi, S. V. Jeffers, and D. Pinfield. Red Optical Planet Survey: a new search for habitable earths in the southern sky. *Mon. Not. R. Astron. Soc*, 424:591–604, 2012.

[15] G. Basri, L. M. Walkowicz, N. Batalha, R. L. Gilliland, J. Jenkins, W. J. Borucki, D. Koch, D. Caldwell, A. K. Dupree, D. W. Latham, G. W. Marcy, S. Meibom, and T. Brown. Photometric Variability in Kepler Target Stars. Ii. an Overview of Amplitude, Periodicity, and Rotation in First Quarter Data. *The Astronomical Journal*, 141(1):20, 1 2011.

[16] T. S. Bastian, A. O. Benz, and D. E. Gary. RADIO EMISSION FROM SOLAR FLARES. *Annual Review of Astronomy and Astrophysics*, 36(1):131–188, 9 1998.

[17] T. S. Bastian, G. A. Dulk, and Y. Leblanc. A Search for Radio Emission from Extrasolar Planets. *The Astrophysical Journal*, 545(2):1058–1063, 12 2000.

[18] K. Batygin and M. E. Brown. EVIDENCE FOR A DISTANT GIANT PLANET IN THE SOLAR SYSTEM. *The Astronomical Journal*, 151:22, 2016.

[19] R. H. Becker, R. L. White, and D. J. Helfand. The FIRST Survey: Faint Images of the Radio Sky at Twenty Centimeters. *The Astrophysical Journal*, 450:559, 9 1995.

[20] M. Bentum and A. J. Boonstra. OLFAR - Orbiting Low Frequency Antenna for Radio Astronomy. *20th Annual Workshop on Circuits, Systems and Signal Processing, ProRISC*, pages 1–6, 2009.

[21] E. Berger. Flaring up All OverRadio Activity in Rapidly Rotating Late M and L Dwarfs. *The Astrophysical Journal*, 572(1):503–513, 6 2002.

[22] . Bhatnagar. Calibration and Imaging Challenges at Low Radio Frequencies: A Review of the State of the Art. *The Low-Frequency Radio Universe ASP Conference Series*, 407, 2009.

[23] E. K. BIGG. Influence of the Satellite Io on Jupiter's Decametric Emission. *Nature*, 203(4949):1008–1010, 9 1964.

[24] P. M. S. Blackett. The Magnetic Field of Massive Rotating Bodies. *Nature*, 159:658–666, 1947.

[25] J. J. Bochanski, A. J. Burgasser, R. A. Simcoe, and A. A. West. FIRE SPECTROSCOPY OF THE ULTRA-COOL BROWN DWARF, UGPS J072227.51054031.2: KINEMATICS, ROTATION AND ATMOSPHERIC PARAMETERS. *The Astronomical Journal*, 142:169–9, 2011.

[26] I. Boisse, F. Bouchy, G. Hébrard, X. Bonfils, N. Santos, and S. Vauclair. Disentangling between stellar activity and planetary signals. *Astronomy & Astrophysics*, 528:A4, 4 2011.

[27] X. Bonfils, X. Delfosse, S. Udry, T. Forveille, M. Mayor, C. Perrier, F. Bouchy, M. Gillon, C. Lovis, F. Pepe, D. Queloz, N. C. Santos, D. Ségransan, and J.-L. Bertaux. The HARPS search for southern extra-solar planets. *Astronomy & Astrophysics*, 549:A109, 1 2013.

[28] J. A. Bookbinder and F. M. Walter. A VLA survey of an X-ray selected sample of F dwarfs. In *Cool Stars, Stellar Systems, and the Sun*, pages 260–261. Springer Berlin Heidelberg, Berlin, Heidelberg, 1987.

[29] W. J. Borucki, D. Koch, G. Basri, N. Batalha, T. Brown, D. Caldwell, J. Caldwell, J. Christensen-Dalsgaard, W. D. Cochran, E. DeVore, E. W. Dunham, A. K. Dupree, T. N. Gautier, J. C. Geary, R. Gilliland, A. Gould, S. B. Howell, J. M. Jenkins, Y. Kondo, D. W. Latham, G. W. Marcy, S. Meibom, H. Kjeldsen, J. J. Lissauer, D. G. Monet, D. Morrison, D. Sasselov, J. Tarter, A. Boss, D. Brownlee, T. Owen, D. Buzasi, D. Charbonneau, L. Doyle, J. Fortney, E. B. Ford, M. J. Holman, S. Seager, J. H. Steffen, W. F. Welsh, J. Rowe, H. Anderson, L. Buchhave, D. Ciardi, L. Walkowicz, W. Sherry, E. Horch, H. Isaacson, M. E. Everett, D. Fischer, G. Torres, J. A. Johnson, M. Endl, P. MacQueen,

S. T. Bryson, J. Dotson, M. Haas, J. Kolodziejczak, J. Van Cleve, H. Chandrasekaran, J. D. Twicken, E. V. Quintana, B. D. Clarke, C. Allen, J. Li, H. Wu, P. Tenenbaum, E. Verner, F. Bruhweiler, J. Barnes, and A. Prsa. Kepler planet-detection mission: introduction and first results. *Science (New York, N.Y.)*, 327(5968):977–80, 2 2010.

[30] H. Bouy, J. H. V. Girard, E. L. Martín, N. Huélamo, and P. W. Lucas. Adaptive optics observations of the T10 ultracool dwarf UGPSJ072227.51-054031.2. *Astronomy & Astrophysics*, 526:A55, 2 2011.

[31] G. C. Bower, A. Bolatto, E. B. Ford, and P. Kalas. RADIO INTERFEROMETRIC PLANET SEARCH. I. FIRST CONSTRAINTS ON PLANETARY COMPANIONS FOR NEARBY, LOW-MASS STARS FROM RADIO ASTROMETRY. *The Astrophysical Journal*, 701(2):1922–1939, 8 2009.

[32] P. F. Bowers and M. R. Kundu. VLA search for radio emission from stars with solar-type structures. *The Astronomical Journal*, 86:569, 4 1981.

[33] T. S. Boyajian, K. von Braun, G. van Belle, H. A. McAlister, T. A. t. Brummelaar, S. R. Kane, P. Muirhead, J. Jones, R. White, G. Schaefer, D. Ciardi, T. Henry, M. López-Morales, S. Ridgway, D. Gies, W.-C. Jao, B. Rojas-Ayala, J. R. Parks, L. Sturmann, J. Sturmann, N. H. Turner, C. Farrington, P. J. Goldfinger, and D. H. Berger. Stellar Diameters and Temperatures II. Main Sequence K & M Stars. *The Astrophysical Journal, Volume 757, Issue 2, article id. 112, 31 pp. (2012).*, 757, 8 2012.

[34] D. A. Brain, F. Leblanc, J. G. Luhmann, T. E. Moore, and F. Tian. Comparative Climatology of Terrestrial Planets. In S. J. Mackwell, editor, *Comparative Climatology of Terrestrial Planets*, pages 487–501. University of Arizona Press, 2013.

[35] . Bremer. The Westerbork Northern Sky Survey (WENSS:) A Radio Survey Using the Mosaicing Technique. *Astronomical Data Analysis Software and Systems III*, 61, 1994.

[36] D. S. Briggs and D. S. High Fidelity Interferometric Imaging: Robust Weighting and NNLS Deconvolution. *American Astronomical Society, 187th AAS Meeting, id.112.02; Bulletin of the American Astronomical Society, Vol. 27, p.1444*, 27:1444, 1995.

[37] A. G. A. Brown and E. Al. Gaia Data Release 1. *Astronomy & Astrophysics*, 595:A2, 11 2016.

[38] L. A. Buchhave, D. W. Latham, A. Johansen, M. Bizzarro, G. Torres, J. F. Rowe, N. M. Batalha, W. J. Borucki, E. Brugamyer, C. Caldwell, S. T. Bryson, D. R. Ciardi, W. D. Cochran, M. Endl, G. A. Esquerdo, E. B. Ford, J. C. Geary, R. L. Gilliland, T. Hansen, H. Isaacson, J. B. Laird, P. W. Lucas, G. W. Marcy, J. A. Morse, P. Robertson, A. Shporer, R. P. Stefanik, M. Still, and

S. N. Quinn. An abundance of small exoplanets around stars with a wide range of metallicities. *Nature*, 486(7403):375, 6 2012.

[39] A. J. Burgasser and E. E. Mamajek. On the Age of the TRAPPIST-1 System. 6 2017.

[40] B. F. Burke. PROSPECTS FOR THE STUDY OF PLANETARY RADIO EMISSION. In *Planetary Radio Emission III*, pages 485–488, 1992.

[41] B. F. Burke and K. L. Franklin. Observations of a Variable Radio Source Associated with the Planet Jupiter. *Journal of Geophysical Research*, 60(2):213–217, 1955.

[42] M. R. Burleigh, F. J. Clarke, E. Hogan, C. S. Brinkworth, P. Bergeron, P. Dufour, P. D. Dobbie, A. J. Levan, S. T. Hodgkin, D. W. Hoard, and S. Wachter. The 'DODO' survey - I. Limits on ultra-cool substellar and planetary-mass companions to van Maanen's star (vMa?2). *Monthly Notices of the Royal Astronomical Society: Letters*, 386(1):L5–L9, 5 2008.

[43] J. O. Burns, J. Lazio, S. Bale, J. Bowman, R. Bradley, C. Carilli, S. Furlanetto, G. Harker, A. Loeb, and J. Pritchard. Probing the first stars and black holes in the early Universe with the Dark Ages Radio Explorer (DARE). *Advances in Space Research*, 49(3):433–450, 2 2012.

[44] R. P. Butler, S. S. Vogt, G. Laughlin, J. A. Burt, E. J. Rivera, M. Tuomi, J. Teske, P. Arriagada, M. Diaz, B. Holden, and S. Keiser. The LCES HIRES/Keck Precision Radial Velocity Exoplanet Survey. *The Astronomical Journal*, 153(5), 2 2017.

[45] J. C. Cain, P. Beaumont, W. Holter, Z. Wang, and H. Nevanlinna. The magnetic bode fallacy. *Journal of Geophysical Research*, 100(E5):9439, 1995.

[46] A. J. Cannon and E. C. Pickering. VizieR Online Data Catalog: Henry Draper Catalogue and Extension, published in Ann. Harvard Obs. 91-100 (1918-1925). *VizieR On-line Data Catalog: III/135A. Originally published in: 1993yCat.3135....0C*, 3135, 1993.

[47] T. D. Carozzi. Imaging on a sphere with interferometers: the spherical wave harmonic transform. *Monthly Notices of the Royal Astronomical Society: Letters*, 451(1):L6–L10, 5 2015.

[48] A. Chiavassa, L. Bigot, P. Kervella, A. Matter, B. Lopez, R. Collet, Z. Magic, and M. Asplund. Three-dimensional interferometric, spectrometric, and planetary views of Procyon. *Astronomy and Astrophysics*, 540, 1 2012.

[49] U. R. Christensen. Iron snow dynamo models for Ganymede. *ICARUS*, 247:248–259, 2015.

[50] U. R. Christensen and J. Aubert. Scaling properties of convection-driven dynamos in rotating spherical shells and application to planetary magnetic fields. *Geophysical Journal International*, 166(1):97–114, 7 2006.

[51] U. R. Christensen, V. Holzwarth, and A. Reiners. Energy flux determines magnetic field strength of planets and stars. *Nature*, 457(7226):167–9, 1 2009.

[52] K. R. Chu. The electron cyclotron maser. *Reviews of Modern Physics*, 76(2):489–540, 5 2004.

[53] A. S. Cohen, W. M. Lane, W. D. Cotton, N. E. Kassim, T. J. W. Lazio, R. A. Perley, J. J. Condon, and W. C. Erickson. The VLA Low-Frequency Sky Survey. *The Astronomical Journal*, 134(3):1245–1262, 9 2007.

[54] O. Cohen, J. J. Drake, A. Glocer, C. Garraffo, K. Poppenhaeger, J. M. Bell, A. J. Ridley, and T. I. Gombosi. MAGNETOSPHERIC STRUCTURE AND ATMOSPHERIC JOULE HEATING OF HABITABLE PLANETS ORBITING M-DWARF STARS. *The Astrophysical Journal*, 790(1):57, 7 2014.

[55] J. J. Condon, W. D. Cotton, E. W. Greisen, Q. F. Yin, R. A. Perley, G. B. Taylor, and J. J. Broderick. The NRAO VLA Sky Survey. *The Astronomical Journal*, 115(5):1693–1716, 5 1998.

[56] J. E. P. Connerney. Magnetic fields of the outer planets. *Journal of Geophysical Research*, 98(E10):18659, 1993.

[57] T. J. Cornwell, K. Golap, and S. Bhatnagar. The Noncoplanar Baselines Effect in Radio Interferometry: The W-Projection Algorithm. *IEEE Journal of Selected Topics in Signal Processing*, 2(5):647–657, 10 2008.

[58] W. D. Cotton and J. J. Condo. Calibration and Imaging of 74 MHz data from the Very Large Array. *Proceedings of the URSI General Assembly*, 2002.

[59] W. D. Cotton and J. M. Uson. Beam Squint and Stokes V on the VLA (EVLA Memo 113). Technical report, NRAO.

[60] L. R. Dartnell. Ionizing Radiation and Life.

[61] C. L. Davison, R. J. White, T. J. Henry, A. R. Riedel, W.-C. Jao, J. I. Bailey III, S. N. Quinn, J. R. Cantrell, J. P. Subasavage, and J. G. Winters. A 3D SEARCH FOR COMPANIONS TO 12 NEARBY M DWARFS. *The Astronomical Journal*, 149(3):106, 2 2015.

[62] E. de Lera Acedo. SKALA: A log-periodic antenna for the SKA. In *2012 International Conference on Electromagnetics in Advanced Applications*, pages 353–356. Ieee, 9 2012.

[63] E. de Lera Acedo, A. J. Faulkner, and J. G. B. de Vaate. SKA low frequency aperture array. In *2016 United States National Committee of URSI National Radio Science Meeting (USNC-URSI NRSM)*, pages 1–2. IEEE, 1 2016.

[64] E. de Lera Acedo, N. Razavi-Ghods, N. Troop, N. Drought, and A. J. Faulkner. SKALA, a log-periodic array antenna for the SKA-low instrument: design, simulations, tests and system considerations. *Experimental Astronomy*, 8 2015.

[65] M. De Vos, A. W. Gunst, and R. Nijboer. The LOFAR telescope: System architecture and signal processing. *Proceedings of the IEEE*, 97:1431–1437, 2009.

[66] X. Delfosse, T. Forveille, D. Ségransan, J.-L. Beuzit, S. Udry, C. Perrier, and M. Mayor. Accurate masses of very low mass stars IV. Improved mass-luminosity relations. *Astron. Astrophys*, 364:217–224, 2000.

[67] A. P. Dempster, N. M. Laird, and D. B. Rubin. Maximum Likelihood from Incomplete Data via the EM Algorithm. *Journal of the Royal Statistical Society. Series B (Methodological)*, 39(1):1–38, 1977.

[68] M. D. Desch. Neptune radio emission: Predictions based on planetary scaling laws. *Geophysical Research Letters*, 15(1):114–117, 1 1988.

[69] M. D. Desch and C. H. Barrow. Direct evidence for solar wind control of Jupiter's hectometer-wavelength radio emission. *Journal of Geophysical Research*, 89(A8):6819, 8 1984.

[70] M. D. Desch and M. L. Kaiser. Predictions for Uranus from a radiometric Bode's law. *Nature*, 310(5980):755–757, 8 1984.

[71] M. D. Desch and H. O. Rucker. The relationship between Saturn kilometric radiation and the solar wind. 1983.

[72] . Desch and . Kaiser. A radiometric Bode's Law: Predictions for Uranus. *Unknown*, 1984.

[73] P. Dewdney, P. Hall, R. Schilizzi, and T. Lazio. The Square Kilometre Array. *Proceedings of the IEEE*, 97(8):1482–1496, 8 2009.

[74] . DeBreuck, . Tang, . deBruyn, . Rottgering, and . vanBreugel. VizieR Online Data Catalog: The WISH catalogue at 352 MHz (de Breuck+ 2002). *VizieR On-line Data Catalog: VIII/69A. Originally published in: 2002A&A...394...59D*, 2004.

[75] R. F. Diaz, A. Santerne, J. Sahlmann, G. Hebrard, A. Eggenberger, N. C. Santos, C. Moutou, L. Arnold, I. Boisse, X. Bonfils, F. Bouchy, X. Delfosse, M. Desort, D. Ehrenreich, T. Forveille, A.-M. Lagrange, C. Lovis, F. Pepe, C. Perrier, D. Queloz, D. Segransan, S. Udry, and A. Vidal-Madjar. The SOPHIE search for northern extrasolar planets. *Astronomy & Astrophysics*, 545(A113):A55, 2012.

[76] R. H. Dicke. The Measurement of Thermal Radiation at Microwave Frequencies. *Review of Scientific Instruments*, 17(7):268, 1946.

[77] J. A. Dittmann, J. M. Irwin, D. Charbonneau, and E. R. Newton. CALIBRATION OF THE MEARTH PHOTOMETRIC SYSTEM: OPTICAL MAGNITUDES AND PHOTOMETRIC METALLICITY ESTIMATES FOR 1802 NEARBY M-DWARFS. *The Astrophysical Journal*, 818(153), 2016.

[78] J. J. Drake, O. Cohen, S. Yashiro, and N. Gopalswamy. IMPLICATIONS OF MASS AND ENERGY LOSS DUE TO CORONAL MASS EJECTIONS ON MAGNETICALLY ACTIVE STARS. *The Astrophysical Journal*, 764(2):170, 2 2013.

[79] S. A. Drake, T. Simon, and A. Brown. Detection of radio continuum emission from Procyon. *The Astrophysical Journal*, 406:247, 3 1993.

[80] G. A. Dulk. Io-Related Radio Emission from Jupiter. *Science*, 148(3677), 1965.

[81] S. Eggl, E. Pilat-Lohinger, B. Funk, N. Georgakarakos, and N. Haghighipour. Circumstellar habitable zones of binary-star systems in the solar neighbourhood. *Monthly Notices of the Royal Astronomical Society*, 428(4):3104–3113, 2 2013.

[82] S. S. W. Ellingson, T. E. T. Clarke, A. Cohen, J. Craig, N. E. N. Kassim, Y. Pihlstrom, L. J. Richard, G. G. B. Taylor, L. Rickard, and G. G. B. Taylor. The Long Wavelength Array, 8 2009.

[83] S. W. Ellingson. Sensitivity of Antenna Arrays for Long-Wavelength Radio Astronomy. *IEEE Transactions on Antennas and Propagation*, 59(6):1855–1863, 6 2011.

[84] M. Endl, W. D. Cochran, M. Kuerster, D. B. Paulson, R. A. Wittenmyer, P. J. MacQueen, and R. G. Tull. Exploring The Frequency Of Close-In Jovian Planets Around M Dwarfs. *The Astrophysical Journal, Volume 649, Issue 1, pp. 436-443.*, 649:436–443, 6 2006.

[85] J. Farihi, M. A. Barstow, S. Redfield, P. Dufour, and N. C. Hambly. Rocky Planetesimals as the Origin of Metals in DZ Stars. *Monthly Notices of the Royal Astronomical Society*, 404:2123–2135, 1 2010.

[86] J. Farihi, E. E. Becklin, and B. A. Macintosh. Mid-Infrared Observations of van Maanen 2: No Substellar Companion. *The Astrophysical Journal*, 608(2):L109–L112, 6 2004.

[87] J. Farihi, E. E. Becklin, and B. Zuckerman. Spitzer IRAC Observations of White Dwarfs. II. Massive Planetary and Cold Brown Dwarf Companions to Young and Old Degenerates. *The Astrophysical Journal*, 681(2):1470–1483, 7 2008.

[88] J. Farihi, H. E. Bond, P. Dufour, N. Haghighipour, G. H. Schaefer, J. B. Holberg, M. A. Barstow, and M. R. Burleigh. Orbital and Evolutionary Constraints on the Planet Hosting Binary GJ 86 from the Hubble Space Telescope. *Monthly Notices of the Royal Astronomical Society*, 430:652–660, 12 2012.

[89] J. Farihi, M. Jura, and B. Zuckerman. INFRARED SIGNATURES OF DISRUPTED MINOR PLANETS AT WHITE DWARFS. *The Astrophysical Journal*, 694(2):805–819, 4 2009.

[90] W. M. Farrell, M. D. Desch, T. J. Lazio, T. Bastian, and P. Zarka. Limits on the Magnetosphere/Stellar Wind Interactions for the Extrasolar Planet about Tau Bootes. 294, 2003.

[91] W. M. Farrell, M. D. Desch, and P. Zarka. On the possibility of coherent cyclotron emission from extrasolar planets. *Journal of Geophysical Research: Planets*, 104(E6):14025–14032, 6 1999.

[92] W. M. Farrell, M. D. Desch, and P. Zarka. On the possibility of coherent cyclotron emission from extrasolar planets. *Journal of Geophysical Research*, 104(E6):14025, 6 1999.

[93] F. Ferrari and E. Szuszkiewicz. Cosmic Rays: A Review for Astrobiologists. *Astrobiology*, 9(4):413–436, 5 2009.

[94] D. A. Fischer and J. Valenti. The PlanetMetallicity Correlation. *The Astrophysical Journal*, 622(2):1102–1117, 4 2005.

[95] H.-J. Fischer and T. Spohn. Thermal-Orbital Histories of Viscoelastic Models of Io (J1). *ICARUS*, 83:39–65, 1990.

[96] E. W. Flesch and E. W. The Million Optical - Radio/X-ray Associations (MORX) Catalogue. *Publications of the Astronomical Society of Australia, Volume 33, id.e052 9 pp.*, 33, 9 2016.

[97] E. B. Fomalont and W. L. Sanders. RADIO OBSERVATIONS OF A COMPLETE SAMPLE OF NEARBY STARS. *THE ASTRONOMICAL JOURNAL*, 98(1), 1989.

[98] F. Fressin, G. Torres, D. Charbonneau, S. T. Bryson, J. Christiansen, C. D. Dressing, J. M. Jenkins, L. M. Walkowicz, and N. M. Batalha. THE FALSE POSITIVE RATE OF KEPLER AND THE OCCURRENCE OF PLANETS. *The Astrophysical Journal*, 766(2):81, 4 2013.

[99] B. Fuhrmeister, J. H. M. M. Schmitt, and P. H. Hauschildt. Multi-wavelength observations of a giant flare on CNLeonis. *Astronomy and Astrophysics*, 511:A83, 2 2010.

[100] Y. Futaana, S. Barabash, M. Yamauchi, S. McKenna-Lawlor, R. Lundin, J. Luhmann, D. Brain, E. Carlsson, J.-A. Sauvaud, J. Winningham, R. Frahm, P. Wurz, M. Holmström, H. Gunell, E. Kallio, W. Baumjohann, H. Lammer, J. Sharber, K. Hsieh, H. Andersson, A. Grigoriev, K. Brinkfeldt, H. Nilsson, K. Asamura, T. Zhang, A. Coates, D. Linder, D. Kataria, C. Curtis, B. Sandel, A. Fedorov, C. Mazelle, J.-J. Thocaven, M. Grande, H. E. Koskinen, T. Sales,

W. Schmidt, P. Riihela, J. Kozyra, N. Krupp, J. Woch, M. Fränz, E. Dubinin, S. Orsini, R. Cerulli-Irelli, A. Mura, A. Milillo, M. Maggi, E. Roelof, P. Brandt, K. Szego, J. Scherrer, and P. Bochsler. Mars Express and Venus Express multi-point observations of geoeffective solar flare events in December 2006. *Planetary and Space Science*, 56(6):873–880, 5 2008.

[101] J. Gagné, D. Ere, R. Doyon, L. Malo, and E. Artigau. BANYAN. II. VERY LOW MASS AND SUBSTELLAR CANDIDATE MEMBERS TO NEARBY, YOUNG KINEMATIC GROUPS WITH PREVIOUSLY KNOWN SIGNS OF YOUTH. *The Astrophysical Journal*, 783(35pp), 2014.

[102] J. Gagné, J. K. Faherty, K. L. Cruz, D. Lafreniére, R. Doyon, L. Malo, A. J. Burgasser, M.-E. Naud, . Artigau, S. Bouchard, J. E. Gizis, and L. Albert. BANYAN. VII. A NEW POPULATION OF YOUNG SUBSTELLAR CANDIDATE MEMBERS OF NEARBY MOVING GROUPS FROM THE BASS SURVEY. *The Astrophysical Journal Supplement Series*, 219:33, 2015.

[103] D. L. Gallagher and N. D'Angelo. Correlations between solar wind parameters and auroral kilometric radiation intensity. *Geophysical Research Letters*, 8(10):1087–1089, 10 1981.

[104] C. Garraffo, J. J. Drake, and O. Cohen. THE SPACE WEATHER OF PROXIMA CENTAURI b. 2016.

[105] C. Garraffo, J. J. Drake, O. Cohen, J. D. Alvarado-Gómez, and S. P. Moschou. The Threatening Magnetic and Plasma Environment of the TRAPPIST-1 Planets. *The Astrophysical Journal*, 843(2):L33, 7 2017.

[106] G. Gatewood. Lalande 21185. *American Astronomical Society Meeting Abstracts #188*, 188, 5 1996.

[107] G. Gatewood, L. Coban, and I. Han. An Astrometric Study of the Low-Mass Binary Star Ross 614. *The Astronomical Journal*, 125(3):1530–1536, 3 2003.

[108] S. J. George and I. R. Stevens. Giant Metrewave Radio Telescope low-frequency observations of extrasolar planetary systems. *Monthly Notices of the Royal Astronomical Society*, 382(1):455–460, 11 2007.

[109] R. E. Gershberg, M. M. Katsova, M. N. Lovkaya, A. V. Terebizh, and N. I. Shakhovskaya. Catalogue and bibliography of the UV Cet-type flare stars and related objects in the solar vicinity. *Astronomy and Astrophysics Supplement Series*, 139(3):555–558, 11 1999.

[110] M. Gillon, E. Jehin, S. M. Lederer, L. Delrez, J. de Wit, A. Burdanov, V. Van Grootel, A. J. Burgasser, A. H. M. J. Triaud, C. Opitom, B.-O. Demory, D. K. Sahu, D. Bardalez Gagliuffi, P. Magain, and D. Queloz. Temperate Earth-sized planets transiting a nearby ultracool dwarf star. *Nature*, 533(7602):221–224, 5 2016.

[111] M. Gillon, A. H. M. J. Triaud, B.-O. Demory, E. Jehin, E. Agol, K. M. Deck, S. M. Lederer, J. de Wit, A. Burdanov, J. G. Ingalls, E. Bolmont, J. Leconte, S. N. Raymond, F. Selsis, M. Turbet, K. Barkaoui, A. Burgasser, M. R. Burleigh, S. J. Carey, A. Chaushev, C. M. Copperwheat, L. Delrez, C. S. Fernandes, D. L. Holdsworth, E. J. Kotze, V. Van Grootel, Y. Almleaky, Z. Benkhaldoun, P. Magain, and D. Queloz. Seven temperate terrestrial planets around the nearby ultracool dwarf star TRAPPIST-1. *Nature*, 542(7642):456–460, 2 2017.

[112] G. A. Glatzmaier and P. H. Roberts. A three-dimensional convective dynamo solution with rotating and finitely conducting inner core and mantle. *Physics of the Earth and Planetary Interiors*, 91(1-3):63–75, 9 1995.

[113] N. Gopalswamy. Interplanetary Radio Bursts. In *Solar and Space Weather Radiophysics*, pages 305–333. Springer Netherlands, Dordrecht, 2004.

[114] N. Gopalswamy and N. Corona Mass Ejections: a Summary of Recent Results. *Proceedings of the 20th National Solar Physics Meeting, held 31 May - 4 June, 2010 in Papradno, Slovakia, p. 108-130*, pages 108–130, 2010.

[115] N. Gopalswamy, W. T. Thompson, J. M. Davila, M. L. Kaiser, S. Yashiro, P. Mäkelä, G. Michalek, J.-L. Bougeret, and R. A. Howard. Relation Between Type II Bursts and CMEs Inferred from STEREO Observations. *Solar Physics*, 259(1-2):227–254, 10 2009.

[116] K. M. Gorski, E. Hivon, A. J. Banday, B. D. Wandelt, F. K. Hansen, M. Reinecke, and M. Bartelmann. HEALPix: A Framework for High-Resolution Discretization and Fast Analysis of Data Distributed on the Sphere. *The Astrophysical Journal*, 622(2):759–771, 4 2005.

[117] J. Grießmeier, U. Motschmann, G. Mann, and H. O. Rucker. The influence of stellar wind conditions on the detectability. 726:717–726, 2005.

[118] J.-M. Grießmeier, M. Khodachenko, H. Lammer, J. L. Grenfell, A. Stadelmann, and U. Motschmann. Stellar activity and magnetic shielding. *Proceedings of the International Astronomical Union*, 5(S264):385–394, 8 2009.

[119] J.-M. Griessmeier, A. Stadelmann, U. Motschmann, N. K. Belisheva, H. Lammer, and H. K. Biernat. Cosmic ray impact on extrasolar earth-like planets in close-in habitable zones. *Astrobiology*, 5(5):587–603, 10 2005.

[120] J.-M. Grießmeier, P. Zarka, and H. Spreeuw. Predicting low-frequency radio fluxes of known extrasolar planets. *Astronomy and Astrophysics*, 475(1):359–368, 11 2007.

[121] R. T. Groves. Analysis of the Radio Astronomy Explorer lunar orbit mission. In *AIAA & AAS, Astrodynamics Conference*, Palo Alto, CA, 9 1972.

[122] E. W. Guenther and G. Wuchterl. Companions of old brown dwarfs, and very low mass stars. *Astronomy & Astrophysics*, 401(2):677–683, 4 2003.

[123] D. A. Gurnett, W. S. Kurth, G. B. Hospodarsky, A. M. Persoon, P. Zarka, A. Lecacheux, S. J. Bolton, M. D. Desch, W. M. Farrell, M. L. Kaiser, H.-P. Ladreiter, H. O. Rucker, P. Galopeau, P. Louarn, D. T. Young, W. R. Pryor, and M. K. Dougherty. Control of Jupiter's radio emission and aurorae by the solar wind. *Nature*, 415(6875):985–7, 2 2002.

[124] D. A. Gurnett, A. Lecacheux, W. S. Kurth, A. M. Persoon, J. B. Groene, L. Lamy, P. Zarka, and J. F. Carbary. Discovery of a north-south asymmetry in Saturn's radio rotation period. *Geophysical Research Letters*, 36(16):L16102, 8 2009.

[125] C. B. Haakonsen and R. E. Rutledge. XID II: Statistical Cross-Association of ROSAT Bright Source Catalog X-ray Sources with 2MASS Point Source Catalog Near-Infrared Sources. *The Astrophysical Journal Supplement, Volume 184, Issue 1, pp. 138-151 (2009).*, 184:138–151, 2009.

[126] G. Hallinan. The Owens Valley LWA. In *Exascale Radio Astronomy*, volume 2, 2014.

[127] G. Hallinan, A. Antonova, J. G. Doyle, S. Bourke, C. Lane, and A. Golden. Confirmation of the Electron Cyclotron Maser Instability as the Dominant Source of Radio Emission from Very Low Mass Stars and Brown Dwarfs. *The Astrophysical Journal*, 684(1):644–653, 9 2008.

[128] G. Hallinan, S. K. Sirothia, A. Antonova, C. H. Ishwara-Chandra, S. Bourke, J. G. Doyle, J. Hartman, and A. Golden. Looking for a Pulse: A Search for Rotationally Modulated Radio Emission from the Hot Jupiter, τ BOÖTIS b. *The Astrophysical Journal*, 762(1):34, 1 2013.

[129] E. Han, S. X. Wang, J. T. Wright, Y. K. Feng, M. Zhao, J. I. Brown, C. Hancock, and C. Hancock. The Exoplanet Orbit Database II: Updates to exoplanets.org. *Publications of the Astronomical Society of Pacific, Volume 126, Issue 943, pp. 827 (2014).*, 126:827, 9 2014.

[130] Y. Harada, S. Goossens, K. Matsumoto, J. Yan, J. Ping, H. Noda, and J. Haruyama. Strong tidal heating in an ultralow-viscosity zone at the core-mantle boundary of the Moon. *Nature Geoscience*, 7(8):569–572, 7 2014.

[131] G. Heald, J. Mckean, R. Pizzo, G. Van Diepen, J. E. Van Zwieten, R. J. Van Weeren, D. Rafferty, S. Van Der Tol, L. Birzan, A. Shulevski, J. Swinbank, E. Orrù, F. De Gasperin, L. Ker, A. Bonafede, G. Macario, and C. Ferrari. Progress with the LOFAR Imaging Pipeline.

[132] G. H. Heald, R. F. Pizzo, E. Orrú, R. P. Breton, D. Carbone, C. Ferrari, M. J. Hardcastle, W. Jurusik, G. Macario, D. Mulcahy, D. Rafferty, A. Asgekar, M. Brentjens, R. A. Fallows, W. Frieswijk, M. C. Toribio, B. Adebahr, M. Arts, M. R. Bell, A. Bonafede, J. Bray, J. Broderick, T. Cantwell, P. Carroll, Y. Cendes, A. O. Clarke, J. Croston, S. Daiboo, F. de Gasperin, J. Gregson, J. Harwood, T. Hassall, V. Heesen, A. Horneffer, A. J. van der Horst, M. Iacobelli, V. Jelić, D. Jones, D. Kant, G. Kokotanekov, P. Martin, J. P. McKean, L. K. Morabito, B. Nikiel-Wroczyński, A. Offringa, V. N. Pandey, M. Pandey-Pommier, M. Pietka, L. Pratley, C. Riseley, A. Rowlinson, J. Sabater, A. M. M. Scaife, L. H. A. Scheers, K. Sendlinger, A. Shulevski, M. Sipior, C. Sobey, A. J. Stewart, A. Stroe, J. Swinbank, C. Tasse, J. Trüstedt, E. Varenius, S. van Velzen, N. Vilchez, R. J. van Weeren, S. Wijnholds, W. L. Williams, A. G. de Bruyn, R. Nijboer, M. Wise, A. Alexov, J. Anderson, I. M. Avruch, R. Beck, M. E. Bell, I. van Bemmel, M. J. Bentum, G. Bernardi, P. Best, F. Breitling, W. N. Brouw, M. Brüggen, H. R. Butcher, B. Ciardi, J. E. Conway, E. de Geus, A. de Jong, M. de Vos, A. Deller, R. J. Dettmar, S. Duscha, J. Eislöffel, D. Engels, H. Falcke, R. Fender, M. A. Garrett, J. Grießmeier, A. W. Gunst, J. P. Hamaker, J. W. T. Hessels, M. Hoeft, J. Hörandel, H. A. Holties, H. Intema, N. J. Jackson, E. Jütte, A. Karastergiou, W. F. A. Klijn, V. I. Kondratiev, L. V. E. Koopmans, M. Kuniyoshi, G. Kuper, C. Law, J. van Leeuwen, M. Loose, P. Maat, S. Markoff, R. McFadden, D. McKay-Bukowski, M. Mevius, J. C. A. Miller-Jones, R. Morganti, H. Munk, A. Nelles, J. E. Noordam, M. J. Norden, H. Paas, A. G. Polatidis, W. Reich, A. Renting, H. Röttgering, A. Schoenmakers, D. Schwarz, J. Sluman, O. Smirnov, B. W. Stappers, M. Steinmetz, M. Tagger, Y. Tang, S. ter Veen, S. Thoudam, R. Vermeulen, C. Vocks, C. Vogt, R. A. M. J. Wijers, O. Wucknitz, S. Yatawatta, and P. Zarka. The LOFAR Multifrequency Snapshot Sky Survey (MSSS) I. Survey description and first results. 2015.

[133] W. G. Henning and T. Hurford. TIDAL HEATING IN MULTILAYERED TERRESTRIAL EXOPLANETS. *The Astrophysical Journal*, 789(1):30, 7 2014.

[134] E. Herrero, I. Ribas, C. Jordi, E. F. Guinan, and S. G. Engle. Optimizing exoplanet transit searches around low-mass stars with inclination constraints. *Astronomy & Astrophysics*, 537:A147, 1 2012.

[135] S. L. G. Hess and P. Zarka. Modeling the radio signature of the orbital parameters, rotation, and magnetic field of exoplanets. *Astronomy & Astrophysics*, 531:A29, 6 2011.

[136] . Högbom. Aperture Synthesis with a Non-Regular Distribution of Interferometer Baselines. *Astronomy and Astrophysics Supplement*, 15, 1974.

[137] E. R. Houdebine. Observation and modelling of main-sequence star chromospheres - XVII. Rotation of dM4 stars. *Monthly Notices of the Royal Astronomical Society*, 421(4):3180–3188, 4 2012.

[138] N. Hurley-Walker, J. R. Callingham, P. J. Hancock, T. M. O. Franzen, L. Hindson, A. D. Kapińska, J. Morgan, A. R. Offringa, R. B. Wayth, C. Wu, Q. Zheng, T. Murphy, M. E. Bell, K. S. Dwarakanath, B. For, B. M. Gaensler, M. Johnston-Hollitt, E. Lenc, P. Procopio, L. Staveley-Smith, R. Ekers, J. D. Bowman, F. Briggs, R. J. Cappallo, A. A. Deshpande, L. Greenhill, B. J. Hazelton, D. L. Kaplan, C. J. Lonsdale, S. R. McWhirter, D. A. Mitchell, M. F. Morales, E. Morgan, D. Oberoi, S. M. Ord, T. Prabu, N. U. Shankar, K. S. Srivani, R. Subrahmanyan, S. J. Tingay, R. L. Webster, A. Williams, and C. L. Williams. GaLactic and Extragalactic All-sky Murchison Widefield Array (GLEAM) survey I. A low-frequency extragalactic catalogue. *Monthly Notices of the Royal Astronomical Society*, 464(1):1146–1167, 1 2017.

[139] H. T. Intema. SPAM: A data reduction recipe for high-resolution, low-frequency radio-interferometric observations. 2 2014.

[140] H. T. Intema, P. Jagannathan, K. P. Mooley, and D. A. Frail. The GMRT 150 MHz all-sky radio survey: First altnerative data release TGSS ADR1. *Astronomy & Astrophysics*, 598:A78, 2 2017.

[141] J. M. Irwin, Z. K. Berta-Thompson, D. Charbonneau, J. Dittmann, E. E. Falco, E. R. Newton, and P. Nutzman. The MEarth-North and MEarth-South transit surveys: searching for habitable super-Earth exoplanets around nearby M-dwarfs. page 5, 9 2014.

[142] L. G. Jaime, L. Aguilar, and B. Pichardo. Habitable Zones with Stable Orbits for Planets around Binary Systems. *Monthly Notices of the Royal Astronomical Society, Volume 443, Issue 1, p.260-274*, 443:260–274, 1 2014.

[143] J. M. Jenkins, D. A. Caldwell, H. Chandrasekaran, J. D. Twicken, S. T. Bryson, E. V. Quintana, B. D. Clarke, J. Li, C. Allen, P. Tenenbaum, H. Wu, T. C. Klaus, C. K. Middour, M. T. Cote, S. McCauliff, F. R. Girouard, J. P. Gunter, B. Wohler, J. Sommers, J. R. Hall, A. K. Uddin, M. S. Wu, P. A. Bhavsar, J. Van Cleve, D. L. Pletcher, J. A. Dotson, M. R. Haas, R. L. Gilliland, D. G. Koch, and W. J. Borucki. OVERVIEW OF THE KEPLER SCIENCE PROCESSING PIPELINE. *The Astrophysical Journal*, 713(2):L87–L91, 4 2010.

[144] J. S. Jenkins, L. W. Ramsey, H. R. A. Jones, Y. Pavlenko, J. Gallardo, J. R. Barnes, and D. J. Pinfield. ROTATIONAL VELOCITIES FOR M DWARFS. *The Astrophysical Journal*, 704(2):975–988, 10 2009.

[145] S. Jester and H. Falcke. Science with a lunar low-frequency array: From the dark ages of the Universe to nearby exoplanets. *New Astronomy Reviews*, 53(1-2):1–26, 5 2009.

[146] D. Jones, R. Allen, J. Basart, T. Bastian, B. Dennison, K. Dwarakanath, W. Ericksong, D. Finley, M. Kaiser, N. Kassim, T. Kuiperl, R. Macdowall, M. Mahoney, R. Perley, R. Preston, M. Reiner, P. O. Rodriguez, R. Stone, S. Unwin,

K. O. Weiler, G. Woan, and R. Wool. The Astronomical Low Frequency Array : Explorer Mission for Radio Astronomy A Proposed Explorer Mission for Radio Astronomy. In R. G. Stone, K. W. Weiler, M. L. Goldstein, and J.-L. Bougeret, editors, *Radio Astronomy at Long Wavelengths*, pages 339–349. American Geophysical Union, 2000.

[147] M. L. Kaiser. Time-variable magnetospheric radio emissions from Jupiter. *Journal of Geophysical Research*, 98(E10):18757, 1993.

[148] M. L. Kaiser, T. A. Kucera, J. M. Davila, O. C. St. Cyr, M. Guhathakurta, and E. Christian. The STEREO Mission: An Introduction. *Space Science Reviews*, 136(1-4):5–16, 4 2008.

[149] M. M. Kao, G. Hallinan, J. S. Pineda, I. Escala, A. Burgasser, S. Bourke, and D. Stevenson. AURORAL RADIO EMISSION FROM LATE L AND T DWARFS: A NEW CONSTRAINT ON DYNAMO THEORY IN THE SUB-STELLAR REGIME. 2016.

[150] N. E. Kassim, T. J. W. Lazio, W. C. Erickson, R. A. Perley, W. D. Cotton, E. W. Greisen, A. S. Cohen, B. Hicks, H. R. Schmitt, and D. Katz. The 74 MHz System on the Very Large Array. *The Astrophysical Journal Supplement Series*, 172(2):686–719, 10 2007.

[151] J. Kasting. Habitable Zones around Main Sequence Stars. *Icarus*, 101(1):108–128, 1 1993.

[152] J. T. Kent. The Fisher-Bingham Distribution on the Sphere. *Journal of the Royal Statistical Society. Series B (Methodological)*, 44(1):71–80, 1982.

[153] M. L. Khodachenko, I. Ribas, H. Lammer, J.-M. Griessmeier, M. Leitner, F. Selsis, C. Eiroa, A. Hanslmeier, H. K. Biernat, C. J. Farrugia, and H. O. Rucker. Coronal mass ejection (CME) activity of low mass M stars as an important factor for the habitability of terrestrial exoplanets. I. CME impact on expected magnetospheres of Earth-like exoplanets in close-in habitable zones. *Astrobiology*, 7(1):167–84, 2 2007.

[154] J. D. Kirkpatrick, C. R. Gelino, M. C. Cushing, G. N. Mace, R. L. Griffith, M. F. Skrutskie, K. a. Marsh, E. L. Wright, P. R. Eisenhardt, I. S. McLean, A. K. Mainzer, A. J. Burgasser, C. G. Tinney, S. Parker, and G. Salter. FURTHER DEFINING SPECTRAL TYPE Y AND EXPLORING THE LOW-MASS END OF THE FIELD BROWN DWARF MASS FUNCTION. *The Astrophysical Journal*, 753(2):156, 7 2012.

[155] M. Kivelson, K. Khurana, C. Russell, R. Walker, P. Coleman, F. Coroniti, J. Green, S. Joy, R. McPherron, C. Polanskey, D. Southwood, L. Bennett, J. Warnecke, and D. Huddleston. Galileo at Jupiter: Changing states of the magnetosphere and first looks at Io and Ganymede. *Advances in Space Research*, 20(2):193–204, 1 1997.

[156] M. Kivelson, K. Khurana, and M. Volwerk. The Permanent and Inductive Magnetic Moments of Ganymede. *Icarus*, 157(2):507–522, 6 2002.

[157] M. Knapp. SOLARA/SARA: First steps toward a space-based radio interferometry constellation. In *Proceedings of the International Astronautical Congress, IAC*, volume 6, 2014.

[158] M. Knapp, F. Robey, R. Volz, F. Lind, A. Fenn, A. Morris, M. Silver, S. Klein, and S. Seager. Vector antenna and maximum likelihood imaging for radio astronomy. In *IEEE Aerospace Conference Proceedings*, volume 2016-June, 2016.

[159] M. Knapp, R. Volz, F. Lind, F. Robey, A. Fenn, K. Johnson, M. Silver, A. Morris, and S. Klein. HF vector sensor for radio astronomy: Ground testing results. In *AIAA Space and Astronautics Forum and Exposition, SPACE 2016*, 2016.

[160] M. E. Knapp. SOLARA/SARA: first steps toward a space-based radio interferometry constellation. In *65th International Astronautical Congress (IAC)*, Toronto, Canada, 2014.

[161] V. Krupar, M. Maksimovic, O. Santolik, E. P. Kontar, B. Cecconi, S. Hoang, O. Kruparova, J. Soucek, H. Reid, and A. Zaslavsky. Statistical Survey of Type III Radio Bursts at Long Wavelengths Observed by the Solar TErrestrial RElations Observatory (STEREO)/Waves Instruments: Radio Flux Density Variations with Frequency. *Solar Physics*, 289(8):3121–3135, 8 2014.

[162] Y. N. Kulikov, H. Lammer, H. I. M. Lichtenegger, T. Penz, D. Breuer, T. Spohn, R. Lundin, and H. K. Biernat. A Comparative Study of the Influence of the Active Young Sun on the Early Atmospheres of Earth, Venus, and Mars. *Space Science Reviews*, 129(1-3):207–243, 6 2007.

[163] D. Lafreniere, R. Doyon, C. Marois, D. Nadeau, B. R. Oppenheimer, P. F. Roche, F. Rigaut, J. R. Graham, R. Jayawardhana, D. Johnstone, P. G. Kalas, B. Macintosh, and R. Racine. The Gemini Deep Planet Survey. *The Astrophysical Journal*, 670(2):1367–1390, 12 2007.

[164] D. V. Lal. GMRT Observer s Manual. 2013.

[165] W. M. Lane, W. D. Cotton, J. F. Helmboldt, and N. E. Kassim. VLSS redux: Software improvements applied to the very large array low-frequency sky survey. *Radio Science*, 47(May):1–9, 2012.

[166] W. M. Lane, W. D. Cotton, S. van Velzen, T. E. Clarke, N. E. Kassim, J. F. Helmboldt, T. J. W. Lazio, and a. S. Cohen. The very large array low-frequency sky survey redux (VLSSr). *Monthly Notices of the Royal Astronomical Society*, 440(1):327–338, 3 2014.

[167] J. Lazio, W. M. Farrell, J. Dietrick, E. Greenlees, E. Hogan, C. Jones, and L. A. Hennig. The Radiometric Bode's Law and Extrasolar Planets. *The Astrophysical Journal*, pages 511–518, 2004.

[168] T. J. W. Lazio, S. Carmichael, J. Clark, E. Elkins, P. Gudmundsen, Z. Mott, M. Szwajkowski, and L. a. Hennig. A Blind Search for Magnetospheric Emissions from Planetary Companions to Nearby Solar-type Stars. *The Astronomical Journal*, 139(1):11, 2009.

[169] T. J. W. Lazio and W. M. Farrell. Magnetospheric Emissions from the Planet Orbiting τ Bootis: A Multiepoch Search. *The Astrophysical Journal*, 668(2):1182–1188, 10 2007.

[170] T. J. W. Lazio, P. D. Shankland, W. M. Farrell, and D. L. Blank. RADIO OBSERVATIONS OF HD 80606 NEAR PLANETARY PERIASTRON. *The Astronomical Journal*, 140(6):1929–1933, 12 2010.

[171] A. Lecavelier des Etangs, S. K. Sirothia, P. Gopal-Krishna, and P. Zarka. GMRT radio observations of the transiting extrasolar planet HD189733b at 244 and 614MHz. *Astronomy & Astrophysics*, 500(3):L51–L54, 6 2009.

[172] A. Lecavelier des Etangs, S. K. Sirothia, P. Zarka, and A. L. Etangs. GMRT search for 150MHz radio emission from the transiting extrasolar planets HD189733b and HD209458b. *Astronomy & Astrophysics*, 533:A50, 8 2011.

[173] A. Lecavelier des Etangs, S. K. Sirothia, P. Zarka, and A. Lecavelier des Etangs. Hint of 150 MHz radio emission from the Neptune-mass extrasolar transiting planet HAT-P-11b. *Astronomy & Astrophysics*, 552:A65, 3 2013.

[174] W. W. Lee, M. Parent, and G. San Antonio. High frequency vector sensor design and testing. *NRL Review*, 2013.

[175] S. K. Leggett, D. Saumon, M. S. Marley, K. Lodders, J. Canty, P. Lucas, R. L. Smart, C. G. Tinney, D. Homeier, F. Allard, B. Burningham, A. Day-Jones, B. Fegley, M. Ishii, H. R. A Jones, F. Marocco, D. J. Pinfield, and M. Tamura. THE PROPERTIES OF THE 500 K DWARF UGPS J072227.51054031.2 AND A STUDY OF THE FAR-RED FLUX OF COLD BROWN DWARFS. *The Astrophysical Journal*, 748(17pp), 2012.

[176] J.-F. Lestrade, R. B. Phillips, D. L. Jones, and R. A. Preston. Search for extrasolar planets around radio-emitting stars by very long baseline interferometry astrometry. *Journal of Geophysical Research: Planets*, 101(E6):14837–14841, 6 1996.

[177] F. D. Lind, C. J. Lonsdale, A. J. Faulkner, P. Alexander, and C. Mattmann. Radio array of portable interferometric detectors (RAPID). In *2013 IEEE International Symposium on Phased Array Systems and Technology*, pages 676–683. IEEE, 10 2013.

[178] F. D. Lind, C. J. Lonsdale, A. J. Faulkner, C. Mattmann, N. Razavi-Ghods, E. de Lera Acedo, P. Alexander, J. Marchese, R. McWhirter, C. Eckert, J. Vierinen, R. Schaefer, W. Rideout, R. Cappallo, V. Pankratius, D. Oberoi,

S. Khudikyan, M. Joyce, C. Goodale, M. Boustani, L. Cinquini, R. Verma, and M. Starch. Radio Array of Portable Interferometric Detectors (RAPID): Development of a deployable multiple application radio array. In *2015 International Conference on Electromagnetics in Advanced Applications (ICEAA)*, pages 1337–1340. IEEE, 9 2015.

[179] C. Lonsdale, R. Cappallo, M. Morales, F. Briggs, L. Benkevitch, J. Bowman, J. Bunton, S. Burns, B. Corey, L. deSouza, S. Doeleman, M. Derome, A. Deshpande, M. Gopala, L. Greenhill, D. Herne, J. Hewitt, P. Kamini, J. Kasper, B. Kincaid, J. Kocz, E. Kowald, E. Kratzenberg, D. Kumar, M. Lynch, S. Madhavi, M. Matejek, D. Mitchell, E. Morgan, D. Oberoi, S. Ord, J. Pathikulangara, T. Prabu, A. Rogers, A. Roshi, J. Salah, R. Sault, N. Shankar, K. Srivani, J. Stevens, S. Tingay, A. Vaccarella, M. Waterson, R. Wayth, R. Webster, A. Whitney, A. Williams, and C. Williams. The Murchison Widefield Array: Design Overview. *Proceedings of the IEEE*, 97(8):1497–1506, 8 2009.

[180] C. J. Lonsdale. Configuration Considerations for Low Frequency Arrays. 345, 2005.

[181] P. W. Lucas, M. G. Hoare, A. Longmore, A. C. Schröder, C. J. Davis, A. Adamson, R. M. Bandyopadhyay, R. De Grijs, M. Smith, A. Gosling, S. Mitchison, A. Gáspár, M. Coe, M. Tamura, Q. Parker, M. Irwin, N. Hambly, J. Bryant, R. S. Collins, N. Cross, D. W. Evans, E. Gonzalez-Solares, S. Hodgkin, J. Lewis, M. Read, M. Riello, E. T. Sutorius, A. Lawrence, J. E. Drew, S. Dye, and M. A. Thompson. The UKIDSS galactic plane survey. *Monthly Notices of the Royal Astronomical Society*, 391(1):136–163, 11 2008.

[182] P. W. Lucas, C. G. Tinney, B. Burningham, S. K. Leggett, D. J. Pinfield, R. Smart, H. R. A. Jones, F. Marocco, R. J. Barber, S. N. Yurchenko, J. Tennyson, M. Ishii, M. Tamura, A. C. Day-Jones, A. Adamson, F. Allard, and D. Homeier. The discovery of a very cool, very nearby brown dwarf in the Galactic plane. *Monthly Notices of the Royal Astronomical Society: Letters*, 408(1):L56–L60, 10 2010.

[183] R. Luger, M. Sestovic, E. Kruse, S. L. Grimm, B.-O. Demory, E. Agol, E. Bolmont, D. Fabrycky, C. S. Fernandes, V. Van Grootel, A. Burgasser, M. Gillon, J. G. Ingalls, E. Jehin, S. N. Raymond, F. Selsis, A. H. M. J. Triaud, T. Barclay, G. Barentsen, L. Delrez, J. de Wit, D. Foreman-Mackey, D. L. Holdsworth, J. Leconte, S. Lederer, M. Turbet, Y. Almleaky, Z. Benkhaldoun, P. Magain, B. Morris, K. Heng, and D. Queloz. A terrestrial-sized exoplanet at the snow line of TRAPPIST-1. 3 2017.

[184] K. L. Luhman and K. L. Discovery of a ˜250 K Brown Dwarf at 2 pc from the Sun. *The Astrophysical Journal Letters, Volume 786, Issue 2, article id. L18, 6 pp. (2014).*, 786, 4 2014.

[185] R. Lundin, S. Barabash, M. Holmström, H. Nilsson, Y. Futaana, R. Ramstad, M. Yamauchi, E. Dubinin, and M. Fraenz. Solar cycle effects on the ion escape from Mars. *Geophysical Research Letters*, 40(23):6028–6032, 12 2013.

[186] C. R. Lynch, T. Murphy, D. L. Kaplan, M. Ireland, and M. E. Bell. A search for circularly polarized emission from young exoplanets. *Monthly Notices of the Royal Astronomical Society*, 467(3):3447–3453, 5 2017.

[187] R. J. MacDowall, S. D. Bale, L. Demaio, N. Gopalswamy, D. L. Jones, M. L. Kaiser, J. C. Kasper, M. J. Reiner, and K. W. Weiler. Solar Imaging Radio Array (SIRA): A multi-spacecraft mission. In G. J. Komar, J. Wang, and T. Kimura, editors, *Enabling Sensor and Platform Technologies for Spaceborne Remote Sensing*, volume 5659, pages 284–292. 1 2005.

[188] V. V. Makarov. A Substellar Companion to van Maanen 2. *The Astrophysical Journal*, 600(1):L71–L73, 1 2004.

[189] K. A. Marsh, E. L. Wright, J. D. Kirkpatrick, C. R. Gelino, M. C. Cushing, R. L. Griffith, M. F. Skrutskie, and P. R. Eisenhardt. Parallaxes and Proper Motions of Ultracool Brown Dwarfs of Spectral Types Y and Late T. *The Astrophysical Journal, Volume 762, Issue 2, article id. 119, 9 pp. (2013).*, 762, 11 2012.

[190] P. L. Martin, J. D. Bray, A. M. M. Scaife, I. B. A., K. A., and M. A. J. Limits on the validity of the thin-layer model of the ionosphere for radio interferometric calibration. *Monthly Notices of the Royal Astronomical Society*, 459(4):3525–3531, 7 2016.

[191] T. Mauch, T. Murphy, H. J. Buttery, J. Curran, R. W. Hunstead, B. Piestrzynski, J. G. Robertson, and E. M. Sadler. SUMSS: A Wide-Field Radio Imaging Survey of the Southern Sky. II. The Source Catalogue. *Monthly Notice of the Royal Astronomical Society, Volume 342, Issue 4, pp. 1117-1130.*, 342:1117–1130, 3 2003.

[192] M. Mayor and D. Queloz. A Jupiter-mass companion to a solar-type star. *Nature*, 378(6555):355–359, 11 1995.

[193] M. McLean, E. Berger, and A. Reiners. THE RADIO ACTIVITY-ROTATION RELATION OF ULTRACOOL DWARFS. *The Astrophysical Journal*, 746(1):23, 2 2012.

[194] J. P. McMullin, B. Waters, D. Schiebel, W. Young, K. Golap, J. P. McMullin, B. Waters, D. Schiebel, W. Young, and K. Golap. CASA Architecture and Applications. *Astronomical Data Analysis Software and Systems XVI (ASP Conference Series 376*, 376:127, 2007.

[195] J. Meloling, J. W. Rockway, M. P. Daly, A. R. Monges, J. C. Allen, W. R. Nielsen, P. M. Mcginnis, R. B. Thompson, and N. A. Mozaffar. An Advanced HF

Direction Finding Vector-Sensing Antenna System. Technical Report January, SPAWAR System Center Technical Report 2069, 2015.

[196] H. Meusinger, R.-D. Scholz, and H. Jahreiss. SPECTROSCOPIC DETECTION OF A SPECTACULAR FLARE ON DX Cn. *COMMISSIONS 27 AND 42 OF THE IAU INFORMATION BULLETIN ON VARIABLE STARS*, 5755, 2007.

[197] M. A. Million and C. K. Goertz. Prediction of radio frequency power generation of Neptune's magnetosphere from generalized radiometric Bode's law. *Geophysical Research Letters*, 15(1):111–113, 1 1988.

[198] . Mohan and . Rafferty. PyBDSM: Python Blob Detection and Source Measurement. *Astrophysics Source Code Library*, 2015.

[199] D. Montes, J. López-Santiago, M. Gálvez, M. Fernández-Figueroa, E. De Castro, and M. Cornide. Late-type members of young stellar kinematic groups - I. Single stars. *Monthly Notices of the Royal Astronomical Society*, 328(1):45–63, 11 2001.

[200] T. Moon. The expectation-maximization algorithm. *IEEE Signal Processing Magazine*, 13(6):47–60, 1996.

[201] W. B. Moore. Tidal heating and convection in Io. *Journal of Geophysical Research*, 108(E8):5096, 2003.

[202] . Morgan, . Hurley-Walker, . Wayth, and MWA. Widefield Surveys of the Low-Frequency Radio Sky with the Murchison Widefield Array. *American Astronomical Society*, 2014.

[203] J. Morin, J.-F. Donati, P. Petit, X. Delfosse, T. Forveille, and M. M. Jardine. Large-scale magnetic topologies of late M dwarfs. *Mon. Not. R. Astron. Soc*, 407:2269–2286, 2010.

[204] C. Moutou, G. Hébrard, F. Bouchy, A. Eggenberger, I. Boisse, X. Bonfils, D. Gravallon, D. Ehrenreich, T. Forveille, X. Delfosse, M. Desort, A.-M. Lagrange, C. Lovis, M. Mayor, F. Pepe, C. Perrier, F. Pont, D. Queloz, N. C. Santos, D. Ségransan, S. Udry, and A. Vidal-Madjar. Photometric and spectroscopic detection of the primary transit of the 111-day-period planet HD80606b. *Astronomy and Astrophysics*, 498(1):L5–L8, 4 2009.

[205] G. D. Mulders, I. Pascucci, and D. Apai. AN INCREASE IN THE MASS OF PLANETARY SYSTEMS AROUND LOWER-MASS STARS. *The Astrophysical Journal*, 814(2):130, 11 2015.

[206] D. Murphy and M. Lacy. VLA Sky Survey Science Website.

[207] S. J. Murphy, H. Shibahashi, and D. W. Kurtz. Super-Nyquist asteroseismology with the Kepler Space Telescope. *Monthly Notices of the Royal Astronomical Society*, 430(4):2986–2998, 2 2013.

[208] T. Murphy, M. E. Bell, D. L. Kaplan, B. M. Gaensler, A. R. Offringa, E. Lenc, N. Hurley-Walker, G. Bernardi, J. D. Bowman, F. Briggs, R. J. Cappallo, B. E. Corey, A. A. Deshpande, D. Emrich, R. Goeke, L. J. Greenhill, B. J. Hazelton, J. N. Hewitt, M. Johnston-Hollitt, J. C. Kasper, E. Kratzenberg, C. J. Lonsdale, M. J. Lynch, S. R. McWhirter, D. A. Mitchell, M. F. Morales, E. Morgan, D. Oberoi, S. M. Ord, T. Prabu, A. E. E. Rogers, D. A. Roshi, N. U. Shankar, K. S. Srivani, R. Subrahmanyan, S. J. Tingay, M. Waterson, R. B. Wayth, R. L. Webster, A. R. Whitney, A. Williams, and C. L. Williams. Limits on low-frequency radio emission from southern exoplanets with the Murchison Widefield Array. *Monthly Notices of the Royal Astronomical Society*, 446(3):2560–2565, 11 2014.

[209] T. Murphy, M. E. Bell, D. L. Kaplan, B. M. Gaensler, A. R. Offringa, E. Lenc, N. Hurley-Walker, G. Bernardi, J. D. Bowman, F. Briggs, R. J. Cappallo, B. E. Corey, A. A. Deshpande, D. Emrich, R. Goeke, L. J. Greenhill, B. J. Hazelton, J. N. Hewitt, M. Johnston-Hollitt, J. C. Kasper, E. Kratzenberg, C. J. Lonsdale, M. J. Lynch, S. R. McWhirter, D. A. Mitchell, M. F. Morales, E. Morgan, D. Oberoi, S. M. Ord, T. Prabu, A. E. E. Rogers, D. A. Roshi, N. U. Shankar, K. S. Srivani, R. Subrahmanyan, S. J. Tingay, M. Waterson, R. B. Wayth, R. L. Webster, A. R. Whitney, A. Williams, and C. L. Williams. Limits on low-frequency radio emission from southern exoplanets with the Murchison Widefield Array. *MNRAS*, 446(3):2560–2565, 11 2015.

[210] D. Naef, D. W. Latham, M. Mayor, T. Mazeh, J. L. Beuzit, G. A. Drukier, D. Queloz, J. P. Sivan, G. Torres, S. Udry, S. Zucker, C. Perrier-Bellet, D. Queloz, J. P. Sivan, G. Torres, S. Udry, and S. Zucker. HD 80606 b, a planet on an extremely elongated orbit. *Astronomy and Astrophysics*, 375(2):L27–L30, 8 2001.

[211] D. Naef, M. Mayor, G. L. Curto, F. Bouchy, C. Lovis, C. Moutou, W. Benz, F. Pepe, D. Queloz, N. C. Santos, D. Segransan, S. Udry, X. Bonfils, X. Delfosse, T. Forveille, G. Hebrard, C. Mordasini, C. Perrier, I. Boisse, and D. Sosnowska. The HARPS search for southern extrasolar planets. XXIII. 8 planetary companions to low-activity solar-type stars. *arXiv preprint arXiv: ...*, 15:8, 2010.

[212] T. Nakajima and J.-I. Morino. POTENTIAL MEMBERS OF STELLAR KINEMATIC GROUPS WITHIN 30 pc OF THE SUN. *The Astronomical Journal*, 143(1):2, 1 2012.

[213] T. Nakajima, B. R. Oppenheimer, S. R. Kulkarni, D. A. Golimowski, K. Matthews, and S. T. Durrance. Discovery of a cool brown dwarf. *Nature*, 378(6556):463–465, 11 1995.

[214] A. Nehorai, K. C. Ho, and B. T. G. Tan. Minimum-noise-variance beamformer with an electromagnetic vector sensor. *IEEE Transactions on Signal Processing*, 47(3):601–618, 1999.

[215] A. Nehorai and E. Paldi. Vector-sensor array processing for electromagnetic source localization. *IEEE Transactions on Signal Processing*, 42(2):376–398, 1994.

[216] J. D. Nichols. Candidates for detecting exoplanetary radio emissions generated by magnetosphere-ionosphere coupling. 9 2012.

[217] R. P. Norris A, A. M. Hopkins B, J. C. Afonso, S. A. Brown, J. J. Condon D, L. E. Dunne, I. A. Feain, R. A. Hollow, M. F. Jarvis, M. G. Johnston-Hollitt, E. A. Lenc, E. H. Middelberg, P. I. Padovani, I. J. Prandoni, L. K. Rudnick, N. L. Seymour, G. M. Umana, H. N. Andernach, D. M. Alexander U, P. N. Appleton O, D. P. Bacon, J. A. Banfield, W. Q. Becker, M. J. I Brown R, P. S. Ciliegi, C. A. Jackson, S. T. Eales, A. C. Edge U, B. M. Gaensler V, G. J. Giovannini, C. A. Hales A, P. V. Hancock, M. T. Huynh W, E. X. Ibar, R. J. Ivison X, R. Z. Kennicutt, A. E. Kimball D, A. M. Koekemoer AA, B. S. Koribalski A, A. R. L opez-S anchez B, M. Y. Mao A, T. V. Murphy, H. C. Messias, K. A. Pimbblet R, A. P. Raccanelli, K. E. Randall A, T. H. Reiprich AD, I. G. Roseboom AE, D. J. Saikia AG, R. G. Sharp AH, O. B. Slee A, I. U. Smail, M. A. Thompson F, J. S. Urquhart A, J. V. Wall AI, and G.-b. P. Zhao. EMU: Evolutionary Map of the Universe. *Publications of the Astronomical Society of Australia*, 28:215–248, 2011.

[218] R. W. Noyes, L. W. Hartmann, S. L. Baliunas, D. K. Duncan, and A. H. Vaughan. Rotation, convection, and magnetic activity in lower main-sequence stars. *The Astrophysical Journal*, 279:763, 4 1984.

[219] D. Oberoi and J.-L. Pinçon. A new design for a very low frequency space borne radio interferometer. In *American Geophysical Union Fall Meeting*, number 1988, page 17, 12 2003.

[220] F. Ochsenbein, P. Bauer, and J. Marcout. The VizieR database of astronomical catalogues. *Astronomy and Astrophysics Supplement Series*, 143(1):23–32, 4 2000.

[221] C. P. O'Dea and W. B. McKinnon. VLA observations of radio sources near Wolf 359. *Publications of the Astronomical Society of the Pacific*, 99:1039, 10 1987.

[222] A. R. Offringa, A. G. de Bruyn, S. Zaroubi, and M. Biehl. A LOFAR RFI detection pipeline and its first results. 7 2010.

[223] A. R. Offringa, B. McKinley, N. Hurley-Walker, F. H. Briggs, R. B. Wayth, D. L. Kaplan, M. E. Bell, L. Feng, A. R. Neben, J. D. Hughes, J. Rhee, T. Murphy, N. D. R. Bhat, G. Bernardi, J. D. Bowman, R. J. Cappallo, B. E. Corey, A. A. Deshpande, D. Emrich, A. Ewall-Wice, B. M. Gaensler, R. Goeke, L. J. Greenhill, B. J. Hazelton, L. Hindson, M. Johnston-Hollitt, D. C. Jacobs, J. C. Kasper, E. Kratzenberg, E. Lenc, C. J. Lonsdale, M. J. Lynch, S. R. McWhirter,

D. A. Mitchell, M. F. Morales, E. Morgan, N. Kudryavtseva, D. Oberoi, S. M. Ord, B. Pindor, P. Procopio, T. Prabu, J. Riding, D. A. Roshi, N. U. Shankar, K. S. Srivani, R. Subrahmanyan, S. J. Tingay, M. Waterson, R. L. Webster, A. R. Whitney, A. Williams, and C. L. Williams. WSClean: an implementation of a fast, generic wide-field imager for radio astronomy. 2014.

[224] P. Olson and U. R. Christensen. Dipole moment scaling for convection-driven planetary dynamos. 2006.

[225] R. A. Osten, S. L. Hawley, J. C. Allred, C. M. JohnsKrull, and C. Roark. From Radio to XRay: Flares on the dMe Flare Star EV Lacertae. *The Astrophysical Journal*, 621(1):398–416, 3 2005.

[226] P. Pal and P. P. Vaidyanathan. Nested arrays: A novel approach to array processing with enhanced degrees of freedom. *IEEE Transactions on Signal Processing*, 58(8):4167–4181, 2010.

[227] E. N. Parker and E. N. Hydromagnetic Dynamo Models. *The Astrophysical Journal*, 122:293, 9 1955.

[228] A. Parsons, D. Biesecker, D. Odstrcil, G. Millward, S. Hill, and V. Pizzo. Wang-Sheeley-Arge-Enlil Cone Model Transitions to Operations. *Space Weather*, 9(3):n/a–n/a, 3 2011.

[229] A. A. Pavlov, A. K. Pavlov, M. J. Mills, V. M. Ostryakov, G. I. Vasilyev, and O. B. Toon. Catastrophic ozone loss during passage of the Solar system through an interstellar cloud. *Geophysical Research Letters*, 32(1):L01815, 1 2005.

[230] S. J. Peale and P. Cassen. Contribution of tidal dissipation to lunar thermal history. *Icarus*, 36(2):245–269, 1978.

[231] S. J. Peale, P. Cassen, and R. T. Reynolds. Melting of Io by Tidal Dissipation. *Science*, 203(2), 1979.

[232] B. R. Pettersen. Discovery of Flare Activity on the Very Low Luminosity Red Dwarf G 51-15. *A&A*, 95:135–137, 1980.

[233] . Pilkington and . Scott. A survey of radio sources between declinations 20° and 40°. *Memoirs of the Royal Astronomical Society*, 69, 1965.

[234] E. Polisensky, W. M. Lane, S. D. Hyman, N. E. Kassim, S. Giacintucci, T. E. Clarke, W. D. Cotton, E. Cleland, and D. A. Frail. EXPLORING THE TRANSIENT RADIO SKY WITH VLITE: EARLY RESULTS. *The Astrophysical Journal*, 832, 2016.

[235] R. Prangé, L. Pallier, K. C. Hansen, R. Howard, A. Vourlidas, R. Courtin, and C. Parkinson. An interplanetary shock traced by planetary auroral storms from the Sun to Saturn. *Nature*, 432(7013):78–81, 11 2004.

[236] R. Prangé, P. Zarka, G. E. Ballester, T. A. Livengood, L. Denis, T. Carr, F. Reyes, S. J. Bame, and H. W. Moos. Correlated variations of UV and radio emissions during an outstanding Jovian auroral event. *Journal of Geophysical Research*, 98(E10):18779, 10 1993.

[237] D. Queloz, G. W. Henry, J. P. Sivan, S. L. Baliunas, J. L. Beuzit, R. A. Donahue, M. Mayor, D. Naef, C. Perrier, and S. Udry. No planet for HD 166435. *Astronomy and Astrophysics*, 379(1):279–287, 11 2001.

[238] D. Rafferty and N. Mohan. PyBDSM Documentation, 2012.

[239] G. Ramsay, J. G. Doyle, P. Hakala, D. Garcia-Alvarez, A. Brooks, T. Barclay, and M. Still. Short-duration high-amplitude flares detected on the M dwarf star KIC 5474065. *Monthly Notices of the Royal Astronomical Society*, 434(3):2451–2457, 9 2013.

[240] A. P. Rao. Ionospheric Effects in Radio Astronomy. In *Low Frequency Radio Astronomy*, volume 3, chapter 16, pages 1–8. NCRA, TIFR.

[241] R. Redmer, T. R. Mattsson, N. Nettelmann, and M. French. The phase diagram of water and the magnetic fields of Uranus and Neptune. *Icarus*, 211(1):798–803, 1 2011.

[242] H. Rein. A proposal for community driven and decentralized astronomical databases and the Open Exoplanet Catalogue. *arXiv.org*, 1211:7121, 11 2012.

[243] A. Reiners and U. R. Christensen. A magnetic field evolution scenario for brown dwarfs and giant planets. page 7, 7 2010.

[244] A. Reiners, J. H. M. M. Schmitt, and C. Liefke. Rapid magnetic flux variability on the flare star CN Leonis. *Astronomy and Astrophysics, Volume 466, Issue 2, May I 2007, pp.L13-L16*, 466:L13–L16, 3 2007.

[245] F. Robey, M. Knapp, A. Fenn, M. Silver, K. Johnson, F. Lind, R. Volz, S. Seager, and F. Neylon-Azad. High Frequency (HF) Radio Astronomy from a Small Satellite. In *30th Annual AIAA/USU Conference on Small Satellites*, 2016.

[246] F. C. Robey. A Covariance Modeling Approach to Adaptive Beanmforming and Detection. *MIT Lincoln Laboratory Technical Report 918*, 1991.

[247] F. C. Robey. High Frequency Geolocation and System Characterization (HFGeo) Phase 1B Proposers' Day Briefing: HFGeo Phase 0 and Phase 1B Test and Evaluation, 2012.

[248] H. Röttgering, J. Afonso, P. Barthel, F. Batejat, P. Best, A. Bonafede, M. Brüggen, G. Brunetti, K. Chy Zy, J. Conway, E. Orrù, R. Pizzo, D. Rafferty, A. Shulevski, C. Tasse, I. Van Bemmel, B. Van Der Tol, R. Van Weeren, M. Verheijen, G. White, and M. Wise. LOFAR and APERTIF Surveys of the Radio Sky: Probing Shocks and Magnetic Fields in Galaxy Clusters. *J. Astrophys. Astr*, 32:557–566, 2011.

[249] T. Rückriemen, D. Breuer, and T. Spohn. The Fe snow regime in Ganymede's core: A deep-seated dynamo below a stable snow zone. *Journal of Geophysical Research: Planets*, 120(6):1095–1118, 6 2015.

[250] G. Rupprecht, F. Pepe, M. Mayor, D. Queloz, F. Bouchy, G. Avila, W. Benz, J.-L. Bertaux, X. Bonfils, T. Dall, B. Delabre, H. Dekker, W. Eckert, M. Fleury, A. Gilliotte, D. Gojak, J. C. Guzman, D. Kohler, J.-L. Lizon, G. Lo Curto, A. Longinotti, C. Lovis, D. Megevand, L. Pasquini, J. Reyes, J.-P. Sivan, D. Sosnowska, R. Soto, S. Udry, A. Van Kesteren, L. Weber, and U. Weilenmann. The exoplanet hunter HARPS: performance and first results. In A. F. M. Moorwood and M. Iye, editors, *Ground-based Instrumentation for Astronomy. Edited by Alan F. M. Moorwood and Iye Masanori. Proceedings of the SPIE*, volume 5492, pages 148–159, 9 2004.

[251] C. T. Russell, R. C. Elphic, and J. A. Slavin. Limits on the possible intrinsic magnetic field of Venus. *Journal of Geophysical Research*, 85(A13):8319, 12 1980.

[252] V. Ryabov, P. Zarka, and B. Ryabov. Search of exoplanetary radio signals in the presence of strong interference: enhancing sensitivity by data accumulation. *Planetary and Space Science*, 52(15):1479–1491, 12 2004.

[253] . Sabater, . Verdes-Montenegro, . Best, and LofarCollaboration. LOFAR: current status and observing opportunities. *Highlights of Spanish Astrophysics VII*, 2013.

[254] P. Saint-Hilaire, N. Vilmer, and A. Kerdraon. A DECADE OF SOLAR TYPE III RADIO BURSTS OBSERVED BY THE NANÇAY RADIOHELIOGRAPH 1998-2008. *The Astrophysical Journal*, 762(60):16, 1 2013.

[255] N. N. Samus, V. P. Goranskii, O. V. Durlevich, A. V. Zharova, E. V. Kazarovets, N. N. Kireeva, E. N. Pastukhova, D. B. Williams, and M. L. Hazen. An electronic version of the second volume of the General Catalogue of Variable Stars with improved coordinates. *Astronomy Letters*, 29(7):468–479, 7 2003.

[256] G. Schubert and K. M. Soderlund. Planetary magnetic fields: Observations and models. *Physics of the Earth and Planetary Interiors*, 187:92–108, 2011.

[257] M. Segatz, T. Spohn, M. Ross, and G. Schubert. Tidal dissipation, surface heat flow, and figure of viscoelastic models of Io. *Icarus*, 75(2):187–206, 8 1988.

[258] A. Segura, L. M. Walkowicz, V. Meadows, J. Kasting, and S. Hawley. The effect of a strong stellar flare on the atmospheric chemistry of an earth-like planet orbiting an M dwarf. *Astrobiology*, 10(7):751–71, 9 2010.

[259] A. Seiff, D. B. Kirk, S. C. Sommer, R. E. Young, R. C. Blanchard, D. W. Juergens, J. E. Lepetich, P. F. Intrieri, J. T. Findlay, and J. S. Derr. Structure of the Atmosphere of Venus up to 110 Kilometers: Preliminary Results from the

Four Pioneer Venus Entry Probes. *Science (New York, N.Y.)*, 203(4382):787–90, 2 1979.

[260] J. R. Shaw, K. Sigurdson, U.-L. Pen, A. Stebbins, and M. Sitwell. All-Sky Interferometry With Spherical Harmonic Transit Telescopes. *The Astrophysical Journal*, 781(2):57, 2014.

[261] T. Shibayama, H. Maehara, S. Notsu, Y. Notsu, T. Nagao, S. Honda, T. T. Ishii, D. Nogami, and K. Shibata. SUPERFLARES ON SOLAR-TYPE STARS OBSERVED WITH KEPLER . I. STATISTICAL PROPERTIES OF SUPERFLARES. *The Astrophysical Journal Supplement Series*, 209(1):5, 11 2013.

[262] T. W. Shimwell, H. J. A. Röttgering, P. N. Best, W. L. Williams, T. J. Dijkema, F. de Gasperin, M. J. Hardcastle, G. H. Heald, D. N. Hoang, A. Horneffer, H. Intema, E. K. Mahony, S. Mandal, A. P. Mechev, L. Morabito, J. B. R. Oonk, D. Rafferty, E. Retana-Montenegro, J. Sabater, C. Tasse, R. J. van Weeren, M. Brüggen, G. Brunetti, K. T. Chyży, J. E. Conway, M. Haverkorn, N. Jackson, M. J. Jarvis, J. P. McKean, G. K. Miley, R. Morganti, G. J. White, M. W. Wise, I. M. van Bemmel, R. Beck, M. Brienza, A. Bonafede, G. Calistro Rivera, R. Cassano, A. O. Clarke, D. Cseh, A. Deller, A. Drabent, W. van Driel, D. Engels, H. Falcke, C. Ferrari, S. Fröhlich, M. A. Garrett, J. J. Harwood, V. Heesen, M. Hoeft, C. Horellou, F. P. Israel, A. D. Kapińska, M. Kunert-Bajraszewska, D. J. McKay, N. R. Mohan, E. Orrú, R. F. Pizzo, I. Prandoni, D. J. Schwarz, A. Shulevski, M. Sipior, D. J. B. Smith, S. S. Sridhar, M. Steinmetz, A. Stroe, E. Varenius, P. P. van der Werf, J. A. Zensus, and J. T. L. Zwart. The LOFAR Two-metre Sky Survey. *Astronomy & Astrophysics*, 598:A104, 2017.

[263] B. D. Shizgal and G. G. Arkos. Nonthermal escape of the atmospheres of Venus, Earth, and Mars. *Reviews of Geophysics*, 34(4):483, 1996.

[264] D. Shulyak, A. Seifahrt, A. Reiners, O. Kochukhov, and N. Piskunov. Rotation, magnetism and metallicity of M dwarf systems. *Monthly Notices of the Royal Astronomical Society*, 418(4):2548–2557, 12 2011.

[265] S. K. Sirothia, A. L. Etangs, and N. G. Kantharia. Search for 150 MHz radio emission from extrasolar planets in the TIFR GMRT Sky Survey. 108:1–9, 2014.

[266] S. K. Sirothia, N. G. Kantharia, C. H. Ishwar-Chandra, and Gopal-Krishna. TIFR GMRT Sky Survey (TGSS), 2013.

[267] A. A. G. Smith and T. D. T. Carr. Radio-Frequency Observations of the Planets in 1957-1958. *The Astrophysical Journal*, 130:641, 9 1959.

[268] A. M. S. Smith, A. C. Cameron, J. Greaves, M. Jardine, G. Langston, and D. Backer. Secondary radio eclipse of the transiting planet HD 189733 b: an upper limit at 307-347 MHz. *Monthly Notices of the Royal Astronomical Society*, 395(1):335–341, 5 2009.

[269] D. S. Smith and J. M. Scalo. Habitable Zones Exposed: Astrosphere Collapse Frequency as a Function of Stellar Mass. *Astrobiology*, 9(7):673–681, 9 2009.

[270] E. J. Smith, L. Davis, D. E. Jones, P. J. Coleman, D. S. Colburn, P. Dyal, and C. P. Sonett. Jupiter's Magnetic Field. Magnetosphere, and Interaction with the Solar Wind: Pioneer 11. *Science*, 188(4187), 1975.

[271] E. J. Smith, L. Davis, D. E. Jones, P. J. Coleman, D. S. Colburn, P. Dyal, C. P. Sonett, and A. M. A. Frandsen. The planetary magnetic field and magnetosphere of Jupiter: Pioneer 10. *Journal of Geophysical Research*, 79(25):3501–3513, 9 1974.

[272] V. Stamenković, D. Breuer, and T. Spohn. Thermal and transport properties of mantle rock at high pressure: Applications to super-Earths. *Icarus*, 216(2):572–596, 12 2011.

[273] V. Stamenković, L. Noack, D. Breuer, and T. Spohn. the Influence of Pressure-Dependent Viscosity on the Thermal Evolution of Super-Earths. *The Astrophysical Journal*, 748:41, 2012.

[274] V. Stamenković and S. Seager. EMERGING POSSIBILITIES AND INSUPERABLE LIMITATIONS OF EXOGEOPHYSICS: THE EXAMPLE OF PLATE TECTONICS. *The Astrophysical Journal*, 825, 2016.

[275] S. Stanley and J. Bloxham. Convective-region geometry as the cause of Uranus' and Neptune's unusual magnetic fields. *Nature*, 428(6979):151–153, 3 2004.

[276] D. J. Stevenson. Reducing the non-axisymmetry of a planetary dynamo and an application to saturn. *Geophysical & Astrophysical Fluid Dynamics*, 21(1-2):113–127, 8 1982.

[277] D. J. Stevenson. Planetary magnetic fields. *Earth and Planetary Science Letters*, 208:1–11, 2003.

[278] R. J. Strangeway. Factors controlling ionospheric outflows as observed at intermediate altitudes. *Journal of Geophysical Research*, 110(A3):A03221, 2005.

[279] A. Stroe, I. A. G. Snellen, and H. J. A. Röttgering. A stringent upper limit to 18 cm radio emission from the extrasolar planet system ¡i¿τ¡/i¿ Boötis. *Astronomy & Astrophysics*, 546:A116, 10 2012.

[280] A. Suárez Mascareño, R. Rebolo, and J. I. González Hernández. Magnetic cycles and rotation periods of late-type stars from photometric time series. *Astronomy & Astrophysics*, 595:A12, 11 2016.

[281] A. Suárez Mascareño, R. Rebolo, J. I. González Hernández, and M. Esposito. Rotation periods of late-type dwarf stars from time series high-resolution spectroscopy of chromospheric indicators. *Monthly Notices of the Royal Astronomical Society*, 452(3):2745–2756, 9 2015.

[282] G. B. Taylor, C. L. Carilli, and R. A. Perley, editors. *Synthesis Imaging in Radio Astronomy II*. Astron. Soc. Pac.,, San Francisco, CA, 1999.

[283] B. J. Teegarden, S. H. Pravdo, M. Hicks, S. B. Shaklan, K. Covey, O. Fraser, S. L. Hawley, T. McGlynn, I. N. Reid, and I. N. Reid. Discovery of a New Nearby Star. *The Astrophysical Journal, Volume 589, Issue 1, pp. L51-L53.*, 589:L51–L53, 2 2003.

[284] A. R. Thompson, J. M. Moran, and G. W. Swenson. *Interferometry and Synthesis in Radio Astronomy*. New York, NY, 2001.

[285] R. A. Treumann. The electroncyclotron maser for astrophysical application. *Astron Astrophys Rev*, 13:229–315, 2006.

[286] S. D. Tun Beltran, S. Cutchin, and S. White. A New Look at Type-III Bursts and Their Use as Coronal Diagnostics. *Solar Physics*, 290(9):2423–2437, 9 2015.

[287] M. Tuomi, H. R. A. Jones, J. R. Barnes, G. Anglada-Escudé, and J. S. Jenkins. Bayesian search for low-mass planets around nearby M dwarfs estimates for occurrence rate based on global detectability statistics. *Monthly Notices of the Royal Astronomical Society*, 441(2):1545–1569, 6 2014.

[288] J. Turner, J.-M. Griessmeier, and P. Zarka. The search for radio emission from the 55 Cnc exoplanetary system using LOFAR. *American Astronomical Society, DPS meeting #48, id.122.29*, 48, 2016.

[289] J. D. Turner, J. . M. Grießmeier, P. Zarka, and I. Vasylieva. THE SEARCH FOR RADIO EMISSION FROM EXOPLANETS USING LOFAR LOW-FREQUENCY BEAM-FORMED OBSERVATIONS: DATA PIPELINE AND PRELIMINARY RESULTS FOR THE 55 CNC SYSTEM. 2017.

[290] R. Vainio, L. Desorgher, D. Heynderickx, M. Storini, E. Flückiger, R. B. Horne, G. A. Kovaltsov, K. Kudela, M. Laurenza, S. McKenna-Lawlor, H. Rothkaehl, and I. G. Usoskin. Dynamics of the Earths Particle Radiation Environment. *Space Science Reviews*, 147(3-4):187–231, 11 2009.

[291] D. Valencia, R. J. O'Connell, and D. Sasselov. Internal structure of massive terrestrial planets. *Icarus*, 181(2):545–554, 4 2006.

[292] J. A. Van Allen. The geomagnetically trapped corpuscular radiation. *Journal of Geophysical Research*, 64(11):1683–1689, 11 1959.

[293] P. van de Kamp, N. G. Gokkaya, and W. D. Heintz. Parallax, proper motion, and orbital motion of the visual binary SIG 2398. *The Astronomical Journal*, 73:361, 6 1968.

[294] S. van der Tol, B. Jeffs, and A.-J. van der Veen. Self-Calibration for the LOFAR Radio Astronomical Array. *IEEE Transactions on Signal Processing*, 55(9):4497–4510, 9 2007.

[295] G. Van Moorsel and D. Medlin. VLA CASA Calibration Pipeline Science Website, 2016.

[296] R. J. Van Weeren, W. L. Williams, M. J. Hardcastle, T. W. Shimwell, D. A. Rafferty, J. Sabater, G. Heald, S. S. Sridhar, T. J. Dijkema, G. Brunetti, M. Brüggen, F. Andrade-Santos, G. A. Ogrean, H. J. A. Röttgering, W. A. Dawson, W. R. Forman, F. De Gasperin, C. Jones, G. K. Miley, and L. Rudnick. LOFAR FACET CALIBRATION. *The Astrophysical Journal Supplement Series*, 223, 2016.

[297] A. Vanderburg, J. A. Johnson, S. Rappaport, A. Bieryla, J. Irwin, J. A. Lewis, D. Kipping, W. R. Brown, P. Dufour, D. R. Ciardi, R. Angus, L. Schaefer, D. W. Latham, D. Charbonneau, C. Beichman, J. Eastman, N. McCrady, R. A. Wittenmyer, and J. T. Wright. A disintegrating minor planet transiting a white dwarf. *Nature*, 526(7574):546–549, 2015.

[298] A. A. Vidotto, M. Jardine, J. Morin, J.-F. Donati, P. Lang, and A. J. B. Russell. Effects of M dwarf magnetic fields on potentially habitable planets. *A&A*, 557, 2013.

[299] J. Villadsen, G. Hallinan, and S. Bourke. Radio spectroscopy of stellar flares: magnetic reconnection & CME shocks in stellar coronae. *International Astronomical Union*, 2015.

[300] S. S. Vogt, R. A. Wittenmyer, R. P. Butler, S. O'Toole, G. W. Henry, E. J. Rivera, S. Meschiari, G. Laughlin, C. G. Tinney, H. R. A. Jones, J. Bailey, B. D. Carter, and K. Batygin. A SUPER-EARTH AND TWO NEPTUNES ORBITING THE NEARBY SUN-LIKE STAR 61 VIRGINIS. *The Astrophysical Journal*, 708(2):1366–1375, 1 2010.

[301] B. Vollmer, B. Gassmann, S. Derrière, T. Boch, M. Louys, F. Bonnarel, P. Dubois, F. Genova, and F. Ochsenbein. The SPECFIND V2.0 catalogue of radio cross-identifications and spectra. *Astronomy and Astrophysics*, 511:A53, 3 2010.

[302] R. Volz, M. Knapp, F. Lind, and F. Robey. Covariance Estimation in Terms of Stokes Parameters with Application to Vector Sensor Imaging. In *50th Asilomar Conference on Signals, Systems and Computers*, Pacific Grove, CA, 2016.

[303] I. Vorgul, B. J. Kellett, R. a. Cairns, R. Bingham, K. Ronald, D. C. Speirs, S. L. McConville, K. M. Gillespie, and A. D. R. Phelps. Cyclotron maser emission: Stars, planets, and laboratory. *Physics of Plasmas*, 18(5):056501, 2011.

[304] L. M. Walkowicz, G. Basri, N. Batalha, R. L. Gilliland, J. Jenkins, W. J. Borucki, D. Koch, D. Caldwell, A. K. Dupree, D. W. Latham, S. Meibom, S. Howell, T. M. Brown, and S. Bryson. White-Light Flares on Cool Stars in the Kepler Quarter 1 Data. *The Astronomical Journal*, 141(2):50, 2 2011.

[305] S. Wang, D.-H. Wu, T. Barclay, and G. P. Laughlin. UPDATED MASSES FOR THE TRAPPIST-1 PLANETS. 2017.

[306] C. L. Watson and C. L. The International Variable Star Index (VSX). *The Society for Astronomical Sciences 25th Annual Symposium on Telescope Science. Held May 23-25, 2006, at Big Bear, CA. Published by the Society for Astronomical Sciences., p.47*, 25:47, 2006.

[307] R. B. Wayth, E. Lenc, M. E. Bell, J. R. Callingham, K. S. Dwarakanath, T. M. O. Franzen, B. Q. For, B. Gaensler, P. Hancock, L. Hindson, N. Hurley-Walker, C. A. Jackson, M. Johnston-Hollitt, A. D. Kapinska, B. McKinley, J. Morgan, A. R. Offringa, P. Procopio, L. Staveley-Smith, C. Wu, Q. Zheng, C. M. Trott, G. Bernardi, J. D. Bowman, F. Briggs, R. J. Cappallo, B. E. Corey, A. A. Deshpande, D. Emrich, R. Goeke, L. J. Greenhill, B. J. Hazelton, D. L. Kaplan, J. C. Kasper, E. Kratzenberg, C. J. Lonsdale, M. J. Lynch, S. R. McWhirter, D. A. Mitchell, M. F. Morales, E. Morgan, D. Oberoi, S. M. Ord, T. Prabu, A. E. E. Rogers, A. Roshi, N. U. Shankar, K. S. Srivani, R. Subrahmanyan, S. J. Tingay, M. Waterson, R. L. Webster, A. R. Whitney, A. Williams, and C. L. Williams. GLEAM: The GaLactic and Extragalactic All-sky MWA survey. *Publications of the Astronomical Society of Australia, Volume 32, id.e025 12 pp.*, 32, 5 2015.

[308] R. R. Weber, J. K. Alexander, and R. G. Stone. The Radio Astronomy Explorer satellite, a low-frequency observatory. *Radio Science*, 6(12):1085–1097, 1971.

[309] L. M. Weiss and G. W. Marcy. THE MASS-RADIUS RELATION FOR 65 EXOPLANETS SMALLER THAN 4 EARTH RADII. *The Astrophysical Journal*, 783(1):L6, 2 2014.

[310] M. Wenger, F. Ochsenbein, D. Egret, P. Dubois, F. Bonnarel, S. Borde, F. Genova, G. Jasniewicz, S. Lalo, S. Lesteven, and R. Monier. The SIMBAD astronomical database. *Astronomy and Astrophysics Supplement Series*, 143(1):9–22, 4 2000.

[311] F. Wesemael, J. L. Greenstein, J. Liebert, R. Lamontagne, G. Fontaine, P. Bergeron, and J. W. Glaspey. An atlas of optical spectra of white-dwarf stars. *Publications of the Astronomical Society of the Pacific*, 105(689):761, 7 1993.

[312] A. A. West, S. L. Hawley, L. M. Walkowicz, K. R. Covey, N. M. Silvestri, S. N. Raymond, H. C. Harris, J. A. Munn, P. M. McGehee, . Ivezić, and J. Brinkmann. Spectroscopic Properties of Cool Stars in the Sloan Digital Sky Survey: An Analysis of Magnetic Activity and a Search for Subdwarfs. *The Astronomical Journal*, 128(1):426–436, 7 2004.

[313] S. M. White, P. D. Jackson, and M. R. Kundu. A VLA survey of nearby flare stars. *The Astrophysical Journal Supplement Series*, 71:895, 12 1989.

[314] I. Wienbrucb and T. Spobn. A self sustained magnetic field on IO? 43:1035–1057.

[315] A. J. Willes and K. Wu. Electron-cyclotron maser emission from white-dwarf pairs and white-dwarf planetary systems. *Mon. Not. R. Astron. Soc*, 348:285–296, 2 2004.

[316] D. R. Williams. Planetary Fact Sheet, 2017.

[317] P. K. G. Williams, B. A. Cook, and E. Berger. TRENDS IN ULTRACOOL DWARF MAGNETISM. I. X-RAY SUPPRESSION AND RADIO ENHANCEMENT. *The Astrophysical Journal*, 785(920pp), 2014.

[318] R. F. Willson, K. R. Lang, and P. Foster. VLA observations of dwarf M flare stars and magnetic stars. *Astronomy and Astrophysics (ISSN 0004-6361), vol. 199, no. 1-2, June 1988, p. 255-261.*, 199(1-2):255–261, 1988.

[319] R. M. Winglee, G. A. Dulk, and T. S. Bastian. A search for cyclotron maser radiation from substellar and planet-like companions of nearby stars. *The Astrophysical Journal*, 309:L59, 10 1986.

[320] L. M. Winter and K. Ledbetter. Type II and Type III Radio Bursts and Their Correlation With Solar Energetic Proton Events. *The Astrophysical Journal*, 809(1):105, 2015.

[321] D. Winterhalter, T. Kuiper, W. Majid, I. Chandra, J. Lazio, P. Zarka, C. Naudet, G. Bryden, W. Gonzalez, and R. Treumann. Search for Radio Emissions from Extrasolar Planets: the Observation Campaign. In H. Rucker, W. Kurth, and G. Mann, editors, *Planetary Radio Emissions VI*, page 595. Verl. d. Osterr. Akad. d. Wiss, 2006.

[322] D. Winterhalter, W. Majid, T. Kuiper, C. Naudet, G. Bryden, I. Chandra, Y. Gupta, J. Lazio, P. Zarka, and W. Gonzalez. Search for Radio Emissions from Extrasolar Planets at 150 MHz. *American Astronomical Society Meeting Abstracts*, 207:77, 12 2005.

[323] D. Winterhalter, E. J. Smith, and R. J. Marquedant. The compact electric and magnetic sensor. In B. Tsurutani, editor, *Small Instruments for Space Physics*, pages 2–33. Pasadena, CA, 1993.

[324] A. Wolszczan and D. A. Frail. A planetary system around the millisecond pulsar PSR1257 + 12. *Nature*, 355(6356):145–147, 1 1992.

[325] K. T. Wong and M. D. Zoltowski. Uni-Vector-Sensor ESPRIT for Multisource Azimuth, Elevation, and Polarization Estimation. *IEEE Transactions on Antennas and Propagation*, 45(10):1467–1474, 1997.

[326] K. T. Wong and M. D. Zoltowski. Closed-form direction finding and polarization estimation with arbitrarily spaced electromagnetic vector-sensors at unknown locations. *IEEE Transactions on Antennas and Propagation*, 48(5):671–681, 2000.

[327] Y. Wu and N. Murray. Planet Migration and Binary Companions: The Case of HD 80606b. *The Astrophysical Journal*, 589(1):605–614, 5 2003.

[328] M. C. Wyatt, G. Kennedy, B. Sibthorpe, A. Moro-Martin, J. F. Lestrade, R. J. Ivison, B. Matthews, S. Udry, J. S. Greaves, P. Kalas, S. Lawler, K. Y. L. Su, G. H. Rieke, M. Booth, G. Bryden, J. Horner, J. J. Kavelaars, and D. Wilner. Herschel imaging of 61 Vir: implications for the prevalence of debris in low-mass planetary systems. page 20, 6 2012.

[329] W. F. Yantis, I. Sullivan, W. T., and W. C. Erickson. A Search for Extra-Solar Jovian Planets by Radio Techniques. *Bulletin of the American Astronomical Society, Vol. 9, p.453*, 9:453, 1977.

[330] V. P. Zalinian, H. M. Tovmassian, O. Cardona, and M. Chavez. Observations of Flare Stars V577 Mon and AD Leo. *Information Bulletin on Variable Stars, No. 5272, #1.*, 5272, 2002.

[331] P. Zarka. The auroral radio emissions from planetary magnetospheres: What do we know, what don't we know, what do we learn from them? *Advances in Space Research*, 12(8):99–115, 8 1992.

[332] P. Zarka. Auroral radio emissions at the outer planets: Observations and theories. *Journal of Geophysical Research*, 103(E9):20159, 8 1998.

[333] P. Zarka. Radio and plasma waves at the outer planets. *Advances in Space Research*, 33(11):2045–2060, 1 2004.

[334] P. Zarka. Plasma interactions of exoplanets with their parent star and associated radio emissions. *Planetary and Space Science*, 55(5):598–617, 4 2007.

[335] P. Zarka, J. W. Lazio, and G. Hallinan. Magnetospheric Radio Emissions from Exoplanets with the SKA.

[336] P. Zarka, J. Queinnec, B. P. Ryabov, V. B. Ryabov, V. A. Shevchenko, A. V. Arkhipov, H. O. Rucker, L. Denis, A. Gerbault, P. Dierich, and C. Rosolen. GROUND-BASED HIGH SENSITIVITY RADIO ASTRONOMY AT DECAMETER WAVELENGTHS. *Austrian Acad. Sci. Press*, 1997.

[337] P. Zarka, R. A. Treumann, B. P. Ryabov, V. B. Ryabov, P. Zarka, R. A. Treumann, B. P. V. B. Ryabov, and B. P. V. B. Ryabov. Magnetically-Driven Planetary Radio Emissions and Application to Extrasolar Planets. *Astrophysics and Space Science*, 277(1/2):293–300, 2001.

Appendix A

List of Acronyms

AAVSO	American Association of Variable Star Observers
ADC	Analog-to-Digital Converter
AGI	Analytical Graphics, Inc. (maker of STK)
AKR	Auroral Kilometric Radiation (same as TKR)
ALMA	Atacama Large Millimeter/submillimeter Array
AO	Adaptive Optics
ASTRON	Netherlands Institute for Radio Astronomy
AU	Astronomical Unit
AWS	Amazon Web Services
CASA	Common Astronomy Software Applications [194]
CMB	Core-Mantle Boundary
CME	Coronal Mass Ejection
CMI	Cyclotron Maser Instability [52]
DAM	Decametric
DEBRIS	Disc Emission via a Bias-free Reconnaissance in the Infrared/Submillimetre
DI	Dynamo Index
DEVS	Deployable Vector Sensor

DIM	Decimetric
EM	Electromagnetic
EMI	Electromagnetic Interference
EMVS	Electromagnetic Vector Sensor
EUV	Extreme Ultraviolet
FIRST	Faint Images of the Radio Sky at Twenty cm [19]
FITS	Flexible Image Transport System
FOV	Field of View
FX	
GB	Gigabyte
GCR	Galactic Cosmic Rays
GEO	Geosynchronous (orbit)
GLEAM	Glactic and Extragalacitc All-sky MWA (Survey) [307]
GMRT	Giant Metrewave Radio Telescope [164]
GPS	Global Positioning System
HBA	High Band Array (LOFAR)
HD	Henry Draper (catalog) [46]
HeRO	Helosphysics Radio Observer
IPM	Interplanetary Medium
IR	Infrared
IRTF	Infrared Telescope Facility
ISM	Interstellar Medium
LBA	Low Band Array (LOFAR)
LHCP	Left Hand Circularly Polarized
LNA	Low Noise Amplifier
LOFAR	Low Frequency Array [65]
LoSoTo	LOFAR Solutions Tool
LTA	Long Term Archive (LOFAR)
LWA	Long Wavelength Array [82]

MFS	Multi-frequency Synthesis
MS	Measurement Set
MSSS	Multifrequency Snapshot Sky Survey [132]
MWA	Murchison Widefield Array [179]
NDPPP	New Default Pre-Processing Pipeline (LOFAR)
NIST	National Institute of Standards and Technology
NKR	Neptunian Kilometric Radiation
NRAO	National Radio Astronomy Observatory
NRL	Naval Research Laboratory
NVSS	NRAO VLA Sky Survey [55]
OVRO LWA	Owens Valley Radio Observatory Long Wavelength Array [126]
pc	parsec
PI	Principal Investigator
PiLL	Pipeline for LOFAR LBA
PSF	Point Spread Function
PT	Plate Tectonics
PyBDSM	Python Blob Detection and Source Detector (earlier name of PyBDSF)
PyBDSF	Python Blob Detection and Source Finder [198]
RAE-2	Radio Astronomy Explorer-2 []
RAPID	Radio Array of Portable Interferometric Detectors [177]
RFI	Radio Frequency Interference
RHCP	Right Hand Circularly Polarized
RMS	Root Mean Square
ROSAT	Rntgensatellit
SB	Sub-band
S-GEO	Skewed Geosynchronous (orbit)
SEFD	System Equivalent Flux Density
SEP	Solar Energetic Particles

SINR	Signal-to-Interference plus Noise Ratio
SKA	Square Kilometre Array [73]
SKALA	SKA Log-periodic Antenna [62]
SKR	Saturnian Kilometric Radiation
SIMBAD	Set of Identifications, Measurements and Bibliography for Astronomical Data [310]
SL	Stagnant Lid
SNR	Signal-to-Noise Ratio
SPAM	Source Peeling and Atmosphere Modeling [139]
SSD	Solid State Disk
STEREO	Solar Terrestrial Relations Observatory [148]
STK	System Tool Kit
T1	TRAPPIST-1 abbrv.
TAC	Time Allocation Committee
TB	Terabyte
TEC	Total Electron Content
TGSS	TFIR GMRT Sky Survey [265]
TGSS ADR1	TGSS Alternative Data Release 1 [140]
TKR	Terrestria Kilometric Radiation (same as AKR)
TFIR	Tata Institute of Fundamental Research
TRAPPIST	Transiting Planets and Planetesimals Small Telescope
TTV	Transit Timing Variations
UKIDSS	United Kingdom Infrared Telescope Deep Sky Survey
UKR	Uranian Kilometric Radiation
UGPS	UKIDSS Galactic Plane Survey [181]
UV	Ultraviolet
VLA	Very Large Array
VLBA	Very Long Baseline Array
VLBI	Very Long Baseline Interferometry

VLITE	VLA Low Band Ionospheric and Transient Experiment [234]
VLSS	VLA Low-frequency Sky Survey
VLSSr	VLA Low-frequency Sky Survey redux [166]
VO	Virtual Observatory
VS	Vector Sensor
WSClean	W-Stacking CLEAN [223]
WSRT	Westerbork Synthesis Radio Telescope
XUV	X-ray/UV
ZDI	Zeeman Doppler Imaging